Contact Maturing and Aging of Silica Sand

by

Zhijie Wang

A dissertation submitted in partial fulfillment
of the requirements for the degree of
Doctor of Philosophy
(Civil Engineering)
in the University of Michigan
2017

Doctoral Committee:

Professor Radoslaw L. Michalowski, Chair
Associate Professor Adda Athanasopoulos-Zekkos
Professor James R. Barber
Professor Roman D. Hryciw

DEDICATION

To my family

Acknowledgements

I would like to express my deepest gratitude to my advisor, Professor Radoslaw Michalowski, for his guidance on my research. He has led me through a challenging, thought-provoking and rewarding journey with his exceptional knowledge, curiosity, enthusiasm, and patience.

My deep appreciation also goes to my dissertation committee, consisting of Associate Professor Adda Athanasopoulos-Zekkos, Professor James Barber, and Professor Roman Hryciw, for their valuable suggestions as my studies progressed from a preliminary idea to a completed dissertation. I would also like to thank Professor Emeritus Richard Woods, Associate Professor Dimitrios Zekkos, Professor Jerome Lynch and Professor Wei Lu for their interesting and educating classes.

I am very grateful to the organizations and individuals that have supported this research in various forms. Through the Itasca Education Partnership, I have been granted access to the PFC2D/3D software suites from Itasca Consulting Group and have received priceless advice on the distinct element method from Dr. David Potyondy. I would like to thank the Michigan Center for Materials Characterization for use of the instruments and staff assistance. Special thanks go to Mr. Merrick Burch for his assistance in the design and construction of my laboratory testing apparatus. I am indebted to Dr. Srinivasa Nadukuru for mentoring me on laboratory testing. I am also thankful for the inspiring tutoring on dissertation writing I received from Dr. Elizabeth Hildinger.

My sincere thanks also go to the friends who have made my study, research and life in Ann Arbor enjoyable. I thoroughly enjoyed the friendship and academic teamwork with Dr. Xunchang Fei, Junxing Zheng, Athena Grizi, Jon Hubler, Dr. Clinton Carlson, and Dowon Park. I also want to thank Professor Michalowski and his wife, Mrs. Kari Michalowski, for inviting me to numerous delightful holiday gatherings.

Finally, I cannot say enough thank you to my parents, my sister and my brother-in-law, for their constantly unconditional love, support, and confidence in me.

Contents

List of Figures

List of Tables

Abstract

For more than three decades, sand has been observed to alter its engineering properties over time, but no consensus has been reached on the driving mechanisms behind this phenomenon. Silica sand freshly deposited or after recent disturbance tends to undergo delayed changes in small strain stiffness, penetration resistance, or liquefaction resistance. In the same category of phenomena is a delayed increase of the shaft resistance of displacement piles after installation (pile setup). Micromechanical behavior at grain scale and the contact scale is coming to be understood as the most plausible mechanism among the proposals suggested in the available literature, but only very limited research has been conducted at the contact scale in studies of sand aging.

A *static fatigue hypothesis* is advocated in this thesis; it suggests that delayed fracturing of micro-morphological features on grain surfaces at contacts, such as asperities and mineral debris, is a key contributor to aging of silica sand. The static fatigue process at inter-grain contacts induces changes in micromechanical properties of the contacts, a process termed *maturing* in this research, and it triggers rearrangements of sand grains over time. Maturing of contacts and rearrangement of grains are hypothesized to be the cause of the observed changes in macroscopic engineering properties of sand over time. To support this hypothesis, this research focuses on exploring micromechanical behavior of inter-grain contacts through micro-scale experiments complemented with numerical simulations.

The following major tasks were accomplished:

(1) Micro-scale laboratory experiments were conducted to study time-dependent response of inter-grain contacts under sustained loads; they produced the first set of data of its kind.

(2) Laboratory experiments on sand grain assemblies were performed to provide evidence that the contact behavior induces aging effects in sand; factors affecting rates of aging, such as loads, pore fluid acidity and grain sizes were explored.

(3) Simulations of a single inter-grain contact were performed with the distinct element method, and possible consequences of contact fatigue/maturing were demonstrated.

(4) Finally, a preliminary finite element framework was developed to explore the evolution of grain surface textures to shed light on the effects of pore fluid chemistry on aging rates.

Chapter 1

Introduction

1.1. Background and Motivation

Although sand aging has been a well-documented phenomenon for more than three decades, no consensus has been reached on what the driving mechanism is. The aging phenomenon, especially pronounced in freshly disturbed or deposited silica sand, has been manifested as continued changes in engineering properties of sand such as stiffness, penetration resistance, liquefaction resistance, and bearing capacity of driven piles (Afifi and Woods 1971, Seed 1979, Mitchell and Solymar 1984, Dowding and Hryciw 1986, Chow et al. 1997, and Leon et al. 2006). Most of the observed changes are beneficial and the aging effects could be employed in engineering practice if the changes could be predicted. However, reliable predictions are impossible without thorough understanding of the mechanisms causing the aging effects in sand.

Various hypotheses have been proposed to explain the observed time-delayed effects in silica sand to loads. The major hypotheses are buildup of chemical cementations at contacts due to mineral deposition (Mitchell and Solymar 1984), structuration process of grains (Mesri et al. 1990, Schmertmann 1991, and Bowman and Soga 2003), and time-dependent fracturing of grains (Lade and Karimpour 2010). Other hypotheses were also proposed to explain time-dependent

effects under special circumstances, such as gas dissipation after blasting (Hryciw 1986) and microbiological processes (Kroll 1990, Mitchell and Santamarina 2005, and DeJong et al. 2006). Among the hypotheses, the structuration process of grains is the most widely accepted mechanism, which is associated with increased interlocking of grains and grain surface features (asperities). . However, no explanation is available as to what causes continued restructuration of grains, especially under low stress levels when crushing of grains does not occur.

Some researchers have used micromechanical processes of sand grains and inter-grain contacts to enhance understanding and predictions of aging effects. Distinct element modeling (DEM) has been used to incorporate micromechanical behavior of contacts to models of grain assemblies and to reproduce the observed aging behavior in sand (Kuhn 1987, Wang et al. 2008, Suarez 2009, Kwok and Bolton 2010). However, the micromechanics in sand was described with *a priori* constitutive models that have not been backed by grain-scale laboratory studies. Improved understanding of micromechanical behavior at the contact scale will lead to better understanding of aging effects in sand and better predictions of the consequences of aging effects.

A *static fatigue hypothesis* is advocated in this thesis, which suggests that delayed fracturing of micro-morphological features on grain surfaces at contacts, such as asperities and mineral debris, is a key contributor to aging of silica sand. The static fatigue process at inter-grain contacts induces changes in micromechanical properties of the contacts and triggers minute changes in configuration of grain, referred to often as structuration. In turn, these changes cause the macroscopic engineering properties of sand to change over time. Of primary importance in this hypothesis is the behavior of an intergranular contacts under sustained load. To gain evidence supporting this hypothesis, laboratory experiments at grain-scale and sample-scale were carried out. The granular assembly-scale experiments were performed under variety of conditions (for instance, various pore fluid acidity) to explore factors affecting rates of aging. Simulations with the distinct element method (DEM) of a single inter-grain contact were performed. The model was calibrated with the a single-contact testing. The outcomes of simulations was consistent with the static fatigue hypothesis. Finally, a preliminary finite element framework was developed based on an interface migration theory to explore the evolution of grain surface textures under a combined

influence of stress and chemical reactions, to shed light on the effects of pore fluid chemistry on rates of aging.

1.2.   Organization of Dissertation

This dissertation is organized into eight chapters.

In Chapter 2, a literature review is presented on previous research focusing on aging effects in sand. The chapter is organized by: (1) the reported field and laboratory observations of time-dependent changes of sand behavior, (2) numerical simulations of aging effects, and (3) the driving mechanisms of sand aging proposed by previous researchers.

Chapter 3 gives a detailed description of the static fatigue hypothesis and the objectives of this thesis. This hypothesis states that the delayed fracturing of micro-morphological features (such as asperities) at sand grain surfaces under loading is the key cause of sand aging.

Grain-scale experiments and observations from these experiments are presented in Chapter 4. A microscopic laboratory test was developed to investigate time-dependent response of single sand grains subjected to sustained loads. The observed rates of deformation over time showed a strong dependency of time-dependent behavior on roughness of the grain surfaces. The test results provided support for the static fatigue hypothesis.

Soft-ring oedometer tests, introduced in Chapter 5, were conducted to analyze time-dependent settlement and increase in horizontal stress in sand grain assemblies. Tests were performed with sand samples with different particle sizes. Both dry and saturated samples were tested; pore fluids with different pH values were used in the saturated samples. The results showed that the rates of settlement and time-dependent increase in horizontal stress in the samples were significantly affected by particle sizes, the presence of pore fluid, and pH of the pore fluid. The testing results are presented and discussed.

Chapter 6 presents the method, implementations, and results of distinct element method simulations of an individual inter-grain contactSand grains were simulated as groups of sub-

3

particles bonded together and a stress corrosion model was used to allow static fatigue of the grain material. The model was calibrated with the laboratory single-grain test, and then a contact between two grains was simulated. The simulation results showed development of static fatigue fracturing and the evolution of load transferring at inter-grain contacts over time. Based on the simulation results, changes in mechanical properties of an inter-grain contact over time was discussed and the conclusions supported the static fatigue hypothesis.

A finite element modeling (FEM) framework was developed to investigate the evolution of surface textures of sand grains during aging in a coupled chemo-mechanical environment, and this is described in Chapter 7. The simulations helped explain effects of chemical properties of pore fluids on rates of aging effects, as observed in the sample-scale experiments. The FEM framework was developed based on an interface migration theory. The usefulness of the framework was tested with preliminary qualitative simulations. The simulation results demonstrated patterns of evolution of the geometry of a surface, and indicated that the evolution might be accelerated by an angular surface texture and presence of surface mechanical loads.

Finally, Chapter 8 gives a summary of work accomplished and the conclusions from each chapter.

Chapter 2

Literature Review

Aging effects in sand have attracted wide attention since Mitchell and Solymar (1984) reported surprising behavior of sand over time after it was densified by blasting and vibrocompaction at the Jebba Dam site in Nigeria. The three decades after this observation to date, a lot more observations, from both the field and laboratory, have been reported by many researchers, on different aspects of time-dependent sand behavior. Numerical simulations, especially the discrete element method (DEM), have been employed to improve understanding of the observed aging effects. Based on the observations and simulations, a variety of different driving mechanisms have been proposed.

2.1. Field/Laboratory Observations

So far, reported field and laboratory observations of changes as results of aging effects in sand fall into the following aspects – soil stiffness, penetration resistance, shear strength, liquefaction resistance and pile setup. Observations from the literature are reviewed below and are grouped according to the abovementioned five aspects.

Soil Stiffness

One of the earliest investigations on changes in stiffness of constantly-loaded sand over time was done by Afifi and Woods (1971). They performed resonant column tests to measure changes in small strain shear stiffness of sand samples over time under constant confining stress. The results showed that the small stain stiffness of air-dry sand continued increasing for durations up to 430 days. The results also indicated that shear modulus increased faster in samples with smaller particle sizes after initial consolidation of 1,000 minutes, 5-12 % in silts and only 2-5 % in air-dry sands per log cycle of time, respectively. However, very little increase in density was observed in the same samples during the tests. Figure 2.1 shows changes of vertical strain and small strain shear stiffness of an air-dry Ottawa sand sample with a confining stress of 30 psi and a void ratio of 0.49.
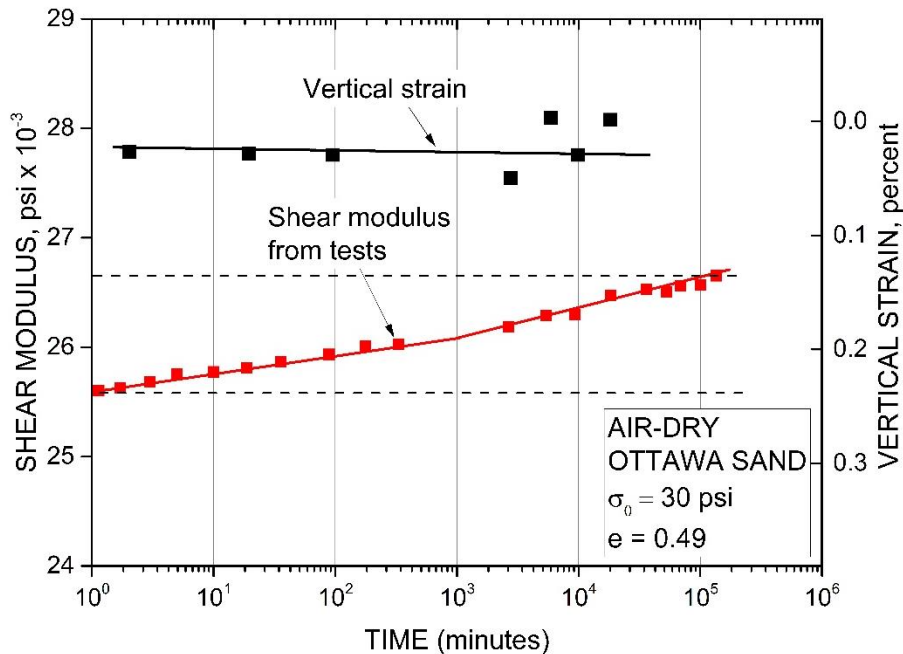
Figure 2.1. Time-dependent gain in small strain shear stiffness in air-dry Ottawa sand (redrawn from Afifi and Woods 1971).

Afifi and Richart (1973) evaluated dynamic shear modulus of more types of sands with different overconsolidation conditions with resonant column tests. Dynamic shear moduli of the samples were measured over different time under constant confining stresses. Their results

6

illustrated strong dependency of increase rate in shear modulus on average sand grain sizes. Little increase in low amplitude shear modulus was observed in samples with average grain sizes larger than 0.04 mm, while more increase was observed in samples with finer particles. The increase rate in shear modulus was noticed to be slightly reduced by overconsolidation.

Anderson and Stokoe (1978) later summarized the results from resonant column tests and proposed the following equations to qualitatively predict increase in small strain shear modulus over time:

$$N_G = \frac{\Delta G}{G_{1000}} / \log(t_2 / t_{1000}) \qquad (2.1)$$

$$G_t = G_{1000}(1 + N_G \log \frac{t_2}{t_{1000}}) \qquad (2.2)$$

where N_G is the ratio of shear modulus increase with time, t_{1000} is a reference time representing the completion of primary consolidation (1,000 minutes is taken), t_2 is the time over which the increase in small strain modulus in evaluated, ΔG is the increase in small strain shear modulus from time t_{1000} to t_2, G_{1000} and G_t are the small strain shear modulus at t_2 and t_{1000}, respectively.

Jamiolkowski and Manassero (1995) reported N_G values of 0.01 to 0.13 for silica sands, 0.04 for sand with 50% glauconite and 0.05 to 0.12 for carbonate sands.

Daramola (1980) studied effects of aging on saturated Ham River sand samples through triaxial tests. The samples were tested after under a constant confining stress of 400 kPa for different amounts of time, up to 152 days. The secant Young's modulus increased 50% in the sample under the consolidating pressure for 152 days comparing to the sample tested without aging. The peak strengths of the samples varied very little to the aging process, but the strain at failure decreased in samples that went through longer aging time. The results are shown in Figure 2.2.
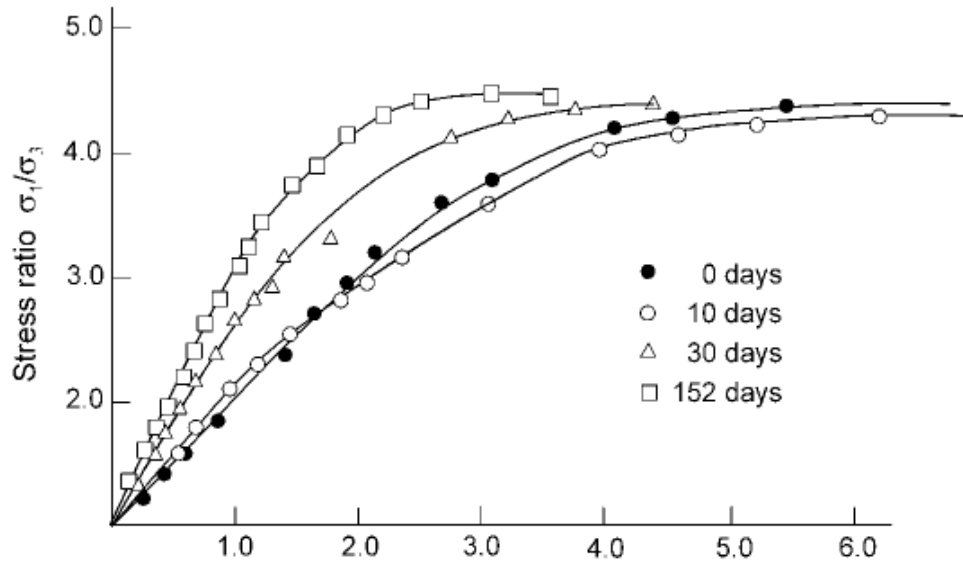
Figure 2.2. Effects of aging on stress-stain behavior of Ham River sand during triaxial tests (from Daramola 1980, redrawn by Nadukuru 2013).

Howie, et al. (2002) conducted a series of triaxial tests on very loose Fraser River sand samples to study the effects of aging time under sustained confining stresses and confining stress ratios (σ_1'/σ_3') on stress-strain behavior of the samples. The results showed faster increase of small strain shear modulus (deduced from second Young's modulus E by assuming linear elastic behavior) in samples aged under higher stress ratios, while shear stiffness without aging was higher in samples under isotropic confining stress. Consistently with previous observations (by Afifi and Woods 1971, Afifi and Rechart 1973, Anderson and Stokoe 1978), the rate of increase was linear with log cycle of time up to 10,000 minutes (1 week). All samples showed reduced contractive volumetric strain pattern during triaxial tests after aging and Howie et al. (2002) argued that this makes the sand harder for pore-pressure buildup in the samples under seismic loads, thus more resistant to liquefaction. The N_G values measured from the tests were summarized in Table 2.1.

Table 2.1. Increase in stiffness in loose Fraser River sand during aging (data from Howie, et al. 2002).

Stress ratio for aging $(\sigma_1{}'/\sigma_3{}')$	G at 1 min (MPa)	N_G $t = 1000$ min
G at 0.02% strain		
1.0	23	1%
2.0	10	2%
2.8	5.5	3%
G at 0.1% strain		
1.0	14	<0.5%
2.0	7	1%
2.8	4	1.2%

Baxter and Mitchell (2004) conducted aging tests on sands with under sustained vertical effective stress of 100 kPa. Two types of sand were tested: Evanston Beach sand (a poorly graded fine sand with subangular grains) and Density sand (a poorly graded fine to medium sand with rounded grains). A total of 22 tests were carried out with different combinations of the following conditions: two different temperatures (25˚C and 40˚C), two different relative densities (40% and 80%), air-dry and submerging with three different pore fluids (distilled water, ethylene glycol and CO_2 saturated water). While the samples were sustained under constant load, measurements of small strain shear modulus, electrical conductivity, pore fluid chemistry, and minicone penetration resistance were taken after different aging periods. The small strain shear modulus was measured with bender elements while the loads were sustained and the increases in small strain stiffness in all the 22 tests are summarized in Table 2.2. The measured increases in N_G generally fell into the range of 1% - 4% as shown in earlier literature (Jaimiolkowski and Manassero 1995). Results showed that increase in small strain shear stiffness was accelerated significantly by higher sample density and presence of pore fluids. Samples submerged in distilled water and CO2 saturated water were observed to increase faster in small strain shear modulus than those submerged in ethylene

glycol. Higher temperature was noticed to accelerate this process too, but not as significantly as sample density and presence of pore fluids.

Table 2.2. Values of N_G for Evanston Beach sand and Density sand under various conditions (data from Baxter and Mitchell 2004).

Temperature (˚C)	Initial relative density (%)	N_G (%)			
		Distilled water	Ethylene glycol	CO2 saturated water	Dry
Evanston Beach sand					
25	40	1.7	0.5	1.8	-
25	80	2.8	0.8	2.8	0.5
40	40	1.6	0.1	-	-
40	80	4.0	1.3	-	-
Density sand					
25	40	-0.6	0.8	-0.7	-
25	80	0.3	0.8	0.3	2.2
40	40	-0.1	-0.7	-	-
40	80	1.0	0.1	-	-

Wang and Tsui (2007) reported time-dependent changes in small strain shear stiffness and damping ratios in two types of standard sands in the laboratory, through resonant column tests. The two types of sands used in the tests were Ottawa 20-30 sand, a medium to coarse rounded-grained sand, and Toyoura sand, a fine to medium angular-gained sand. Resonant column tests were performed on samples aged for different time periods with different initial densities, under different confining stresses, loading paths and stress histories. Results showed the following trends: (1) small strain stiffness increased faster with time up to 7 days in looser samples under a lower confining (35 kPa), but under a higher confining stress (100 kPa) faster increase was observed in denser samples up to 7 days; (2) unloading-reloading could erase some aging effects but the

remaining aging effects were restored if the sample was reloaded to its original confining stress during its initial aging process; (3) unloading, reloading and overconsolidation reduced increase rates in small strain shear stiffness during aging; (4) aging effects were lost after the samples were sheared to a large strain; (5) adding kaolinite fines into the samples accelerated aging rates of small strain stiffness. The changes in small strain shear stiffness reported by Wang and Tsui (2009) are summarized in Table 2.3. Most of the N_G values reported in Table 2.3 fall into the range of 1% to 4% as reported by Jaimiolkowski and Manassero (1995).

Table 2.3. Changes in small strain shear stiffness in Ottawa 20-30 sand and Toyoura sand after aging of 7 days (data from Wang and Tsui 2007).

Sand tested	Aging at 35 kPa		Aging at 100 kPa	
	(ΔG at 7d) / (G at 1min) (%)	N_G (%)	(ΔG at 7d) / (G at 1min) (%)	N_G (%)
Dense Ottawa	5.5	2.3	3.6	1.0
Loose Ottawa	6.0	3.2	2.4	1.1
Dense Toyoura	3.9	-0.3	8.6	4.4
Loose Toyoura	7.1	1.9	4.8	1.3

There are not many observations on increase of sand stiffness during aging in the field. Troncoso and Garces (2000) evaluated time-dependent gain in small strain shear stiffness with in situ downhole wave propagation tests. They performed tests in Chile on four abandoned tailing dam sites of low plasticity silts with 50-99% fines contents. The downhole tests showed significant increase in small strain shear stiffness on the sites after aging periods of 10 to 40 years, as shown in Figure 2.3.
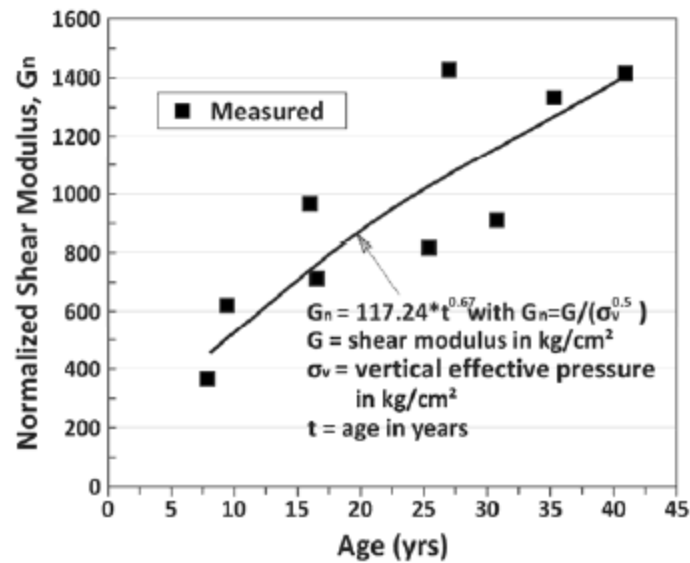
Figure 2.3. Normalized small strain shear modulus as function of aging periods of tailing dams (from Troncoso and Garces 2000).

Penetration Resistance

Changes in penetration resistance of sand is the mostly well documented changes in sand during aging process. A large variety of observations on changes in penetration resistance of sand over time are reported both from laboratory and field tests.

Denisov et al. (1963) (cited by Schmertmann 1991) were among the first to report observed gain in penetration resistance in the field. They measured the number of blows required to drive a 74 mm diameter cone into the ground by 10 cm by dropping a 60 kgf hammer 80 cm above. The soil was a hydraulically placed, saturated quartz river sand. The number of blows were measured to increase from 2.1 for 10-20 days of aging to 4.4 for 100-140 days of aging.

More attention was drawn to aging effects in sand by the Mitchell and Solymar (1984) who reported field observations of changes in penetration resistance in sand after densification. Mitchell and Solymar (1984) reported time-dependent changes in cone penetration resistance of a deposit of clean sand under a hydroelectric dam in Nigeria following densification with blasting and vibrocompaction. The sand was a medium to coarse silica sand with sub-rounded grain shapes. It

12

was the foundation of a 42 m high earth and rockfill hydroelectric dam on the Niger River in Nigeria. Mitchell and Solymar (1984) performed cone penetration tests on the sand after different periods of time following densification work with blasting and vibrocompaction. They observed that penetration resistance decreased immediately after explosive compaction and vibrocompaction; then penetration resistance started to increase 1-2 weeks after blasting and vibrocompaction, and the increase continued for months. Figure 2.4 shows cone penetration measurements of the sand after different time periods following vibrocompaction.
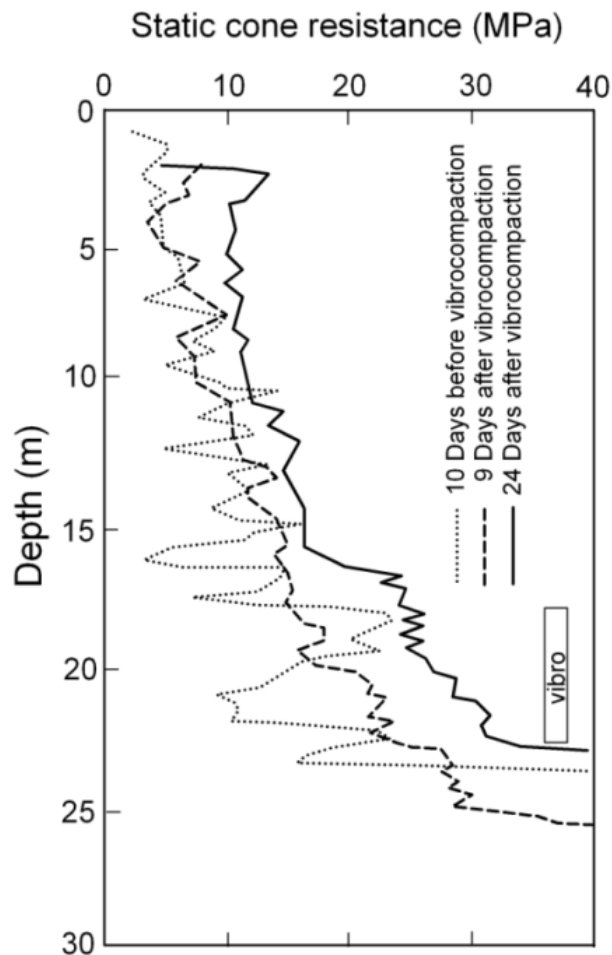
Figure 2.4. Changes of CPT resistance in sand bed after vibrocompaction, Jebba Dam site, Nigeria (redrawn from Mitchell 2008).

Dowding and Hryciw (1986) reported increase of minicone penetration resistance in Evanston Beach sand samples compacted with blasting. The sand sample, Evanston Beach sand,

13

was a poorly graded silica sand ($D_{50} = 0.2$ mm, $C_u = 1.5$) and was placed to a thickness of 660 mm in a cylindrical liquefaction tank (1 m in both height and diameter). Explosive charges were introduced in the middle of the tank and minicone penetration tests were performed at distances of 100, 200, 300 and 400 mm after different periods of time following the blast. The testing results are plotted in Figure 2.5. Increase in penetration resistance over time was measured in all tests, including the one without blast. Penetration resistance increased faster in the tests with explosive charges and at positions closest to the charges. In the tests with two charges with shorter time intervals (0, 17 ms and 25 ms),   minicone penetration increase faster than with one blast. However, penetration resistance at the position of 100 mm away from the blast stayed the same or even decreased with two blasts.

Skempton (1986) (cited by Mitchell 2008) estimated changes in Standard Penetration Test results over much longer aging times. He represented the results with a standard penetration N-value normalized with an effective overburden pressure of 1 atm and the relative density of sand (($N_1)_{60}/D_r^2$). The results were summarized by Michell (2008) in and are shown in Table 2.4.

Table 2.4. Increase in SPT resistance during aging in normally consolidated fine sands (values from Skempton 1986, table reproduced from Mitchell 2008)

	Age, years	$(N_1)_{60}/D_r^2$
Laboratory Tests	10^{-2}	35
Recent Fills	10	40
Natural Deposits	$>10^2$	55
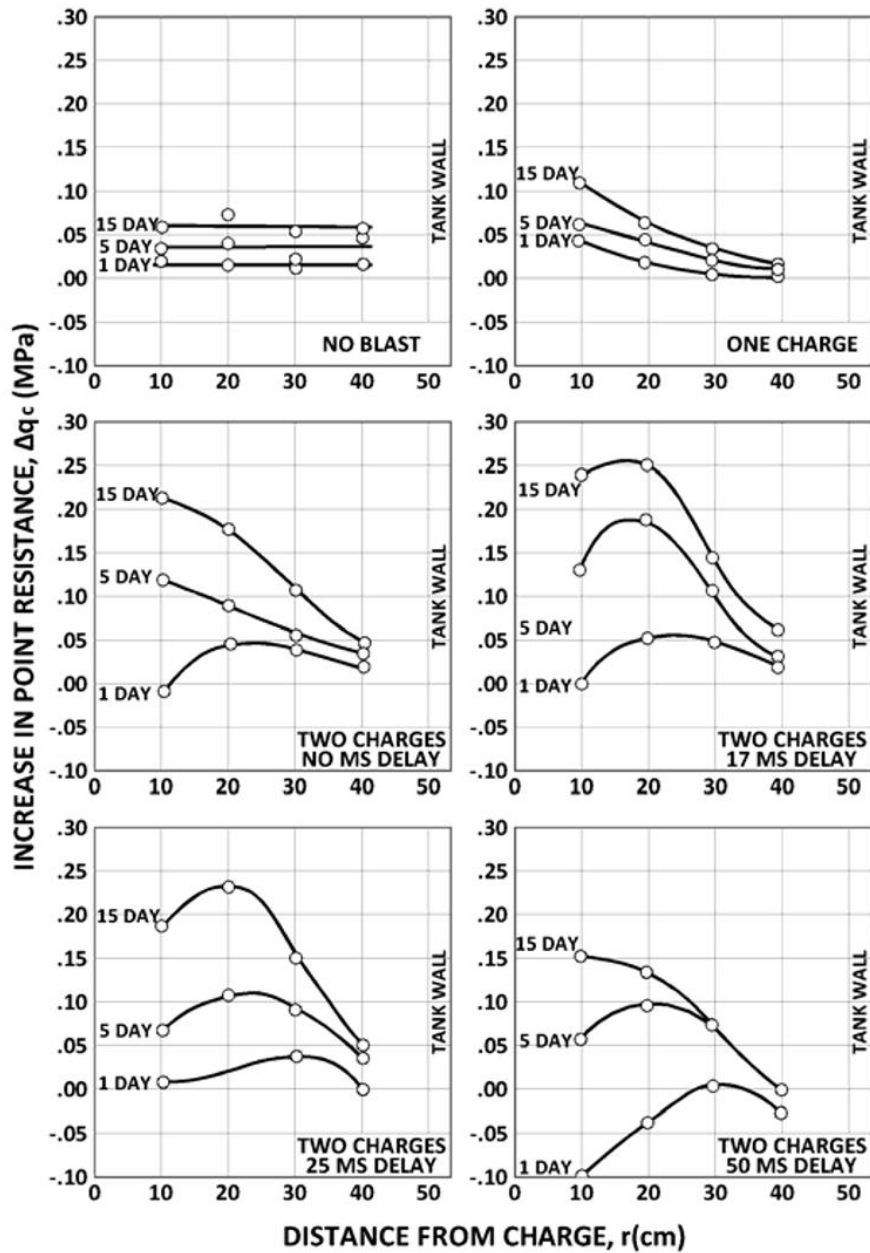
Figure 2.5. Effects of aging on the minicone penetration resistance in Evanston Beach sand compacted with blasting (from Dowding and Hryciw 1986, redrawn by Mitchell 2008).

Dumas and Beaton (1986) reported time-dependent increase in CPT resistance in a 6- to 17-m thick deposit of medium to coarse clean sand densified by dynamic compaction, as shown in Figure 2.6. The sand fill (average grain size 0.79 mm and $C_u = 3.06$) was deposited loosely into the sea by end dumping. The CPT results showed increase in measurements of penetration

resistance immediately after compaction and even more increase 18 days after compaction. Their results showed some distinctive characteristics with comparison to those observed in Jebba Dam site by Mitchell and Solymar (1984): (1) increase in CPT resistance was much faster; (2) no apparent decrease immediately after compaction was observed; (3) increase in CPT resistance was greater near the surface than deep down, and Dumas and Beaton (1986) believed that this trend was related to the attenuation of dynamic stresses from compaction with depth.
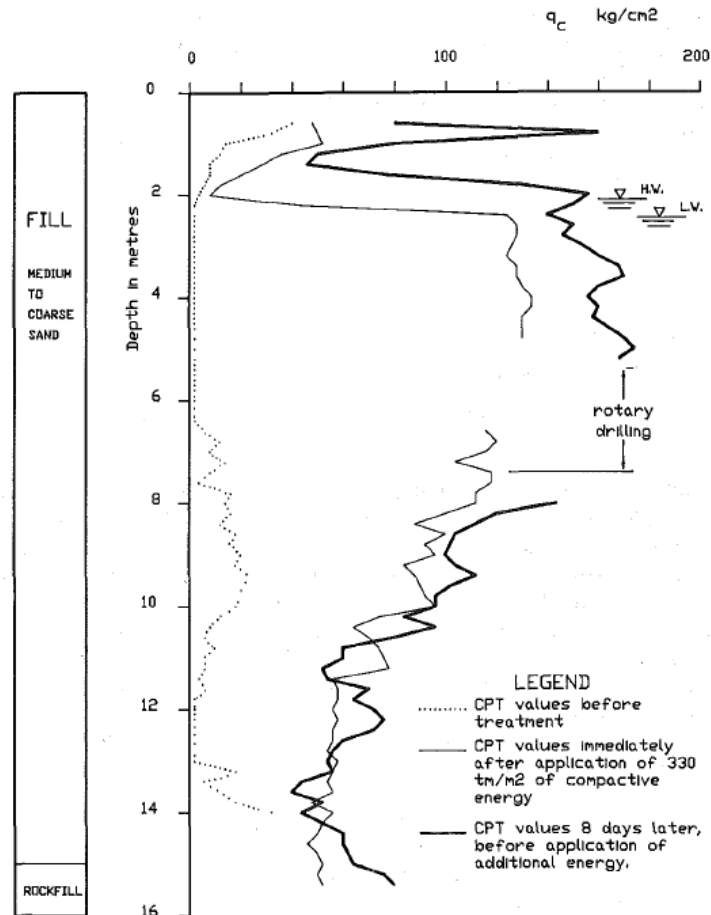
Figure 2.6. Changes in penetration resistance with time after dynamic compaction at the Pointe Noire deep sea harbor, Quebec (from Dumas and Beaton 1986).

Schmertmann (1991) reported increase in CPT resistance of a 10-m thick silty sand layer with time after dynamic compaction. These results were initially used by Schmertmann (1987) in discussion with results of time-dependent penetration changes observed by Mitchell and Solymar

(1984). The site was in Jacksonville, Florida and the dynamic compaction was performed by dropping a 33-ton weight from a height of 105 feet. The results are shown in Figure 2.7 where the static-cone bearing capacity values was normalized with the corresponding initial values immediately following dynamic compaction. The results in Figure 2.7 show three characteristics: (1) static-cone bearing capacity increased with time up to 70 days after dynamic compaction; (2) increase in static-cone bearing capacity slowed down after about two weeks; (3) more increase in static-cone bearing capacity was generated by increasing number of weight drops.
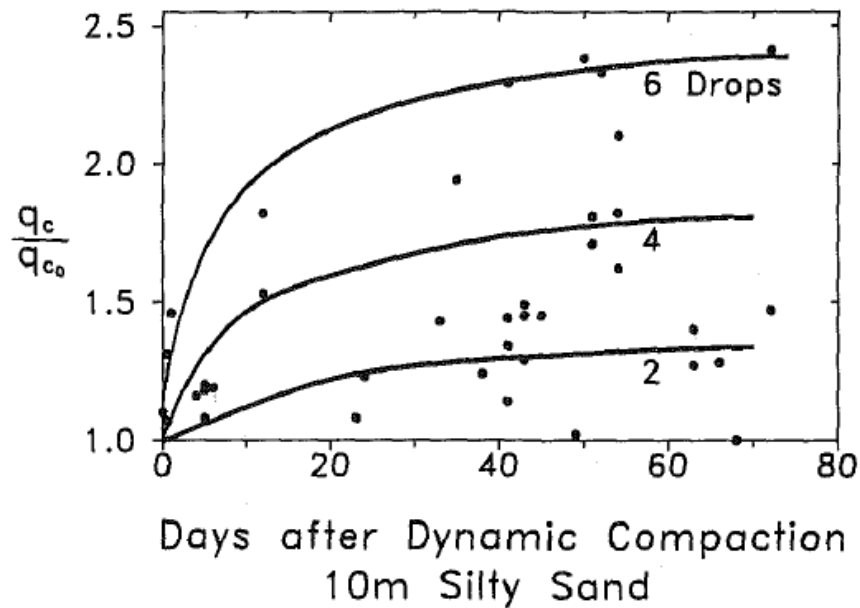
Figure 2.7. Normalized increase in static-cone bearing capacity after dynamic compaction on silty sand site, Jacksonville, FL (from Schmertmann 1991).

Charlie et al. (1992) reported changes in CPT measurements with time in a saturated layered sandy alluvium. The top layer of the sand alluvium was a 1.5-m thick layer of poorly grated medium fine sand and the bottom layer is a dense poorly graded gravely sand with a thickness of 3.6 m. They reported the measurements of three CPT components, tip resistance, local friction and friction ratio, after different time periods following blasting. The results showed that tip resistance decreased immediately after blasting and started to show increase 1 week after blasting till 18 weeks after blasting. Tip resistance increase by 18% from week 1 to week 18 after blasting. The

changes in tip resistance was consistent with observations by Mitchel and Solymar (1984) and Schmertmann (1987, 1991). Charlie et al. (1992) compared increase in normalized tip resistance (divided by tip resistance 1 week after blasting) with previously reported results and found out that increase in their results were slower than those carried out under higher temperatures (Mitchell and Solymar 1984, Schmertmann 1987, 1991) but faster than those under lower temperatures. From this comparison, Charlie et al. (1992) concluded that time-dependent gain in CTP tip resistance was faster under higher temperatures; they also claimed that this trend is an indication of that chemical bonding between particles was responsible for aging effects as chemical reaction rates are affected by temperature. The measured CPT local friction from their results decreased with time, which was opposite to a previous suggestion by Schmertmann (1987) that horizontal stress in sand increases with time.

Jefferies and Rogers (1993), in a discussion on Charlie et al. (1992), reported changes in CTP resistance over time in a pigotted clean sand fill in the Molikpaq mobile caisson after the sand is densified with blasting. The caisson, with a square cross-section of 70 m by 70 m and a height of 100 m, was filled with hydraulically placed sand to provide resistance to large horizontal forces exerted by moving ice in the Arctic during the winter season. Jefferies and Rogers (1993) presented CPT measurements in sand fill of one of the deployed caissons after different aging periods following blasting. The results showed that CPT resistance in the sand fill decreased immediately after blasting and didn't show any increase until 2-5 days after blasting when a 50% increase in CPT resistance was observed; the increase continued for several weeks in a decaying rate. The changing pattern in the results of Jefferies and Rogers (1993) was similar to those reported by Mitchell and Solymar (1984) and Schmertmann (1987). Jefferies and Rogers (1993) pointed out that the CPT tests were performed under a temperature of -1.0˚C - -1.5˚C, not -10˚C as given in the discussion on influence of temperature on aging effects in sand in Charlie et al. (1992).

Joshi et al. (1995) measured minicone penetration resistance of local river sand and Beaufort Sea sand dry, in distilled water and in sea water. The sand samples were deposited into cylindrical cells, vibrated to desired densities and confined under a vertical stress of 100 kPa to let them age for two years. On each sample, seven minicone penetration tests were performed with a

10 mm diameter penetrometer. The increase ratio of penetration resistance was larger in sand in distilled water than dry sand, and even larger in sand in sea water.

Baxter and Mitchell (2004) observed no change in minicone penetration resistance in their 22 laboratory tests on two types of sand under various conditions after aging periods, although changes in small strain stiffness, electrical conductivity and chemical composition were observed during the same time.

Ashford et al. (2004) measured changes in CPT resistance in a saturated hydraulic sand fill, with clean fine sand in upper layer and silt in deeper layer, over different time periods after blasting. The site was located in Treasure Island National Experimentation Site. The sand fill liquefied during the controlled blasting process, thus not surprisingly CPT resistance decreased within from measurements within two days after blasting. However, measurements performed 42 days after blasting showed CPT resistance 2.5 times that of two days after blasting. The pattern of increase in CPT resistance was similar those reported by Mitchell and Solymar (1984), Schmertmann (1987, 1991), Charlie et al. (1992), etc.
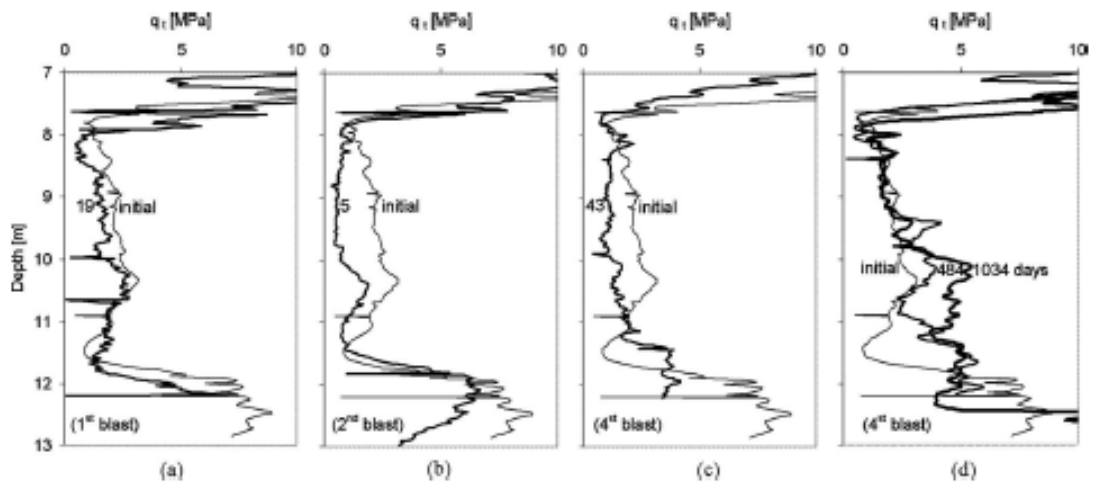
Figure 2.8. Changes in CPT resistance in a 6 m thick loose fine sand layer before and after blasts in South Carolina: (a) 19 days after the first blast, (b) 5 days after the second blast, (c) 43 days after the fourth blast, and (c) 484 days and 1034 days after the fourth blast. (from Narsilio et al. 2009).

19

Narsilio et al. (2009) reported changes in CPT tip resistance with time in a 6 m thick loose fine sand (D_{50} = 0.20-0.29, C_u = 1.40-1.88) layer in South Carolina densified with blasting. Four explosive charges were carried out over a period of eight months. Penetration resistance was observed to decrease immediately after each of the four blasts. During the eight-month blasting period and after the final blast, no increase in tip resistance was observed from the CPT measurements until 484 days after the fourth blast and the resistance further increased 1,034 days after the final blast. The CPT results during the blasting process and after the fourth blast are shown in Figure 2.8, together with the CPT measurement before the first blast.

Saftner (2011) studied aging effects in soil improvement with explosive densification and vibroseis shaking at a site in Griffin, Indiana. The test site was a 14 m soil layer, with a 2 m thick clay layer on top, a 3 m thick layer of loose sand, a 5 m thick dense sand layer, and a underlying 4 m thick layer of loose gravelly sand. Different aging effects were observed in different layers after blasting. In the dense sand and loose gravelly sand layers, CPT resistance decreased immediately after blasting. Resistance in dense sand did not show any increase over two years after blasting. Increase in CPT resistance with time occurred in the loose gravelly sand layer, but the resistance had not yet restored it pre-blasting value after two years. In the loose sand layer, CPT resistance did not change immediately following blasting, but it showed obvious increase after one month and continued in the two years thereafter.

Saftner (2011) performed CPT tests at the same site in Griffin, Indiana, after vibroseis shaking. Measurements were taken before shaking, 48 hours, one month and nice months after shaking. No obvious change in CPT tip resistance was observed from the measurements, which indicated vibroseis shaking did not create noticeable effect on CPT resistance of the soil layer. The results from CPT measurements on the site with both blasting and vibroseis shaking are summarized by the authors in Table 2.5. Based on these observations, Saftner (2011) concluded that aging effects are influenced by intensity of disturbance energy.

Table 2.5. Change in SPT resistance with time in sand site densified with blasting and vibroseis shaking (summarized from Saftner 2011)

	Loose sand	Dense sand	Loose gravelly sand
Thickness (m)	3	5	4
Saturation condition	Saturated at bottom 2 m	Saturated	Saturated
Explosive densification			
Immediately post-blasting	No change	Decreased	Decreased
Time dependent change	Increased over time, beyond pre-blasting resistance after 1 month	No change over time, still less than pre-blasting measurement after 2 years	Increased over time, but did not reach back to pre-blasting resistance after 2 years
Vibroseis shaking			
Immediately post-shaking	No change	No change	No change
Time dependent change	No change	No change	No change

The readers should be aware that there are reported observations on penetration resistance in sand that did not increase over certain periods of aging after disturbance. Mitchell (2008) summarized several reported observations of this kind. Human (1992), observed no change in CPT resistance of a 4 m thick silty sand fill in Alameda, CA, 4, 14, 30, 65 and 317 days after the 1989 Loma Prieta Earthquake. Evidence of liquefaction, sand soils on top of the silty sand layer, was observed on this site during the earthquake. Gohl et al. (1994) reported results of CPT tests on a loose sand underlying 2-3 m thick random fill after blast densification in British Columbia. Although blasting caused liquefaction indicated by up to 1-m settlement and water discharging at ground surface, no increase in CPT resistance was observed up to 450 days after blasting. Liao and Mayne (2006) used blasting to induce and study liquefaction and post-liquefaction changes of sand layers in the New Madrid Seismic Zone. While the short-term decrease (10%) in CPT resistance was observed, no obvious increase was observed in the following eight months. Mitchell (2008) speculated that the absence of increase in penetration resistance in these cases were because that the pore fluid is freshwater. In the aging tests performed by Baxter and Mitchell (2004), no

increase in minicone penetration was measured in the any of the 22 tests. They attributed this unexpected result to the difficulty of reproducing various field conditions in the laboratory, such as air/gas cumulation in sand, energy imparted during ground improvement, diverse deposit process, biological processes and the free-field boundary conditions.

Shear Strength

There are very few direct measurements of changes in shear strength of sand during the aging process, compared to measured changes in shear stiffness and penetration resistance. Although some researchers related measured increase in penetration resistance in sand to increase in shear strength as one of the aging effects (Ashford 2004), other researchers argue that penetration resistance is controlled by both sand strength and horizontal stress (Schmertmann 1991, Mitchell 2008).

The results of triaxial tests obtained by Daramola (1980) on Ham River sand samples consolidated under a 400-kPa confining stress showed substantial increase in stiffness with increasing consolidation periods up to 152 days, but nearly no change in shear strength. The results are shown in Figure 2.2.

Measurements of changes in sand strength during aging was obtained by Al-Sanad and Ismael (1996). Direct shear tests were performed on samples of a fine to medium calcareous sand, with trace of silt and fine gravel. The samples were 100 mm×100 mm in horizontal directions, and 22 mm in height, with a relative density of 60%. Before shearing, the samples were aged under a small normal stress of 2 kPa for 1, 3 and 6 months, at a constant temperature of 20°C and constant relative humidity of 100%. Direct shear results showed that the internal friction angles (φ) increased from 36° for fresh samples to 38.7° for samples aged for 6 months, which was corresponding to a 10% increase in shear strength. The results from these direct shear tests are shown in Figure 2.9.

(a)

(b)

$$\Phi = \Phi_i + 3.81\,t\,/\,(2.82 + t)$$
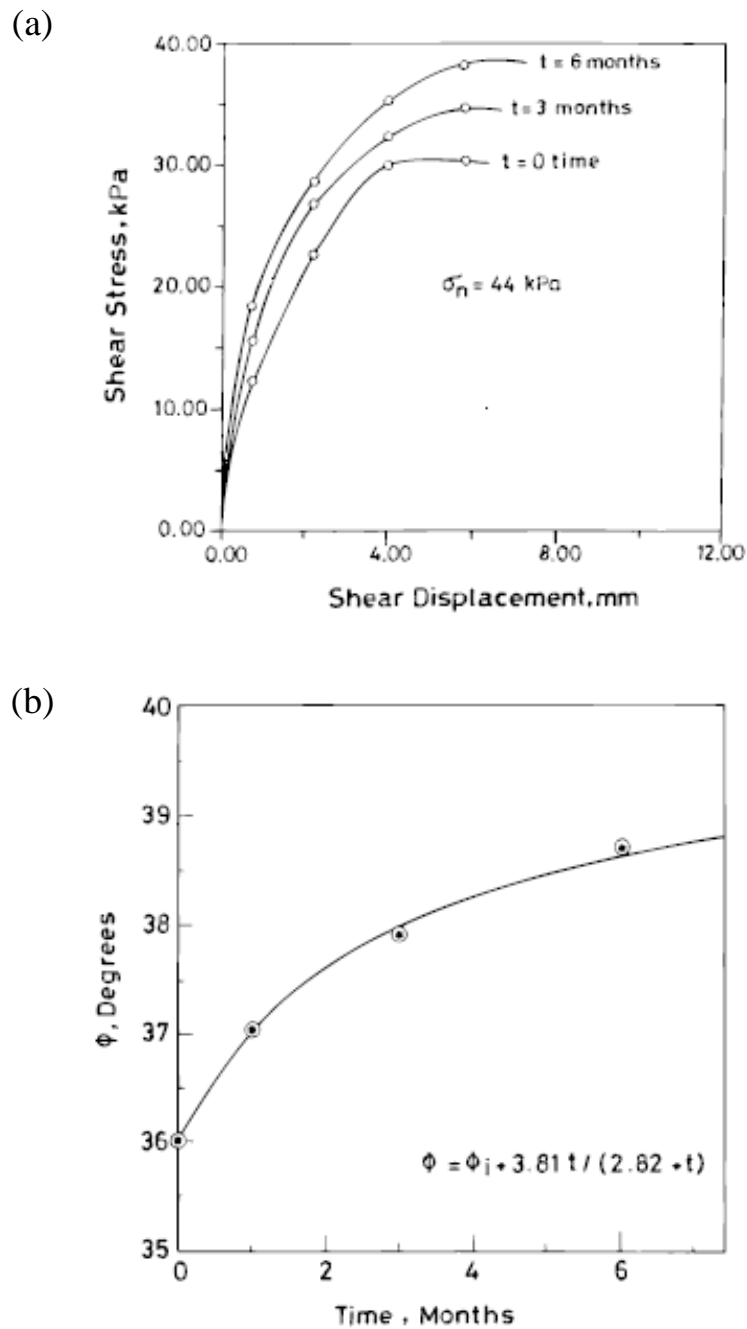
Figure 2.9. Increase in shear strength over time in fine to medium sand samples under direct shear tests: (a) shear displacement curves, (b) increase in friction angles (from Al-Sanad and Ismael 1996).

Liquefaction Resistance

Studies of aging effects on liquefaction resistance of soils consider changes in a geological time scale (tens of thousands of years), rather than engineering time scale (months to serval years).

Seed (1979) reported results of laboratory tests on undisturbed sand samples and freshly deposited samples of the same sands, to evaluate effects of aging on liquefaction resistance of sands. The results are shown in Figure 2.10. Based on these results, Seed (1979) predicted a possible increase of 75% in cyclic mobility resistance in sands under a sustained pressure over long periods.
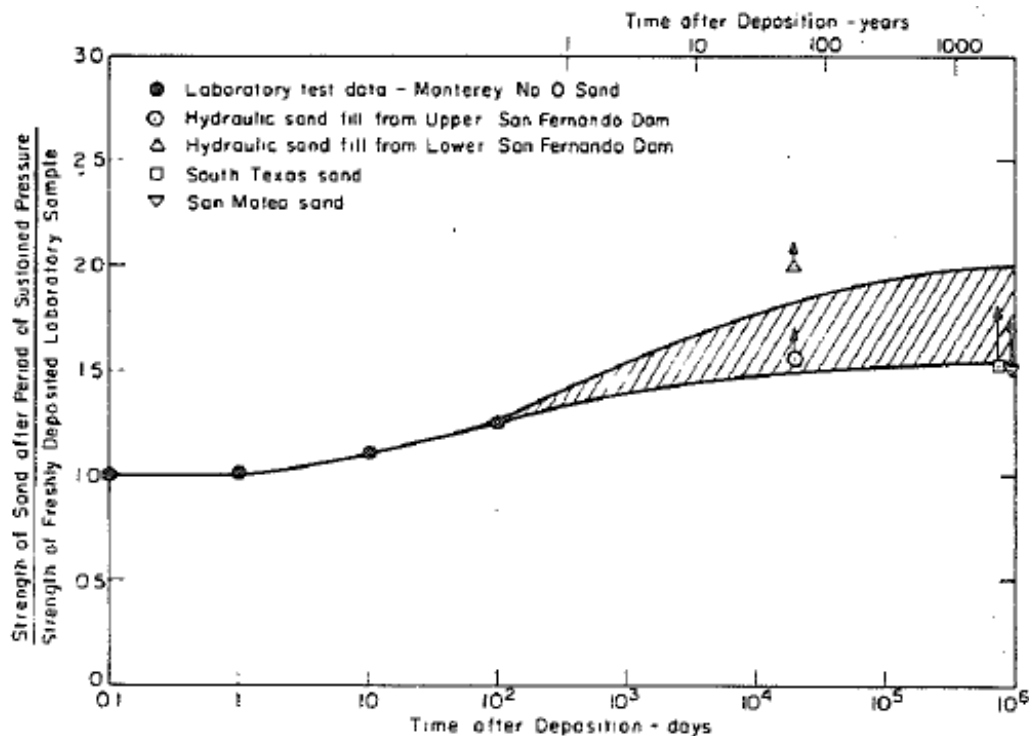
Figure 2.10. Effects of aging under sustained pressure on stress ratio causing 100% peak cyclic pore pressure (from Seed 1979).

Arango et al. (2000) complemented the plot by Seed (1979) in Figure 2.10 based on predictions proposed by Seed (1979), Skempton (1986), Kulhawy and Mayne (1999), and historic records of cyclic shear strength of Miocene-age clayey sand from Charleston, NC. A synthesized

plot for prediction on time-dependent gain in liquefaction resistance of sand is prepared by Arango (2000) and is shown in Figure 2.11.
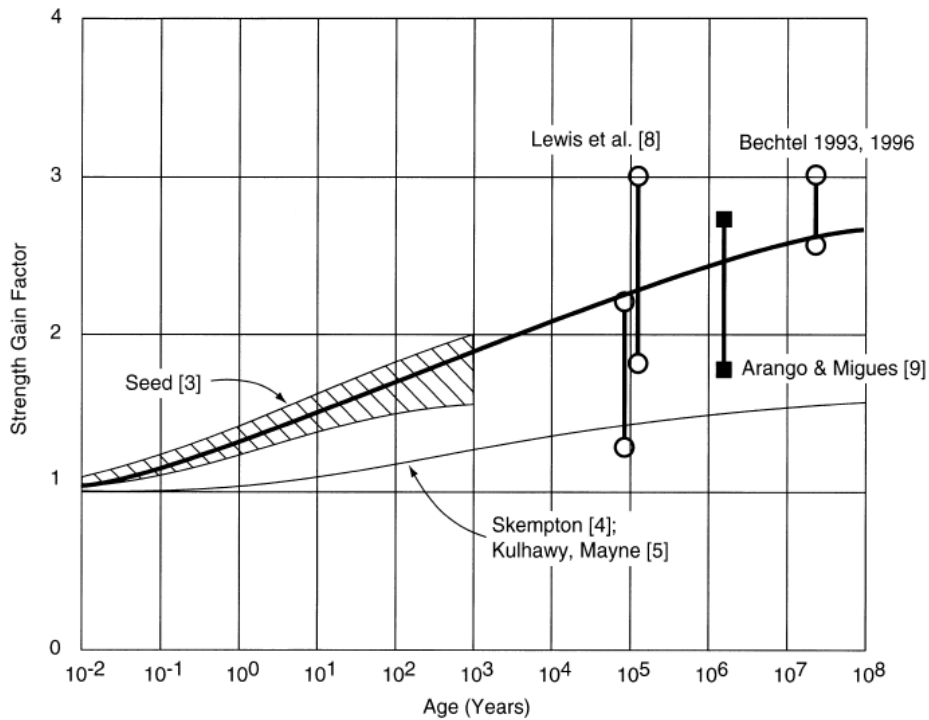
Figure 2.11. Updated field cyclic strength of aged sand deposites (from Arango et al. 2000).

Leon et al. (2006) measured SPT, CPT, and V_s values of four sites in the South Carolina Coastal Plain (SCCP) where prehistoric earthquake-induced liquefactions (aged for 200,000 to 450,000 years) were identified. Leon et al. (2006) proposed a method to estimate the SPT, CPT, and V_s values of freshly deposited Holocene age sands with these measurements of aged sands, and then use these estimated values together with the existing empirical liquefaction boundary curves to evaluate liquefaction potential of old/aged Holocene sand deposits. The results showed that accounting for aging of sands in the SCCP sites generated less conservative liquefaction potential. Therefore, Leon et al. (2006) concluded that aging effects increased liquefaction resistance of fresh sand deposits.

Saftner (2011) performed cyclic triaxial tests on reconstructed sand samples from a testing site in Griffin, IN. The samples were prepared to a relative density of 50% and consolidated for 0,

3, 7, 14, and 28 days before tested. The results showed increase in the number of cycles to failure at a given cyclic stress ratio with consolidation time.

Pile Setup

Field measurements have been reported to show that load capacity of driven piles in sand continue to increase significantly for months even years, long after completion of pore water dissipation (hours). This time-dependent gain in load-carrying capacity of driven piles in sand has been termed as "*pile setup*".
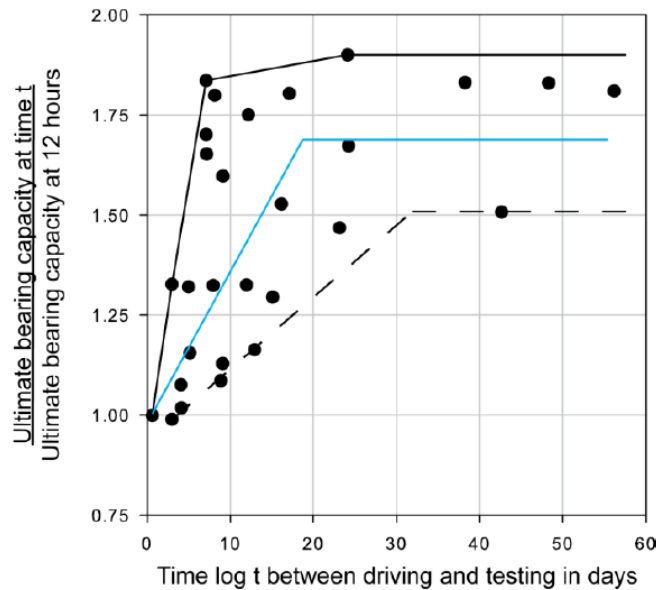
Figure 2.12. Changes of ultimate bearing capacity over time of concrete piles driven in sand in Quebec City (from Tavenas and Audy 1972, redrawn by Nadukuru 2013).

Tavenas and Audy (1972) studied aging effects on pile capacity by performing 45 loading tests on driven concrete piles in a uniform medium sand (relative density 58% ± 15%) on both of St. Charles River shores in downtown Quebec City. The results (Figure 2.12) showed a 70% average increase in ultimate bearing capacity compared to the value measured 12 hours after pile installation. Most the increase occurred in the first two to three weeks and slowed down thereafter. Tavenas and Audy (1972) excluded dissipation of pore pressure as the explanation for the capacity

gain by pointing out that the high permeability ($K = 10^{-2}$ cm/sec) of the sand would have allowed a full pore water dissipation in a few hours. Instead, they considered changes in the sand structure around the pile to be responsible for setup in these piles.

Chow et al. (1998) studied effects of aging on pile bearing capacity by performing loading tests on open-ended pipe piles in a dense marine sand at Dunkirk, northern France. The site was 100 m from the sea and consisted of about a 30 m thick layer of medium to very dense (relative density about 75%) marine Flandrian sand underlying a 3 m thick layer of hydraulic sand fill with very high density. In the tests with 11 m long piles, they observed an average increase of 85% in shaft resistance during the period between six months and five years after pile installation. Chow et al. (1998) also summarized pile setup data from the literature and plotted all of them, together with their new data, on a figure showing linear correlation in increase rate vs log time, as shown in Figure 2.13.
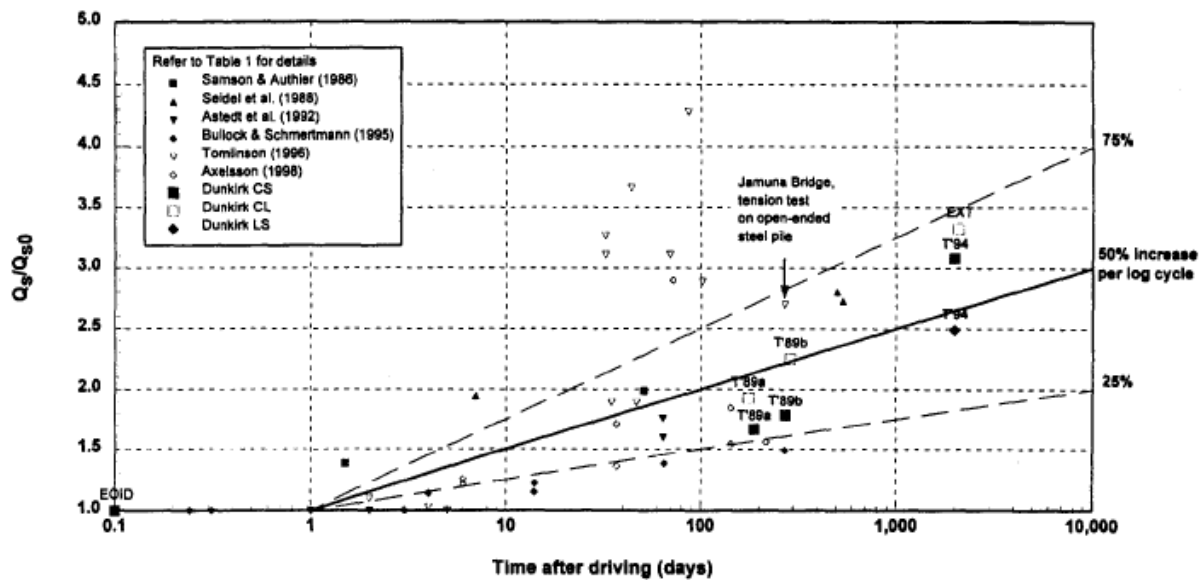
Figure 2.13. Increase in shaft resistance over time during pile setup (from Chow et al. 1998).

Axelsson (2000) performed field loading tests on 30 m long, 270 mm square concrete driven piles in saturated medium dense glacial sand in Stockholm, Sweden. The piles are equipped with sensors to measure horizontal stresses and pile-toe pressure. The results showed a 60% increase in bearing capacity 22 months after pile installation comparing to the measurement after

one day. The increase was found linear per log cycle of time up to 22 months. The results from tracking of horizontal stresses acting on the shaft showed increase in horizontal stress in the sand around the shaft occurred at rest and during loading tests. However, almost no increase in pile-toe pressure with time was observed.

Bowman and Soga (2005) performed triaxial creep tests on three types of granular samples to explore mechanisms of pile setup. The samples were standard clean Leighton Buzzard silica sand, a natural silica beach sand, and near-spherical glass beads. The results showed that more dilatancy occurred in denser and stronger sands during high stress ratio creep tests and moisture did not affect creep in clean sands. Based on these results, Bowman and Soga (2005) proposed a new mechanism for pile setup which states that pile setup is caused by "kinematically restrained dilatant creep of dense sand under high shear stress".

Jardine et al. (2006) performed axial tension shaft capacity tests on steel pipe piles in dense sand in Dunkirk, northern France, in study of pile setup. The results showed that more increase in shaft resistance occurred than expected based on previous database, but load-displacement curves in aged piles showed significantly brittle failure mode. They also found out that previous testing to failure degraded capacity of aged piles, so suggested that cautions be given to capacity-time trends obtained from repeatedly tested piles.

Yang et al. (2015) organized a new database of testing results on setup of piles driven in sands. The database, named Zhejiang University/Imperial College London (ZJU-ICL) database, consisted of 80 entries of results from field loading test results that meet certain criteria. The ZJU-ICL database was made publicly accessible by Yang et al. (2015) and can be downloaded from a website hosted by Zhejiang University (http://mypage.zju.edu.cn/en/zxyang/682156.html).

Rimoy et al. (2015) performed laboratory model tests with model piles equipped heavily with sensors and a chamber filled with sand with boundary stress control. 22 tests with stainless steel model piles with two diameters of 12 mm and 36 mm and various pile installation methods and stress conditions. Only the tests with manually increased lateral stress showed an increase in bearing capacity over time, while other tests failed to reproduce this trend. However, the model tests showed increase in shaft capacity under low-level cyclic load.

Zhang and Wang (2015) also performed laboratory driving and loading tests on model pile in an instrumented chamber filled with a sand deposit. A model pile was a closed-ended, flat tip aluminum pipe pile with a length of 600 mm and an outer diameter of 16 mm. The chamber was pluviated with dry Toyoura sand to a relative density of about 80%. Stress sensors were embedded in the sand deposit to monitor changes in lateral and hoop stresses in the deposit during pile driving and pile setup processes. The sand samples were allowed to age for 80 h under a vertical pressure of 75 kPa, before pile installation, to mimic the natural aging process of the sand as in the field. The model pile was then driven 225 mm deep into the sand by dropping a 0.96 kg hammer from a height of 10-700 mm. Then two static compression tests were carried out, one at two hours after installation and another 80 hours later, and increase in shaft resistance was observed, as shown in Figure 2.14. Only little changes in radial stress and hoop stress in the sand around the model pile was detected, not providing much support to the hypothesis of increase in radial stress while hoop stress breaking down in explaining pile setup.
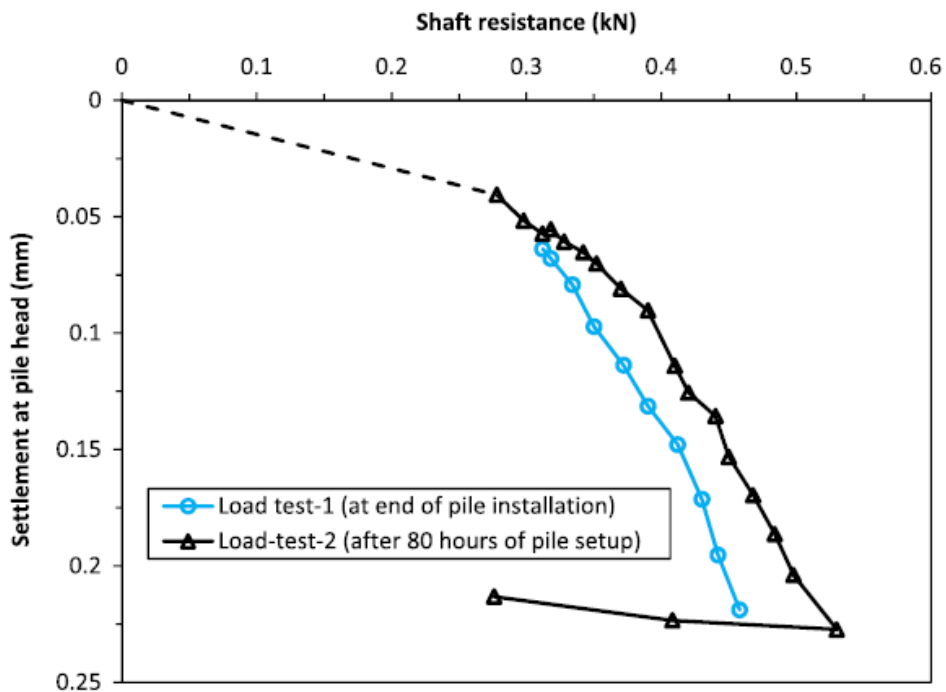
Figure 2.14. Compression test results on a model pile at end of pile installation and 80 hours later (from Zhang and Wang 2015).

2.2. Numerical Simulations

Numerical simulations have been employed to simulate aging effects in sand, especially discrete element methods (DEM). Focus has been given to interactions between contacting particles. However, as far as the authors are aware of, all the simulations assumed idealized inter-particle models to reproduce macroscopic behavior of the particle assemblies observed in physical tests. None of these idealized contact models was based on direct observations or simulations of microscopic behavior of individual granular particles or inter-granular contacts.

Kuhn (1987) was among the first few researchers to use DEM to simulate creep in soil. Although Kuhn (1987) was trying to simulate aging behavior of clay, the methodology of using DEM by incorporating user-defined inter-particle contact models was adopted by later researchers in simulations of aging behavior in sand. A visco-frictional model describing inter-particle sliding of two particles in contact was proposed based on the chemical reaction Rate Process Theory. A main feature of this model was that the friction coefficient varied linearly with log of sliding velocity between two particles. With this contact model that he termed as a "Sinh-Dashpot", Kuhn (1987) was able to simulate creep behavior that was observed in soils with a two-dimensional DEM model.

Wang et al. (2008) simulated aging effects of sand with DEM by assigning an assumed visco-elastic model to inter-particle contacts. The simulations were in two dimensions. By allowing "creep" at contacts, the simulated grain assembly was able to "age" under constant confining stresses. Numerical biaxial tests were performed on samples with and without aging to study changes in sand properties during aging. By comparing results from aged and unaged samples, Wang et al. (2008) observed that after the simulated aging effects, (1) contacts forces became more uniformly distributed both in orientations and magnitudes; (2) small strain stiffness, early strength and dilatancy of the sample increased. It was interesting to note Wang et al. (2008) repeated biaxial tests on samples with the same porosities as the aged samples but without aging process, and the results did not show the changes observed in the aged samples. Based on these simulation results, they concluded that the major cause for aging effects in sand was not decrease in void ratio, but redistribution of contact forces towards uniformity.

Suarez (2009) adopted the contact model used by Kuhn (1987) to simulate aging effects in sand. The simulation results reproduced aging behavior in sand observed in laboratory tests, such as increase in small strain stiffness, temperature dependency of rate of aging, and change in volumetric strain; the results also showed results that have not been observed in tests, such as contact force redistribution (also decrease in average contact forces) and increase in horizontal stress.

Kwok and Bolton (2010) performed more DEM simulations on aging effects of sand by adopting the contact model proposed by Kuhn (1987). With a three dimensional DEM model incorporating the contact model by Kuhn (1987), Kwok and Bolton (2010) reproduced many of the aging phenomena. Kwok and Bolton (2010) finally suggested possible improvements that could be introduced to the existing contact model.

Michalowski and Nadukuru (2012) proposed the static fatigue hypothesis which states that time effects in sand is caused by delayed fracturing damages of micromorphological features at intergranular contacts. Michalowski and Nadukuru (2012) assumed that disturbance cause loss of old contacts and formation of fresh contacts, and the stiffness of fresh contacts are smaller than the old contacts because the intact roughness micromorphological features at surface. Then during the aging process, as they assumed, stiffness of contacts gradually increase due to static fatigue of these fresh roughness on grain surfaces in contact, which causes the aging effects in sand. To sought support for this hypothesis, Michalowski and Nadukuru (2012) performed three dimensional simulations with a particle assembly. To account for the non-spherical nature of sand grains, the model consisted of 75% spherical particle and 25% peanut-shaped two-particle clumps. The radii of all particles were first reduced by 0.1% so that most contact forces and the effective stress in the assembly became zero, so the stress state change due to disturbance such as liquefaction was simulated. Then new contact stiffness that was half of the original values were assigned to account for the smaller stiffness of the fresh contacts. After that, the contact stiffness (both normal stiffness and shear stiffness) of the model was increased to account for aging effects at inter-granular contacts. Horizontal-to-vertical stress ratio was measured in the model at different stages: right after liquefaction, and over different time periods after liquefaction (represented with gradually increasing contact stiffness). The results showed that horizontal-to-vertical stress ratio

31

decrease immediately after liquefaction and then increased over time (with increasing contact stiffness). The increase of horizontal-to-vertical stress ratio with contact stiffness from the simulation results are shown in Table 2.6.

Table 2.6. Change in SPT resistance with time in sand site densified with blasting and vibroseis shaking (data from Michalowski and Nadukuru 2012).

Normal contact stiffness (MN/m)	Shear contact stiffness (MN/m)	Horizontal-to-vertical stress ratio
2.0	0.8	0.339
2.2	0.88	0.365
2.4	0.96	0.378
2.6	1.04	0.391
2.8	1.12	0.399
3.0	1.2	0.413
3.2	1.28	0.424
3.4	1.36	0.433
3.6	1.44	0.442
3.8	1.52	0.451
4.0	1.6	0.459

Zhang and Wang (2016) simulated aging effects in sand with DEM by incorporating microfracturing of contacts observed by Nadukuru and Michalowski (2014) and Wang and Michalowski (2015). Zhang and Wang (2016) assumed that friction of the contacts would reduce because of contact fracturing, so in their three-dimensional DEM model friction of the contacts was reduced to account for aging effects. This model reproduced the key experimental findings on sand aging: stress path-dependent deformation, increase in macroscopic stiffness and dilatancy during drained compression, increases in stiffness and shear strength during undrained compression, and changes in void ratios and K_0 during 1D secondary compression. However, the authors argue that the assumed decrease in frictional resistance of contacts is opposite to the

observations in the experiments and simulations in this thesis, as will be introduced in next few chapters.

Cil and Alshibli (2014) simulated an assembly of crushable particles in DEM by simulating each particle with several cemented sub-particles, to study effects of particle crushing on stress-strain behavior of sand particle assemblies. However, no time effects were included in this model.

2.3. Aging Mechanisms

By adopting the way used by Mitchell (2008), the proposed mechanisms behind aging effects in sand are categorized into three types of processes – chemical, micro-biological, and mechanical. These three types of mechanisms are discussed and commented separately below.

Chemical Processes

Although chemical processes, such as inter-particle bonding (precipitation) and de-bonding (dissolution), have been proposed as the cause of sand aging effects and are supported by some observations, this proposed mechanism received wide arguments and disagreements primarily based on the difficulty for such processes to occur under the reported environmental condition. Therefore, this mechanism is not considered as a major one behind aging effects in sand.

Mitchell and Solymar (1984) proposed time-dependent development of chemical bonding or cementation at inter-grain contacts as the mechanism behind the observed changes in penetration at the Jebba Dam site (Figure 2.4). They suggest that damage of these bonds in natural sand during disturbance from blasting and vibrocompaction induced the initial decrease in penetration resistance post densification, and reformation of these bonds over time thereafter causes time-dependent increase of penetration resistance.

Joshi et al. (1995) carried out laboratory aging tests and the results showed that more changes over time occurred in samples submerged in distilled water and sea water. Scanning electron microscopic images showed precipitated minerals on the surfaces of samples submerged in distilled water and sea water for two years.

Baxter and Mitchell (2004) observed increase in electrical conductivity in most of the tests and decrease in two tests. They stated that the increase in conductivity was an indication of chemical dissolution during aging, while the decrease was a sign of chemical precipitation. More increase in electrical conductivity was observed in Evanston Beach sand and the authors explained this with the fact that the Evanston Beach sand has fractions of carbonate minerals which are more soluble comparing to Density sand which is primarily quartz with lower solubility. The samples submerged in distilled water and CO_2 saturated water showed much more significantly increase in electrical conductivity than those in ethylene glycol. Mineralogical and chemical analysis showed evidence of precipitation of carbonates and silica in at least two of the tests, which was consistent with the electrical conductivity measurements. No visible evidence of precipitation was obtained with scanning electron microscopy.

Mitchell (2008) estimated that only 0.00005 kg of quartz per 1 kg sand per year could dissolve into the water by assuming an upper-bound solubility as in a 0.0001 m NaCl solution. Michell (2008) argues that even if totally precipitates on sand grain or at contacts, this small amount of precipitation is not likely to cause any significant increase in strength of sand. Mitchell (2008) also pointed out that the chemical bonding assumption cannot explain the aging effects that were measured in dry sands.

Finally, Mitchell (2008) quoted a comment made by Mesri et al. (1990) : "… a hypothesis that implies cementing bonds forming at grain contacts of clean silica sands in a matter of weeks to months would preclude the existence of any uncemented natural sand deposits".

Based on the abovementioned observations, estimations and arguments, chemical bonding does not seem like a plausible mechanism, at least not a major one, behind aging effects in sand.

Micro-Biological Processes

Although micro-biological processes have been proposed by several researchers as the cause of aging effects in sand, it has received very little support. While it is difficult for chemical bonding to become a major role in sand aging, the authors consider it is even harder for micro-biological processes to play a significant role in aging effects in sand, primarily because the stricter conditions

needed for microorganisms to survive and prosper to create impactful changes. Additionally, the author doubt this proposed mechanism because that the magnitudes of time-dependent changes observed follow certain trends under a large variety of environmental conditions, such as the nearly-linear increase of shaft resistance with log cycle of time during pile setup (Figure 2.13). However, bacteria populations and activities should be very different under these different conditions and cause significantly different aging effects in magnitudes, not likely following such good trends as observed. Therefore, micro-biological processes may cause part of time effects in sand, but unlikely to be a major cause.

Mitchell and Santamarina (2005) concluded that, quoted by Mitchell (2008), "Microbial processes influence rock weathering, mineralization, soil formation and fabric, and soil grain surface properties. They can produce slime, gel, polymer, and biomass, cause pore and filter clogging, and change the deformation and strength properties of soils". They pointed out that microorganisms pervasively exit in natural soils.

DeJong et al. (2006) treated Ottawa sand with Bacillus pasteurii under controlled conditions and successfully generated calcite cementations at inter-particle contacts. Isotropically consolidated undrained compression (CIUC) triaxial tests were conducted on both treated and un-treated sand samples. The results showed that the shear strength of the treated samples exhibited a larger initial stiffness and ultimate shear strength that the untreated sample. Later, they carried out scanning electron microscopy and X-ray compositional mapping, results from both analyses confirmed formation of calcite cementations between particles.

Mitchell (2008) described the very strict conditions required to introduce and maintain a meaningful bacteria population, such as initial influx of large amounts of bacteria, sufficient source of energy and nutrients.

Mechanical Processes

After chemical cementation was proposed by Mitchell and Solymar (1984) to explain their observations at the Jebba Dam site, Schmertmann (1987), Mesri et al. (1990), and other researchers provided alternative explanations associating aging in sands to the evolution of sand fabric due to

delayed rearrangement of particles. Lade and Karimpour (2010), Nadukuru and Michalowski (2012), Michalowski and Nadukuru (2014), and Wang and Michalowski (2015) further proposed that particle-scale time-dependent response to load is the root cause of macroscopic rearrangements of particles and in turn, aging effects in sand.

Dowding and Hryciw (1986) proposed that the observed changes in minicone penetration were due to slow dissipation of gases in the pores generated by explosion. They estimated 100 cm^2 of gases would be generated from each blasting cap, but no gases were observed to escape from the surface of the sand deposit. The existence of trapped gases was verified by the rising bubbles they noticed when liquefying the sand for later tests, but these bubbles were limited to regions very close to the explosions (distance <15 cm). Although gas dissipation is possibly a cause of the aging effects observed in sand disturbed by blasting where large amounts of gases are introduced by explosions, it cannot explain the aging effects that occur without introduction of trapped gases, such as vibrocompaction.

Schmertmann (1987) suggests that changes in lateral stress in the soil is responsible for the changes of penetration resistance during aging effects. As suggested by Schmertmann (1987), the ground improvement methods induce decrease in lateral stress in the zones around the blast or vibrocompaction point. The lateral stress then increases with time and creates increase in cone penetration measurements. Schmertmann (1987, 1991) further states that reorientations of particles occur during secondary compression and this process increase stiffness and strength of sand because of increased effective friction.

Mesri et al. (1990) excludes chemical bonding as the mechanism by pointing out that cementing bonds forming at contacts because of silica precipitation takes a long time. The time needed for silica precipitation is much longer than weeks or months during which the changes due to aging effects are usually observed. Rather, Mesri et al. (1990) suggests that aging effects in drained clean sand is a result of continued rearrangements of sand particles over time after disturbance, during which there is increased frictional resistance and effective horizontal stress "through microinterlocking of particles and microinterlocking of surface roughness".

Bowman and Soga (2003) provided experimental evidence for the particle rearrangement hypothesis. By using resin injection and observing sections with optical microscopy, they found out that upon application of vertical load, particles were aligned more perpendicular to the load direction, but over time under load, they rotated in space. Additionally, the results showed that initially the particles were distributed evenly in space, but they grouped or clustered together with time. Based on these observations, Bowman and Soga (2003) suggest that aging starts with frictional slippage of particles along weak force chains and this process leads to adjustment of strongly-loaded particle columns. The result of these adjustments is a strong interlocking particle network that is more resistant to load. This mechanism proposed by Bowman and Soga (2003) is illustrated by Figure 2.15. Results of triaxial tests on Ham River sand samples by Daramola (1980) provided support to this hypothesis, as shown in Figure 2.16. The samples showed increased dilatancy with aging time under sustained confining stress due to the proposed macro-interlocking. More recently, Suarez (2012) also reported delayed reorientation of particles under 1D compression with a constant load from results of X-Ray CT reconstruction of the fabric.
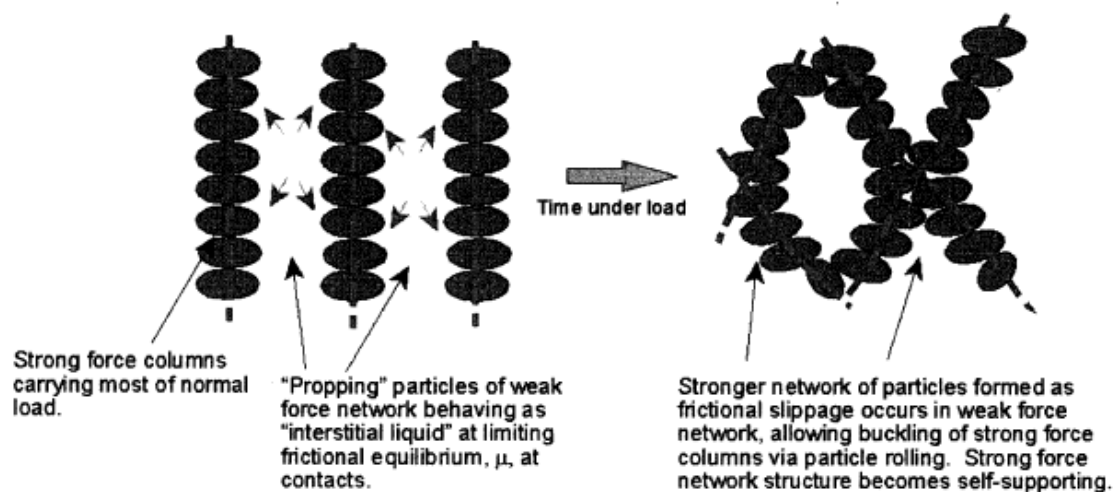
Figure 2.15. Mechanism of evolution of force chains during aging, resulting in a structured fabric (from Bowman and Soga 2003).
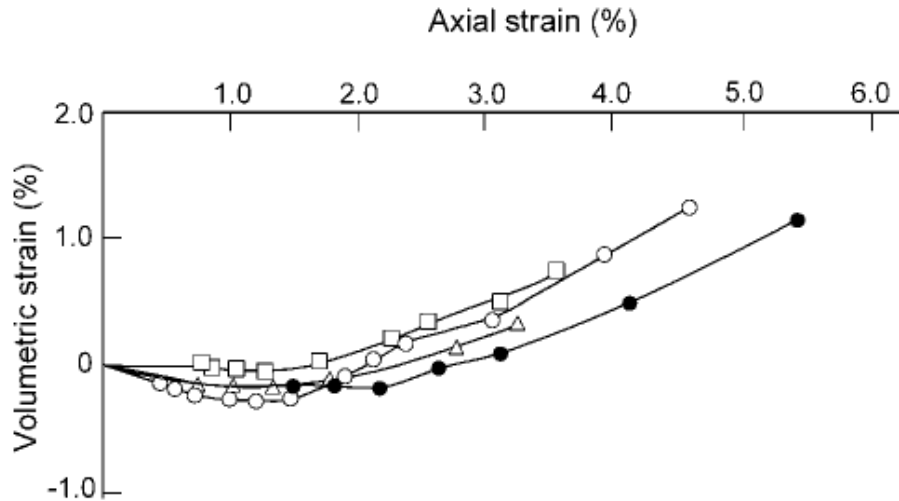
Figure 2.16. Increased dilatancy with time under constant confining pressure for Ham River sand (from Daramola 1980, redrawn by Nadukuru 2013).

In explaining pile setup, Axelsson (2000) reported observations of increases in the horizontal stress on the shafts of concrete piles. Chow et al. (1998) proposed a mechanism which states that pile setup is caused by gradual increase in horizontal stress resulting from relaxation of elevated hoop stress from arching effects as a result of pile driving, as illustrated by Figure 2.17. Bowman and Soga (2005) proposed a different mechanism of "kinematically restrained dilatant creep" in sands with strong sand particles under a high shear stress. The shear stress is proposed to be caused by pile installation, with larger-diameter piles generating higher shear stresses. Dilatancy and volumetric expansion then develop with time, but constrained by the pile shaft, result in gradual increase in horizontal stress exerting on the pile shaft.
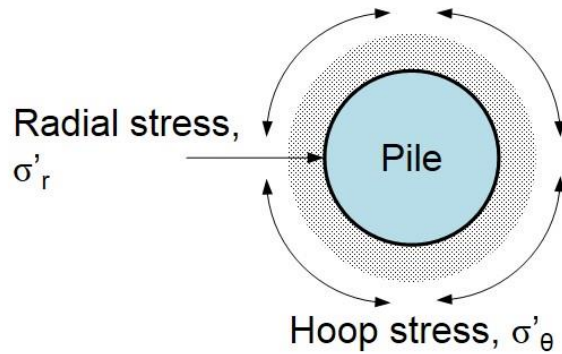
Figure 2.17. Arching mechanisms around pile shaft (redrawn from Chow et al. 1998).

Michalowski and Nadukuru (2012), Nadukuru and Michalowski (2014) and Wang and Michalowski (2015) pointed out that although the abovementioned propositions state rearrangement of particles or evolution of the sand fabric, they failed to explain what is the deeper mechanism that triggered these mechanical processes. Michalowski and Nadukuru (2012) provided a different hypothesis termed as "static fatigue hypothesis" which considers delayed microfracturing of micromorphological features on sand grain surfaces in contact, due to stress corrosion, as the triggering mechanism the series of macroscopic rearrangement of particles and evolution of the sand fabric. Nadukuru and Michalowski (2014) and Wang and Michalowski (2015) reported results from 1D compression tests on single inter-grain contacts under constant loads and the results showed time-dependent convergence of the two surfaces at contact with time, which supports the static fatigue hypothesis. Wang and Michalowski (2015) simulated static fatigue of an individual inter-grain contact with DEM and observed increased microscopic contact points between the rough surfaces of two grains in contact. This trend indicates increases in contact stiffness and friction with time, and this evolution provides another explanation for the increase in macroscopic stiffness of sand during aging.

Lade and Karimpour (2010) proposed that time-dependent grain crushing, due to static fatigue, as a key role in time effects in sands. However, this hypothesis cannot explain the aging effects under low stress where crushing of significant amounts of particles does not likely occur, e.g., Dowding and Hryciw (1986) (vertical stress was less than 10 kPa caused only by self-weight

39

of sand). Lade and Karimpour (2010) mentioned that static fatigue fracturing at grain surface was plausible to be responsible for sand aging.

2.4. Summary

- Observations of aging effects in freshly deposited or disturbed sand have been reported for three decades. The mostly reported changes as results of aging effects are: soil stiffness, cone penetration resistance, shear strength, liquefaction resistance, and pile setup.

- Some aging-caused changes in sand, such as an increase in small strain stiffness of sand and an increase in shaft resistance during pile setup, roughly follow a linear relationship with log cycle of time. These correlations could provide guidance in predicting future sand properties. However, the readers are suggested to use these correlations with great caution as aging effects have been found to vary largely under various environmental conditions.

- The rate of deformation and variation in sand properties over time (stiffness in particular) are largely affected by grain sizes, temperature, relative humidity, chemical composition of pore fluids, or disturbance energy.

- Numerical simulations have reproduced some key characteristics of aging behavior of sand. However, the simulation efforts were all based on predetermined microscopic properties of particles and contacts, due to lack of experimental data from tests with individual grains and contacts.

- Chemical, micro-biological, and mechanical processes have been proposed to be the driving mechanisms behind aging effects in sand. Among the three, mechanical processes, specifically continued minute rearrangements of particle structure, have so far been considered as the key mechanism.

Chapter 3

Hypothesis and Research Objectives

3.1. Static Fatigue Hypothesis

The *static fatigue hypothesis* states that delayed fracturing of grain surface micromorphological features on grain surfaces in contact is the predominant mechanism behind aging effects in sand. Surfaces of silica sand grains are rich in micromorphological features, such as asperities, crystalline fragments, or mineral debris. When grains with such micromorphology come into contact, the asperities, crystalline fragments, or mineral debris in the contact area become loaded to a considerable degree. Under the high stress level, microcracks grow in the material over time, a process called *static fatigue.*

Static fatigue, also referred to as *stress corrosion cracking,* is a well-documented phenomenon in brittle materials, such as silica and ceramics, where sub-critical (microscopic) cracks build up in the material over time under constant stress (Charles 1958, Wiederhorn and Bolz 1970, Cuallar et al 1987).

A demonstration of the hypothesized mechanism behind sand aging is summarized in Figure 3.1. In a sand grain assembly with constant load, the transfer of load from grain to grain occurs through discrete contact "points" or pairs of load transferring asperities on two neighboring grains. Stress is concentrated in these loaded small surface features. Over time, static fatigue fracturing develops in the silica material, which alters the micromorphology of the surfaces in the contact and adjusts load transfer between the two surfaces. This evolution process of individual contacts due to static fatigue eventually breaks down the equilibrium of the grain assembly and triggers a minute rearrangement (or structuration) of the grain system to regain equilibrium. The structuration process has been observed by previous researchers (Bowman and Soga 2003 and Suarez 2009). In contrast to previous research, structuration is not considered here as a cause of aging. Rather, it is the consequence of maturing of contacts, which is the essential element of the static fatigue hypothesis.

During the structuration process (Figure 3.1) the contacts may be retained, or they can evolve to become contacts between grain surfaces that were not subjected to fatigue previously. The latter are essentially new contacts that replaced old contacts.

For those contacts that remain the same during structuration, static fatigue of asperities continues occurring and this process is termed *contact maturing* in this thesis. There are three consequences of contact maturing:

(1) Continued convergence of two grains in contact,

(2) increase in the number of contact points (pairs of load transferring asperities), which increases the contact stiffness, and

(3) increase in roughness interlocking between the two rough grain surfaces in contact (manifested as larger deviations of interaction forces from the vertical).

The contacts that were subjected to large relative displacements, are essentially replaced by new contacts between areas not previously subjected to maturing (process ① in Figure 3.1). This renewal process "resets the maturing clock" at the new contacts, shown as process ② in Figure 3.1, and it keeps the grain assembly aging for long periods.

42

If severe chemical reactions take place between grain minerals and the pore fluid, the contact evolution will be controlled by chemical reactions, and static fatigue process will become a secondary mechanism.
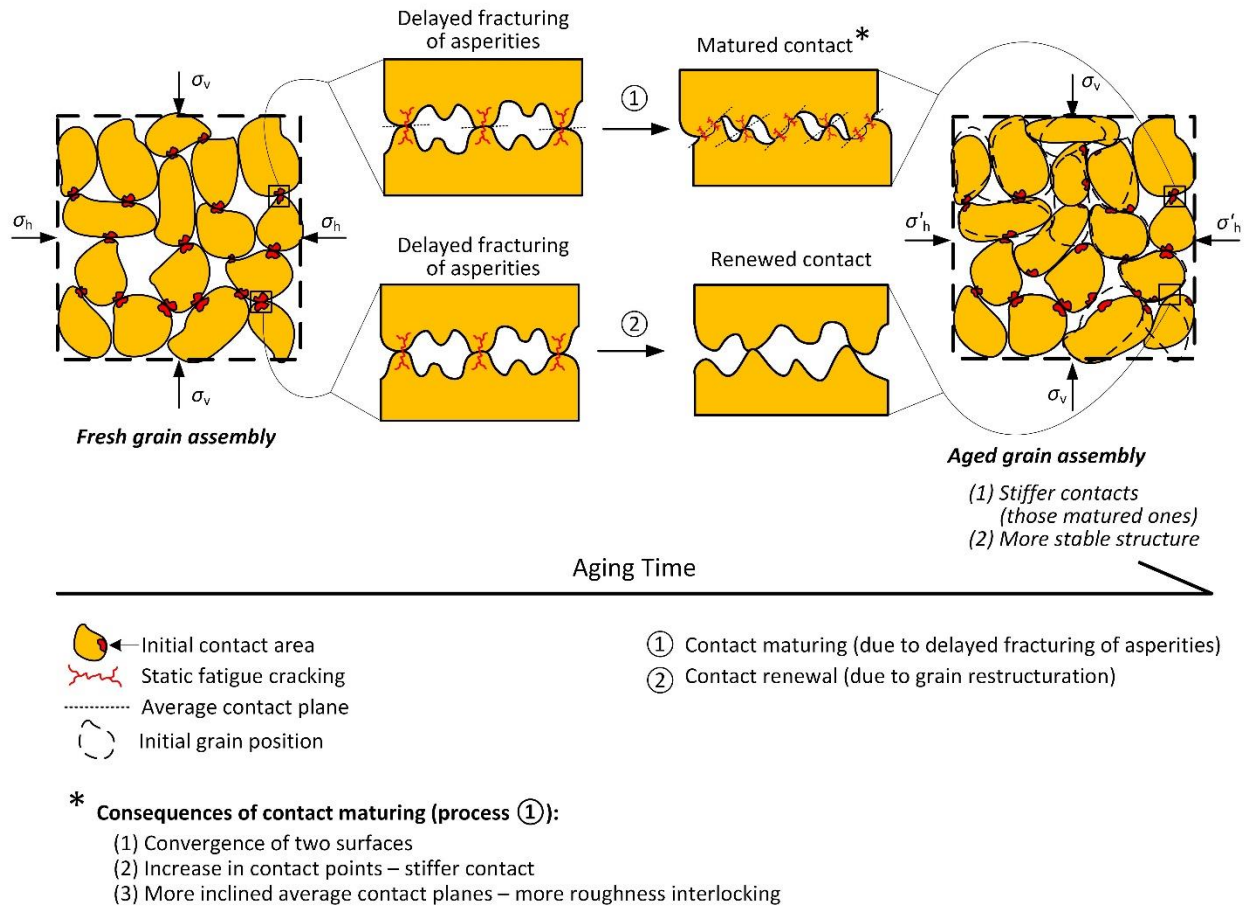
Figure 3.1. Mechanism of sand aging based on the static fatigue hypothesis.

3.2. Research Objectives

This research focuses on gaining better understanding of the aging process in silica sand. To achieve this goal, objectives of this research emphasize collecting grain-scale experimental

evidence to support the static fatigue hypothesis. Numerical simulations of micromechanical behavior of sand are developed to complement the experiments. Specific objectives are:

(1) Obtaining direct experimental evidence for the static fatigue hypothesis and exploring the consequences of contact maturing,

(2) confirming the presence of aging effects in sand grain assemblies through sample-scale testing, and exploring factors that affect rates of aging in sand,

(3) developing reliable numerical modeling tools to simulate grain-scale time-dependent behavior in sand to complement tedious and time-consuming grain-scale experiments, and

(4) developing a preliminary numerical framework for simulations of the evolution of grain surfaces under combined influence of mechanical loads and chemical reactions.

Chapter 4

Laboratory Contact Maturing Experiments

4.1. Introduction

Surface texture of silica sand grains is rich in asperities at many spatial scales, and inter-granular (nominal) contacts are comprised of many "contact points" (or contact subareas). The author advocates a hypothesis that the key cause of time effects in silica sand is in the time-dependent fracturing of textural features (asperities) and mineral debris on grain surfaces at the contacts. This process was referred to as *contact maturing*. In previous simulations work, assemblies of sand grains are often modeled as systems of spheres (or grains of other shapes) with elastic contacts and a frictional limit on the inter-granular shear force. It was demonstrated that the contact behavior is complex, owing to elaborate morphology of the grain surfaces, and time-dependent micro-fracturing process.

A hypothesis was suggested by Michalowski and Nadukuru (2012) that the phenomenon responsible for the time effects in silica sand is the delayed micro-fracturing of textural features (asperities and mineral fragments) on grain surfaces at contacts. This process has been referred to

also as static fatigue (Charles 1958, Scholz 1972, Wiederhorn and Bolz 1970), contact fatigue, stress-corrosion cracking, and could be described also as contact maturing.

In order to gain experimental evidence for this hypothesis, an apparatus was constructed, capable of measuring time-dependent behavior of grain contacts under sustained loads. A single sand grain is placed between two steel plates with parallel and relatively smooth surfaces, and the time-dependent increase in the convergence of the two surfaces is measured while the two contacts are subjected to a sustained load.

Grain-scale tests have been attempted by others (Cole and Peters 2008, Cole et al. 2010, Cavarretta et al. 2010, Cavarretta et al. 2011, Senetakis et al. 2013). However, past research was focused on the immediate response of grains/contacts to load and crushability of grains. No attention has been paid to time-dependent properties and evolution of contacts under sustained loads, which is the key ingredient of the contact maturing hypothesis in Michalowski and Nadukuru (2012). Long-term experiments (weeks and months) present challenges associated with time-dependent behavior of mechanical components of the apparatus subjected to environmental loads. Quantitative measurements of the contact load-convergence behavior are essential to understanding the contact properties and calibrating the contact constitutive models needed in simulations of grain assemblies.

In this chapter, the custom-designed apparatus for contact-maturing tests and its data acquisition system are introduced. The testing procedure is then presented, followed by a discussion of challenges and sources of inaccuracies of the testing system. The testing results are reported and discussed, and finally the conclusions of the contact-maturing tests are given.

4.2. Contact Maturing: A Key Cause of Aging

Surface micro-morphology (texture) of silica sand grains is illustrated in Figure 4.1. Good examples of the richness of the grain textures can also be found in Krinsley and Doornkamp (1973), and Mahaney (2002). When two grains with a surface morphology as in Figure 4.1 come into contact and become loaded, the predominant response is fracturing and crushing of the micro-

morphological features in the contact region, causing comminution (fragmentation) of the material at the contact region.
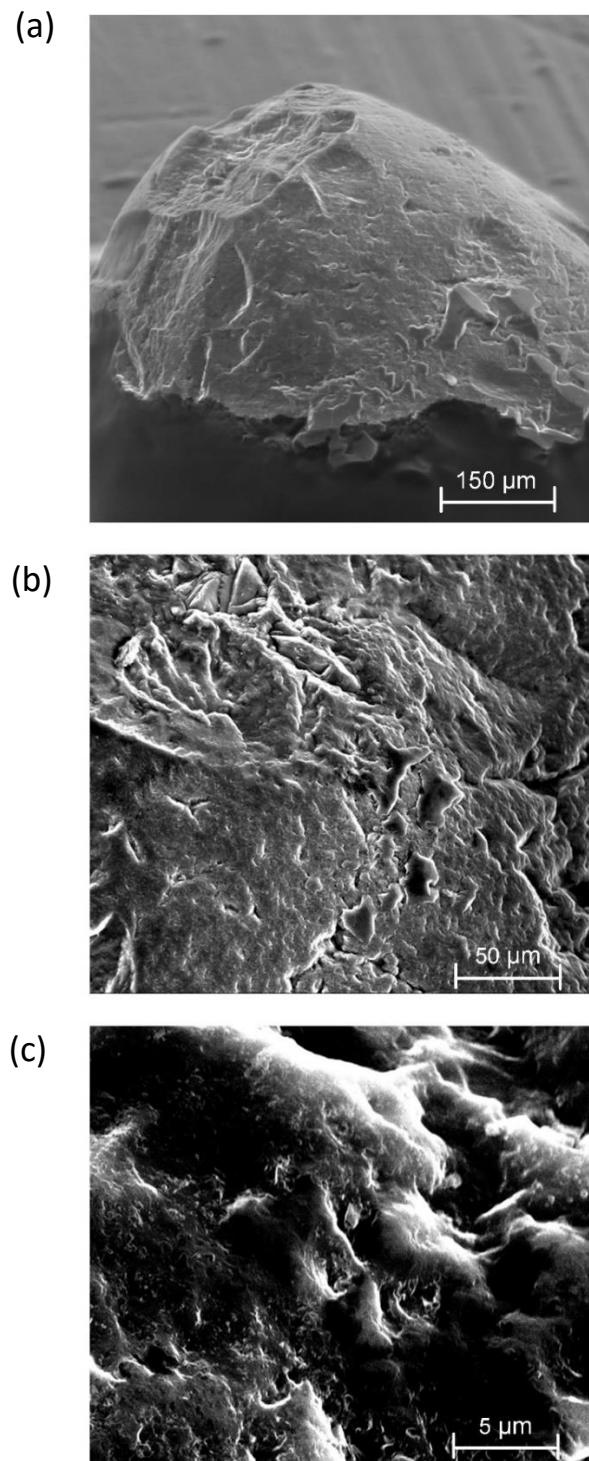
Figure 4.1. Scanning electron microscopic (SEM) images of Ottawa 20-30 sand grain surface.

(a)

RMS = 577 nm

3.5 μm

30 μm

30 μm

(b)

RMS = 321 nm

2.4 μm

30 μm

30 μm

Elevation (μm)

-2.0   0   2.0
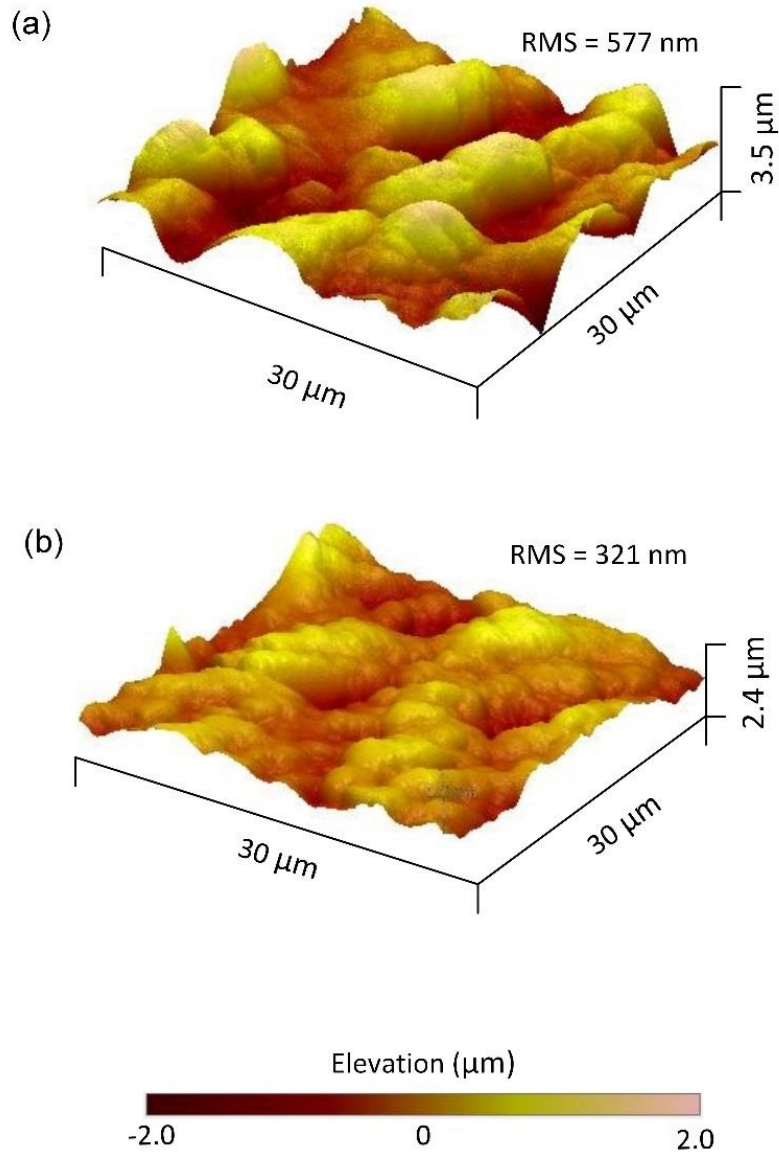
Figure 4.2. Atomic force microscopic (AFM) images of Ottawa 20-30 sand grain surface.

The richness of the surface texture can be quantified with atomic force microscopy (AFM). Two AFM scans of two different grains are shown in Figure 4.2. The roughness of the surface can be described with the root mean square (RMS) of the surface elevation, defined as

$$RMS = \sqrt{\frac{1}{mn}\sum_{i=1}^{m}\sum_{j=1}^{n}\left(z_{ij}-\mu\right)^{2}} \tag{4.1}$$

with μ being is the average elevation of the surface, calculated as

$$\mu = \frac{1}{mn}\sum_{i=1}^{m}\sum_{j=1}^{n}z_{ij} \tag{4.2}$$

where m and n are the number of points in the scan in the x and y directions, respectively, and z_{ij} is an elevation located by i_{th} and j_{th} point in the x and y-direction, respectively. Even though the grains used in Figure 4.1 came from the same batch, the root mean square of the elevation is quite different (577 nm vs. 321 nm). Substantial differences can also occur between roughness at different locations on the same grain.

It was argued earlier (Michalowski and Nadukuru 2012, Wang and Michalowski 2015) that the fracturing of the textural features on the grain surface at the contact does not stop after the loading process is completed; rather, it continues under sustained (constant) load, and the process is referred to as static fatigue or contact maturing. Contacts evolve during the maturing process, leading to an increase in the number of contact points within a nominal contact area. Consequently, the contact stiffness increases. The authors consider contact maturing as a key cause contributing to time effects in sand. This paper is focused on collecting experimental evidence in support of the contact maturing hypothesis. This hypothesis finds its physics underpinning in the rate process theory and fracture kinetics (e.g., Glasstone et al. 1941, Krausz and Krausz 1988, Bažant and Pang 2007).
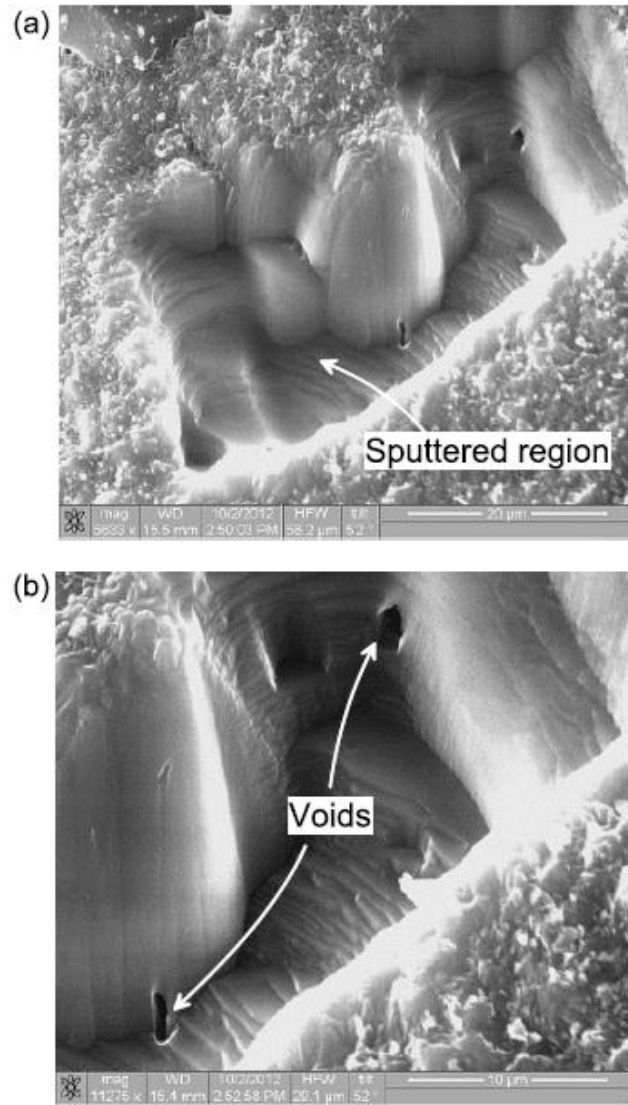
Figure 4.3. SEM image of Focused Ion Beam sputtered region of Ottawa sand grain: (a) sputtered area (image width: 56 μm), and (b) magnified image with two voids (image width: 28 μm) (reproduced from Nadukuru 2013).

The primary objective of the tests was to gain quantitative information about the consequences of contact fatigue on the time-dependent response of the contacts, and the testing was performed at contact forces that did not cause fracture of the entire grain. Nano-indentation tests with Berkovich (1950) tip indenter performed by Nadukuru (2013) indicated Young's modulus of grain mineral in the range of 42 to 110 GPa, which is consistent with amorphous silica.

However, the behavior of grains at larger loads can be affected by imperfections in the mineral core, such as discontinuities and voids. An example of voids is presented in Figure 4.3; this is an image of the "interior" of the grain after the surface material was removed down to a depth of about 10 μm using the Focused Ion Beam (FIB). Because of the large momentum of ions, they can sputter (eject atoms) from a solid target, allowing careful uncovering of the regions below the grain surface. A FIB-sputtered area on a silica sand grain is illustrated in Figure 4.3, with a magnified image of two small voids in Figure 4.3. Such imperfections are likely to facilitate the initiation of grain fracturing at larger loads, an effect classified by Mesri and Vardhanabhuti (2009) as level III damage, and considered by Lade and Karimpour (2010) as a major contributor to time effects of grain assemblies. Grain crushing has received a lot more attention in the literature compared to the contact fatigue (e.g. McDowell and Bolton 1998, Einav 2007, Zhao et al. 2015) and it is not a subject of this thesis.

4.3. Contact Maturing: Early Demonstrations

Several contact maturing tests were carried out with a prototype of the apparatus that will be introduced in this thesis. In this testing, a sand grain was fixed to a scanning electron microscopic (SEM) stand with a fast-acting heavy-duty adhesive on one side and the surface 180˚ from the glued side was loaded with a constant normal force. No rotation was allowed during testing with the sand fixed to the stand, so the contact area could be roughly estimated. This estimated contact area was observed with SEM before and after the test and the images from these two instances were compared to identify static fatigue-caused damage. Although in later tests the author found out that the adhesive creeps over time, lowering the credibility of convergence measurements in these tests, the SEM observations of surface damage still provided visual evidence for contact maturing fracturing.

Figure 4.4 was the projected contact area and changes in morphological features were observed at several locations as highlighted with colored rectangles. However, the observed alteration of the contact region could have happened immediately following application of the load instead of coming from static fatigue over time.
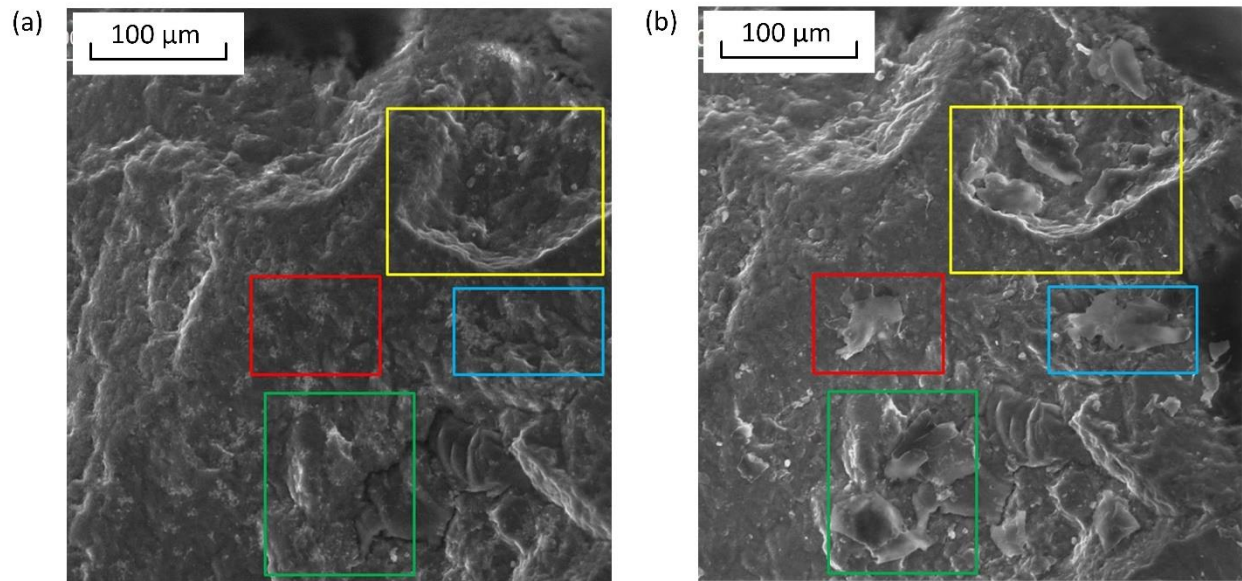
Figure 4.4. SEM images showing micro-cracking on grain surface: (a) before loading, and (b) 8 days after constant load of 1.3 N.
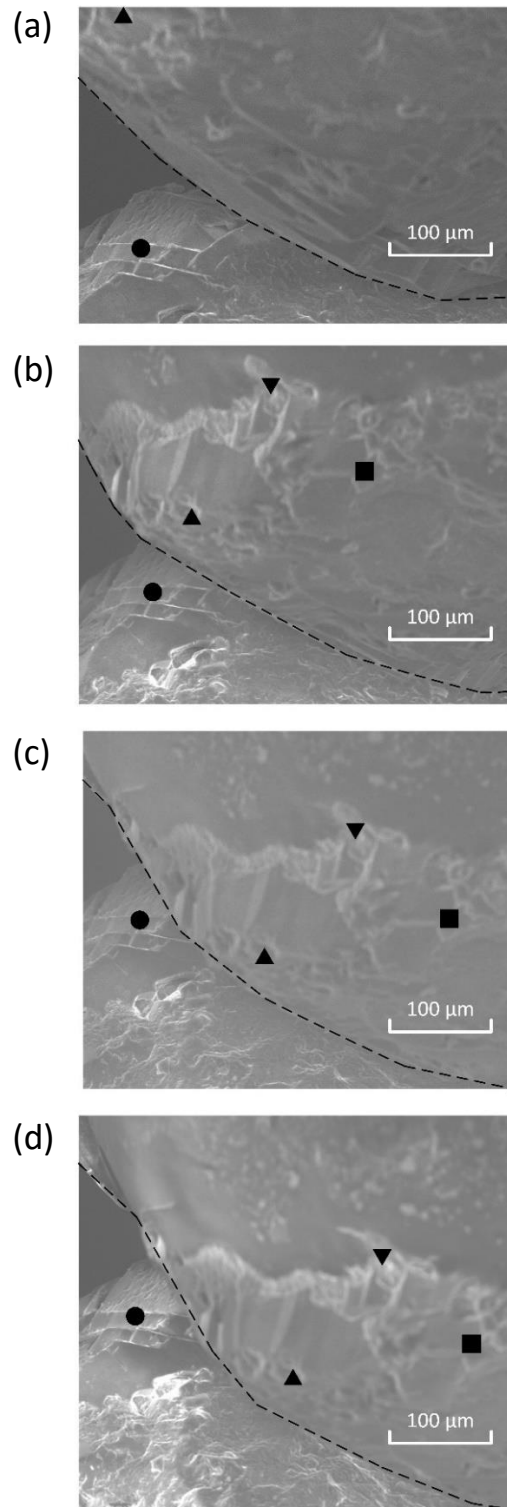
Figure 4.5. Results of demonstration of two grains in contact. relative displacement of two grains under oblique force of 2.5 N: (a) 10 mins after load application, (b) after 2 days, (c) after 3 days, and (d) after 9 days (reproduced from Nadukuru 2013).

A contact loading test between two grains was conducted by Nadukuru (2013) during which the relative displacement of the grains was observed using a scanning electron microscope. Two Ottawa 20-30 Sand grains (grain size between 0.6 – 0.84 mm) were loaded with a force of 2.5 N, and the entire assembly was periodically placed in the SEM chamber to record the image of the relative position of the two grains. The force was applied at an oblique angle to the contact, with the shear component expected to cause relative sliding in addition to normal convergence. The exact obliquity could not be determined for two reasons: (i) true contacts between grains do not have one well-defined normal, and (ii) the contact area was not in direct SEM view (it was obscured by the body of the grain). The four images in Figure 4.5 show the relative configuration of grains 10 min. after the load was applied, and then after 2, 3, and 9 days. The black dashed line indicates the contour of the upper grain. One point is marked on the stationary grain (circular bullet) and three points on the moving grain, to visualize the extent of the relative motion. The quality of these images was compromised by the geometry of the loading setup that made it difficult to capture the electron beam reflected from the grain surfaces; still, the images clearly indicate that the configuration of the two grains subjected to a constant load did not remain stationary. The upper grain is gradually changing its position in the down-right direction over the stationary bottom grain. The projection of the distance travelled by the point marked with a black base triangle was about 300 μm in nine days after application of 2.5 N. The rate of relative displacement was initially large, but this rate decreased with time (decaying process), i.e, the displacement between days 3 and 9 is a lot smaller than that between days 2 and 3. A normally loaded contact would be expected to retain its location on the grain surfaces, and the grains would undergo normal convergence only. However, the contact was loaded with an oblique force and so it shifted in the process. This qualitative test was performed solely as a demonstration of time-dependent kinematics of two grains in contact, subjected to a constant load.

(a)

Temperature / humidity control penal

216

Temperature / humidity control cell

(b)

DAQ

Apparatus

Laptop
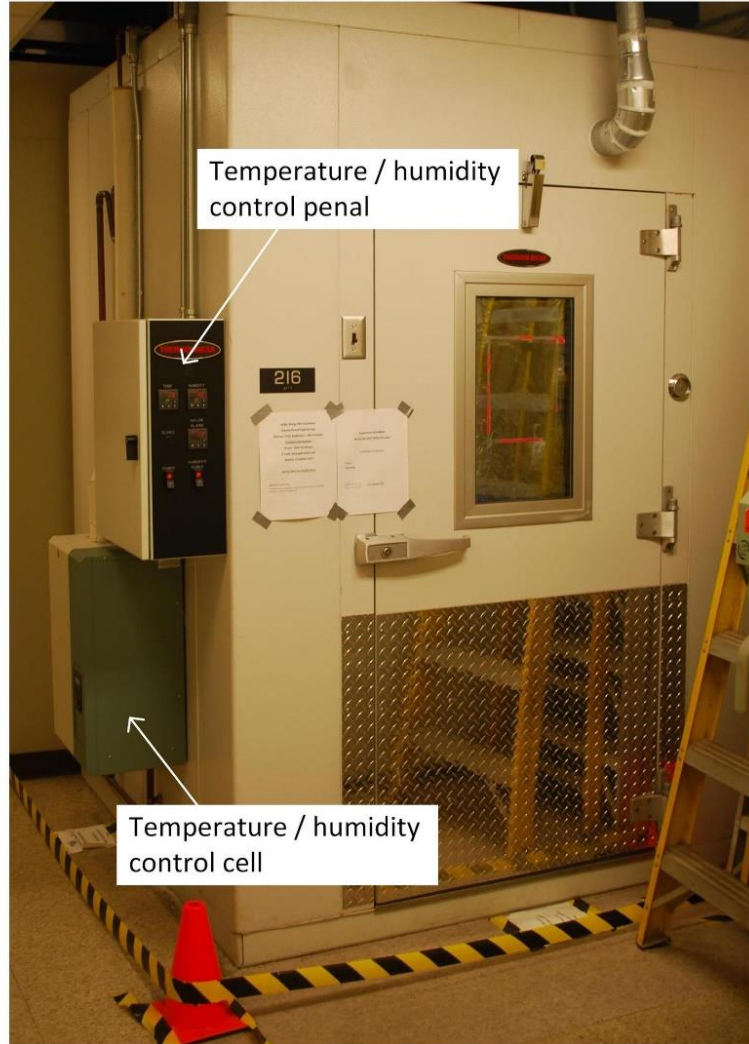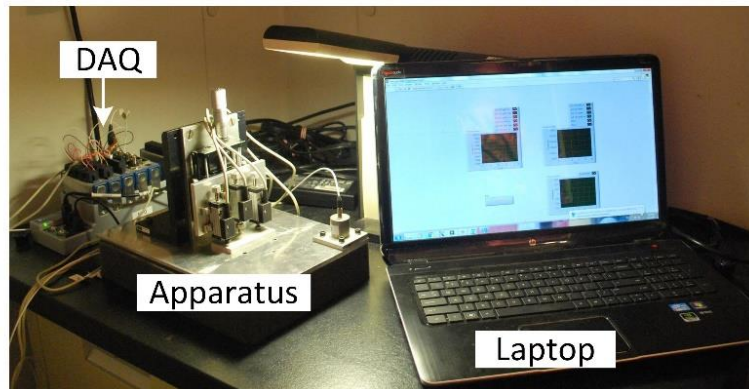
Figure 4.6. Environmental chamber: (a) outside view, and (b) inside view with apparatus and DAQ system.
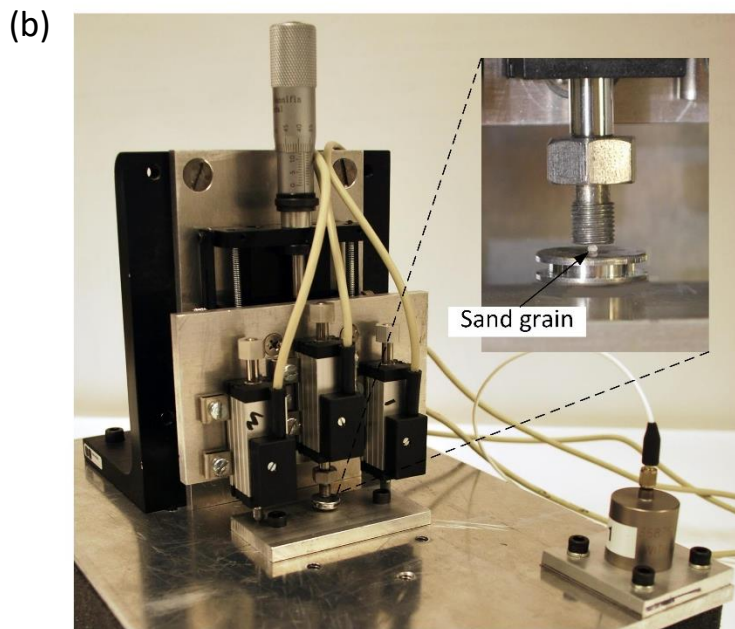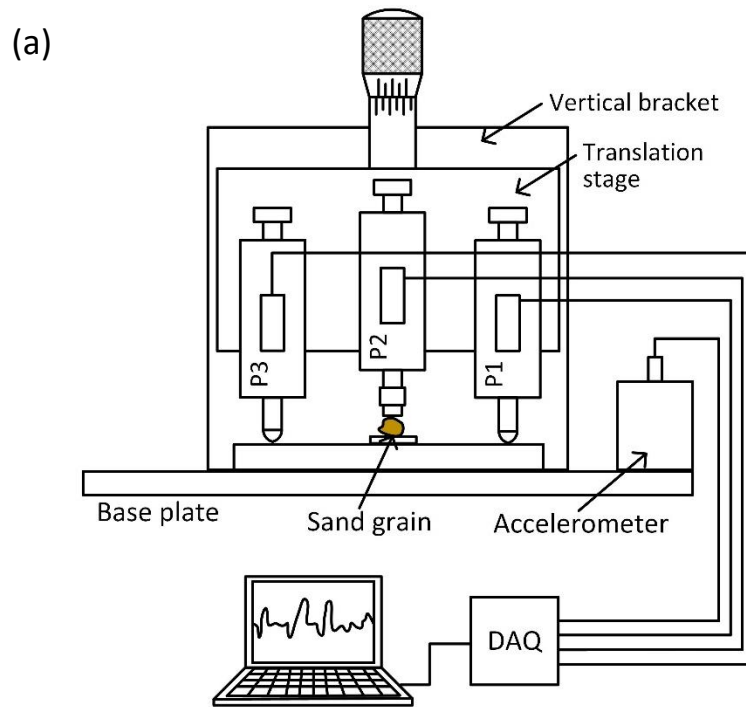
Figure 4.7. Contact fatigue testing apparatus: (a) schematic of apparatus, and (b) photograph of apparatus.
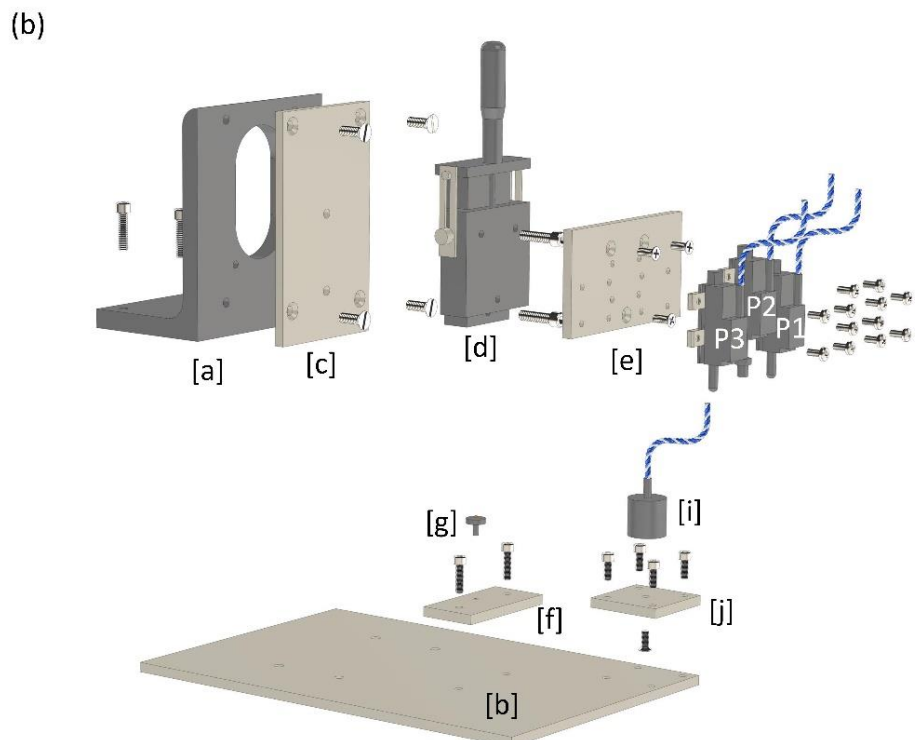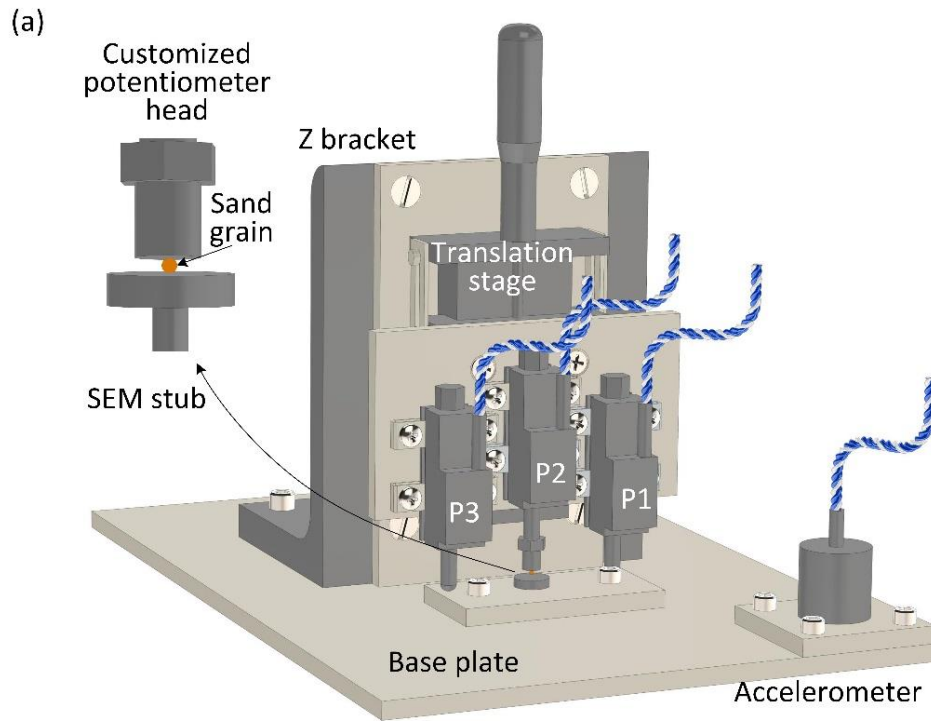
Figure 4.8. SolidWorks drawings of apparatus: (a) general view, and (b) components.

4.4. Apparatus

The objective of constructing the apparatus was testing a response of a single contact between two silica sand grains subjected to sustained (constant) load. These early tests were performed in an apparatus where four stages were used to position the grains and to produce a single contact (Michalowski and Nadukuru 2014). However, the measurements in this apparatus were susceptible to inaccuracies caused by: (a) inherent tolerances in the moving components of the apparatus (stages), and (b) attaching the grains to the loading platens in the apparatus by using an adhesive. Consequently, a new version of the apparatus was designed where no adhesive is used, and the number of moving parts is limited to a minimum. Rather than testing a contact between two grains, this apparatus measures the response of two contacts of one grain with two steel plates located on opposite sides of the grain. The outcomes of such tests are equally indicative of the contact behavior, while eliminating some of the sources of inaccuracies in testing. The apparatus has only one high-quality stage, and the stage is centrally loaded to avoid any possibilities of the rotation of its moving part. Also, the adhesive (glue) is no longer used to attach the grain to the steel surfaces in the device; rather, the grain rests between two horizontal steel surfaces without any adhesive. This apparatus and results are described in the next sections.

Due to the sensitivity of static fatigue to temperature and humidity, the entire testing system is placed in an environmental chamber with temperature and humidity controlled during the testing period (typically, several weeks). Photographs of the chamber seen from outside and devices inside are shown in Figure 4.6. To ensure consistence of testing, temperature and relative humidity in the chamber are monitored with two independent temperature/humidity measurement sensors (labeled as T/H loggers in Figure 4.6(b)) in addition to the sensors in the control system of the environmental chamber.

An overview of the apparatus is given by a schematic and a photograph of the device in Figure 4.7 and details of the components are shown in graphical renderings of the apparatus in Figure 4.8. An L-shape aluminum bracket [a] (depicted in Figure 4.8(b)) with a vertical plate of height 152.4 mm (6") is fastened to a 203.2mm × 304.8mm × 6.4mm (8"×12"×¼") aluminum base plate [b] with four 1/4"–20×1" (diameter – thread count × length) socket head screws (all screws

in this device are standard US machine screws unless specified otherwise). A 152.4mm×88.9mm×6.4mm (6.0"×3.5"×0.25") aluminum plate [c] is mounted on the vertical part of the bracket (with four 1/4"–20×0.75" flat countersunk head screws), and a stage [d] with manual micrometer control is fastened on the aluminum plate [c] (two 1/4"–20×1" socket head screws). This stage allows movement along the vertical axis. An aluminum plate [e] (66.6mm×117.5mm×6.4mm) is fastened on the stage (with three #10–32×0.5" flat countersunk head screws) to provide enough surface area to mount three potentiometers. The potentiometers, labeled as P1, P2 and P3 (Figure 4.8) are fastened to aluminum plate [e], each using two clamps with four ISO 7045 M4×10 pan head screws. Under the potentiometers, a 76.2mm×38.1mm×6.4mm (3"×1.5"×0.25") aluminum plate [f] is fastened to the base plate [b] with two #10 – 32 × 0.75" socket head screws. A stainless steel scanning electron microscopes (SEM) sample-holding stub [g] with a threaded leg is mounted on plate [f] using a predrilled threaded opening.

The stage provides a square flat mounting surface of 66.55 mm×66.55 mm (2.62"×2.62"), and it is driven by a metric micrometer with a traveling range of 25 mm. The potentiometers are contact-type position transducers with a 10-mm measuring range, and they track displacements using the position of the actuating shaft that is associated with the position of a slider on the resistor inside the potentiometer housing. The potentiometers are 17.5 mm in both height and width, and 76.0 mm in length.

The axis of symmetry of the SEM stub is aligned with that of the measuring arm of the central potentiometer P2. During tests, a sand grain is loaded between two horizontal stainless steel surfaces: that of the SEM stub and that on the modified head of the arm of potentiometer P2. Potentiometer P2 (Figure 4.8(a)) performs two functions: (1) it exerts a required force on the grain; for that purpose the force-displacement characteristic of the spring in the potentiometer has to be calibrated, and (2) it measures the change in the relative position of the two plates loading the grain (convergence). The two remaining potentiometers are used to detect whether any rotation of the stage has occurred, and they apply two symmetric forces to avoid any eccentricity in loading that might cause minute rotation of the moving part of the stage.

An accelerometer [i] is mounted at one corner of the base plate to detect any vibrations that may cause undesired effects in the contact behavior. The accelerometer has a measurement range of ±5 g with a broadband resolution of 3 µg RMS (root mean square). It has a sensitivity of 1000 mV/g and its non-linearity is less than 1% (calculated as the maximum difference between the function value and its linear approximation). The excitation voltage is 18 to 30 V, constant current excitation is 2 to 10 mA and the output impedance is less than 500 Ohm. The accelerometer weighs 50 g (1.8 oz) and is 24.6 mm (0.97") in height and 25.1 mm (0.99") in diameter. The accelerometer is first mounted to a 50.8mm×50.8mm×6.35mm aluminum plate [j] with a #10–32×0.5" flat countersunk head screw, and the plate with the accelerometer is fastened to the base plate with four #10–32×0.5" socket head screws. This ensures its sensitivity to high-frequency vibrations. The base board is placed on a 5-cm layer of porous polymeric damper to reduce transmission of external vibrations. This device was successfully used to test time-dependent movement of a grain with respect to a rigid (steel) plate with the contacts subjected to a constant load. The reduction in distance between the two plates loading the grain is referred to here as the convergence.

Potentiometer P2 was customized to meet the testing requirements; this involved two modifications. The first modification was replacing its default ball-point shaft head with a customized stainless steel head with a flat surface. Figure 4.9 shows a disassembled potentiometer, and the customized head is shown in the upper-left corner insert (see also upper-left corner insert in Figure 4.8(a)). This modification was made to provide one of two platens loading the grain (the second platen being the SEM stub). The second modification included replacement of the standard spring in the potentiometer with one capable of generating desired forces within its working range, without jeopardizing its position-measurement sensitivity (standard springs typically require a force larger than 2 N to activate the shaft of the potentiometer). The normal force-displacement correlation of the modified P2 was obtained (for the specific spring used) through a calibration test, where normal forces at various rod positions were measured with a force gage. Linear regression procedure was carried out for data points of normal forces at different displacements, Figure 4.10. The regression results are used to determine positions of the rod for desired normal forces. A good regression fitting was achieved with a coefficient of determination (R2) of 0.9986. The fitting equation is linear and homogeneous

$$F = 0.447d \qquad\qquad (4.3)$$

where F is the normal force exerted by the measuring arm of potentiometer P2 (in N), and d is the displacement of the measuring rod from its zero position (in mm).
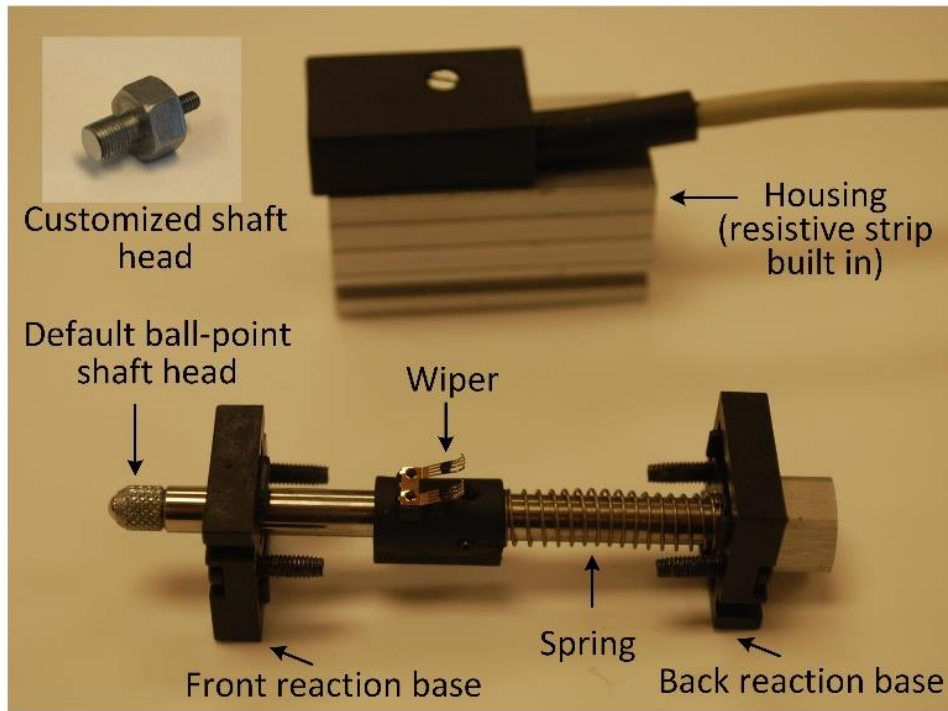
Figure 4.9. Dissembled potentiometer.
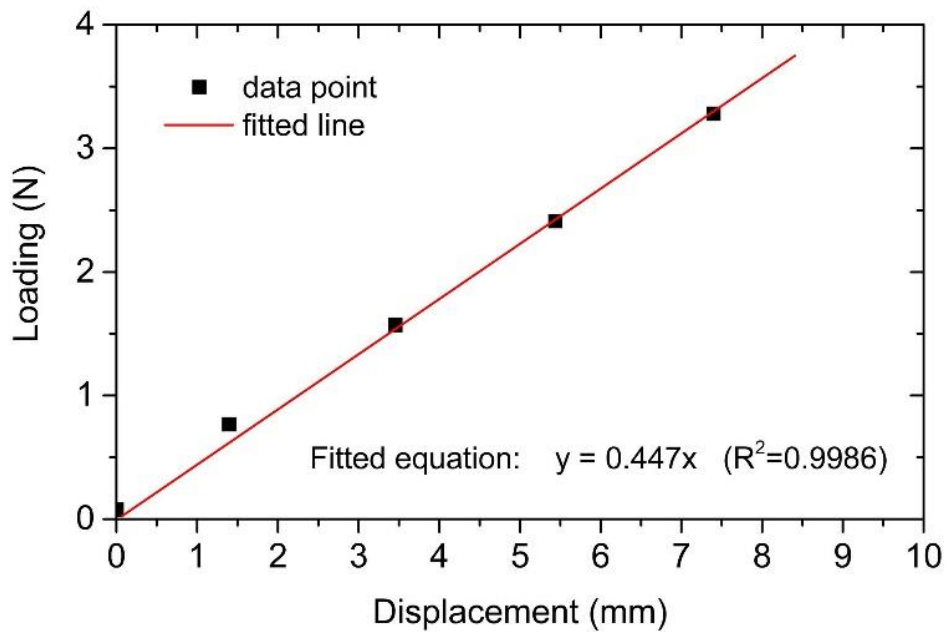
Figure 4.10. Force-displacement calibration for customized potentiometer.
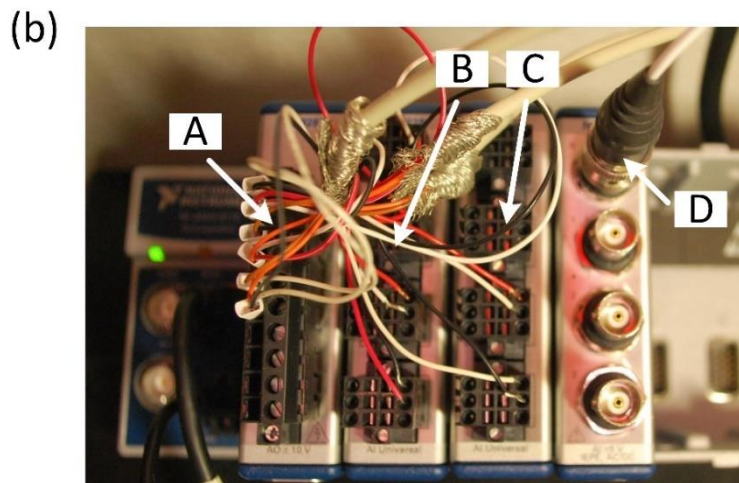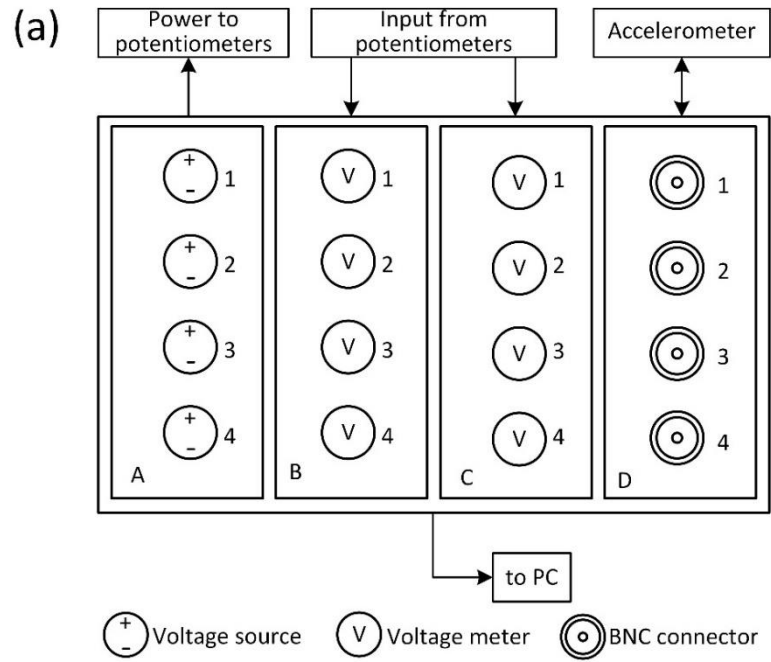
Figure 4.11. Data acquisition system (DAQ): (a) a schematic, and (b) a photograph.

4.5. Data Acquisition System

The data acquisition system (DAQ) provides power sources and reads data from the potentiometers and the accelerometer. Each potentiometer is powered with a separate source with an input DC voltage of 0.5 V and the output voltage (0 to 0.5 V) is measured. The sampling rate of the output voltage measurements is 1 Hz. The displacement of the i-th potentiometer is converted from the voltage readings by

$$d_{(i)} = D_{(i)} \cdot (V_{out(i)} / V_{in(i)})$$
(4.4)

where $d_{(i)}$ is the displacement, $D_{(i)}$ is the measuring range, $V_{out(i)}$ and $V_{in(i)}$ are the output and input voltages of the i-th potentiometer.

The DAQ system, as shown schematically in Figure 4.11, consists of four major modules accommodated in a NI CompactDAQ 8-Slot USB Chassis, NI cDAQ-9178 (all DAQ components were from National Instruments). The system has a 4-channel, 16-bit analog voltage output module A (NI 9263, voltage range ±10 V) powering the potentiometers. Three independent 0.5 V DC voltages are provided by this module to the potentiometers. Modules B and C (NI 9219) are two identical 4-channel 24-bit analog input modules to measure output voltages, as well as input voltages, of the potentiometers. Although module A provides nominal DC voltages of 0.5 V to the potentiometers, the actual output voltages of module A usually vary around the desired value with small drifts. Thus both input and output voltages from each potentiometer are measured to calculate its displacement more accurately. Modules B and C take measurements from the potentiometers at a frequency of 1 Hz. The last module, D, is a 4-channel 24-bit current excitation and AC/DC input module. Module D (NI 9234) is used for current excitation and taking measurements from the accelerometer, with a 2.0 mA excitation current and a ±5 V AC/DC voltage measurement range. This module is connected to the coaxial connector of the accelerometer through one of its 4 BNC connectors. The readings from the potentiometer are obtained at a frequency of 2 kHz.

The DAQ is controlled by a LabVIEW program installed on a portable PC, all placed in an environmental chamber. The computer is connected wirelessly to the Internet, and can be accessed remotely. The real time readings of displacements and accelerations are shown on the LabVIEW interface and are monitored remotely to assure the tests are running without disturbances. With the wireless control of the portable computer, physical entries into the environmental chamber are avoided during tests, and this prevents a major source of external vibrations.

4.6. Testing Procedure

Sand grain preparation and grain loading

The sand grains are washed with a stream of distilled water to remove coarse debris from the surface, and then they are air-dried. Surface topography of sand grains is characterized with scanning electron microscopy (SEM) and atomic force microscopy (AFM) before each test. At least 24 hours before being tested, a sand grain is put in the environmental chamber to make it adapt to the environmental conditions in the testing chamber (the temperature and the relative humidity).

The sand grain to be tested is placed in the middle of the surface of the SEM stub (see upper-left insert in Figure 4.8(a)), under the bottom surface of the rod head of potentiometer P2. Then the three potentiometers mounted on the stage are moved slowly downward using the manual stage micrometer until the flat rod tip surface of potentiometer P2 comes into contact with the grain that is resting beneath on the SEM stub. Next, the grain becomes loaded with a required force. The target displacement of the stage, which generates the target force on the grain, is calculated from the calibration curve (force-displacement correlation of the spring in potentiometer P2, as in Figure 4.10). This target displacement is divided into 4 equal increments. During each increment the stage is moved manually (using the stage micrometer) with a constant low velocity (about 0.1 mm/s), with a 1-minute pause between increments. After the target displacement is reached, the stage is locked in position with two screws on both sides of the stage to maintain the force and to minimize undesired minute rotation of the stage in its rails.

Test duration and monitoring convergence

During the test, the force is maintained at the desired level with the stage locked. Ideally, a normal force would be maintained, but angularity of the grain and the surface texture at contacts may result into some departure from normality. However, the forces on the grain applied at the top and bottom contacts must be collinear and equal in magnitude. Contact fatigue (or contact maturing) causes micro fracturing in the contact asperities, resulting in convergence of two loading platens, thus some relaxation in the spring force of potentiometer P2. This effect on the normal force, however, is less than 1 mN (less than 1‰ of a typical target force), as the fatigue-induced displacement is typically less than 2 μm. With the computer connected to a wireless network, the readings from the sensors are monitored remotely without entering the chamber. Abnormal readings are analyzed and if they turn out to be a result of external excitation (for instance, due to nearby construction) or the temperature/humidity control system failure, which renders the data of little use, the test is stopped. Otherwise, the test continues for designed duration.

The test is stopped typically when the convergence of the two metallic surfaces hardly shows any change in at least three consecutive days. It was found out from preliminary tests that this occurs after about 3 to 4 weeks. To make it easier to locate damage at the upper contact area after the test, a strong cyanoacrylate-based fast-acting adhesive is applied to the bottom contact to "freeze" the grain in the loading orientation to the SEM stub. Then the grain is unloaded by unlocking and moving the translation stage upward in 4 reversed equal steps.

Visualization of static fatigue damage

The post-test visual identification of contact fatigue damage is challenging. In order to achieve this goal, zoomed-in SEM images of contact area before and after the test are needed for comparison. However, the surface areas to be affected cannot be identified a priori, and the method requires scanning large portions of the grain surface with high resolution prior to the test.

4.7. Inaccuracies in Measurements

Inaccuracies in measuring the outcome of the testing may come from external or internal sources. External factors are those due to changes in the environment, such as vibrations or variations in temperature and relative humidity. Internal factors, on the other hand, refer to the performance of the apparatus itself. For instance, undesirable displacements due to tolerances in the rails of the stage may cause incorrect readings, or instability of the electrical signal (drift) may contribute to inaccuracies.
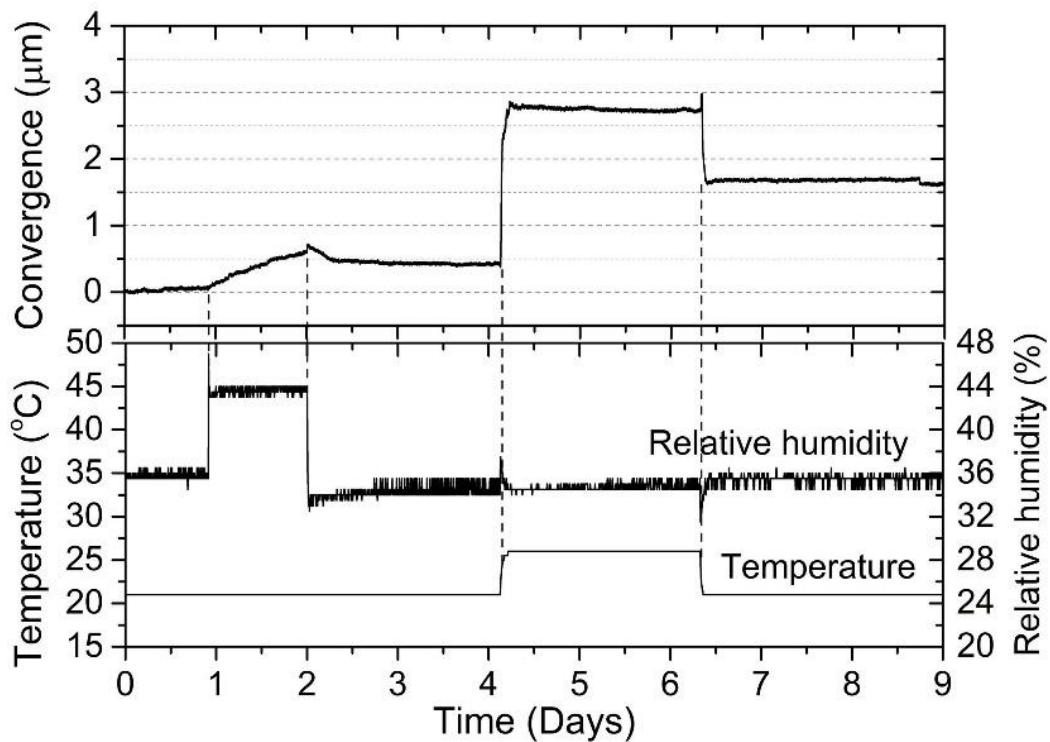
Figure 4.12. Signal variation caused by a change in relative humidity and temperature in a test on a stainless steel sphere.

External factors

These factors include changes in temperature and humidity, and also external vibrations. A 9-day test with a stainless steel sphere was carried out to investigate the sensitivity of the system to temperature and relative humidity. The sphere was 3.125 mm in diameter and was subjected to a constant force of 1.3 N. In the test with a stainless sphere no measurable convergence was expected, thus the measured effects could be attributed to the changes in the environment. The result of the test is shown in Figure 4.12. As expected, no convergence was detected in the first day when the temperature and relative humidity were kept constant at 21˚C and 36%, respectively. In the second day, relative humidity was increased to 44% while the temperature remained at 21˚C. During this period, the reading of convergence was increasing steadily to reach 0.65 μm at the end of the (second) day. Stress corrosion cracking in silica is sensitive to changes in moisture content, but stainless steel is not expected to react in such a distinct fashion. In the subsequent 2 days the relative humidity was set to 35% with temperature remaining at 21˚C. During these two days the convergence reading recovered by 0.15 μm in the first 6 hours and then remained at 0.5 μm. From the 5th day through half of the 7th day, the temperature was set to 26˚C without changing the relative humidity. The convergence now shot up by 2.25 μm in about two hours and showed a steady reading at 2.75 μm afterwards. As the temperature was set back to 21˚C in the middle of day 7, convergence recovered by about 1.1 μm and remained at 1.65 μm in the remaining 2.5 days of the test. Although temperature and relative humidity both returned to their initial values, permanent convergence was recorded at the end. It is evident that the variations in temperature and relative humidity cause changes in readings of potentiometer P2. This may be caused by expansion and contraction of the components of the apparatus (and the stainless steel sphere) while the changes in humidity affect the electrical signal (the changes in humidity may, for instance, affect the electrical properties of the slider in the potentiometer) (Ciprian and Lehman 2009). Simple calculations indicate that a 5°C change in temperature produces extension/contraction of the metal components of the apparatus that are far greater than the magnitudes of the measured convergence. Therefore, changes in temperature need to be avoided during testing. The influence of temperature on the long-term behavior of contacts (weeks) can be assessed from tests, each at a different but constant temperature. Changes in humidity and temperature do affect the rate of contact fatigue in silica sand (Cuellar, et al. 1987), but this effect might be difficult to distinguish from the effects

caused by the inherent response of the apparatus and the electrical system to these changes. For that reason, the tests are performed at constant temperature and humidity.

External vibrations are another environmental cause that may render readings inaccurate. Such excitations can cause instant fracturing of the asperities at the contact, which will be manifested in sudden increases in convergence. The environmental sources of inaccuracies in measurements are mitigated by placing the entire apparatus in an environment chamber with controlled temperature and humidity (both constant), and by placing the device on a 5-cm thick foam-like damper to isolate the device, to some extent, from external vibrations.

Internal factors

Systematic inaccuracies in measurements caused by internal factors include two types: mechanical and electrical. Mechanical inaccuracies refer to minute movements of the device components, in particular, those associated with the moving parts of the stage. Tolerances necessary for the stage to operate allow for minute relative rotation and transverse displacement in the rails of the moving component. To minimize this source of error in measurements, after the required force has been applied on the grain, the stage is locked in place symmetrically on two sides by two screws (standard stages typically come with a locking screw only on one side). The second type of systematic inaccuracies is a result of possible instability in electrical signal and signal drift. This source of errors is worth of some awareness, especially for static fatigue tests which last several weeks.
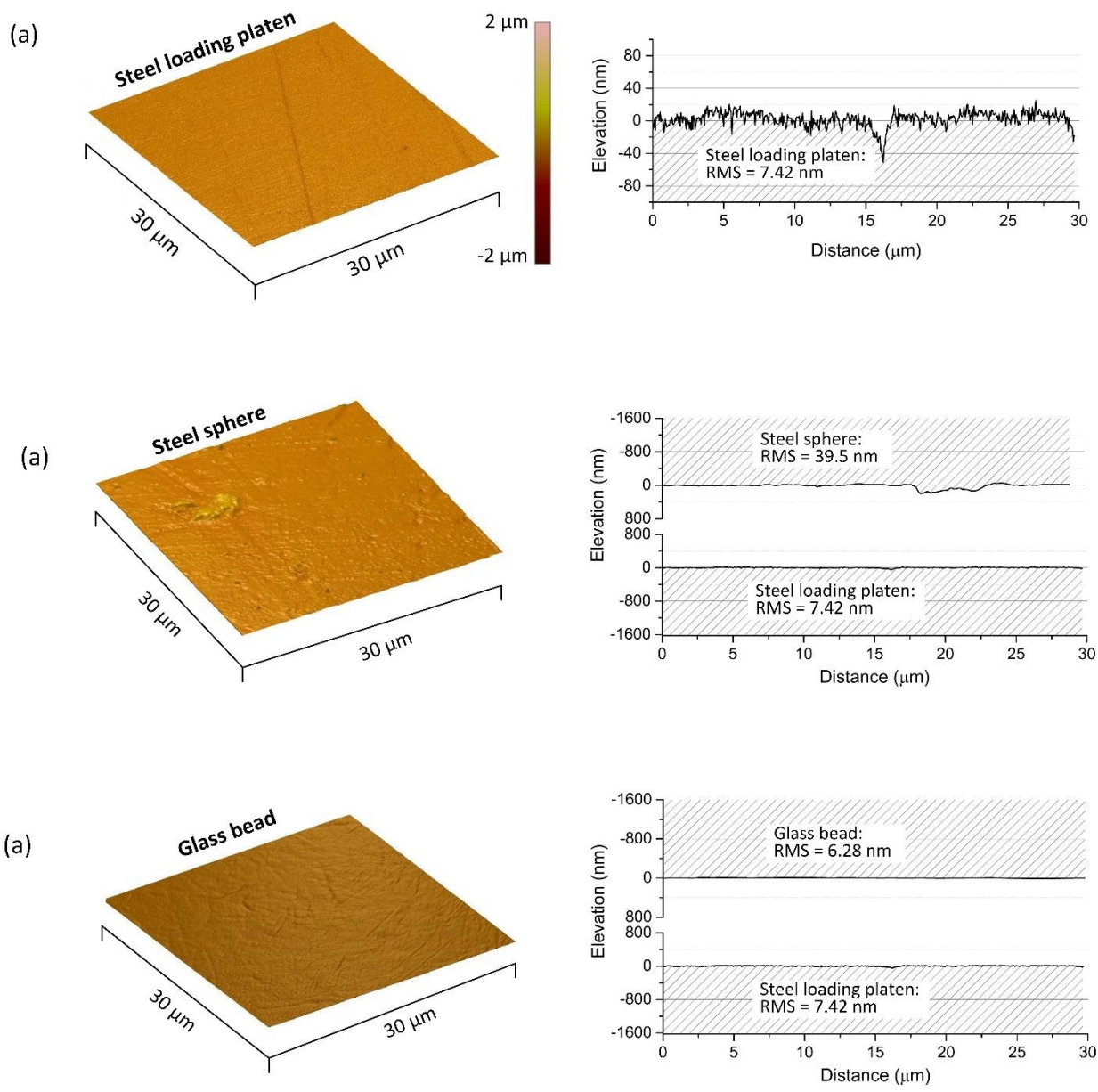
Figure 4.13. AFM measurements (all areas are 30µm×30 µm): (a) the steel loading platen, (b) steel sphere, and (c) borosilicate glass bead.
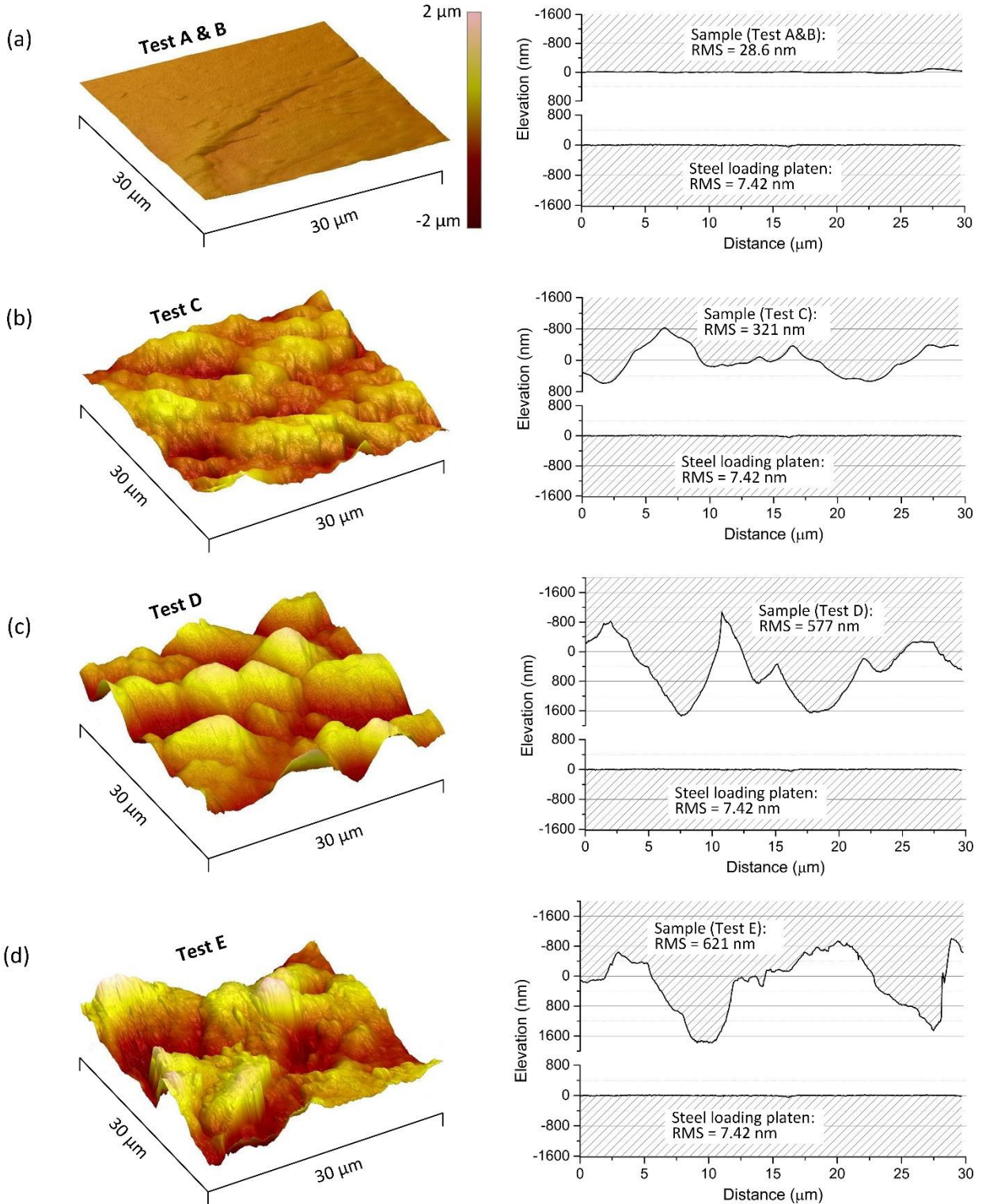
Figure 4.14. AFM measurements of surfaces of the Ottawa sand grains tested (all areas are 30µm×30 µm): (a) sample in Tests A and B, (b) sample in Test C, (c) sample in Test D, and (d) sample in Test E.

71

4.8. Results

Atomic force microscopic (AFM) measurements of all of the surfaces involved in the tests are shown in Figure 4.13 and Figure 4.14. Three dimensional micro-topography (30 µm × 30 µm) and two dimensional profiles of the steel loading platen are shown in Figure 4.13(a). The same measurements of the surface of a steel sphere and a glass bead that were tested are shown in Figure 4.13(b) and Figure 4.13(c), respectively. The 2D profiles of the latter two surfaces were shown together with that of the steel loading platen for comparison. Figure 4.14(a) to Figure 4.14(d) show the same AFM measured results of the surfaces of the four grains used in the tests.
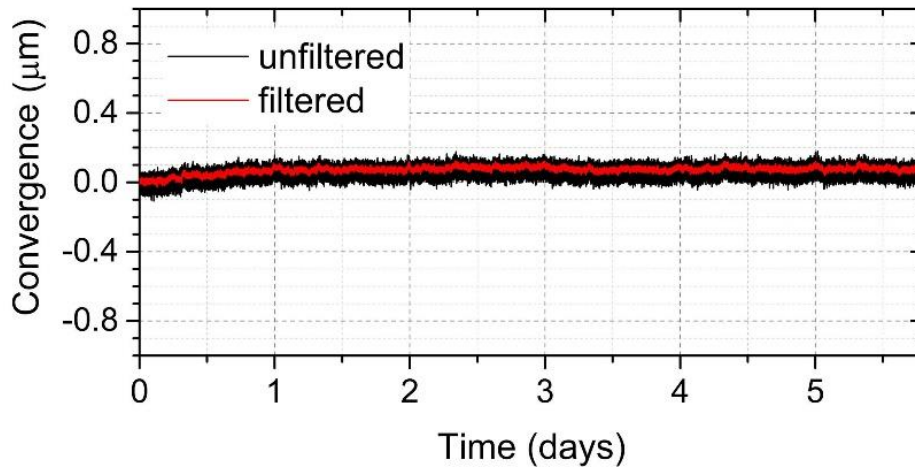
Figure 4.15. Stainless steel sphere testing for signal stability.

Test on a Steel Sphere

The stability of the testing system was evaluated through a test with a loaded stainless steel sphere, 3.125 mm in diameter, under a constant force of 1.3 N. The two loading contacts were both between the steel sphere and steel plates, and they were not expected to be subject to stress corrosion cracking (static fatigue). The result is shown in Figure 4.15 and the signal indicates a very small "adjustment" of the sphere to applied load in the first day (about 100 nm), and no time-dependent convergence thereafter. Thus the system is stable mechanically and electrically, under the desired testing conditions and testing duration. The raw data, with a noise band of about 150

nm, was filtered with a Savitzky-Golay filter (Savitzky and Golay 1964). The filtered data is plotted as the inner band with a reduced noise of 40 nm.
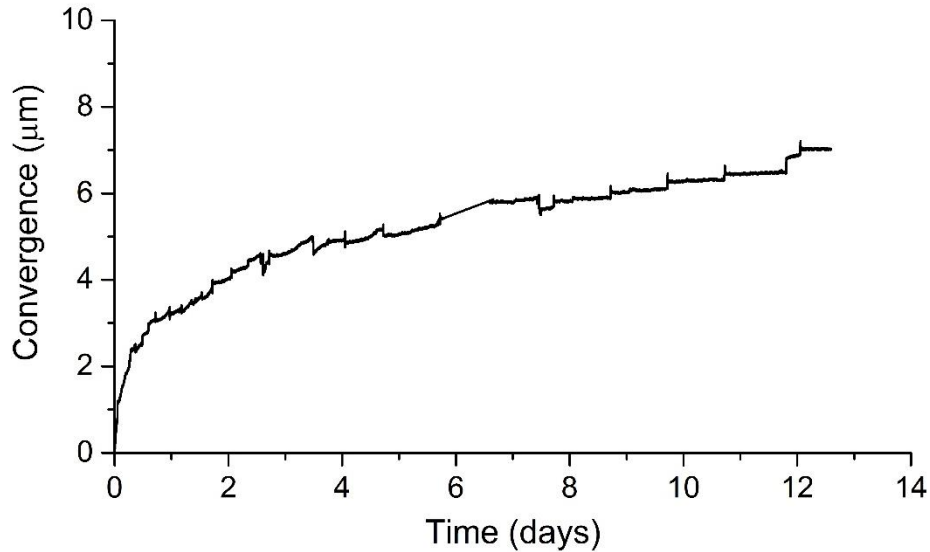
Figure 4.16. Creep of a cured cyanoacrylate-based fast-acting adhesive under a constant load of 1.3 N.

Test on a Cured Adhesive

Creep of cured adhesives was confirmed with a test on a cured deposit of a strong cyanoacrylate-based fast-acting adhesive. The adhesive was allowed to cure for 24 hours after being deposited on the surface of a SEM stand; after the curing time, it covered a circular area with a diameter of about 3 mm and was about 0.5 mm thick in its thickest part; the cured adhesive was then loaded with a constant normal force of 1.3 N. As shown in Figure 4.16, the measured convergence increased about 7 µm in 12.5 days. Possible creep deformation from constant loading was visualized with SEM measurements, as shown in Figure 4.17. This result validated the concerns of using adhesives for grain attachment.

(a)

(b)

(c)
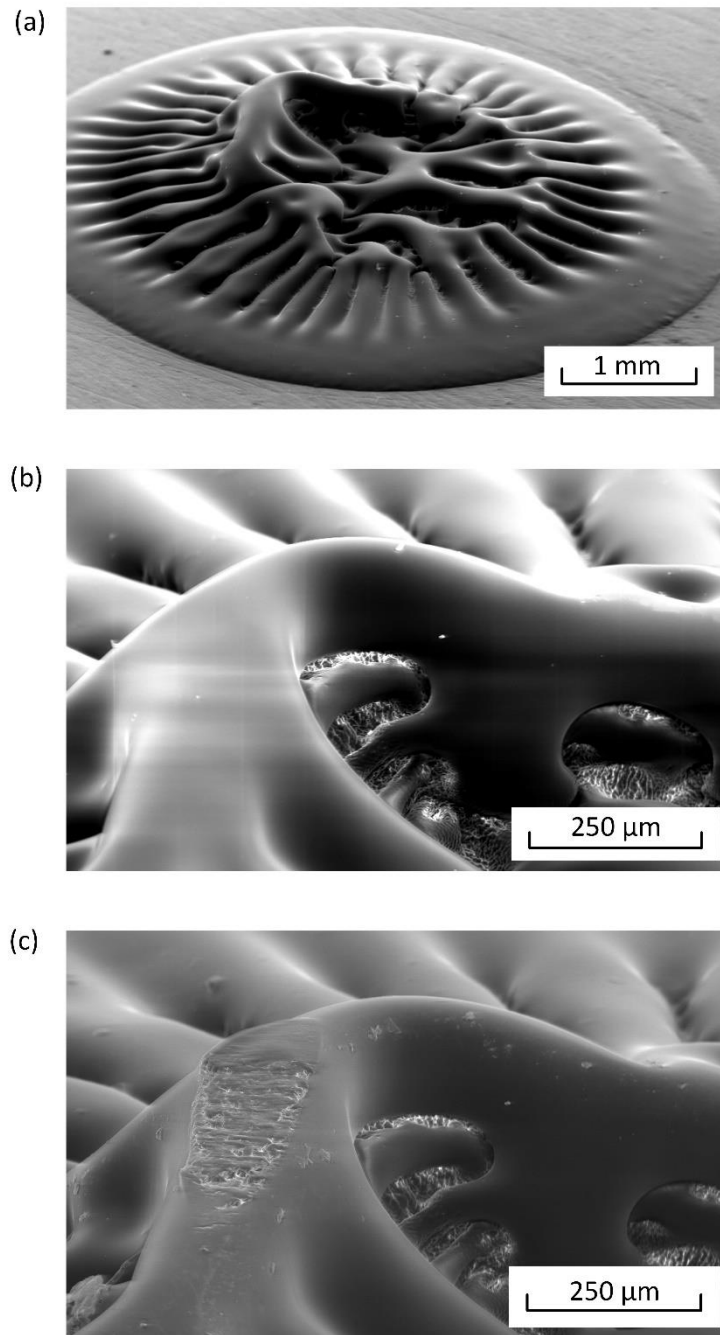
Figure 4.17. Scanning electron microscopic (SEM) image of cyanoacrylate-based fast-acting adhesive: (a) overview of the adhesive deposit, (b) close-up view of a "ridge" before loading, and (c) close-up view of the "ridge" after 12.5-day constant load of 1.3 N.

74

Tests on Sand Grains

Sand grains for testing were selected from a batch of Ottawa sand grains, with a size in the range of 0.6 – 0.84 mm (Ottawa 20-30). Grains with a relatively uniform roughness on the entire surface (inspected by SEM) were selected for testing. Roughness of individual grains was characterized by RMS (Eq. (4.1)) as calculated from AFM scans. Figure 4.14 shows AFM scans of four grains used in the tests and a scan of the surface of one of the loading platens. This figure also indicates the RMS value for each scan, and it shows a cross-section of the scans to further visualize the surface texture. Of course, differences in roughness can occur at different locations on the same grain. Optical microscopic images of the Ottawa sand grains are shown in Figure 4.18.
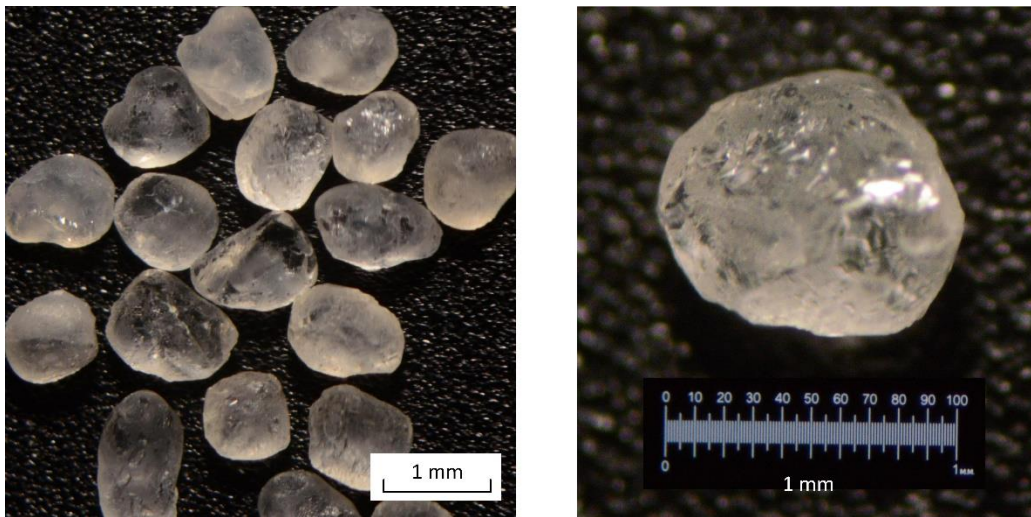
Figure 4.18. Optical images of Ottawa 20-30 sand grains.

The sand grains were loaded with a force of either 2.4 N or 1.3 N. The convergence after the load application ranged between 18 and 67 μm (Table 4.1), dependent on the roughness and the load. Test C displayed a larger immediate convergence than expected, considering the trend in all tests presented. The loading process of this grain exhibited unusually large convergence after the first loading step (27 μm), which was likely caused by an "adjustment" of the grain to applied load (minute grain rotation). The time-dependent convergence for all grains that occurred in the 20 days following application of the load was 1 to 2 orders of magnitude smaller than the immediate response.

The summary of the tests is given in Table 4.1. Grains in tests E, C, and B were all loaded with a force of 2.4 N, but had different roughness measured by RMS: 621 nm, 321 nm, and 28.6 nm, respectively. Not surprisingly, the largest convergence was recorded for Test E, with the largest roughness, and the smallest for Test B. The convergence after 20 days for tests E, C, and B was 2,385 nm, 780 nm, and 310 nm, respectively. A similar conclusion regarding the strong influence of roughness on convergence comes from the two tests with 1.3 N load: D and A, with roughness of 577 nm and 28.6 nm, respectively. Convergence after 20 days for the two tests was recorded as 1,090 nm and 100 nm, respectively. The strong role of the roughness in the convergence process is confirmed by comparison of Tests D and B: even though Test D was performed under 1.3 N load (2.4 N in Test B) it showed a larger convergence, because of a much larger roughness (577 nm vs. 28.6 nm).

Table 4.1. Summary of contact fatigue tests

Test	RMS (nm)	Contact force (N)	Test duration (days)	Convergence 30 min after loading started (μm)	Time-dependent convergence		
					After 1 day (nm)	After 5 day (nm)	After 20 days (nm)
A	28.6	1.3	20	18	5	10	100
B	28.6	2.4	25	39	10	100	310
C	321	2.4	25	67	25	210	780
D	577	1.3	25	22	170	451	1090
E	621	2.4	25	60	845	1582	2385
F[1]	6.28	2.4	6	21	70	99	-

[1]Glass bead
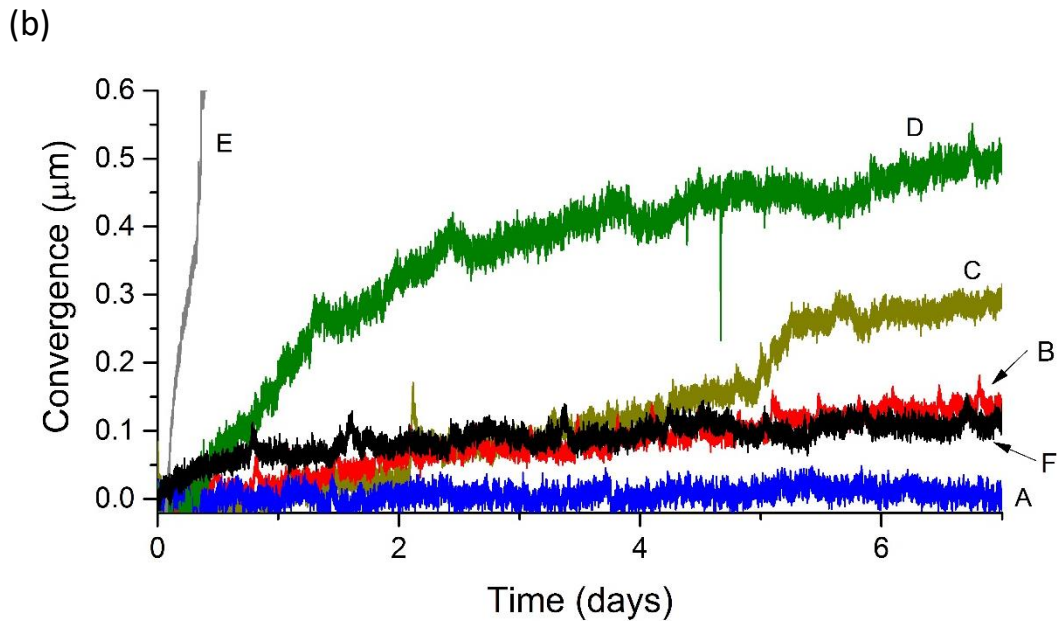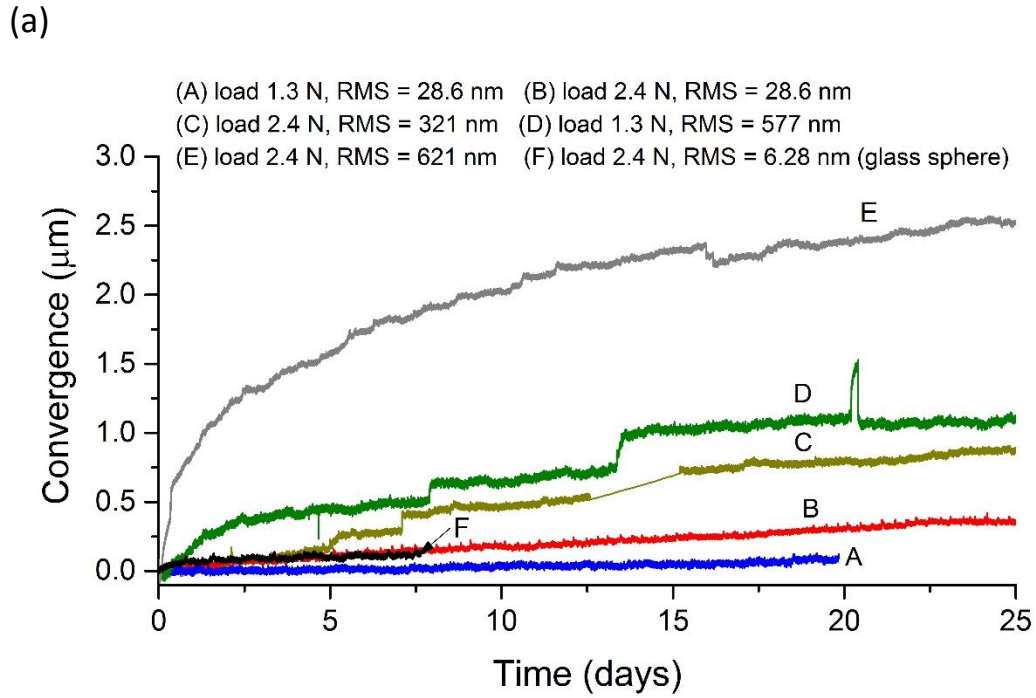
Figure 4.19. Testing results - time-dependent increase of convergence in contact fatigue tests with a glass bead and different Ottawa 20-30 sand grains: (a) the entire 25 days, and (b) expanded view of the first 8 days.

The convergence is a decaying process, still strongly dependent on roughness in the first few days. Calculated based on data in Figure 4.19(a), the convergence rate was about 17.6 nm/h at the end of the first day for the grain with RMS = 621 nm (Test E), but only a little above 2 nm/h for roughness of 321 nm (Test C), and below 2 nm/h for roughness of 28.6 nm (Test B). It is interesting to note that the first day rate in Test D was relatively high despite a lower load (1.3 N): 6.9 nm/h; this is presumably due to a relatively large roughness of 577 nm. After 20 days, the convergence rate for all tests dropped below 1 nm/h; this rate is likely to have a significant component originating from creep of the material inside the grain.

An approximately constant and low rate of convergence reached in tests A and B shortly after loading is probably indicative of the process being strongly influenced by the creep of the core material of the grain, rather than fatigue at the contacts. To obtain some quantitative measure of the influence of creep, an 8-day test was performed on a glass bead (diameter 2.38 mm) with very low roughness (RMS = 6.28 nm). The glass sphere was made of borosilicate glass (known also as Pyrex), with about 80% silicon dioxide (manufacturer's specification: 70 – 87% SiO_2). Time-deflection response of the glass bead is shown in Figure 4.19(b) (Test F). Loaded with 2.4 N, the convergence exhibits some "adjustment" in the first day, possibly due to fracturing some asperities despite the low roughness, but the rate of convergence drops to about 0.1 nm/h after 2 days. This low-rate process is likely to be the effect of creep of the bead material (a smaller bead would likely exhibit smaller convergence). Comparison of the bead data and the data for the tests with low roughness (tests A and B) leads to the conclusion that the convergence in tests A and B is indeed influenced by the creep of the grain material. This is consistent with the roughness profile of the grain in tests A and B (Figure 4.19(b)) compared to those in tests C, D, and E (Figure 4.14(b-d)), i.e., one would not expect substantial contact fatigue occurring for the grain in tests A and B. Of course, creep of the grain material affects the convergence process from the very beginning, but it presents a very small component of convergence for grains with large roughness where contact fatigue is the predominant process in the first several days after loading.
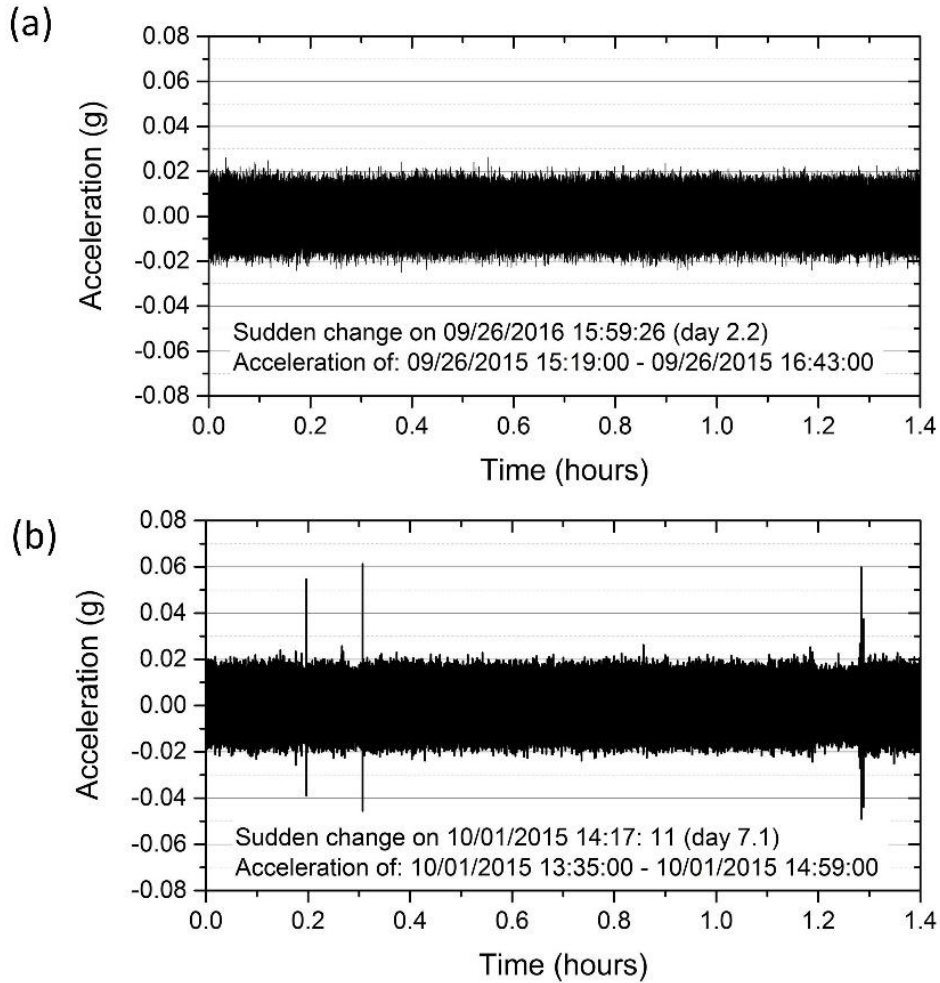
Figure 4.20. Acceleration data from test C: (a) 1.4-hour time interval including a sudden peak in convergence at day 2.2, and (b) 1.4-hour time interval including a sudden convergence at day 7.1.

Vibration Identification

Occasionally a spike or a "jump" in the signal was recorded. These can come from disturbances in the power supply, they can be caused by external excitation, but they can also be triggered by contact micro-instabilities associated with sudden fracture of asperities and mineral fragments, or a minute rotation of a grain between the platens. An accelerometer was mounted on the base plate in order to detect external disturbances (probing at 2 kHz). The spike in the reading of Test D just past 20 days was likely to had been caused by an electrical issue. Two abrupt increases in

convergence happened in Test C at day 2.1 and just past 7.1 days (the view of the first one blocked by overlapping plots); no external vibration was picked up by the accelerometer at the time for the first sudden increase (Figure 4.20(a)), but the second one was likely caused by external excitation, which is documented in Figure 4.20(b). A straight line on the Test C curve between 12.5 and 15 days is due to interrupted power supply during that time. These anomalies in long-term testing were found unavoidable.

In order to identify vibrations detected by the accelerometer during a test, a series of possible disturbance scenarios around the environmental chamber were simulated. A comparison of the acceleration readings from the tests to those from simulated vibrational events helps identifying the sources of vibrations detected during tests. The vibrations simulated included opening/closing the chamber door, moving hardware, an individual jumping off from a certain height, walking/running heavily, knocking/kicking the chamber outside walls and dropping weights around the chamber. Acceleration data from these simulated events, both in time and frequency domains, are presented in Figure 4.21. The acceleration data in frequency domain were obtained from Fast Fourier Transformation (FFT) of the acceleration data in time domain. The background acceleration (or noise) is shown to be varying between -0.02 g and 0.02 g, while the "event-generated" accelerations range from 0.045 g to 0.18 g, two to almost ten times that of the accelerations of ambient vibrations.

To identify the sources of the vibration measured on day 7.1 in Figure 4.20(b), the frequency content of the reading (from FFT) as shown in Figure 4.22, was compared with those from simulated events. It appears that the frequency content of the event resembles that from opening/closing the door as shown in Figure 4.21(b), both with a peak frequency at frequency #2. Therefore, it is plausible that the sudden increase in convergence on day 7.1 was a result of external excitation and these vibrations were likely caused by a person opening and closing the door of the chamber.

(a) Open and close the door

(b)

(c) Move ladder

(d)

(e) Jump from 70 cm above ground

(f)

(g) Run and walk heavily

(h)
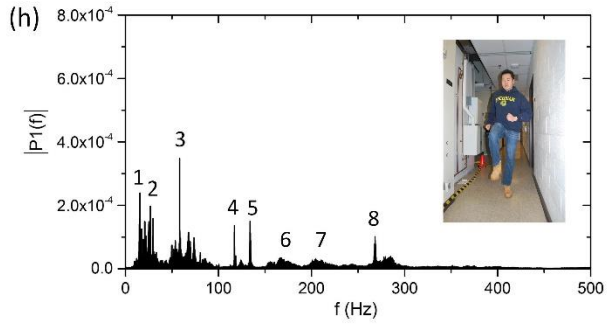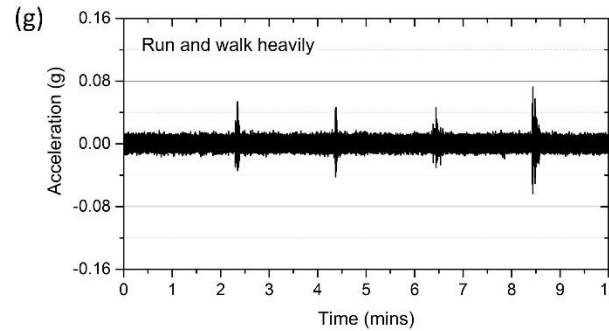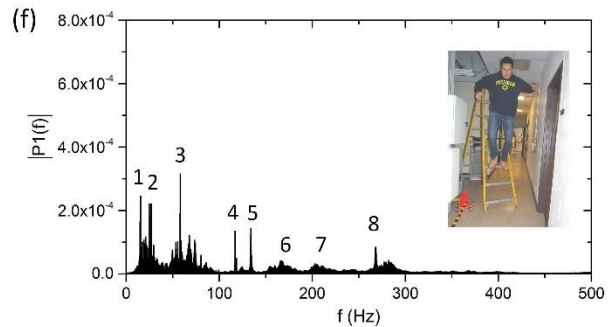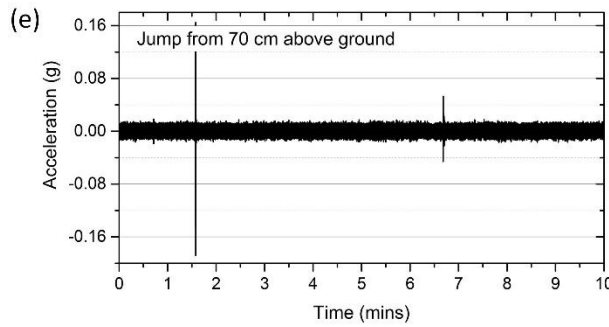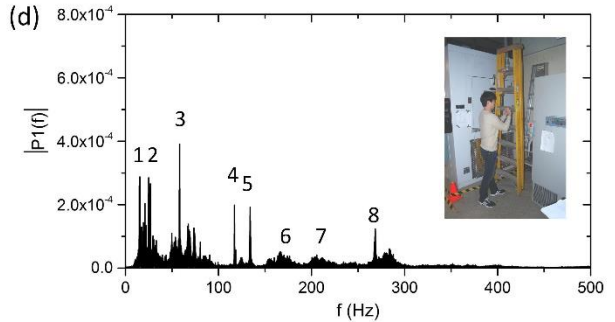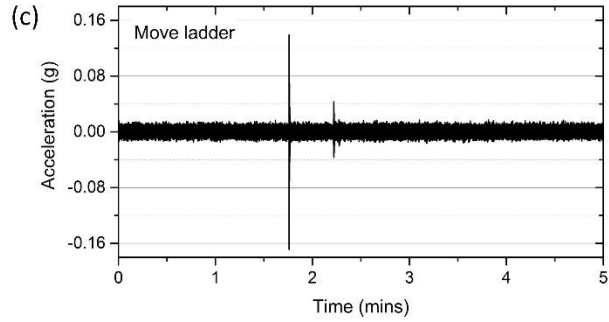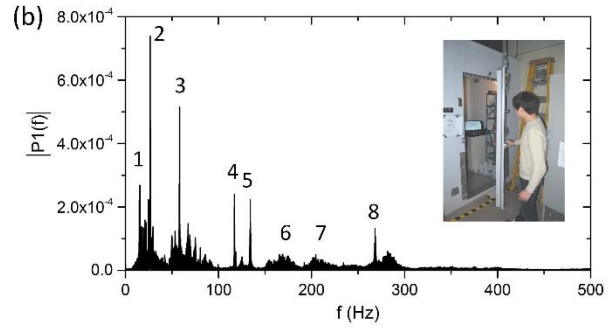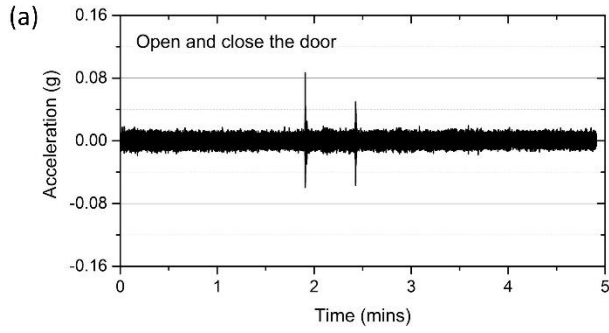
(Continued next page)
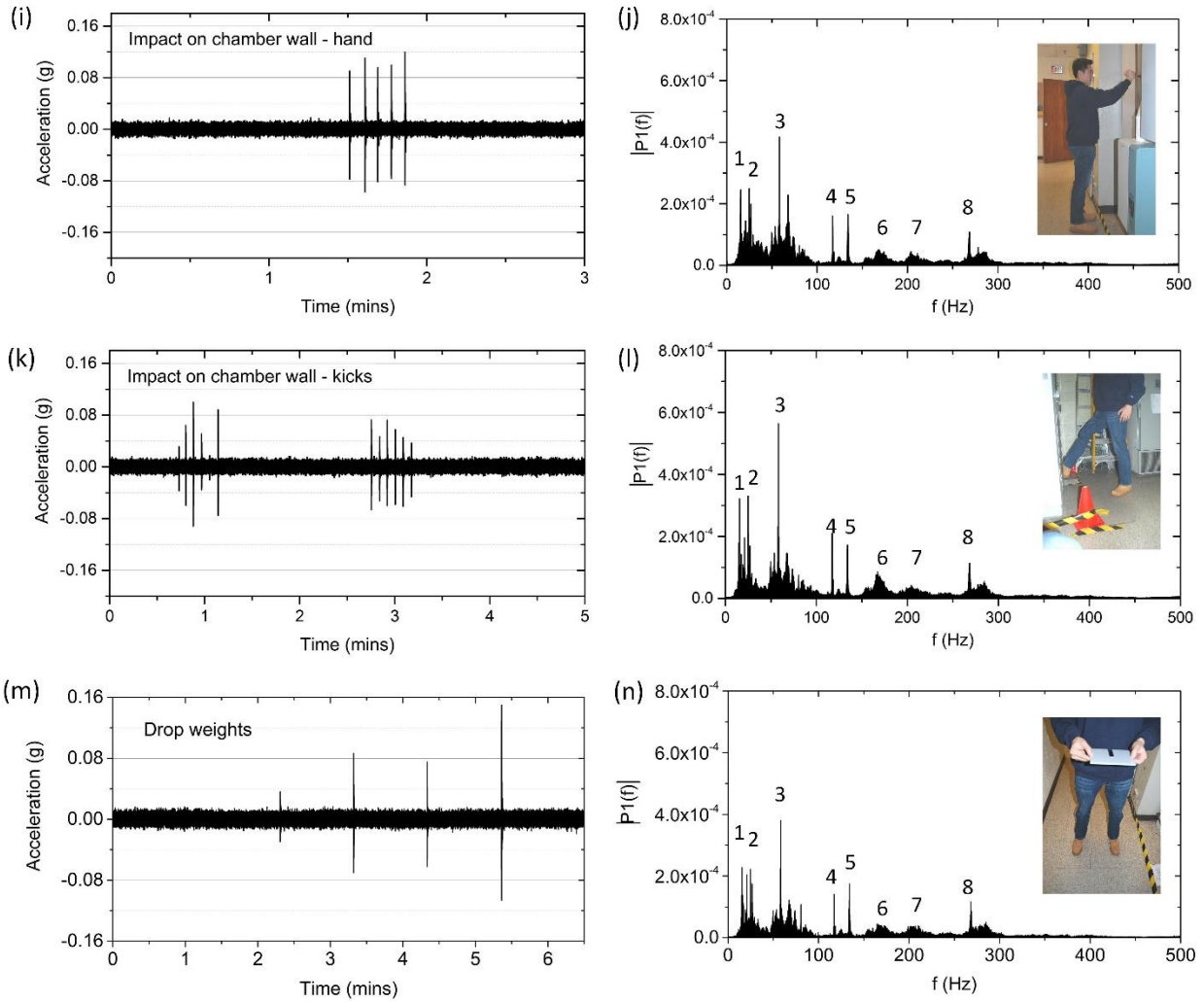
Figure 4.21. Acceleration readings and frequency contents from simulated vibration events: (a)(b) open and close the chamber door, (c)(d) move the ladder, (e)(f) jump from 70 cm above ground, (g)(h) run and walk heavily near the chamber, (i)(j) hit the chamber wall with a hand, (k)(l) kick the chamber wall, (m)(n) drop 1-kg and 2-kg weights from 1 m above ground.
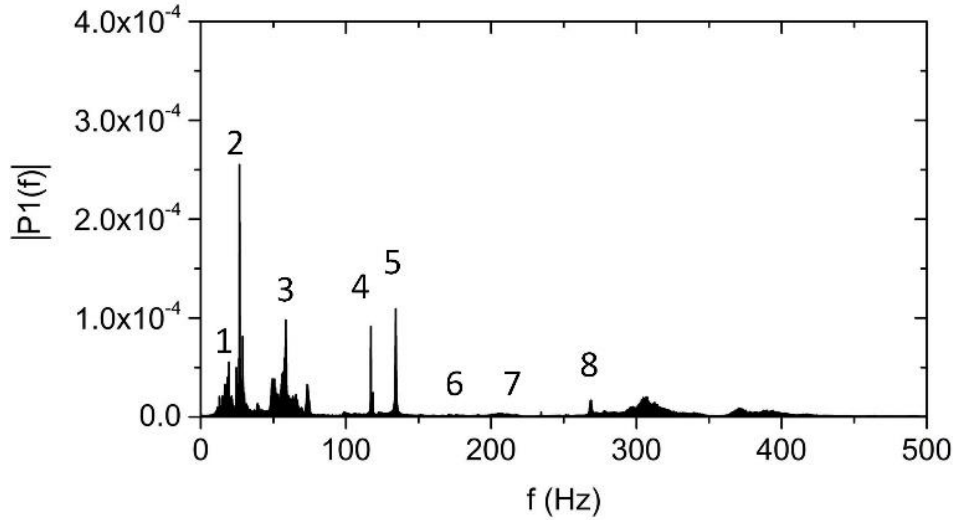
Figure 4.22. FFT of acceleration data around the sudden convergence at day 7.1 during Test C.

4.9. Conclusions

In order to gain insight into microscopic behavior of contacts, an apparatus was constructed that is capable of measuring displacements associated with sustained contact loads. Such testing is challenging, because of the size of the specimens and the distribution of textural features on grain surfaces being unique to every grain. Measuring the displacement of hundreds of nanometers adds to the challenge. These measurements are also sensitive to changes in temperature and humidity, and are affected by even small vibration excitations.

Testing a contact between two grains was found inherently inaccurate, because of creep in adhesive used for mounting the grains and the use of multiple stages (with their inherent tolerances in the rails) needed to form an inter-granular contact. Consequently, an apparatus was constructed for testing grain contacts with steel surfaces, which are equally indicative of sand grain contact behavior. Such a design allowed for elimination of adhesive from the sample preparation and also elimination of multiple stages. The displacement measured by the device is the result of the simultaneous response of two contacts of the grain with two polished steel surfaces, on opposite sides of the grain. The displacement of one loading plate relative to the one on the opposite side of the grain is measured (see insert in Figure 4.8(a)), and it is referred to as a *convergence*. While

83

this is not the same as a contact between two grains, the measurements are indicative of the very same time-dependent characteristics.

- An apparatus was developed to monitor time-dependent deflection of a single sand grain under sustained loads. In each of the tests, a single sand grain was compressed between two smooth steel platens with a constant normal load. The time-dependent deformation of the grain was measured through the change in the distance between the two loading platens (convergence).

- In the tests, silica sand grains with 0.60 to 0.85-mm diameters were loaded with two constant loads: 1.3 N and 2.4 N. During the tests, the two loading platens gradually came closer together by 0.3 μm to 2.4 μm between the period of 30 minutes after application of the loads and 20 days later with sustained loads.

- The rates of convergence of the two loading platens over time in the tests was strongly dependent on the roughness of the surface of the sand grain tested. The convergence of the platens for a grain with a very low roughness (RMS = 28.6 nm) developed additional 0.31 μm of deflection in the 20 days following application of a normal load of 2.4 N. A grain with much larger roughness (RMS = 621 nm), subjected to the same process, converged 2.39 μm during the same period.

- The creep of the grain core material was found to be of secondary importance, compared to maturing of contacts. This conclusion is supported by the results of the tests with sand grains and a glass bead with small surface roughness, which showed very small delayed increase in convergence compared to the results from grains with larger roughness, which showed multiple times larger convergence.

- The result of a test with a high-molybdenum stainless steel sphere (not expected to be subject to static fatigue) showed nearly no convergence, confirming that roughness and fatigue of asperities are the key ingredients of the aging process.

84

Chapter 5

Laboratory Testing on Aging of Sand Grain Assemblies

5.1. Introduction

A result of fracturing of textural features on grain surfaces at an individual contact is an increase in the number of "contact points" (or "contact sub-areas") within the nominal contact area (Wang and Michalowski 2015). The consequence of this process is an increase in the contact stiffness. The increase in the contact stiffness will propagate through the spatial scales and will be manifested as an increase in the small-strain stiffness at the macroscopic scale. The increase in small-strain stiffness is a key consequence of sand aging. In a confined mass, a change in stiffness is likely to cause a change in the stress state. This manifestation of contact maturing was investigated through soft oedometer tests.

There are three purposes for conducting the soft oedometer testing: (1) collecting additional evidence for time-dependent response of silica sand to constant load and demonstrating the time-dependent consequences on the stress state in confined sand, (2) manifesting the consequences of

contact maturing (as observed in Chapter 4) on time-dependent behavior in sand grain assemblies, and (3) investigating the factors that are affecting sand aging. A valuable feature of this test is that the measurements of stresses and strains were nearly continuous with sampling rates ranging from 1 sec to 20 sec. The high sampling rates captured instantaneous adjustments in the samples during the tests which would have not been captured with sampling rates of hours or days.

In this chapter, the testing system is introduced, which consists of the soft-ring oedometer, the sensing system and data acquisition system. A calibration procedure for the soft aluminum ring is presented to obtain the correlation between the readings of the strain gages and the radial stress in the sample. Then, a detailed testing procedure is introduced, followed by descriptions of the sand samples tested. The testing results are presented and discussed, before the final conclusions are given.

5.2. Soft-Ring Testing

Consider a cylindrical specimen, such as one in an oedometer test, loaded in vertical direction with uniform load q. Such a load will induce vertical, radial, and circumferential stresses in the sample: $\bar{\sigma}_z$ (equal to q), $\bar{\sigma}_r$, and $\bar{\sigma}_\theta$, respectively; because of axial symmetry, $\bar{\sigma}_\theta = \bar{\sigma}_r$. The bar indicates that these are averaged stresses in the granular material. Barring any shear stresses at the top and bottom platens, and on the oedometer cylinder, stresses $\bar{\sigma}_z$, $\bar{\sigma}_r$ and $\bar{\sigma}_\theta$ are the principal stresses. While the response of the granular material to loading can be characterized as both elastic and irreversible deformation, consider only a purely elastic process. The energy accumulated in an isotropic specimen while it is loaded from zero to q is

$$W_e = \frac{1}{2E}\left(\bar{\sigma}_z^2 + \bar{\sigma}_r^2 + \bar{\sigma}_\theta^2\right) - \frac{v}{E}\left(\bar{\sigma}_z\bar{\sigma}_r + \bar{\sigma}_r\bar{\sigma}_\theta + \bar{\sigma}_\theta\bar{\sigma}_z\right) \qquad (5.1)$$

where $\bar{\sigma}_z = q$, and E and ν are the Young's modulus and Poisson's ratio, respectively. Assume now that, after the specimen was loaded, the stiffness of the material expressed by Young's modulus E increases (with Poisson's ration remaining constant). This is to account for the increase in the macroscopic stiffness that was caused by the increase in the stiffness of maturing contacts. Consistent with Eq. (5.1), this would lead to a decrease in energy stored in the specimen. Because load q is kept constant, stresses $\bar{\sigma}_r$ and $\bar{\sigma}_\theta$ would have to increase in order to preserve the strain energy. Sand, of course, is not a purely elastic material, and a substantial amount of energy is dissipated during the loading process. Under constant load, some energy may be changed into heat in the frictional process of inter-particle sliding during the "structuration" events, and a portion of energy may be emitted as elastic waves (micro-seismicity) produced by fracturing during the fatigue process. However, if the conjecture regarding fatigue-caused increase in stiffness is true, then it is likely that some increase in the radial and circumferential stresses will occur in time, despite the losses of energy due to elastic wave emission and heat generation. This is consistent with existing evidence regarding evolution of the horizontal stress at rest in confined sand under constant vertical load (Michalowski 2005). To confirm this supposition a soft oedometer testing program was carried out.

The concept of a "soft" oedometer was conceived to enable measuring the radial stress in a loaded sample (Kolymbas and Bauer 1993). It needs to be clearly stated that the measured radial stress is not the K_0-stress, as the measurable radial strain is allowed in the soft oedometer in order to capture the stress evolution. For a thin-walled ring, the circumferential strain in the ring $\varepsilon_\theta^{ring}$ is uniquely related to the radial stress $\bar{\sigma}_r$ in the sample

$$\bar{\sigma}_r = \sigma_\theta^{ring} \frac{t}{r} = E_{ring} \varepsilon_\theta^{ring} \frac{t}{r} \tag{5.2}$$

where t is the ring thickness, r is the radius of the ring (thin-walled), and E_{ring} is the Young's modulus (69 GPa for Aluminum ring). Consequently, time-dependent changes in strain $\varepsilon_\theta^{ring}$ of the

"soft" ring under constant load will be indicative of time-dependent changes in the radial stress $\bar{\sigma}_r$ in the sample.
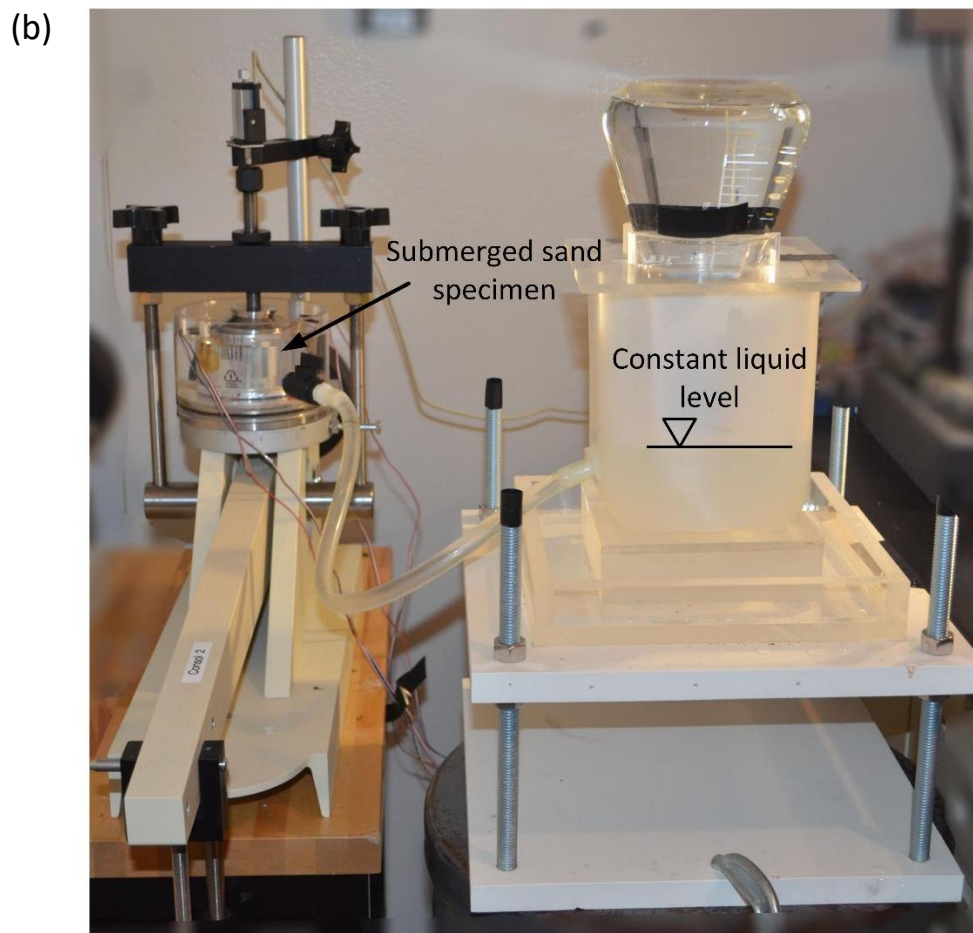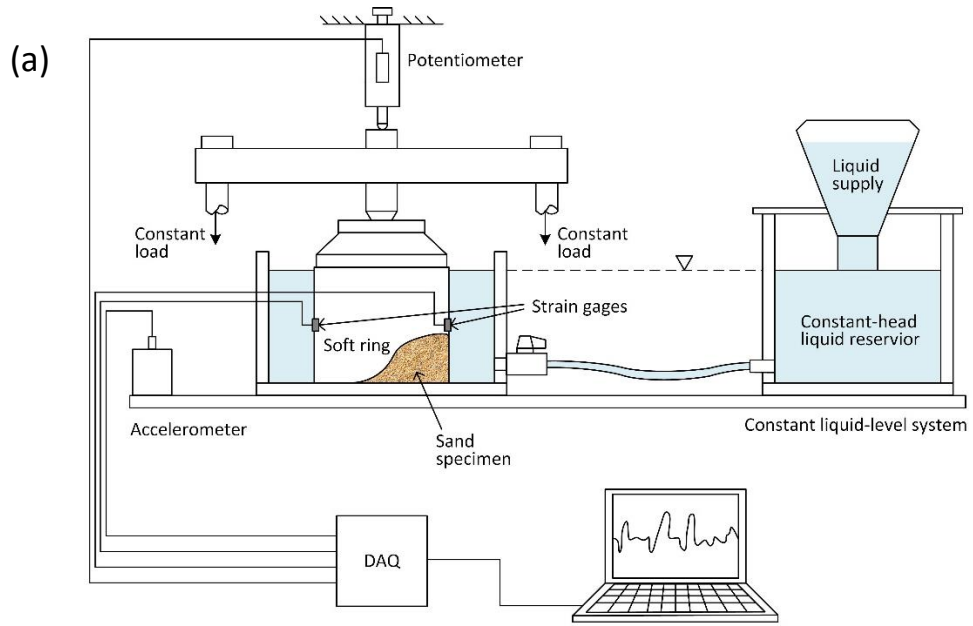
Figure 5.1. Soft oedometer testing apparatus: (a) a schematic, and (b) a photograph.
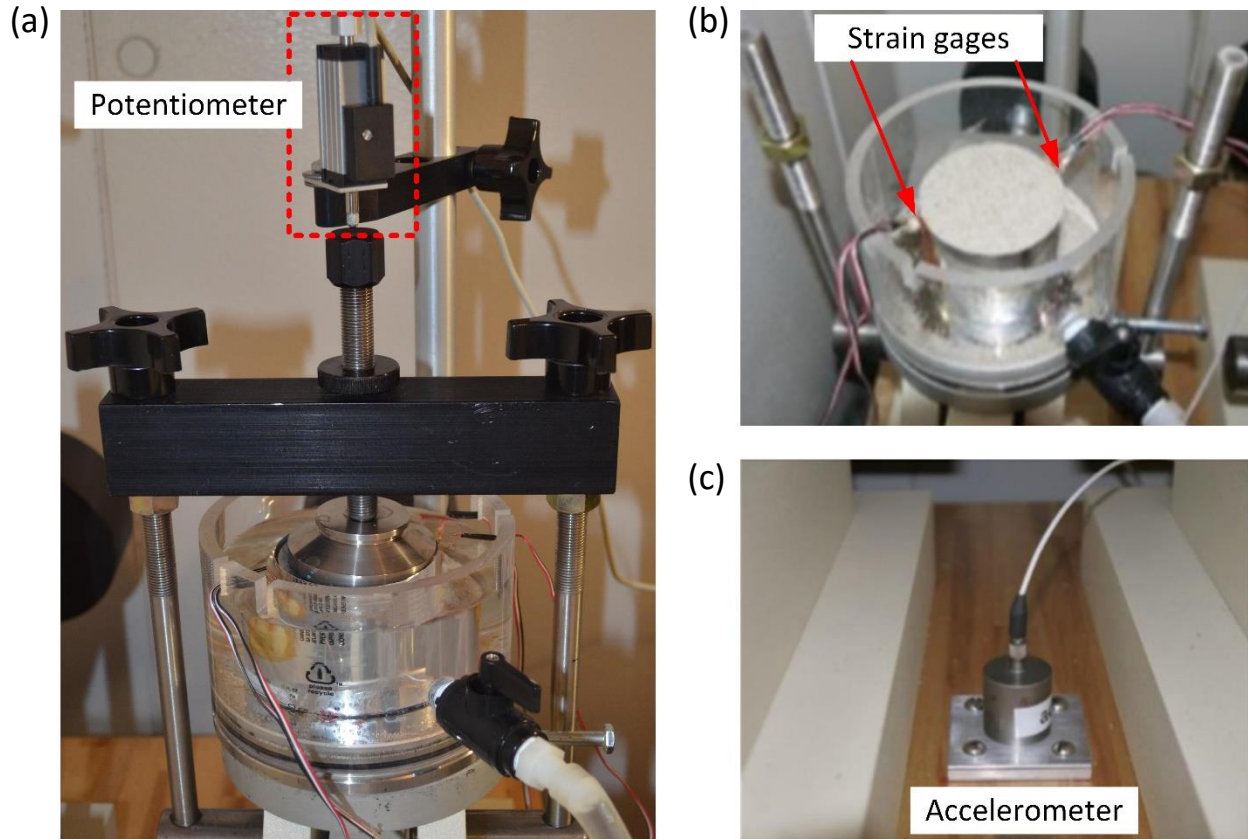
Figure 5.2. Soft oedometer testing apparatus: (a) close-up view of loaded specimen, (b) sand deposited in ring with strain gages installed, and (c) accelerometer mounted on testing platform.

5.3. Apparatus

Overview

A schematic of the soft oedometer ring system is depicted in Figure 5.1. The settlement of the specimen was measured by a potentiometer connected to a compact data acquisition module, as shown in a close-up view in Figure 5.2(a). The circumferential strain of the soft aluminum ring was monitored with two strain gage rosettes installed in middle height of exterior surface of the ring at 180° from each other, as shown in Figure 5.2(b). Signals from two gauges measuring the circumferential strain and from the potentiometer were recorded on a portable computer

continuously with frequencies of 0.1 Hz and 1 Hz, respectively. Initial results indicated a significant influence of the temperature changes in the laboratory on the outcome of the tests. Therefore, the entire assembly was placed in an environmental chamber where a constant temperature of 20°C and constant relative humidity of 30% were maintained. All components of the experimental setup and the material tested (including the pore fluid) were placed in the environmental chamber for at least 24 hours prior to preparation of the samples and start of the test. An accelerometer was placed on the base of the oedometer frame to record any accidental disturbances/vibrations (with data recorded at 2 kHz), as shown in Figure 5.2(c).

The aluminum rings used in the tests had a thickness of 0.1 mm. The diameter and height of the rings used was 66 mm and 50.8 mm, respectively. The small thickness of the ring provided the deformability allowing detection of very small changes in radial stress (about 100 Pa). The soft ring was placed on a mirror-finish stainless steel base plate to reduce the friction between the ring and the specimen, and the base.

A liquid supply system was developed for tests with saturated samples. To avoid drying out of the (saturated) samples, a constant-head reservoir with appropriate supply of the pore liquid was assembled, Figure 5.1, to allow running a 4-week test without entering the chamber to replenish the pore fluid. Entering the chamber is a major disturbance to the tests, and the designed liquid supply system allowed eliminating these disturbances.

(a)

(b)
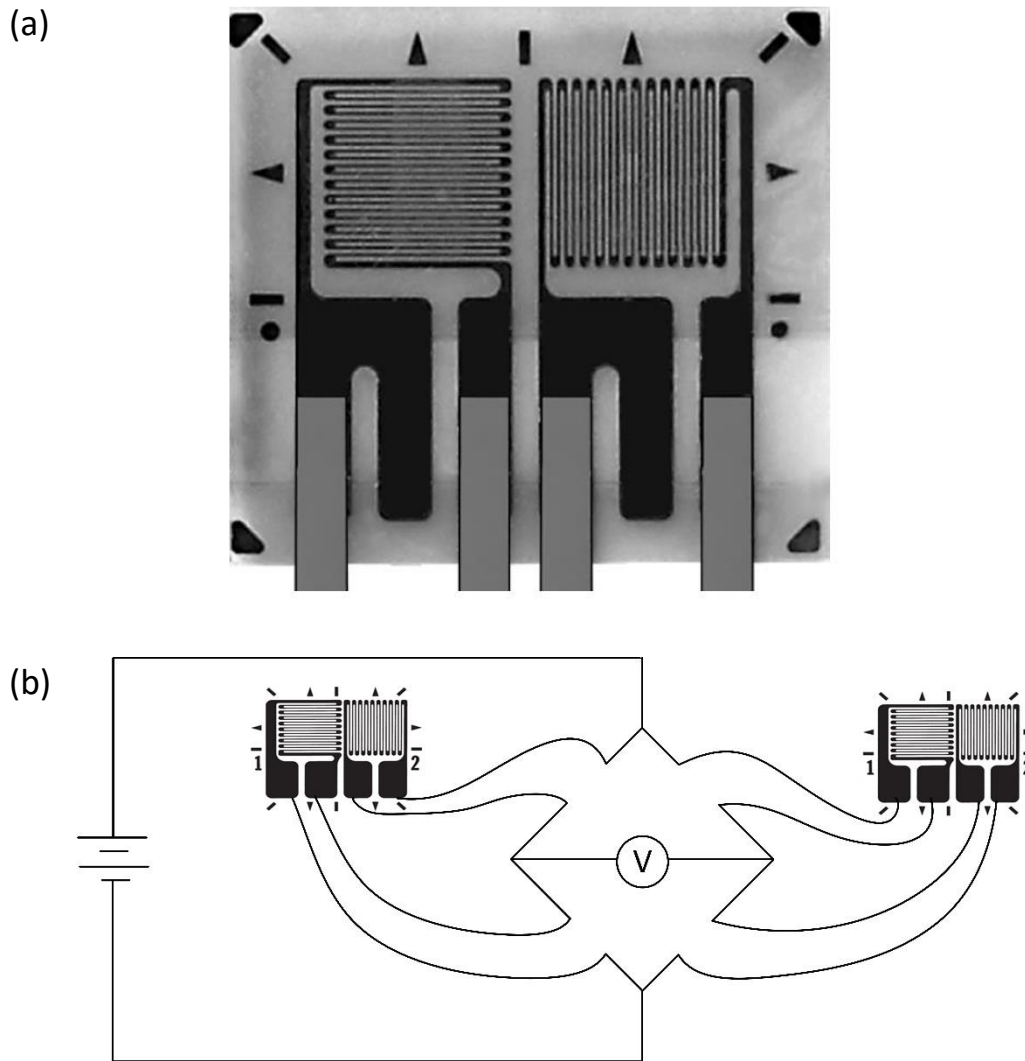
Figure 5.3. A full-bridge circuit with two tee rosette strain gages: (a) a Vishay tee rosette strain gage (from Vishay Precision Group, Inc.), and (b) a full bridge circuit formed with two Vishay tee rosette strain gages.

Construction of the Sensing System

The strain gages installed on the soft aluminum rings are tee type rosettes (Vishay C2A-13-125LT-350). Each of them consists two grids perpendicular to each other, as shown in Figure 5.3(a). To ensure high measurement precision, a full bridge configuration is used with two tee rosette strain gages, as shown in Figure 5.3(b). The strain gages have a strain measuring range of ±3%. They are

1.52 mm× 1.78 mm in grid length and grid width, and 4.17 mm × 4.32 mm in overall length and overall width. The working temperature range of the gages is -60° to +180°F (-50° to +80°C).

In the tests with water and alkali solutions immersion, the strain gages had to operate in extreme conditions for several weeks, so they had to be well protected to prevent damage. All preparation supplies were from Vishay Precision Group (VPG). A systematic procedure was performed to install the strain gages and cover them with proper coatings.

Before installation of strain gages, a four-step preparation procedure was performed to ensure robust gage bonding. Firstly, the gage-bonding surface was degreased with a degreaser (CSM-2 Degreaser in our tests) to remove lubricating and hydraulic oils possibly on the surface. Secondly, the surface was wet-abraded with #400 grid sand paper aided by a mildly acidic conditioner (M-Prep Conditioner A) to accelerate the abrading process. Thirdly, a surface conditioning process was performed by scrubbing the surface with cotton tips while constantly applying Conditioner A; this process was finished until the cotton tips were no longer discolored by the scrubbing. In the fourth step, the surface was neutralized by applying a neutralizer, M-Prep Neutualizer 5A, to bring the surface to 7.0 to 7.5 pH. Detailed description of these steps can be found in VPG's Micro-Measurements Application Note B-129, "Surface Preparation for Strain Gage Bonding".

The strain gages were installed with an adhesive M-Bond AE-15, also from Vishay. It is a type of adhesive that provides high resistance to moisture and chemicals for critical applications. A thorough installation procedure of gage installation with this adhesive can be found in VPG's Introduction Bulletin B-137, "Strain Gage Applications with M-Bond AE-10, AE-15 and GA-2 Adhesive Systems".

Multiple layers of coating were applied to the installed strain gages and their lead wires to protect them from attacks of moisture and chemical solutions for periods of weeks during wet tests. Per consulting with Vishay engineers, two layers of coating materials were used on strain gages in the tests in this thesis. A layer of M-Coat B, 3 mm thick, was first applied. On top of this layer, a 1-mm layer of microcrystalline wax (M-Coat W-1) was applied. The former has good chemical resistance and the latter has strong long-term moisture protection. It turned out that all of the strain

gages survived the chemical conditions during the tests. For detailed introduction on the application procedures of the coatings, the readers are suggested to refer to the following three technical notes prepared by VPG: "Protective Coatings, General Information", "Protective Coating, M-Coat B" and "Protective Coating, M-Coat W1". For tests under unusual or extreme conditions, consulting with the manufacturers is recommended by the author.

The accelerometer was screw-mounted to the base of the oedometers (accelerometer Model 393B04 from PCB Piezotronics). It could measure accelerations ranging from -5g to 5g with a broadband resolution of 3 µg RMS (root mean square). It has a sensitivity of 1000 mV/g and its non-linearity is less than 1% (calculated as the maximum difference between the function value and its linear approximation). The excitation voltage is 18 to 30 V, constant current excitation is 2 to 10 mA and the output impedance is less than 500 Ohm. The accelerometer weighs 50 g (1.8 oz) and is 24.6 mm (0.97") in height and 25.1 mm (0.99") in diameter. The accelerometer was first mounted to a 50.8mm×50.8mm×6.35mm aluminum plate with a #10–32×0.5" flat countersunk head screw, and the plate with the accelerometer is fastened to the wooden platform with four #10 wood screws. For more details of its specifications and mounting instructions, the readers are referred to "Installation and Operation Manual of PCB Piezotronics Model 393B04".

Data Acquisition System

The data acquisition system consists of four modules assembled in a chassis, NI Compact DAQ 8-Slot USB Chassis, NI cDAQ-9178 (all components in this DAQ system were from National Instruments). The system is shown in Figure 5.4. The system has a 4-channel, 16-bit analog voltage output module A (NI 9263, voltage range ±10 V) powering the potentiometers. Three independent 0.5 V DC voltages are provided by this module to the potentiometers. Module B (NI 9219) is a 4-channel 24-bit analog input module to measure output voltages, as well as input voltages, of the potentiometers. Although module A provides nominal DC voltages of 0.5 V to the potentiometers, the actual output voltages of module A usually vary around the desired value with small drifts. Thus both input and output voltages from each potentiometer are measured to calculate its displacement more accurately. Modules B takes measurements from the potentiometers at a frequency of 1 Hz.

(a)

Readings from potentiometers

Accelerometer

Readings from strain gages (via screw terminals)

Power to potentiometers

Voltage source   Voltage meter   RJ50 port   BNC connector

(b)
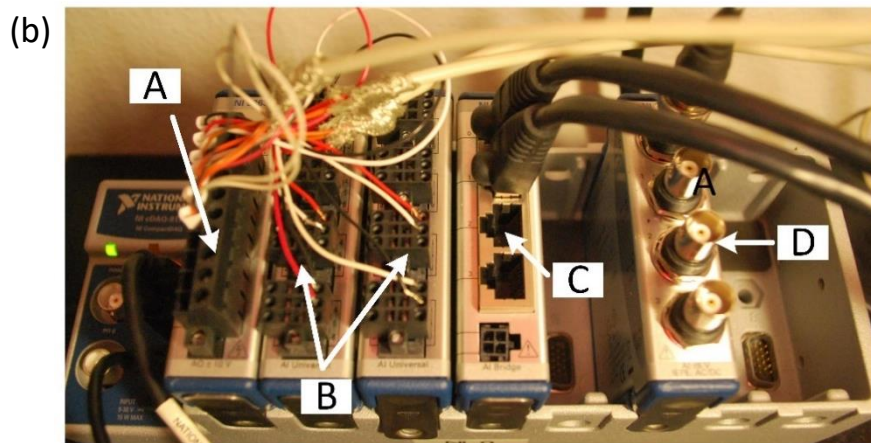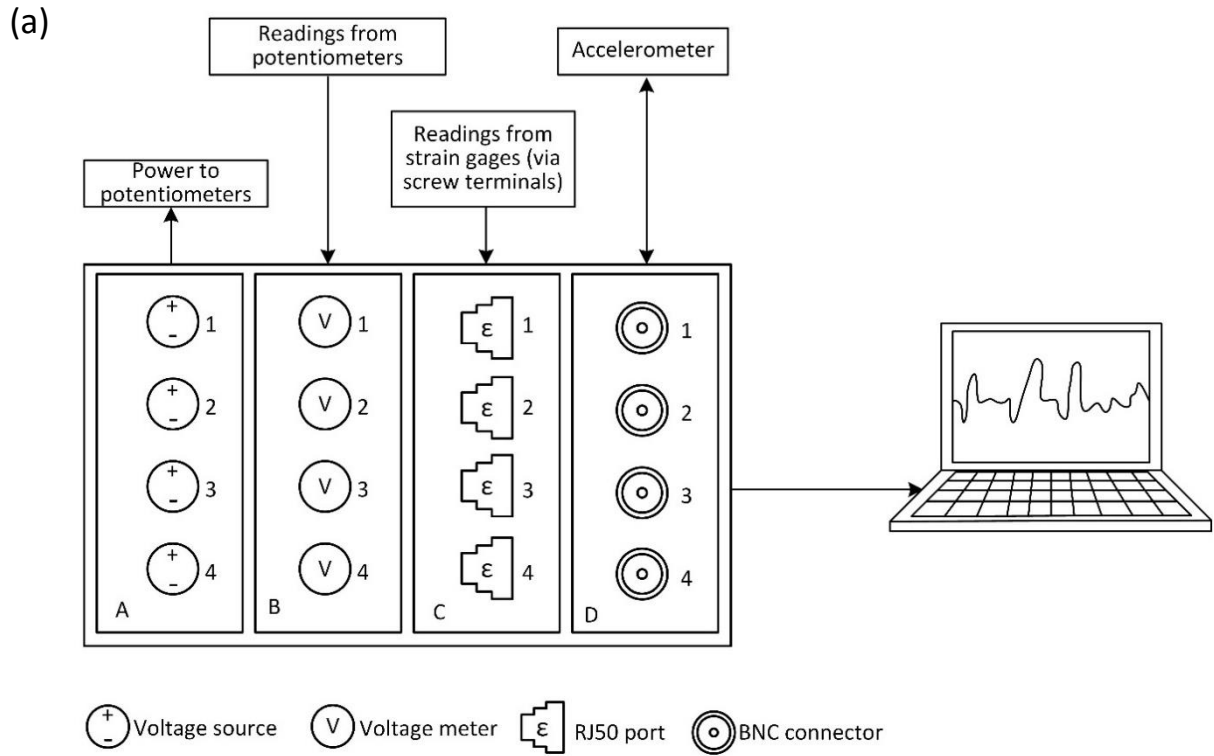
Figure 5.4. Schematic of data acquisition system (DAQ).

Module C (NI 9237) was used obtain reading from the strain gages. Module C is a 4-channel, 24-bit analog simultaneous sampling data acquisition module. It has a max sampling rate of 50,000 samples/second/channel. It can take readings from strain gages in quarter-bridge, half-bridge and full-bridge configurations with corresponding electrical terminals.

The last module, D (NI 9234), is a 4-channel 24-bit current excitation and AC/DC input module. Module D is used for current excitation and taking measurements from the accelerometer, with a 2.0 mA excitation current and a ±5 V AC/DC voltage measurement range. This module is connected to the coaxial connector of the accelerometer through one of its 4 BNC connectors. The readings from the potentiometer are obtained at a frequency of 2 kHz.

More details about the DAQ components can be found in the product manuals that are available from National Instruments' online resources.

The author developed a LabVIEW program for control of the DAQ system.

5.4. Aluminum Ring Calibration

The correlation between radial stress and circumferential strain were calibrated with loading of a water-filled membrane. Although this correlation could be theoretically estimated from elasticity of the aluminum ring, the presence of thick strain-gage coating complicated the calculations. A straightforward and accurate way to obtain this correlation was to calibrate it with loading tests of a membrane-enclosed water mass. As the stress state in water at rest is isotropic, the radial stress exerted on the ring is equal to that applied vertically (of course, radial stress increases with depth hydrostatically). The corresponding circumferential strain for each horizontal stress was obtained from readings of the strain gages. Figure 5.5(b) illustrates radial stress σ_h acting on the ring and circumferential strain ε_θ of the aluminum ring. An appropriate correlation was developed from testing results under a series of different vertical loads.
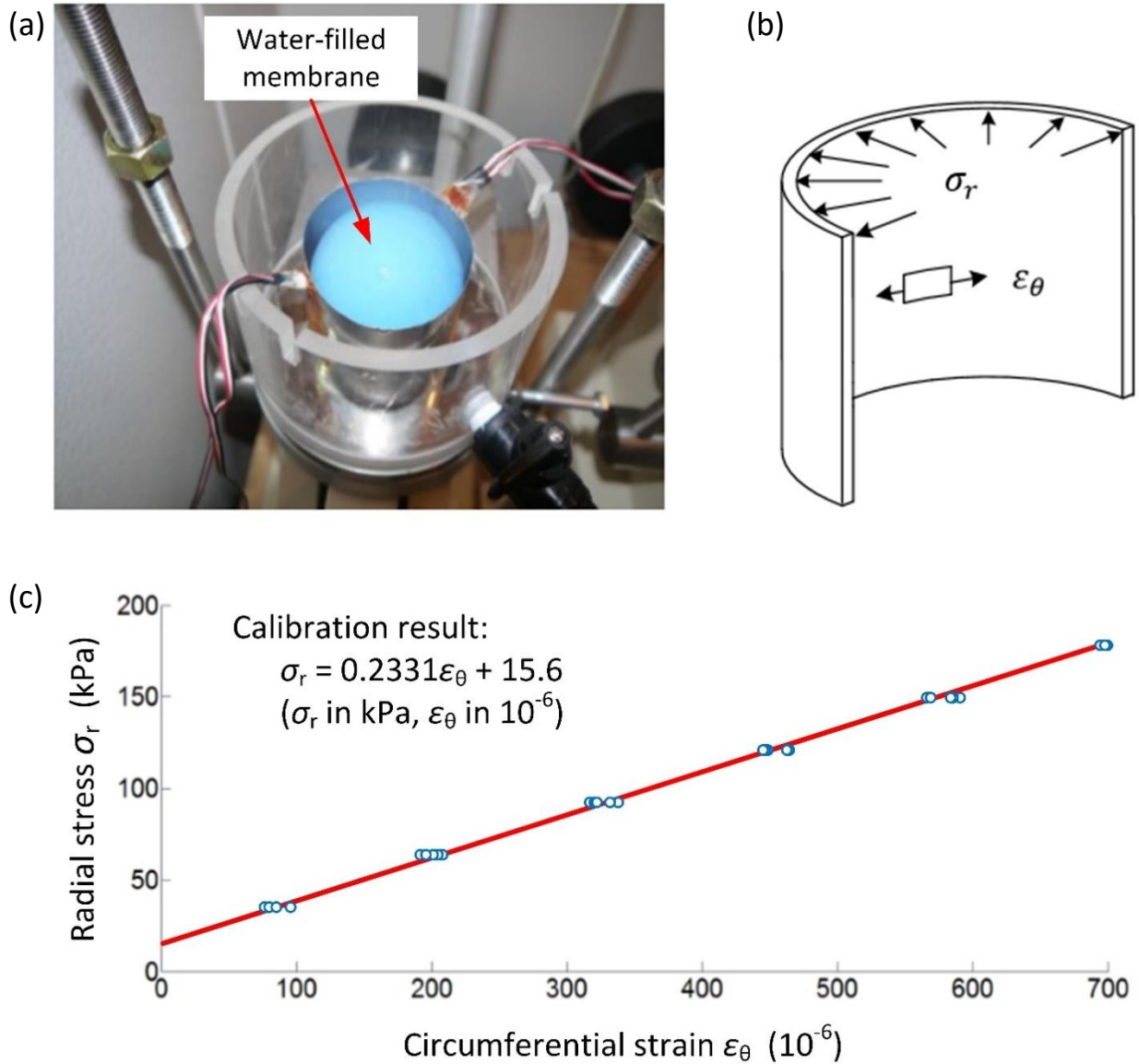
Figure 5.5. Aluminum ring calibration: (a) close-up view of a water-filled membrane in the ring, (b) diagram showing radial stress and circumferential strain, and (c) calibrated relationship between strain gage readings and radial stress.

The configuration of this calibration test is shown in Figure 5.5(a). A rubber membrane container was filled with a volume of water equal to the volume of the soft-ring (testing cylinder). When a vertical load P (in N) is applied to the water body, horizontal stress σh and vertical stress σv were calculated by (in Pa),

$$\sigma_h = \sigma_v = \frac{P}{\pi r^2}$$
(5.3)

where r is the radius of the aluminum ring (in meters). The hydrostatic increase in the pressure through the height of the cylinder was neglected as small compared to the range of stresses used during testing. Six vertical dead loads were applied associated with the mass of 1 kg, 2 kg, 3 kg, 4 kg, 5 kg and 6 kg, so the corresponding vertical and horizontal stresses in the water were 28.6 kPa, 57.3 kPa, 85.9 kPa, 114.6 kPa, 143.2 kPa and 171.9 kPa. The maximum horizontal stress, 171.9 kPa, was higher than the expected maximum horizontal stress in tests to be performed on sand samples (the calibration range included the range of stresses used during testing). The loads were applied in an increasing order and then removed in a decreasing order, in an increment of 1 kg, and three loading/unloading cycles were performed. The results of strain gage readings and the corresponding horizontal stresses from this example calibration test are plotted in Figure 5.5(c). It can be seen that almost all data points fall on a straight line, so the strain gage reading-horizontal stress correlation can be obtained from a line regression. The linear correlation from this linear regression is:

$$\sigma_r = 0.2331\varepsilon_\theta + 15.6$$
(5.4)

where σ_r is in kPa and ε_θ is in 10^{-6}.

Several aluminum rings were used in testing, and every one was calibrated through this process. Correlation, as that in Eq. (5.4), were developed individually for each ring used in testing.

5.5. Testing Procedure

(1) Preparation of testing samples and pore fluids

Sand samples were prepared before the tests. The Ottawa 20-30 sand samples were further sieved to remove traces of grains coarser than the openings of sieve #20 and finer than sieve #30. This process minimized variations of grain size compositions for sands from different manufacturers. Comparison of the grain size distributions before and after the test also allowed for detecting grain crushing (or splitting) during the tests.

Weights of sand samples were measured before each test. The samples were stored in open containers. After deposition of the sample in the soft ring, the sand left in the containers was measured again to calculate the weight of sand deposited in the ring. The weights were back-calculated from the desired porosities, e, of the tested samples

$$e = \frac{V_v}{V_s} = \frac{V_{ring} - V_s}{V_s} \tag{5.5}$$

where V_{ring}, V_s and V_v are the total volume of the sample, i.e., the volume of the soft ring, the volume of solids (sand grains) and the volume of voids, respectively. The volumes of the ring and solid in the sample are given by

$$V_{ring} = \frac{1}{4}\pi d^2 h \tag{5.6}$$

$$V_s = \frac{m_s}{G\rho_w} \tag{5.7}$$

where d and h are the diameter and height of the aluminum rings, 66 mm and 50.8 mm, respectively; m_s is the mass of the sample which can be calculated by the difference of weights of sand in the storage container before and after depositing the sample; G is specific gravity of sand, 2.65 for Ottawa sand; ρ_w is density of water, 1 g/cm^3 at room temperature. For instance, about 277 g Ottawa sand is needed to prepare a sample of a 0.67 void ratio in a ring with dimensions as in these tests. Usually, preparing 30% more sand than the calculated weight is recommended to account for splitting of sand grain outside of the rings during sand deposition.

The pore solutions used in the immersion tests were prepared. From previous observations, at least 4 liters of solution was needed for a test running for 4 weeks to make up for the liquid loss to evaporation.

All components of the experimental setup and the material tested (including the pore fluid) were placed in the environmental chamber for at least 24 hours prior to start of the test. This process ensured all components of the system accustomed to the temperature and humidity before the tests.

(2) Test set up

The submerging solutions were poured into the liquid-supply system, as shown in Figure 5.1, and enough time was allowed to let the liquid flow from the liquid supply into the testing reservoir. The same liquid level was achieved after a couple of minutes. Air bubbles in the tubing were squeezed out to prevent them from flowing into the sample reservoir and causing vibrations.

Deposit the sand samples into the rings. The sand samples were deposited into the rings with an air pluviation process. The samples were deposit into the rings through funnels from specific heights depending on the desired void ratios. In our tests under dry conditions, the samples were deposited into the rings through a funnel with an 8-mm opening from a fall height of 1 cm.

For submerging tests, the reservoir which contains the ring and the sample was first filled with testing solutions. Then sand samples were deposited from 1 cm above the liquid level through a 15-mm opening funnel with a slow flow rate. The reason for using a larger opening for sample deposition in the submerging tests was to prevent clogging of particle flows through the funnel resulting from liquid climbing up through sand flow. This phenomenon was observed in our tests.

Once sand roughly filled up a ring, a scale was moved gently along the upper edge of the ring to create a flat and smooth surface on top of samples. No pressure was applied to the sand from the scale. Small amounts of sand were added to fill the gaps and excessive sand was scrubbed out of the ring, until a flat surface was achieved, as shown in Figure 5.2(b).

(3) Warming up the electrical components

The entire measurement system was turned on with the LabVIEW program 12 hours before starting the tests. This process ensured that all of the sensors in a steady state from the start of the tests. From our observations, when first turned on, the sensors and DAQ system need a warm-up period before reaching a steady state during which no load was applied and the readings from all sensors were constant.

This period was also used to obtain the drift of output voltage of module A (NI 9263). As mentioned above, although it provided a nominal of 0.5-V voltage to the potentiometers, the actual output voltage to the potentiometers (measured with module B NI 9219) were slightly drifted around 0.5 V. The drift has been found out to be relatively constant for each channel of NI 9263 and it was measured during this warm-up period. The drift would be taken into account of when calculating displacements from the readings of potentiometers and this modification would give a better accuracy in displacement calculations.

(4) Starting the tests

After all the preparations, the tests could be started by loading the samples. Depending on the magnitudes of loads, they were usually applied in four equal increments. Weights were added onto the loading plate with great caution. A 1-min pause was introduced between each two adjacent

loading steps, each loading step finished in 2 minutes. When the loading process was finished, the system was checked to make sure all components and wires are secured. For the saturation tests, seal the top of the sample with membrane to minimize liquid evaporation. Lastly, the operator exited the chamber and closed its door.

(5) Monitoring the tests

The portable computer for data acquisition was connected to a wireless network to allow remote access from outside the chamber. The real-time readings of all sensors were monitored daily during the tests. Once some abnormal readings were observed, the situations were evaluated. Some actions were taken either to fix the problems and resume obtaining reasonable measurements. Otherwise, if the problems were irreversible, the tests were stopped to avoid waste of time.

Examples of fixable problems were: short-term power outages, software/program stop-working, full data storage space, etc. These problems could be fixed remotely or would disappear automatically, and the measurements would resume back to normal thereafter.

In some other cases though, the tests had to be terminated. A major example of these cases was broken sensor/sensors when one or several of them constantly gave abnormal readings. If this happened, usually the tests would have been terminated. Some tests were kept running because the rest of the readings were useful and worth continuing the tests. Other examples included long-term power outages and external excitations which caused the readings thereafter unreliable.

(6) Ending the tests

The tests were ended when the changing rates of horizontal stress stayed constant or attenuated for more than 3 days. To end the tests, the loads were removed also in four steps, reversing to the loading process.
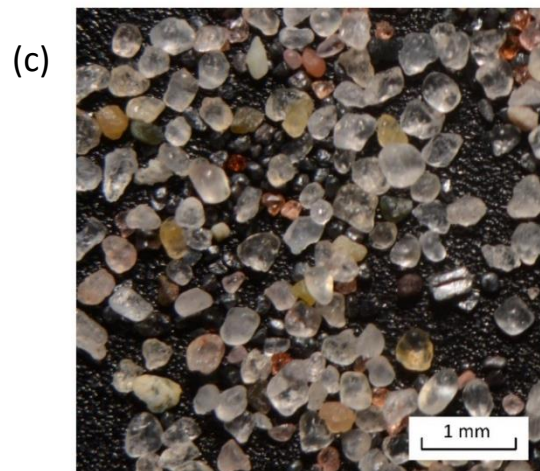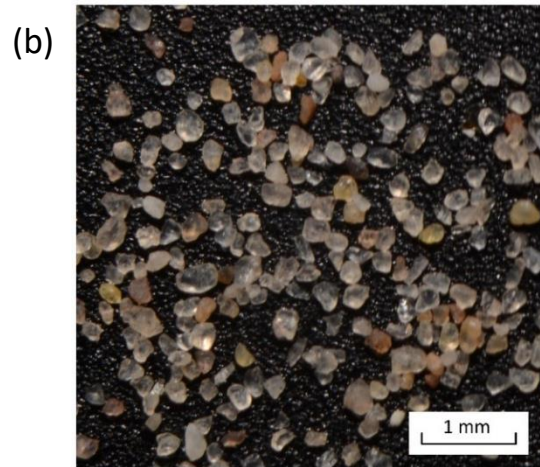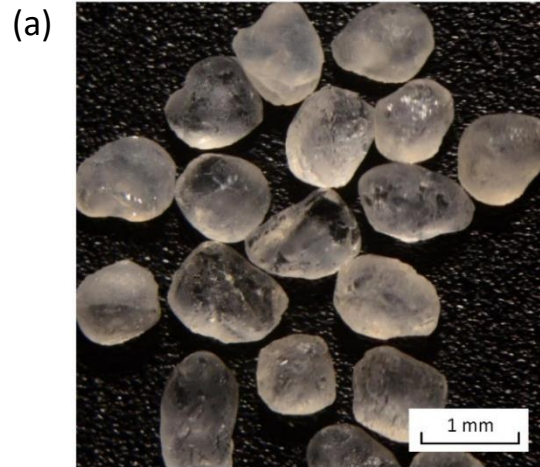
Figure 5.6. Optical microscopic images: (a) Ottawa 20-30 sand, (b) Lake Michigan Dune sand, and (c) Lake Michigan Empire Beach sand.

103
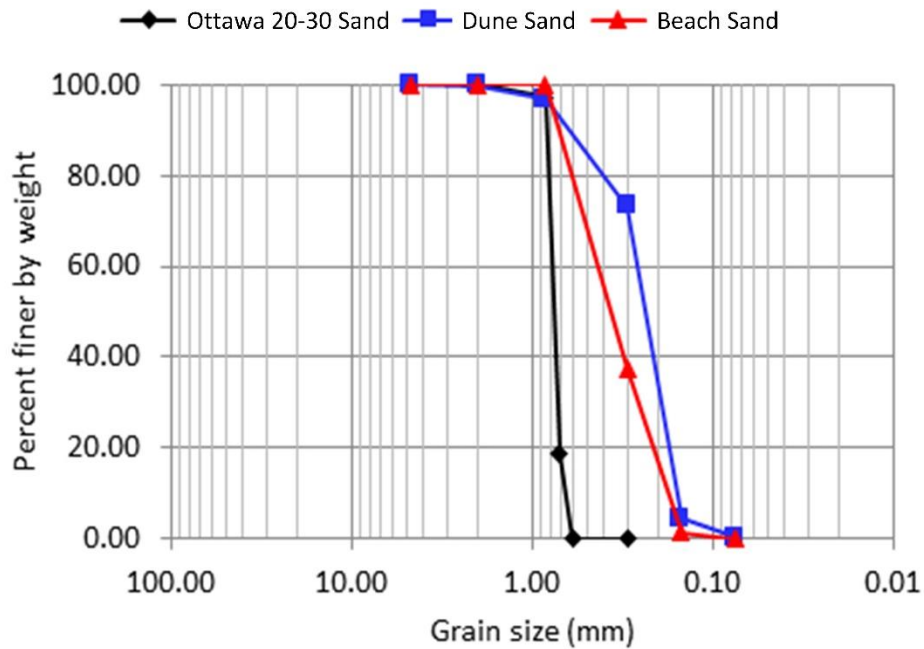
Figure 5.7. Gradation curves for Ottawa 20-30 sand, Lake Michigan Dune sand and Lake Michigan Empire Beach sand.

5.6. Sands Tested

Three types of sand were used in the soft oedometer tests, ASTM standard Ottawa 20-30 sand, Lake Michigan Dune sand and Lake Michigan Empire Beach sand. The Lake Michigan Dune sand and Lake Michigan Empire Beach sand will be referred to as LMD sand and LMEB sand in this thesisFigure 5.6 shows optical microscopic images of these types of sand. The widths of images are about 4 mm. As the images show, Ottawa sand has uniform, well-rounded particles. LMD sand and LMEB sand both consist sand grains much smaller than those of Ottawa sand. Trace of grains with various minerals other than silica can be observed in LMD sand and LMEB sand based on their appearance. Grains of LMD sand are more angular than those of Ottawa sand and LMEB sand.

Particle size gradation curves of the three types of sand were obtained from sieve analysis and are shown in Figure 5.7. Ottawa sand has a narrow gradation with sizes of most of its particles

104

fall to the range of 0.6 mm (#30 US standard sieve size) to 0.85 mm. LMD sand and LMEB sand have slightly better gradations and smaller particles sizes as observed under microscopes. The values of C_u and C_c of the sands are reported in the caption of Figure 5.7.

The Ottawa sand sample were further sieved before each test. The purpose was to remove the trace amount of particles coarser than the #20 sieve and finer than the #30 sieve. This process can improve repeatability of the testing results.

5.7. Results

Stainless steel spheres test

An experiment was performed on a sample comprised of uniform stainless steel spheres by Nadukuru (2013) in order to test the robustness of the ring and to detect a possible drift in the signal fed into the data acquisition system. The diameter of the steel spheres is 3.175 mm (high-molybdenum reflective-finish hardened stainless steel: E52100 Alloy). The specimen was assembled in a cylinder with a height of 25.4 mm. Porosity of the prepared specimen was 0.41, the specimen was loaded to an average vertical stress of 118.3 kPa in 4 equal steps (with two-minute intervals), and the load was maintained for 7 days. Because the stainless steel has a high yield stress and the reflective finish has a low roughness (RMS = 39.5 nm), contact fatigue was not expected to be noticeable under applied loads, as was already indicated in Figure 5.8. Therefore, consistent with the contact maturing hypothesis, contact stiffness and macroscopic stiffness were not expected to increase, and the radial stresses under a sustained load were expected to remain constant.

After application of 118.3 kPa in vertical load, the radial stress increased to slightly over 116.5 kPa, it stabilized within the next hour at about 116.7 kPa, and remained constant for the duration of the test (nearly 7 days), Figure 5.8(a). It is not surprising to notice that the macroscopic stress state was nearly hydrostatic in the assembly of reflective-finish spheres. No time-dependent increase in macroscopic radial stress of the steel spheres assembly was taking place, and, therefore, we conclude that no increase in contact stiffness was taking place during the sustained load. Indeed,

static fatigue was not expected to occur on reflective finish steel surfaces, whereas contact maturing is what the authors consider as the key process in sand aging. The stainless steel spheres specimen did not display any signs of aging in 7 days.

Thirty minutes after application of the load, the settlement was 281.5 µm, which yields a vertical strain of a little over 1%. The settlement increased by less than 3 µm within the first day, stabilized at about 284.3 µm, and remained at this level for the next 6 days, Figure 5.8 (b).
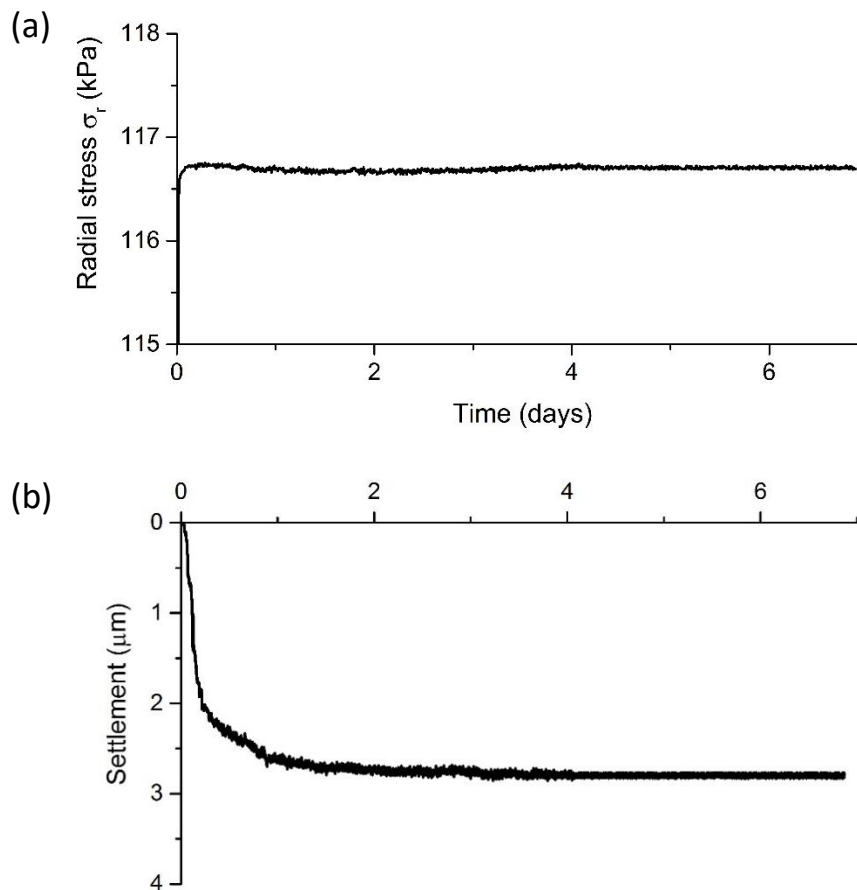
Figure 5.8. Soft oedometer test with steel spheres: (a) change of radial stresses over time, and (b) increase in settlement over time (reproduced from Nadukuru 2013).
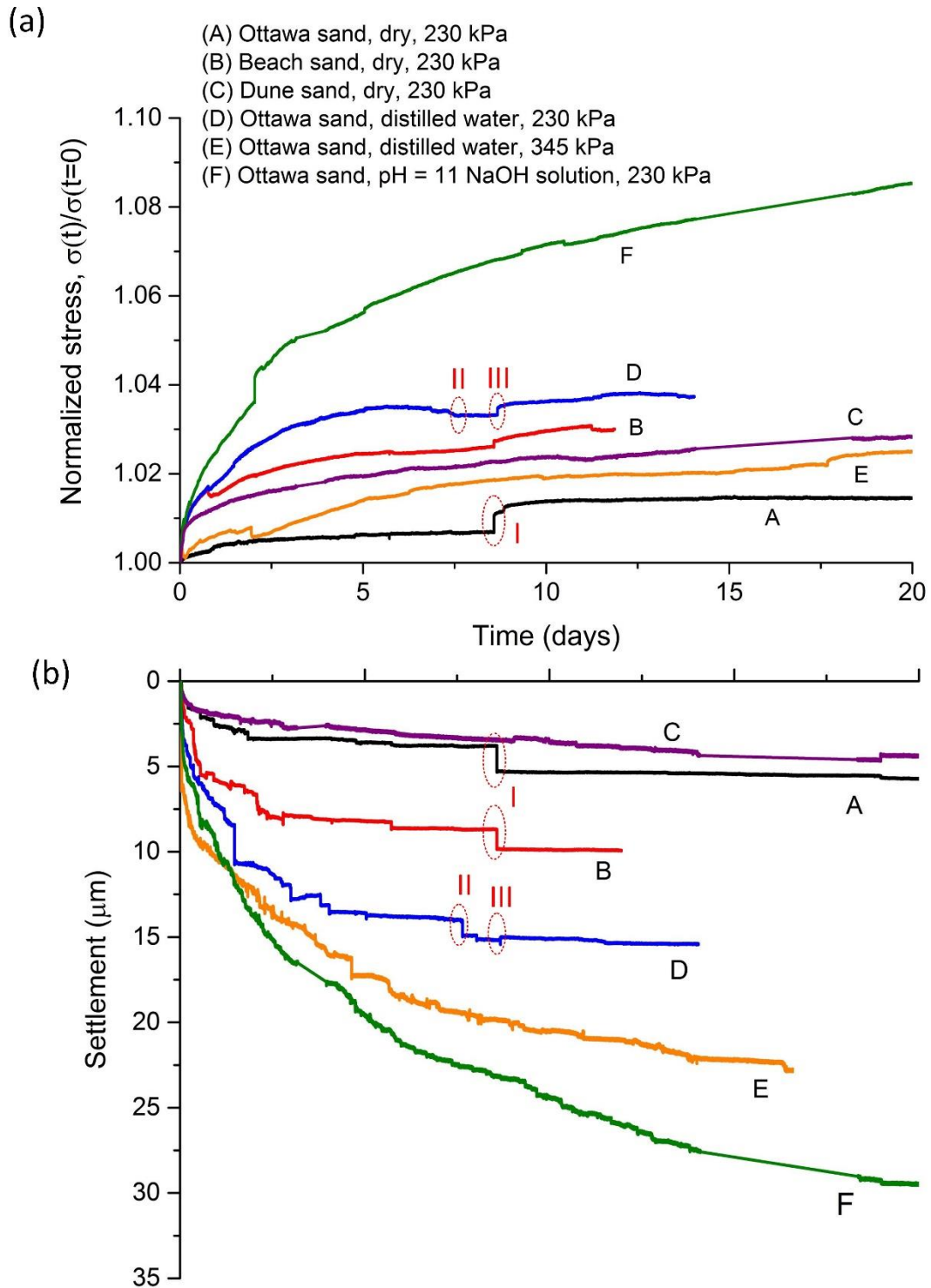
Figure 5.9. Soft oedometer testing results with sand samples: (a) increase in radial stresses over time, and (b) increase in settlement over time (abrupt changes in readings are highlighted).

107

Table 5.1. Summary of soft oedometer tests

Test	Sand	Pore fluid	Porosity	Test duration (days)	30 min after loading started		Radial stress increase		Time-dependent settlement	
					Radial stress (kPa)	Settlement (μm)	After 5 days (kPa)	After 12 days (kPa)	After 5 days (μm)	After 12 days (μm)
A	Ottawa	Air dry	0.40	20	129.62	262.22	0.82	1.82	3.61	5.35
B	Beach1	Air dry	0.38	12	118.90	563.17	2.92	3.57	8.19	9.95
C	Dune2	Air dry	0.40	20	93.64	299.35	1.81	2.24	2.86	3.92
D	Ottawa,	pH = 6.83	0.40	14	130.66	281.51	4.48	4.96	13.54	15.37
E4	Ottawa	pH = 6.83	0.40	20	174.60	355.53	2.46	3.47	17.25	21.04
F	Ottawa,	pH = 11	0.40	20	144.88	467.12	8.15	10.75	19.57	26.07

[1]Lake Michigan Empire Beach Sand   [2]Lake Michigan Dune Sand   [3]Distilled water

[4]Load: 345 kPa; all other tests: 230 kPa

Radial stress and settlement

Tests were carried out on air-dry specimens of all sands and on specimens saturated with water of various pH. Six test results are presented in Figure 5.9, three for air-dry specimens of all three sands, and three Ottawa sand specimens saturated with distilled water under two different loads and an alkaline water solution. Constant temperature of 20° and relative humidity of 30% were maintained during all tests. The influence of temperature on the rate of static fatigue was not part

of this study, and the temperature of 20°C was selected because opening of the chamber door during tests (necessary for resetting the equipment after occasional power failure) produced a small disturbance in the temperature. However, dynamic disturbances could not be avoided (despite an effort to base-isolate the oedometers). The duration of the tests reported varied from 12 to 20 days. It was common for the tests to be terminated because of sensor breakage, power outages or external excitations that made further readings unreliable.

Five specimens were loaded to an average stress of 230 kPa and one to 345 kPa; loading occured in 4 equal steps, every 2 minutes, which resulted in the completion of the entire loading process in about 10 min. The immediate settlement varied from about 260 to 560 μm (from 1 to 2%), whereas the time-dependent settlement in the following 12 days reached about 5 to 26 μm. These results are summarized in Table 5.1, and the time-dependent processes of increasing radial stress and increasing settlement are shown in Figure 5.9. The data in Figure 5.9 are plotted starting 30 min after the loading process began, and the radial stress in Figure 5.9(a) is normalized by its value at 30 min., given in the 6th column of Table 5.1.

Not surprisingly, the largest immediate settlement occurred for the finer and better graded Beach Sand, which also had a slightly lower void ratio (Table 5.1). However, the longer-term process is affected the most by the presence of pore fluid. Earlier research indicated dissolution of silica in water, with the largest rate of the process in alkalic solutions (Krauskopf 1959). This dissolution process causes accelerated fatigue of silica (Charles 1958), which affects both the rate of the radial stress increase and the rate of settlement increase.

The purpose of the tests presented in Figure 5.9 was to collect evidence for contact maturing to be a plausible mechanism causing time effects in silica sand. Observed increase in radial stress in the soft oedometer under sustained load is a manifestation of an increase in macroscopic stiffness of sand caused by maturing contacts. This was argued using the argument of the elastic energy preservation in the aging sand (Eq. (5.1)). In all cases in Figure 5.9 the process appears to be decaying, but the rate depends on the type of sand, the pore fluid and the load.

The lowest rate of increase in the radial stress (and the nearly lowest increase in settlement) is displayed by a poorly graded air-dry Ottawa sand. Finer and better graded Lake Michigan

109

Empire Beach Sand and Lake Michigan Dune Sand exhibit slightly larger rates of radial stress increase. This is consistent with the hypothesis of contact maturing, where the beach sand has more contacts due to its finer grain content (even though the average contact force may be lower).

A larger yet increase in the rate of the aging process is caused by the presence of pore fluid, and the resulting mineral dissolution at contacts. This is not surprising. The process of mineral dissolution at contacts causes a faster increase in the number of "contact points" within each inter-granular nominal contact area, leading to higher rate of increase in the macroscopic stiffness. Hence the faster increase in the radial stress. The process of silica dissolution is faster in highly alkaline solutions (Krauskopf 1959), thus the slower increase in the radial stress in distilled water than in the pH = 11 solution. In geologic time, pressure dissolution is one of the processes leading to formation of sedimentary rock, also known as lithification.

From comparison of results from Test D and E, a larger load caused less increase in radial stress than a smaller load. According static fatigue, the reason for this could be that under larger load, under very a large load, more surface textual features fractured immediately following application of the load, leaving less of these features to develop time-dependent fracturing over time. Thus, sand samples under very large loads show less time-dependent increase in radial stress than those under smaller loads.

Abrupt changes

Both the radial stress and settlement plots in Figure 5.9 have some irregularities indicative of possible external excitation, or an electrical instability. These abrupt changes in reading data were found unavoidable. Most of those occurred within 1 second, therefore the changes in temperature or humidity have been excluded from the possible causes.

To analyze if there are external vibrations, readings of the accelerometer during for the time period during which these events happened were plotted. Fast Fourier Transformation (FFT) was performed on the acceleration data to detect vibrations which might have similar magnitudes as the background vibrations but different frequencies.
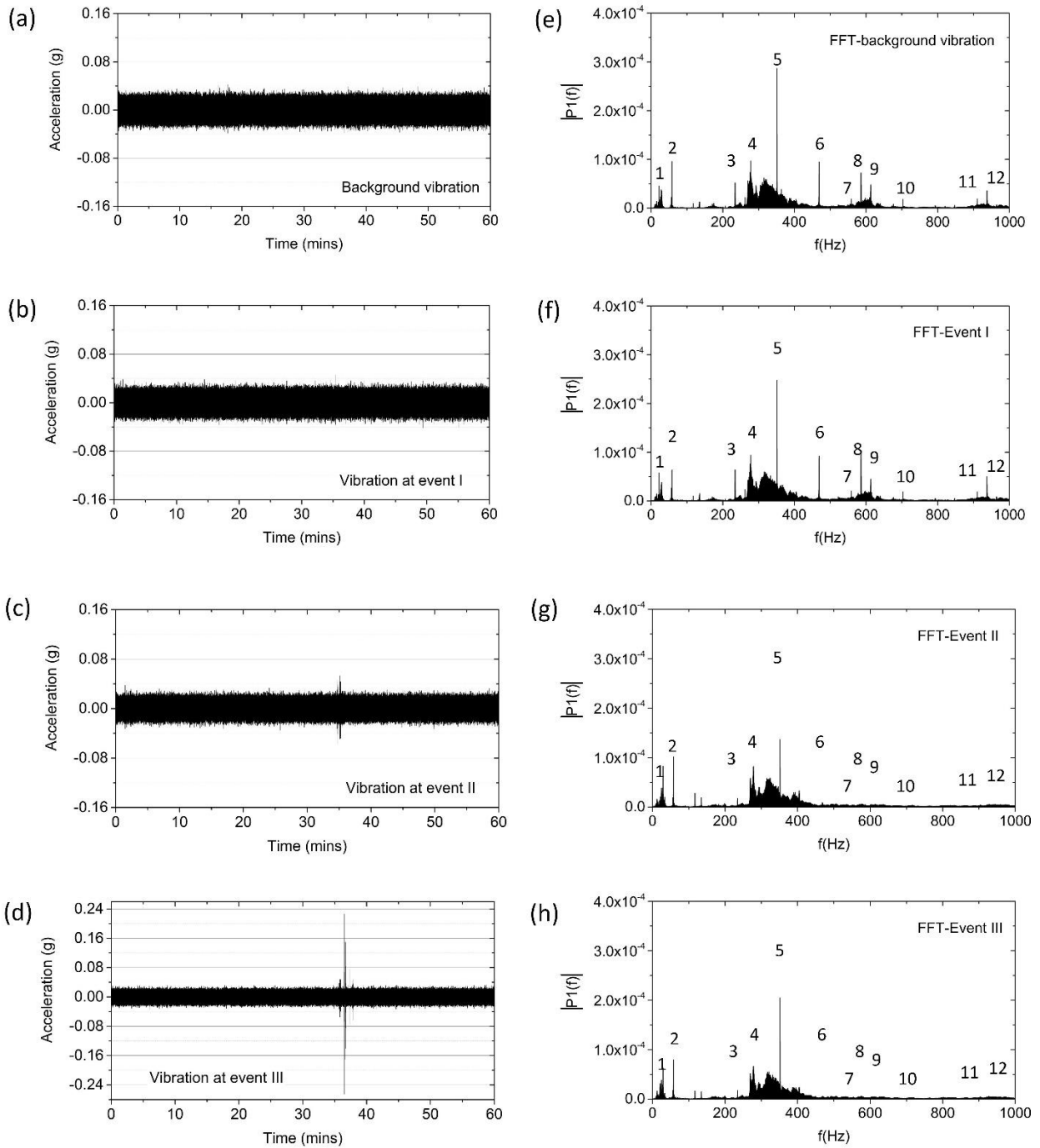
Figure 5.10. Acceleration measurements: (a)-(d) acceleration measurements: background vibration, at event I, II and III; and (e)-(h) FFT of acceleration measurements: background vibration, at event I, II and III.

Analysis on acceleration data from four 1-hour time slots are shown Figure 5.10. a one-hour period during which no abrupt changes was recorded, and a one-hour period during which Event I, II and III happened. Figure 5.10(a)-(d) and Figure 5.10(e)-(h) show the acceleration time histories and FFT results of these four periods, respectively. Event I happened to both Tests A and B which were performed at the same time at day 8. Abrupt changes in both radial stress and settlement were detected in the two tests, as shown in Figure 5.9. However, no vibration was detected between the period between 30 minutes before and after this event. The time history and it FFT of acceleration during this one hour, Figure 5.10(b) and Figure 5.10(e), are both almost identical to those of the background acceleration as shown in Figure 5.10(a) and Figure 5.10(b). Events II and III denotes the two abrupt changes during test D at about 7.5 and 8 days. At both events, vibrations were captured by the accelerometer. As shown in Figure 5.10(c) and Figure 5.10(d): at event II, a couple of vibrations with accelerations of ±0.05 to ±0.06 g were detected comparing to a background acceleration of ±0.03 g; at event III, several vibrations with accelerations ranging from ±0.04 to ± 0.23 were measured. Not surprisingly, FFT results of these two acceleration histories are different from that of the background, with more frequency components under 100 Hz, as shown in Figure 5.10(g) and Figure 5.10(h). Both Events II and III happened at around 7 am in the morning and the author suspects they were caused by activities of the building maintenance staff. Thus, notes and caution tapes were installed around the testing chamber to prevent this type of impacts.

In most of the abrupt changes, no vibration was picked up by the accelerometer. These changes are also possible due of the structuration events. These are instability events when grains assume new equilibrium positions, and are typically associated with some subsidence (Nadukuru et al. 2012).

The readings from the soft oedometer tests are consistent with the hypothesis of contact maturing which considers static fatigue at the contacts as the key cause of aging.

5.8. Discussion

In this section, it is estimated how much increase in radial stress would be observed if the ring was rigid rather than soft. To estimate the additional radial stress, a virtual incremental radial (radial) stress was applied on the sample to recover the measured radial expansion during the aging process. The virtual incremental radial stress was back-calculated by assuming elastic behavior of the sample during this small strain process. The elastic properties of the sample during this process were calculated from the unloading process in the physical test.

Table 5.2. Axial strain and radial stress during Test D

Step	Vertical stress (kPa)	Axial strain (%)	Horizontal stress (kPa)	Radial strain (%)
①	0	0	0	0
②	57.5	0.257	29.3	1.32e-2
③	115.0	0.364	63.2	2.86e-2
④	172.5	0.475	95.5	4.32e-2
⑤	230.0	0.554	129.4	5.86e-2
⑥	230.0	0.584	135.5	6.13e-2
⑦	172.5	0.553	116.6	5.28e-2
⑧	115.0	0.513	91.1	4.12e-2
⑨	57.5	0.477	57.8	2.62e-2
⑩	0	0.312	5.5	2.49e-3

Test D was chosen as an example for this estimation, where an Ottawa sand samples submerged in distilled water was tested with constant vertical load of 230 kPa. Axial stain and radial stress measurements during the entire test are plotted in Figure 5.11. The circled numbers represent the loading steps where steps ① to ⑤ are the loading process from 0 kPa to 230 kPa in four equal increments, ⑤ to ⑥ is the aging process, and ⑥ to ⑩ is the unloading process from 230 kPa to 0 kPa in four equal load increments. Figure 5.11(a) is a plot of axial strain (settlement

divided by sample initial height) as function of vertical stress; Figure 5.11(b) is a plot of radial stress vs. vertical stress. The values are summarized in Table 5.2.
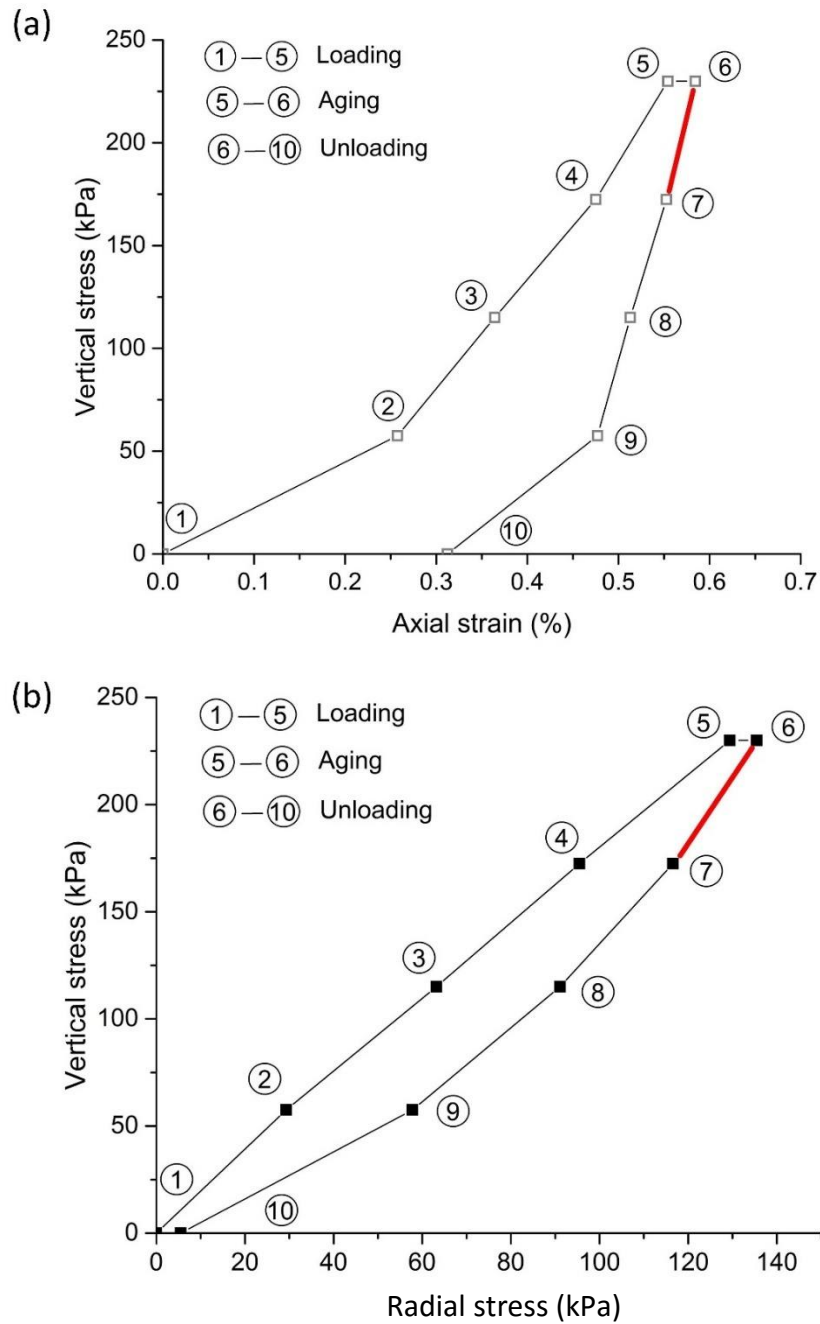
Figure 5.11. Settlement and horizontal stress measurements of Test D: (a) axial strain with vertical stress, and (b) horizontal stress with vertical stress.
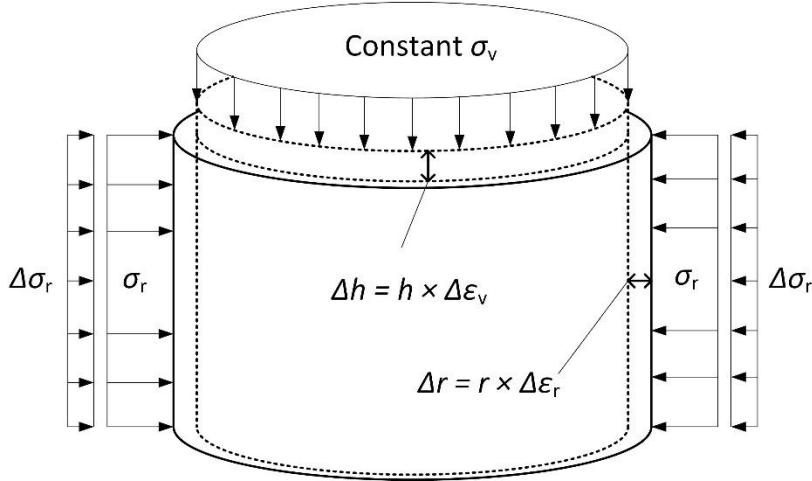
Figure 5.12. Virtual additional horizontal stress to recover radial expansion.

Figure 5.12 shows recovery of the radial expansion when the virtual radial stress is applied. The elastic properties of the sample were adopted from those during the first unloading step ⑥-⑦ (as highlighted by red color in Figure 5.11). According to Hooke's law, the relationships between the strains and stresses in the sample are:

$$\varepsilon_v = \frac{1}{E}\left[\sigma_v - v\left(\sigma_r + \sigma_\theta\right)\right] \tag{5.8}$$

$$\varepsilon_r = \frac{1}{E}\left[\sigma_r - v\left(\sigma_z + \sigma_\theta\right)\right] \tag{5.9}$$

$$\varepsilon_\theta = \frac{1}{E}\left[\sigma_\theta - v\left(\sigma_r + \sigma_z\right)\right] \tag{5.10}$$

where ε_z, ε_r and ε_θ are the axial, radial and circumferential strains in the sample, respectively; σ_z, σ_r and σ_θ are the axial, radial and circumferential stresses in the sample, respectively; E

115

and v are the Young's modulus and Poisson's ratio of the sample, respectively. In this case, $\sigma_r = \sigma_\theta$ and $\varepsilon_r = \varepsilon_\theta$. Therefore, Equations (5.8) to (5.10) can be simplified as:

$$\varepsilon_v = \frac{1}{E}\left[\sigma_v - 2v\sigma_r\right] \tag{5.11}$$

$$\varepsilon_r = \varepsilon_\theta = \frac{1}{E}\left[(1-v)\sigma_r - v\sigma_z\right] \tag{5.12}$$

Equations (5.11) and (5.12) can be written in an incremental form

$$\Delta\varepsilon_v = \frac{1}{E}\left[\Delta\sigma_v - 2v\square\Delta\sigma_r\right] \tag{5.13}$$

$$\Delta\varepsilon_r = \Delta\varepsilon_\theta = \frac{1}{E}\left[(1-v)\square\Delta\sigma_r - v\square\Delta\sigma_z\right] \tag{5.14}$$

where $\Delta\varepsilon_z$, $\Delta\varepsilon_r$, $\Delta\sigma_z$ and $\Delta\sigma_r$ are the incremental strains and stresses.

During the unloading process ⑥-⑦ as shown in Figure 5.11, the incremental stress and strains, from Table 5.2, are $\Delta\varepsilon_z = 3.17\times10^{-4}$, $\Delta\varepsilon_r = -8.55\times10^{-4}$, $\Delta\sigma_z = 57.5$ kPa and $\Delta\sigma_r = 18.9$ kPa. Tensile stresses and strains are considered positive here. By substituting these values into Equations (5.13) and (5.14), the Young's modulus E and Poisson's ratio v of the sample can be obtained as:

$$E = 134.04 \text{ kPa} , v = 0.3974$$

116

The calculated Poisson's ratio ν falls to the range of that of dense sand (0.3-0.4) (Obrzud and Truty 2012). The calculated Young's modulus E is 70% larger than the reported upper-bound value for dense uniformly-graded sand which is around 80 kPa (Obrzud and Truty 2012). This could be a result of aging effects.

Now let us consider the process of recovering the radial expansion developed during the aging process by applying a radial stress increment $\Delta\sigma_r$. During this process, $\Delta\sigma_z = 0$, $\Delta\varepsilon_r = -2.24 \times 10^{-5}$ (radial expansion during the aging process). The stress increment $\Delta\sigma_r$ and the change in axial strain $\Delta\varepsilon_z$ during this recovery process can be calculated by substituting the values of $\Delta\varepsilon_r$ and $\Delta\sigma_z$ into Equations (5.13) and (5.14),

$$\Delta\sigma_r = -4.99 \text{ kPa}, \quad \Delta\varepsilon_z = 2.96 \times 10^{-3}\%$$

According to the calculation results, a radial stress increment of 4.99 kPa is needed to recover the radial expansion developed during aging, about 80% on top of the measured increase in radial stress of 6.1 kPa during the aging process. During the same process, a vertical strain of 2.96×10^{-3}% is recovered which accounts for 10% of the axial strain developed during aging (0.03%). Therefore, based on the analysis, if the ring is rigid, there would be approximately 80% larger increase in radial stress and 10% decrease in vertical settlement during the aging process.

5.9. Conclusions

An increase radial stress in oedometric specimens was detected in soft oedometer testing. Test results presented are consistent with the hypothesis of contact maturing, which indicates time-dependent fracturing of microscopic textural features at contacts as the key cause of aging in silica sand. The process is sensitive to environmental factors, and can be accelerated in the presence of pore water, and even more so in the presence of high pH solutions. As maturing of contacts has a decaying characteristic, engineering consequences in "aged" deposits may be insignificant; however, the process is manifested distinctly in fresh deposits or in disturbed sand with newly formed contacts.

- Time effects were observed in the sand samples tested under sustained (constant) loads, supporting the static fatigue hypothesis.

- The increase in radial stress is the consequence of an increase in macroscopic stiffness in a confined assembly of grains, which is a result of contact maturing on individual contacts. Once contact maturing was not present in the grain assembly, as in the tests with an assembly of stainless steel spheres, no time-dependent increase in radial stress or settlement were observed.

- The increase in the radial stress in time was faster in sands with small grain sizes. This can be attributed to the larger number of inter-grain contacts in finer sand, causing a more significant cumulative impact on macroscopic aging of sand.

- A larger load did not speed up the increase in radial stress in sand samples. This is possibly because a larger load produces larger damage immediately after application of the load. This reduces the contacts' potential for maturing, thus slower increase in radial stress.

- The increase in radial stress was accelerated by saturation with distilled water, and an even larger increase occurred when the sample was saturated with an alkaline water solution. The latter causes pressure dissolution at contacts, thereby accelerated contact maturing and faster increase in radial stress (and settlement).

Chapter 6

Distinct Element Modeling of Aging/Maturing of Contacts

6.1. Introduction

Contact-scale experiments in previous chapters showed evidence of time-dependent cracking of mineral material at sand grain surfaces under load. This microscopic delayed fracturing process at contacts, termed as contact maturing in this thesis, is hypothesized to be responsible for aging behavior of sand (macroscopic phenomenon). Although contact-scale testing provides indispensable opportunities for physical observations on contact maturing, there are some limitations with contact-scale testing. The first limitation is accuracy. As discussed in Chapter 4, any minute instabilities in the apparatus mechanical nature, sensing system, or environmental factors, could cause significant disturbance to the measurements and affect the accuracy of experiments. The second limitation is testing durations. The longer the time, the more chances for abovementioned disturbances to emerge. Also, if a very long time span is of interest, such as years (or centuries), it is not practical to conduct physical tests. The third limitation is from the limited measurement capacities of available sensors. Some processes of interest in contact maturing

process, such as the quantitative geometrical evolution, still cannot be tracked with current sensing technologies.

With all the limitations in physical testing at the contact/grain scale, numerical modeling becomes a valuable complementary tool to study time-dependent behavior of sand at micro-scale. To get a better understanding of contact maturing process, a numerical model of a single inter-grain contact was constructed with the distinct element method (DEM) both in two dimensions and three dimensions. The model incorporated the static fatigue or stress corrosion process in grain material and it successfully reproduced the time-dependent deformations that were observed in contact maturing tests. The numerical parameters of the model were calibrated with the measurements in the contact maturing tests. Then the changes in the micro-morphological and micro-mechanical properties of the model were analyzed. These changes support the static fatigue hypothesis as the mechanism of sand aging.

In this chapter, an introduction on DEM and its applications on simulations of fracturing of geomaterials are reviewed. Then a stress-corrosion model for simulations of stress-corrosion/static fatigue process and its theoretical background are introduced. After the background introduction, the implementations of both the 2D and 3D models of an individual contact are explained, followed by a calibration of the 3D model. After the 3D model was calibrated, a 3D model between two grains was simulated and aging effects in the grain-to-grain contact is discussed. 3D simulations with different particle sizes (resolutions) were conducted and a discussion on simulation resolution is made based on these results. Finally, the presumed changes in contacts during maturing were incorporated into a sand grain assembly simulation to investigate the effects of the changes at contacts on macroscopic behavior of sand grain assemblies. The simulation results are presented and discussed. Limitations of the models are discussed and caution is recommended when using theoretical models.

6.2. DEM Modeling of Stress Corrosion Process

Distinct Element Method (DEM)

Distinct element method (DEM) is one particular method of the family of discrete element methods. It was introduced by Cundall and Strack (1979) to simulate granular assemblies. In this method, granular particles are simulated as discrete discs (in two-dimensional simulations) or spheres (in three-dimensional simulations). Behavior of the particle assemblies are collectively controlled by motions of the particles and interaction of the inter-particle contacts. The DEM platforms used in this thesis are the Particle Flow Codes in 2 Dimension (PFC^{2D}) and Particle Flow Code in 3 Dimension (PFC^{3D}) developed by Itasca Consulting Group (Itasca 2008).

Interaction of the particles in DEM with PFC^{2D} and PFC^{3D} is calculated in dynamic time steps continuously aiming to achieve states of equilibrium. At each calculation step, motion of a particle is calculated by Newton's second law (force = mass × acceleration). The position of the particle in the end of each step is updated with its acceleration calculated from the total resultant force of contact forces from all its contacts. Based on these new particles positions, contact forces at each contact are developed from the relative displacement of the two particles in contact, based on force-displacement law at the contact which can be default or user-defined, linear or nonlinear. Equilibrium is achieved through a large number of calculation cycles as a dynamic process, each cycle representing a small time-step. Usually the criterion of equilibrium is a small pre-determined ratio (default 0.01 in PFC codes) between the mean out-of-balance contact forces across all particles and the mean contact force across all contacts. The time step is chosen to be very small so that movement cannot affect particles other than its immediate neighbors. Energy dissipation in the model is achieved through three forms of damping: friction, contact, and global damping.

For more detailed about theories and applications of DEM modeling with the PFC codes, the readers are referred to the user manuals of PFC^{2D} and PFC^{3D} (Itasca 2008A and Itasca 2008B) and Cundall and Strack (1979).

Bonded-Particle Model (BPM) and Parallel-Bonded Stress Corrosion (PSC) Model

Potyondy and Cundall (2004) proposed a bonded particle model (BPM) to simulate rocks. The rocks in that model are simulated with a dense packing of non-uniformly sized particles, bonded

at inter-particle contacts. This model was implemented in PFC^{2D} and PFC^{3D} software packages. The model captures elasticity of rocks, but also simulates fracturing, and the effects related to fracturing, such as acoustic emission. Parallel-Bonded Stress Corrosion model (PSC) was proposed by Potyondy (2007) as an extension of BPM to include time-dependent behavior of rocks. The time-dependent development of microcracks is often referred to as stress corrosion or static fatigue. More details about PSC model can be found in Potyondy (2007).

The PSC model is applied in this thesis at the microscale to simulate individual sand grains. A single sand grain is built of an assembly of bonded non-uniformly sized sub-particles. Time-dependent fracturing of the textural features at contacts will be mimicked using the PSC model.

$$F^n = K^n U^n$$
$$\Delta F^s = -k^s \Delta U^s$$

Deformability

$$\Delta \bar{F}^n = \bar{k}^n A \Delta U^n$$
$$\Delta \bar{F}^s = -\bar{k}^s A \Delta U^s$$
$$\Delta \bar{M}^n = -\bar{k}^s J \Delta \theta^n$$
$$\Delta \bar{M}^s = -\bar{k}^n I \Delta \theta^s$$

Strength

$$F^s \leq \mu F^n$$

$$\bar{\sigma}^{max} = \frac{-\bar{F}^n}{A} + \frac{|\bar{M}^s|\bar{R}}{I} < \bar{\sigma}_c$$

$$\bar{\tau}^{max} = \frac{|\bar{F}^s|}{A} + \frac{|\bar{M}^n|\bar{R}}{J} < \bar{\tau}_c$$

$$\Delta \bar{M}^s = -\bar{k}^n I \Delta \theta^s$$

Particle behavior
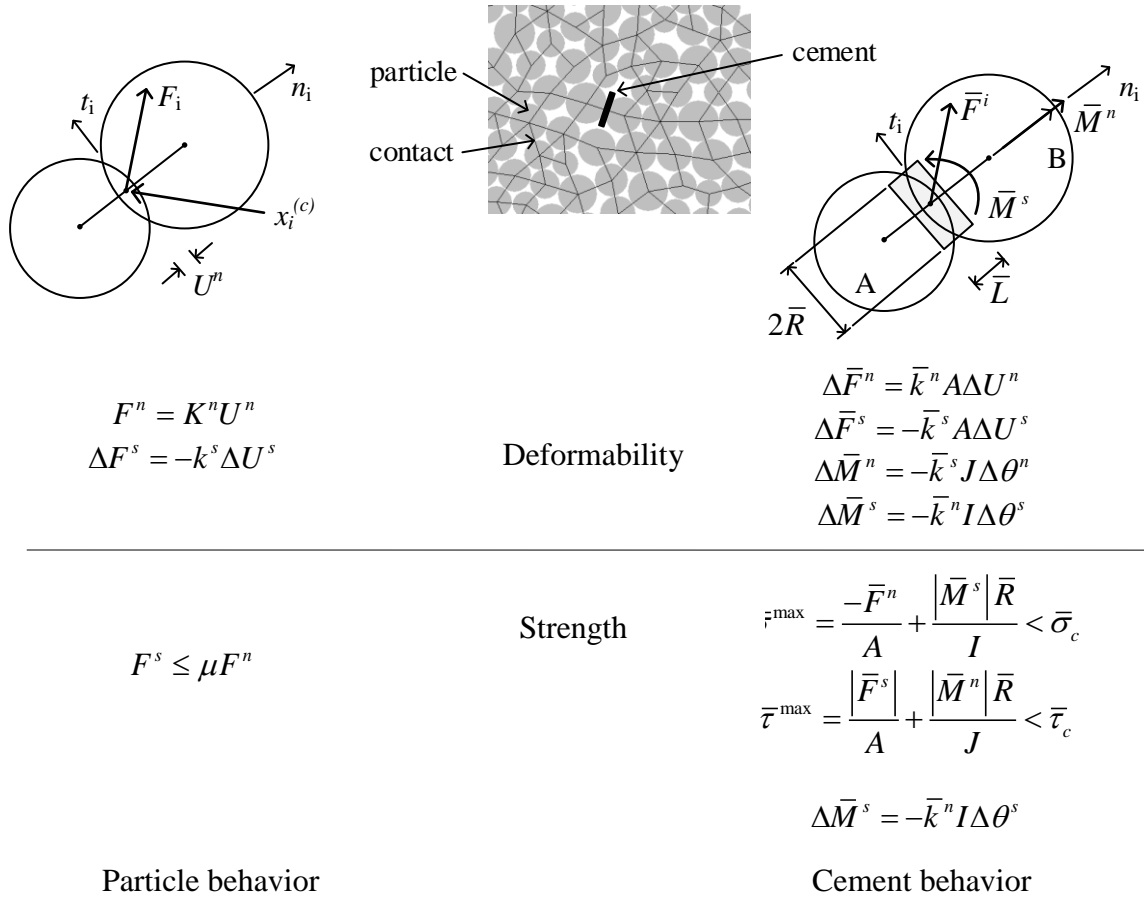
Cement behavior

Figure 6.1. Force-displacement behavior of BPM (redrawn from Potyondy and Cundall 2004).

Input Parameters for BPM and PSC model

In BPM there are three types of geometrical bodies, namely walls, particles, and parallel bonds. The properties of the three types of bodies are defined by two groups of input parameters consisting of geometrical data and physical properties data, respectively (Cundall and Strack 1979; Potyondy and Cundall 2004). The former group of parameters determine the positions and orientations of the walls, the positions and sizes of particles and the sizes of parallel bonds, in a global coordinate system. The latter group assigns physical properties to the walls, balls and parallel bonds.

The particles in BPM are characterized by particle density, particle size distribution, and particle micro-properties. Particle density, ρ, defines the average density of the material that the particles consist of. The particle diameters are normally distributed within a range bounded by a minimum diameter, $D_{\min}$, and a maximum diameter, $D_{\max}$. The diameter ratio, $D_{\min}/D_{\max}$, controls the particle packing of the BPM. Changing $D_{\min}$ alters absolute particle sizes but does not affect particle packing fabric as long as the ratio ($D_{\min}/D_{\max}$) is constant. The micro-properties of particles are specified by the following group of input parameters

$$\{E_c,\ (k_n/k_s),\ \mu\} \tag{6.1}$$

where E_c is Young's modulus of the particles; (k_n/k_s) is the ratio of normal to shear stiffness of the particle contacts; and μ is the particle friction coefficient. After these parameters are declared, the normal and shear stiffnesses are assigned through the following equations

$$k_n = \begin{cases} 2tE_c,\ t=1, & \text{PFC2D} \\ 4RE_c, & \text{PFC3D} \end{cases} \tag{6.2}$$

$$k_s = \frac{k_n}{(k_n / k_s)} \tag{6.3}$$

where t is the thickness of the discs in PFC^{2D}; R is the diameter of the sphere in PFC^{3D}.

The friction coefficient, normal and shear stiffness of a contact between particles A and B is calculated by

$$\mu = \min(\mu^{(A)} + \mu^{(B)}) \tag{6.4}$$

$$K^n = \frac{k_n^{(A)} k_n^{(B)}}{k_n^{(A)} + k_n^{(B)}} \tag{6.5}$$

$$k^s = \frac{k_s^{(A)} k_s^{(B)}}{k_s^{(A)} + k_s^{(B)}} \tag{6.6}$$

with $k_n^{(A)}$, $k_n^{(B)}$, $k_s^{(A)}$, $k_s^{(B)}$, $\mu^{(A)}$ and $\mu^{(B)}$ being stiffnesses and friction coefficients of corresponding particles. Secant normal stiffness of the contact, K^n, is used to calculate normal force from accumulated normal displacement, while tangent shear stiffness, k^s, is used to calculate incremental shear force from incremental shear displacement.

The parallel bonds in BPM are characterized by the following parameters related to bond size and bond micro-properties

$$\left\{ \bar{\lambda}, \ \bar{E}_c, \ (\bar{k}_n / \bar{k}_s), \ \bar{\sigma}_c, \ \bar{\tau}_c \right\} \tag{6.7}$$

where $\bar{\lambda}$ is the radius multiplier used to define sizes of parallel bonds; $\bar{E}_c$ is the Young's modulus of parallel bonds; $(\bar{k}_n / \bar{k}_s)$ is the ratio of normal to shear stiffness of parallel bonds; and $\bar{\sigma}_c$ and $\bar{\tau}_c$ are the normal and shear strengths of the parallel bonds. With these input parameters, the size, normal and shear stiffnesses of a parallel bond are assigned by

$$\bar{R} = \bar{\lambda} \min(R^{(A)}, R^{(B)}) \tag{6.8}$$

$$\bar{k}^n = \frac{\bar{E}_c}{R^{(A)} + R^{(B)}} \tag{6.9}$$

$$\bar{k}^s = \frac{\bar{k}^n}{(\bar{k}^n / \bar{k}^s)} \tag{6.10}$$

where $R^{(A)}$ and $R^{(B)}$ are the radii of the two adjacent particles cemented together.

The deformability and strength behavior of the balls and parallel bonds are summarized in Figure 6.1. Particles cannot be damaged by normal forces, but slip can happen if the shear force arises at the contact exceeds the maximum static friction. Parallel bonds may become damaged when the maximum normal or shear stress surpasses their normal or shear strength. A parallel bond will be totally removed if either of its strengths is overridden and a crack is considered to have occurred at this position.
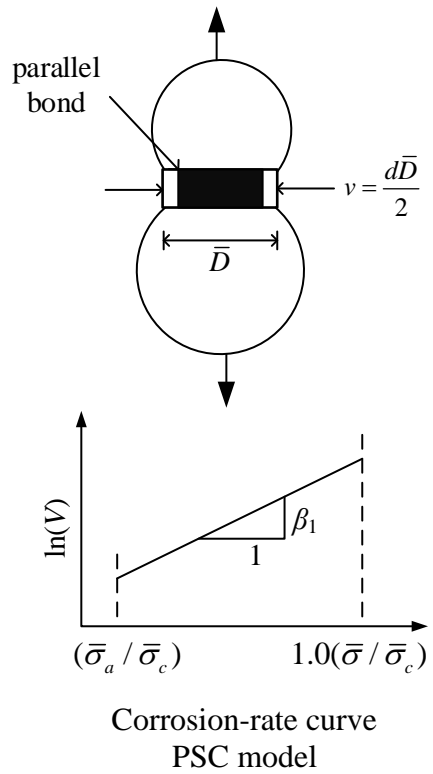
Figure 6.2. Damage-rate mechanism for PSC model (redrawn from Pytondy 2007).

The PSC model is an extension of the BPM. Other characteristics being the same as the BPM, parallel bonds in the PSC model do not maintain their sizes before breakage. If a parallel bond is under a tensile stress higher than an activation stress, bonding material will be removed in a specified rate governed by a damage-rate law; no material is removed when tensile stress is lower than the activation stress. A demonstration of the bonding material-removal mechanism and a damage rate curve are shown in Figure 6.2. A parallel bond is removed either by strength failure or by a reduced size under a threshold value. The damage rate law provides the rate at which the size of a parallel bond decreases and can be expressed as

$$\frac{d\bar{D}}{dt} = \begin{cases} 0, & \bar{\sigma} < \bar{\sigma}_a \\ -\beta_1 e^{\beta_2 (\bar{\sigma}/\bar{\sigma}_c)}, & \bar{\sigma}_a \leq \bar{\sigma} < \bar{\sigma}_c \\ -\infty, & \bar{\sigma} > \bar{\sigma}_c \end{cases} \tag{6.11}$$

where $\bar{\sigma}$ is the tensile stress applied on the parallel bond; $\bar{\sigma}_a$ is the activation stress; $\bar{\sigma}_c$ is the tensile strength; β_1 and β_2 are PSC model constants varying with temperature and chemical environment. According to this damage-rate law, the input parameters for the PSC model are

$$\{\bar{\sigma}_a, \beta_1, \beta_2\} \tag{6.12}$$

6.3. Two Dimensional Simulations

In this section, a two dimensional model of a contact between two grains with PSC model is introduced. The intent of this paper is to determine whether DEM is an appropriate tool to study contact static fatigue, and not to obtain the precise quantitative results. Therefore, this study includes two-dimensional simulations (assemblies of discs as opposed to spheres), which is computationally less costly, yet it is expected to provide an answer to the question of DEM usefulness in rate and time effects simulations.

Model Implementation

In the DEM model in this paper, a contact between two grains was simulated. One grain had a half-disk shape and the other one was of a rectangular shape. Behavior of the parallel bonds in this model were governed by an adopted parallel-bonded stress corrosion model (Potyondy 2007). To study the mechanical properties of inter-granular contacts, unconfined compression loading tests and static fatigue tests (constant load) were conducted on this model. A step-by-step procedure for

the construction of the model is introduced below, and more detail can be found in Potyondy and Cundall (2004). The model construction process is shown in Figure 6.3.

(1) ***Compact initial assembly***. As shown in Figure 6.3(a), an 600µm×600µm square space is first formed bounded by four walls. An assembly of particles is generated in this space. The positions of the particles are randomly chosen in generating the particles. The diameters of the particles follow a normal distribution bounded by the predefined minimum and maximum particles diameters, D_{min} and D_{max}. The ensure a reasonable density of packing, the default overall porosity is set to be 35% for PFC3D (16% for PFC2D). At this step, the particles are first made half of their size to avoid overlap between particles. Then the system is allowed to go through computing cycles, with zero friction between the particles, to rearrange the particles and reach equilibrium.

(2) ***Install specified isotropic stress.*** At this stage, the diameters of the particles are reduced uniformly and the model is cycled to reach equilibrium before the internal isotropic stress is measured. The purpose of this process is to release the excessive internal isotropic stress until a specified stress, σ_0, is reached. The isotropic stress is measured by dividing the total forces acting on the walls inclosing the particle assembly by the areas of the walls. The specified stress is controlled by the desired lock-in stress for a specific material after the parallel bonds are installed in later steps.

(3) ***Reduce the number of "floating" particles.*** At this stage, there are still about 15% floating particles in the particle packing that need to be removed to ensure a dense bond network can be achieved after installation of parallel bonds. A "floating" particle is one that does not have enough engagement with its surrounding particles, which is defined by the number of contacts on the particle. If the particle has less than three contacts with its surrounding particles, it is defined as a "floating" particle or a "floater". By removing the "floaters", a dense parallel bond network will be formed after the installation of parallel bonds by ensuring every particle has at least three parallel bonds connecting it to other particles, thus the network. The model after steps 2 and 3 is shown in Figure 6.3(b).

(4) ***Install parallel bonds.*** At this stage, parallel bonds are installed at all contacts in the model. A parallel bond will be installed automatically between two particles at very close proximity (with a separation less than 10-6 times the mean radius of the two adjacent particles). The parallel bonds are assigned the defined properties. The model after installation of parallel bonds is shown in Figure 6.3(c).

(5) ***Remove from the material vessel.*** The specimen is removed from the vessel by deleting all the six walls and cycling until static equilibrium is reached. The model then went through a relaxation process. The model expands and a lot of locked-in stresses will be generated during the process of self-equilibrium.

(6) ***Carve the model into desired geometry.*** At this stage, the model is carved into the desired geometry, in this case, a semi-circle and a rectangle. This is achieved by removing the particles in the region outside of this desired geometry. The carved model is shown in Figure 6.3(d).

(7) ***Make initial contact.*** This stage is to close the gap between the carved surfaces that was created at the carving stage to avoid collision between the surfaces when the load is applied during the tests. After carving the model, a gap is usually created between the two opposing carved surfaces. When a load is applied, usually by actuating the two surfaces towards each other at a certain velocity, a sudden impact will be exerted on the contact when the first encounter happened. A large instantaneous contact force will be created according to Newton's second law when the two surfaces have to change dramatically in velocities in a short time and the accelerations at that moment will be very large. To avoid this undesired dynamic impact, before the tests, an initial contact is made by actuating the two surfaces towards each other in a very small velocity until a small threshold contact force is reached. At this point, the model is ready for the planned numerical tests.
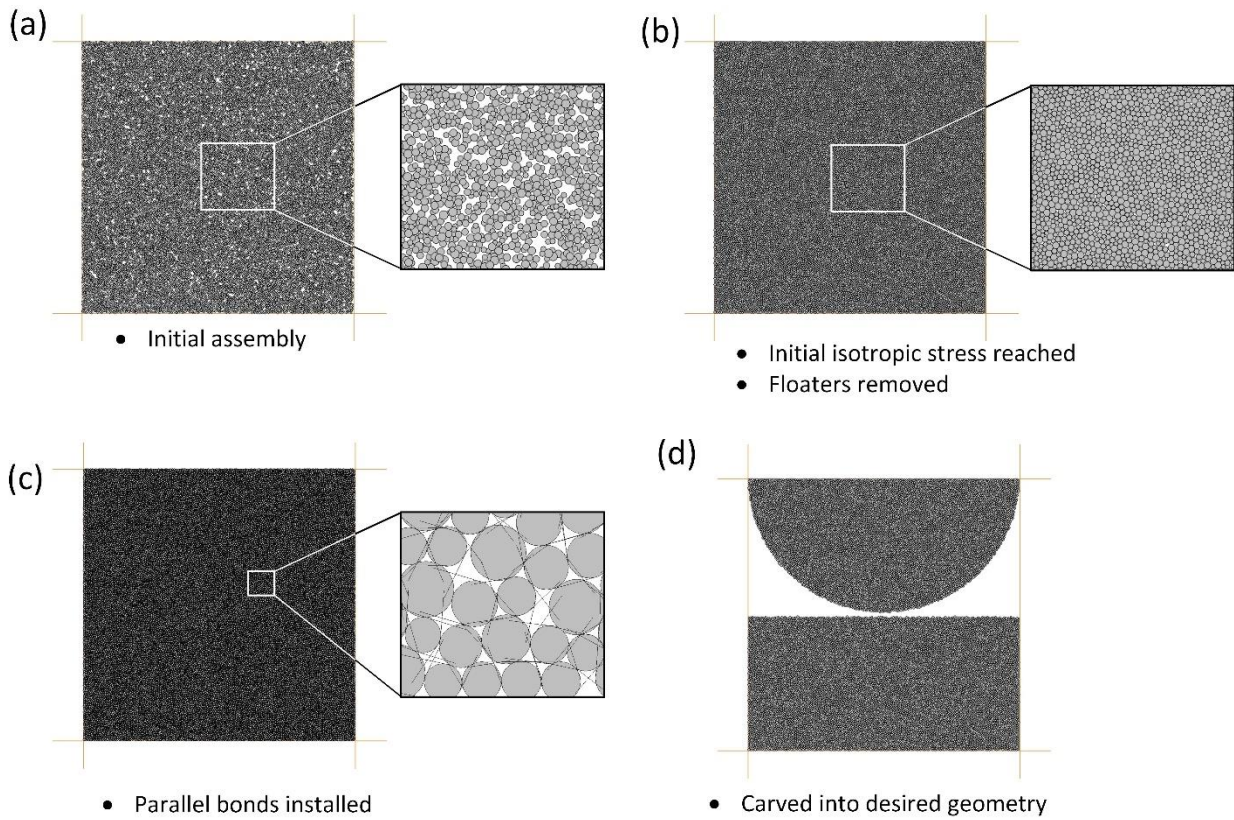
Figure 6.3. Specimen generation process: (a) initial loose packing (specimen dimensions: 0.6 mm×0.6 mm; total # of particles: 26,488), (b) floaters removed and initial isotropic stress reached (specimen dimensions: 0.6 mm×0.6 mm; total # of particles: 26,488), (c) parallel bonds installed (specimen dimensions: 0.6 mm×0.6 mm; total # of particles: 26,488), and (d) specimen carved into desired geometry (total # of particles: 23,190).
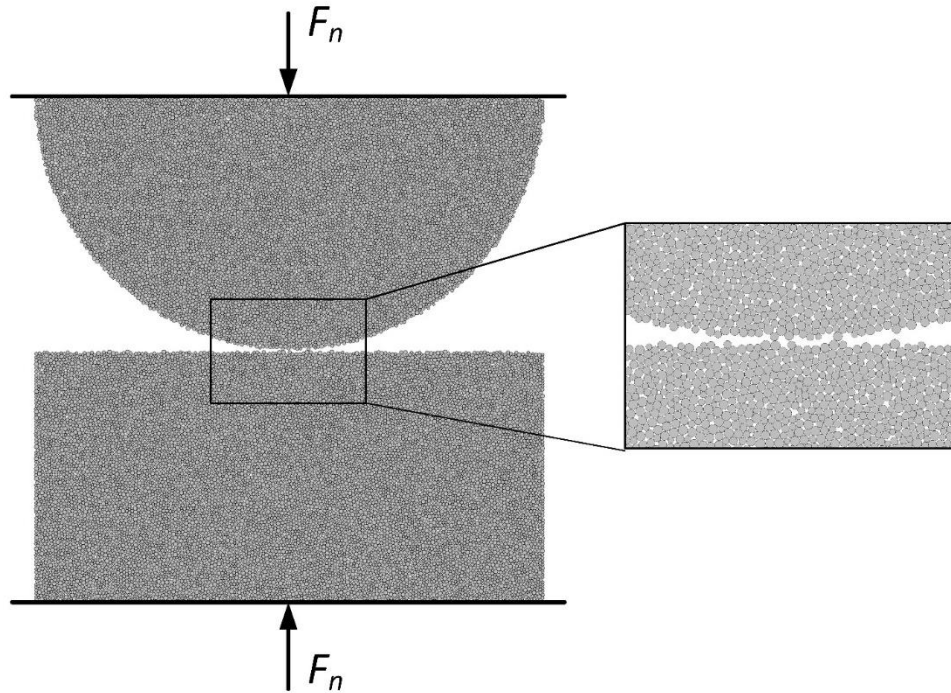
Figure 6.4. Two sand grains in contact simulated by agglomerates of 23190 bonded sub-particles in PFC2D. Upper grain: half disk, diameter 0.6 mm, 150 sub-particles across diameter; lower grain: rectangular, 0.6 mm × 0.3 mm, 150 particles across length.

The complete model is shown in Figure 6.4, with two agglomerates of 23,190 (in total) bonded sub-particles.

Parameters in this model were adopted from previous research. Cil and Alshibli (2012) simulated fracture experiments on ASTM 20-30 Ottawa sand particles with bonded particle model. In their model, each sand grain was simulated by an agglomerate of sub-particles bonded through parallel bonds to allow development of fractures within it. To determine values of parameters for the model, they calibrated it with single particle fracture experiments conducted on Ottawa 20-30 sand particles. These values of parameters were adopted in the simulation of two grains in contact in this paper except that much smaller sub-particles were used, as summarized in Table 6.1. The authors are more interested in the development of local micro-damages on grain surfaces under a load which is not large enough to crush the whole sand grains instantaneously. This requires modeling each grain with a large number of sub-particles to allow rich paths for fracturing in the

surface layers of each grain, because cracks can only happen at inter-particle contacts in PFC. The resolution (number of particles across diameter of sand grain) of the model in this paper is 150, while in the model of Cil and Alshibli (2012) it is only about 10. It is also noteworthy that, besides the difference in resolution, the model in this paper is in 2D rather than 3D as in Cil and Alshibli (2012). The values of long-term parameters for the PSC model in Eq. (6.11) in Potyondy (2007) were calibrated against static-fatigue data of Lac du Bonnet granite from lab experiments. The values of PSC parameters used in Potyondy (2007) were adopted in the model in this paper, as summarized in Table 6.2. Although the model with these adopted parameters might not be quantitatively representative of any actual grain contacts, it is a good start point for qualitative research. The intent of this simulation work was to discover the qualitative trend of micromechanical changes of sand grain surfaces due to static fatigue.

Table 6.1. Short-term parameters used in this model of two grains in contact.

Parameter	Value
Diameter of agglomerate, D	0.6 mm
Wall stiffness	2×10^7 N/m
Sub-particle properties	
Mass density, ρ	2650 kg/m^3
Young's modulus, E_c	70 GPa
Minimum radius, R_{min}	1.5×10^{-3} mm
R_{max}/R_{min}	1.2
Friction coefficient, μ	0.5
Normal stiffness/shear stiffness	2.5
Parallel bond	
Bond radius multiplier, λ	1
Young's modulus, $\overline{E}_C$	70 GPa
Normal stiffness/shear stiffness	2.5
Mean normal strength, σ	475 MPa
Mean shear strength, τ	475 MPa
Normal and shear strength standard deviation	150 Mpa

Table 6.2. Long-term (stress-corrosion) parameters used in this model.

Parameter	Value
Threshold stress, $\overline{\sigma}_a$	70 MPa
Material damage-rate constant, β_1	5×10^{-17} m/s
Material damage-rate constant, β_2	30

Normal Compression Tests

A normal compression test was conducted on the model to determine the unconfined compressive strength of the model. The compressive strength from this test will be used in static fatigue compression tests, which is discussed in next subsection, to make sure the contact was loaded with constant normal forces smaller than the short-term maximum load. In the normal unconfined compression test, the contact was loaded by compressing the two grains with two platens, one on the top and one on the bottom, in a constant displacement rate until a peak compressive force is reached.

The displacement rate was determined through a sensitivity test that will be presented in the result section. The contact was loaded by assigning the same displacement rate to the top and bottom platens. To account for the effects of loading rates on the limit load, tests were conducted with different displacement rates of the platens, from high to low (6 m/s to 0.06 m/s), until the normal force-convergence curve barely changed as the rate further decreased. As indicated in Figure 6.5, when the loading rate decreased by an order of magnitude, from 0.6 m/s to 0.06 m/s, the stress-strain curve didn't change significantly. The long-term limit load was then determined as the load calculated with the boundaries displacement rate of 0.06 m/s, and it was found to be 33.7 N. The limit force from this test was used to select the range of forces to be used in the static-fatigue tests.
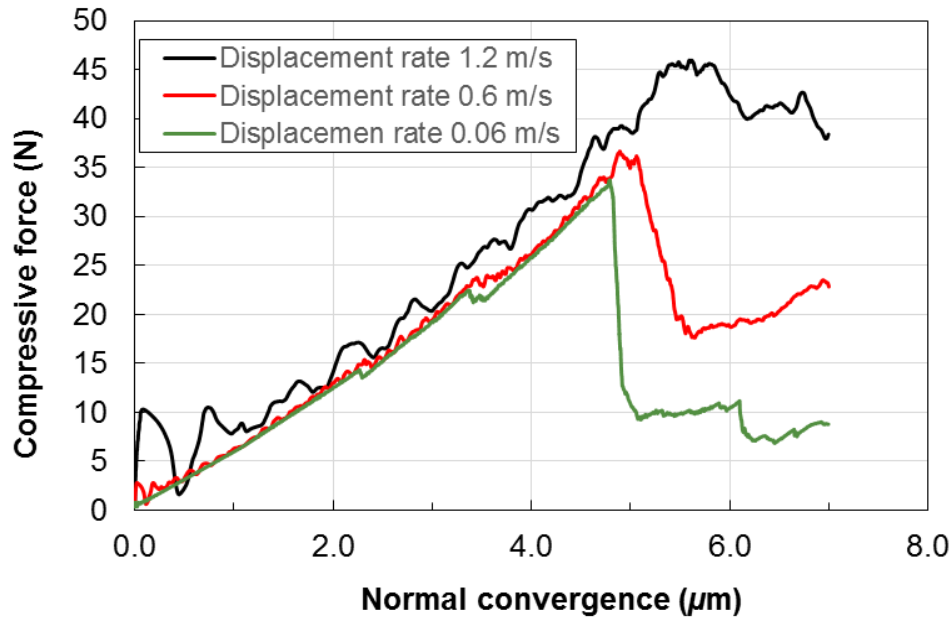
Figure 6.5. Model sensitivity to loading rates in normal loading tests.

Static Fatigue Tests

Numerical static fatigue tests were conducted on the model to study the long-term (time-dependent) behavior of the contact under constant normal forces. To simulate stress corrosion of sand grain textural features under applied load, the Parallel-Bonded Stress Corrosion model (PSC) was used to describe bonding of the sub-particles that built the two grains. The PSC model includes "parallel bonding" of particles that can transfer both forces and moments. The size of each parallel bond between sub-particles reduces under tension as a function of time. The reduction rate is governed by a damage-rate law developed from chemical rate-process theory described by Eq. (6.11) (Potyondy, 2007).

The normal force in each static-fatigue test was maintained by controlling the velocities of the top and bottom boundaries through a numerical servo-mechanism. The results from normal loading tests show that at a normal force of 15 N (slightly less than half of the long-term limit force) cracks at the contact developed immediately after loading. Immediate appearance of cracks is not desirable in static fatigue tests. Therefore, normal forces used were in the range of 13.5 to 7.5 N, every 1.5 N (i.e., a fraction of 0.9 to 0.5 of 15 N). During these tests, the micro-cracks

134

development, the normal contact force, and the relative displacement of the two grains (grain convergence) were monitored against the stress corrosion time. The simulation ending criterion for static fatigue compression tests in this paper was a final normal convergence of 6.0 µm.
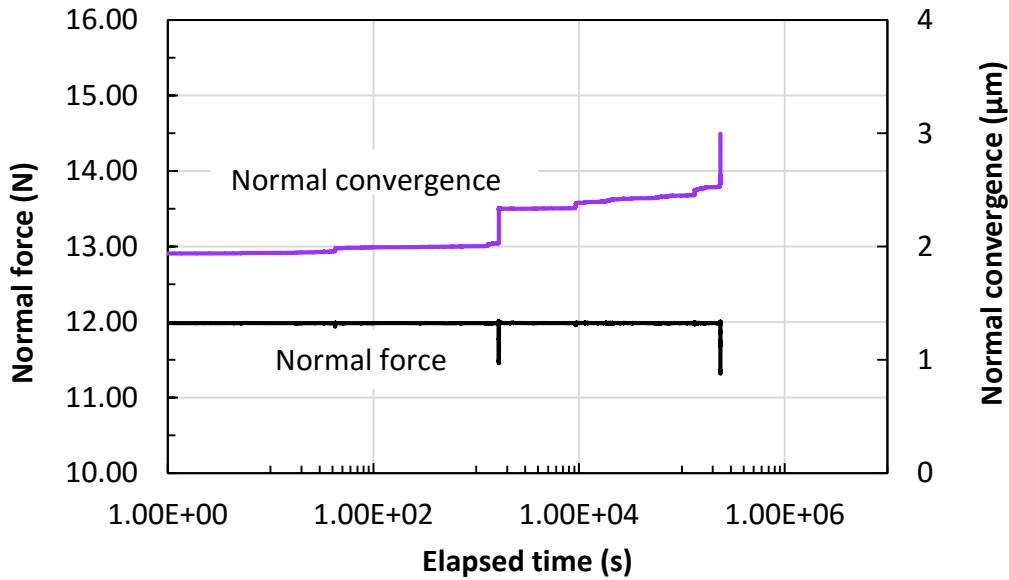
Figure 6.6. Time histories of normal force and normal convergence for the static fatigue test under 12.0 N normal force.

Results of 2D Simulations

Figure 6.6 shows normal convergence and normal force versus time from a static-fatigue test under a constant normal force of 12 N. While the normal force in the test was kept constant at 12 N, the two grains converged to each other slowly with several instantaneous increases in convergence where the normal forces experienced sudden drops but resumed immediately via servo-mechanism, before the samples finally failed of global fracturing and the normal force couldn't be held after 2.4×10^5 s (about 2.8 days). The result in Figure 6.6 shows that the model is able to mimic the process of time-dependent increase in convergence as observed in the contact-scale tests. The servo-mechanism was able to maintain the normal force constant.
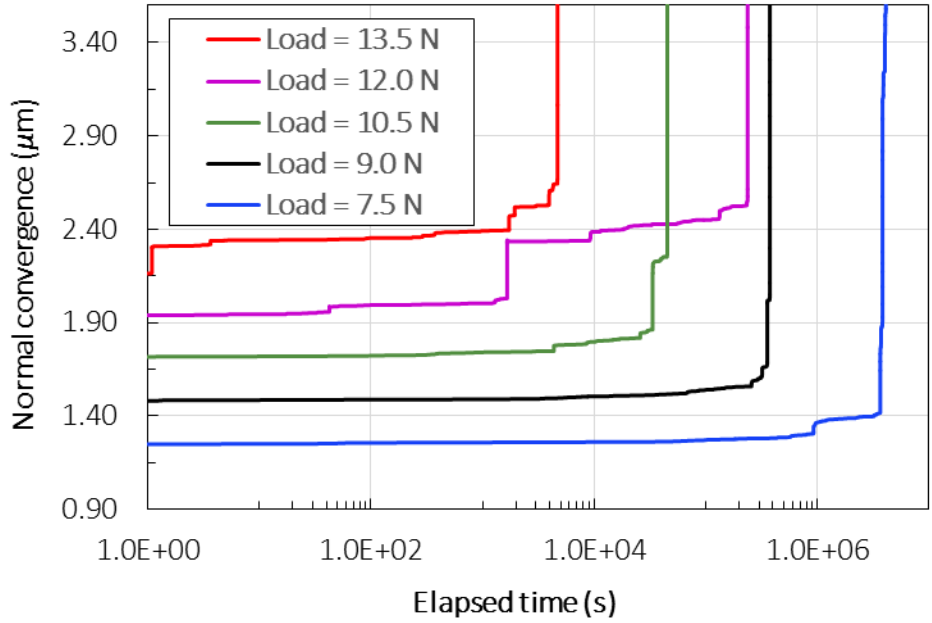
Figure 6.7. Time-dependent increase of normal convergence during static fatigue tests under different normal forces.
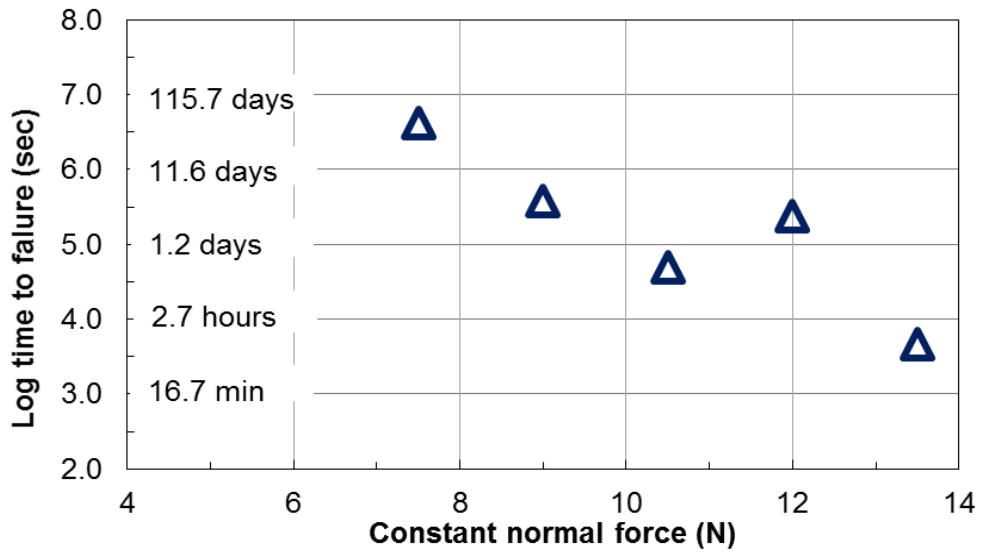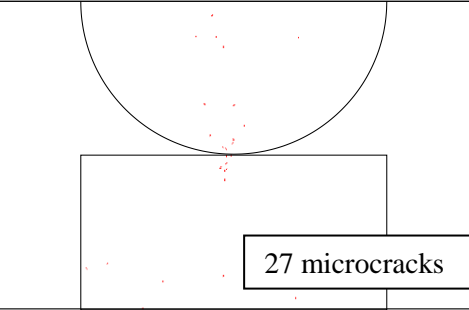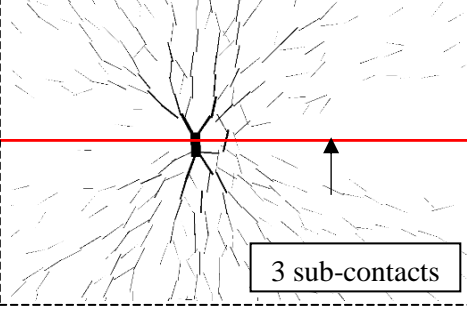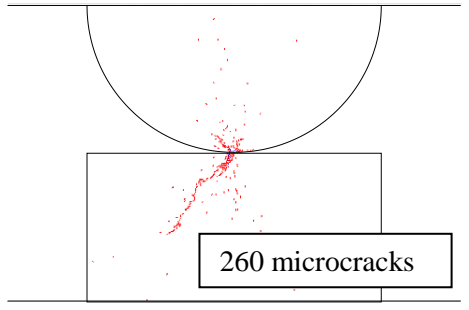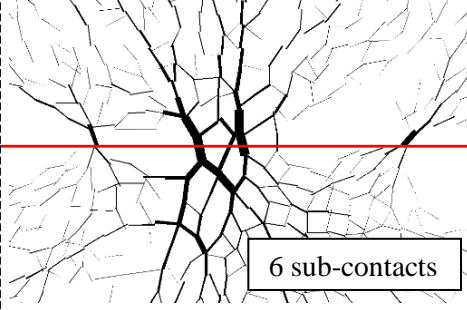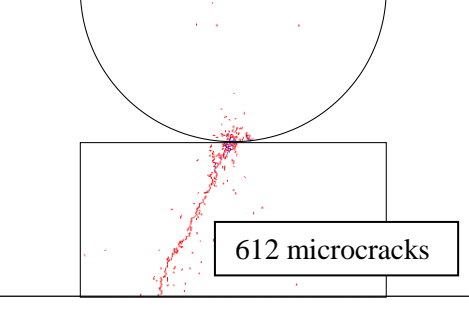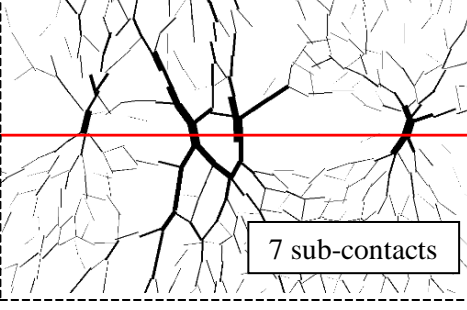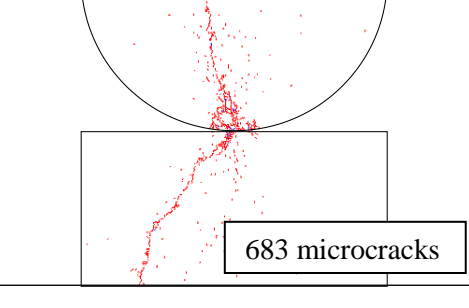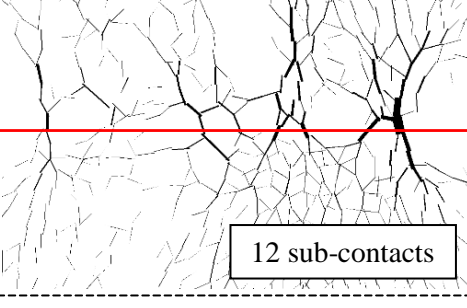
Figure 6.8. Time to failure in static fatigue tests with different normal forces.

136

Figure 6.7 shows the time-dependent increases of normal convergence under five different constant normal forces. The model of contact converged 1.2 µm to 2.2 µm right after the normal loads were applied. Larger forces generated larger immediate convergences. In all five tests, the model experienced time-dependent increases in convergence in the order of several hundreds of nanometers. After periods of slow growth in convergence, the model failed of excessive strains due to fracturing developed throughout the grain bodies, as introduced below. Figure 6.8 summarizes the durations the contact hold different normal forces before failure in static fatigue compression tests. Figure 6.7 and Figure 6.8 illustrate that the contact generally failed faster as the normal force increased, with an exception of the test under 12 N.

Another trend is the increase in number of contact points between the two grains at contact. For the same test under 12 N normal force, Table 6.3 shows the development of microcracks and the corresponding force chains in the two grains. It can be seen from Table 6.3 that under constant load, the stress corrosion microcracks increased time-dependently, first developed near grain surface at contact and then propagate into areas further from the contact, the result of which was the increase of normal convergence between the grains. Another noticeable trend from Table 6.3 was that the number of force chains across the average contact plane increased over time as a result of growing stress corrosion damages of grains surfaces near the contact. Each force chain across the average contact plane corresponds to a sub-contact between two sub-particles on surfaces of the two grains, i.e. the number of force chains across the average contact plane is equal to the number of sub-contacts and the nominal contact between two surfaces are a number of these sub-contacts carrying the load. Figure 6.9 shows clearly that under different normal forces, the number of sub-contacts increased with normal convergence which is normalized by the final normal convergence. It is needed to point out that there are much more actual sub-contacts between two sand-grain surfaces than the numbers shown in Figure 6.9, because the sizes of asperities on a sand grain surface are much smaller than the sizes of sub-particles used in this simulation. Therefore, the trend in Figure 6.9 is likely to hold and be even more obvious between real sand grains. In contact mechanics, this increase in number of contacts is very likely causing increase in contact stiffness and friction and the trend is further discussed in the Discussion section of this chapter.

Table 6.3. Time dependent evolution of microcracks and force chains near contact under a normal force of 12 N

Elapsed time	Development of microcracks	Force chains near contact plane
$t = 0$	27 microcracks	3 sub-contacts
$t = 5$ hours	260 microcracks	6 sub-contacts
$t = 2.8$ days	612 microcracks	7 sub-contacts
$t = 2.8$ days	683 microcracks	12 sub-contacts
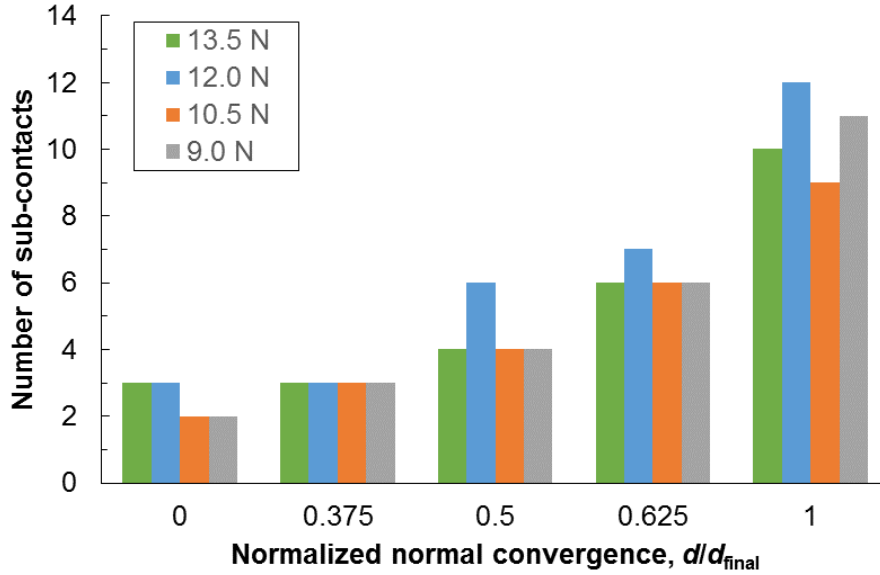
Figure 6.9. Time-depend increase in the number of contact points.

6.4. Three Dimensional Simulations

Three dimensional DEM models were desired and conducted because they are more representative of the real-world geometry of grains and contacts. Models of inter-grain contacts at two different scales were constructed: grain scale and micro-scale of a small surface region. The modeling was implemented by adopting the parallel-bonded stress corrosion model by Potyondy (2007). The first model is a half sand grain loaded against a rigid flat surface to simulate the contact maturing tests and calibrate the model with the testing results. After the model is calibrated, the parameters were used for a smaller length scale model of a contact between two surfaces with richer roughness. The smaller scale model of a contact region allows a higher resolution without using a significantly larger number of sub-particles. The richness of surface geometry of sand grains is better simulated with the higher resolution to provide more insight on the evolution of the contact during static fatigue.

(a)

- Initial assembly

(b)

- Particles refined
- Initial isotropic stress reached
- Floaters removed

(c)

- Parallel bonds installed

(d)

- Carved into semi-spherical shape
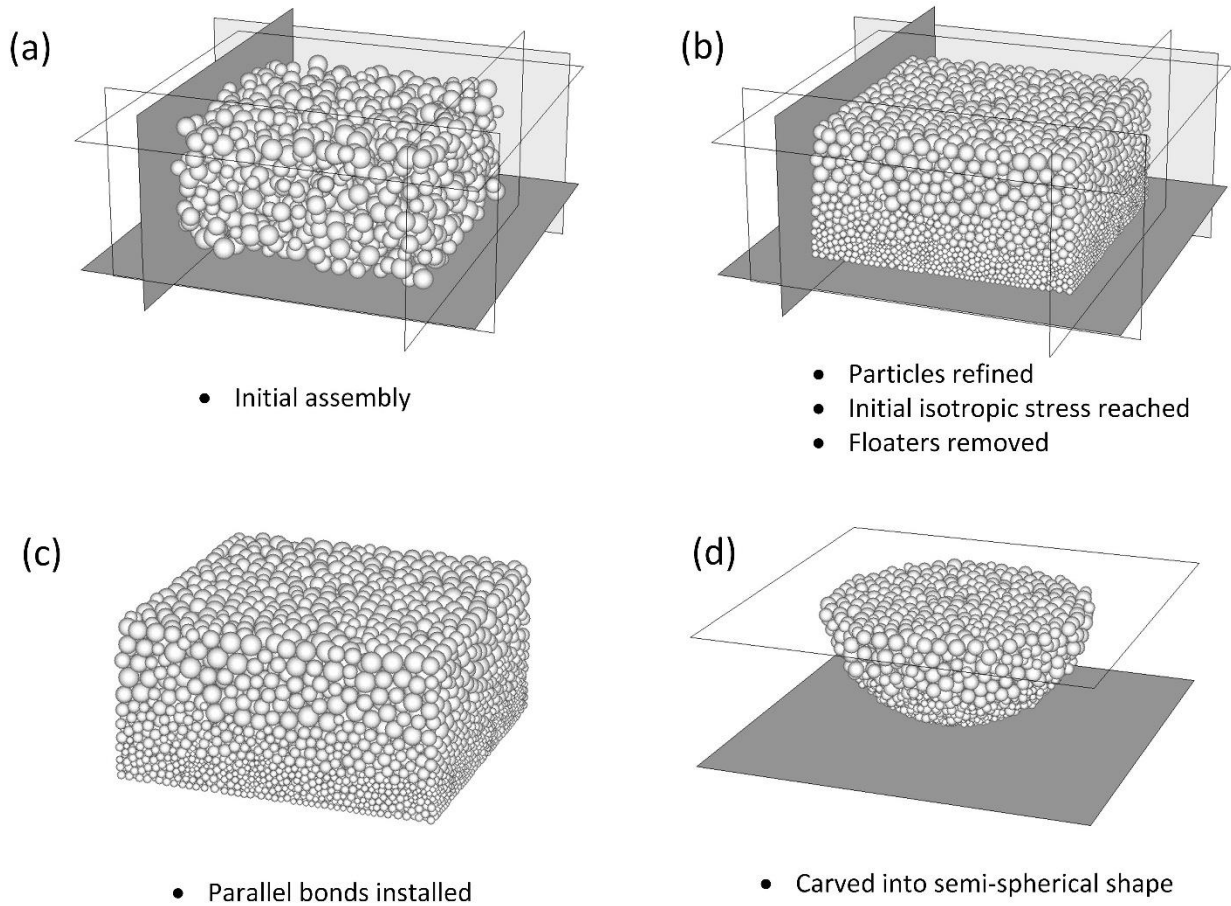
Figure 6.10. Specimen generation process: (a) initial loose packing (specimen dimensions: 800µm×800µm×400µm; total # of particles: 2,110), (b) particles in refinement regions refined, floaters removed and initial isotropic stress reached (specimen dimensions: 800µm×800µm×400µm; total # of particles: 21,641), (c) parallel bonds installed (specimen dimensions: 800µm×800µm×400µm; total # of particles: 21,641), and (d) specimen carved into desired geometry (specimen diameter: 800µm; total # of particles: 5,188).

Model Calibration: a Grain-to-Plate Contact

A three dimensional model between a half of a spherical sand grain and a nearly rigid flat surface was constructed with PFC3D. The model has the same configuration as the contact maturing tests. The sand grain-loading platen system can be treated as an ideally symmetric system along the horizontal center plane across the sand grain. For this reason, only the bottom half of the sand grain was simulated in the model for the sake of computational efficiency. The semi-spherical model of a half of a sand grain was simulated with the parallel-bonded stress corrosion model (Potyondy 2007), as introduced in the previous sections and as has been used in the two dimensional model. The model was calibrated with the result from contact maturing Test E in Chapter 4. The evolution of the contact and stress distribution in the half grain during the static fatigue process were analyzed.

Model Construction

The model construction process is shown in Figure 6.10. The model construction generally followed the 7-step process as introduced in the section of two dimensional simulations, except that one more step of particle size refining was added. An initial loose assembly was first generated in the vessel of a rectangular parallelepiped bounded by six walls, as shown in Figure 6.10(a). An additional refining step was executed between step 2 and 3, in addition to the seven steps used in the two dimensional model. The purpose of introducing the refinement regions was to improve modeling accuracy while still saving computational resources. Depending on the levels of refinement, each particle at the refinement region is replaced by n (n is the predefined refinement level) smaller particles with the same total volume as the original particle. Then the "floaters" are removed and the model is cycled while slowly reducing the particles sizes uniformly until a desired isotropic stress is reached. The model at this point is shown in Figure 6.10(b). Parallel bonds were installed in the model between particles at contact, as shown in Figure 6.10(c). The model with a shape of a rectangular parallelepiped was then carved into the desired shape, a semi-sphere in this case, as shown in Figure 6.10(d). The bottom wall then was displaced slowly towards the carved semispherical model to close the gap created during the carving process and make initial contact

141

between the bottom surface of the semi-sphere and the bottom wall. The model was then ready for the simulated contact maturing tests, as shown in Figure 6.11.
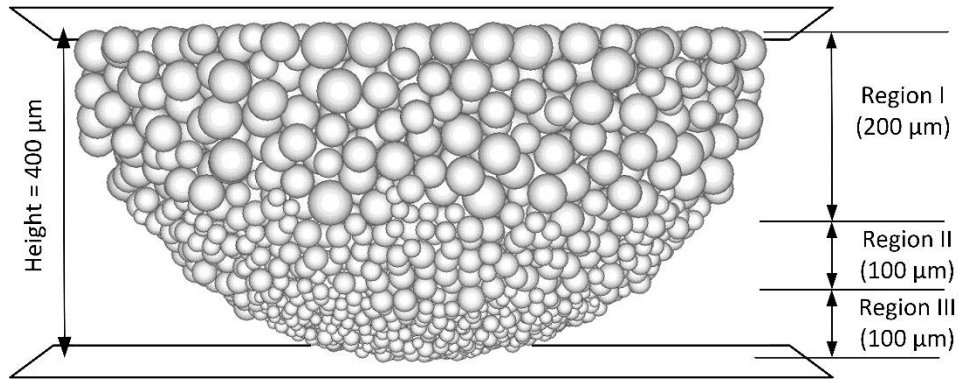
Figure 6.11. Semi-spherical DEM model of a half sand grain: grain radius 0.4 mm, 5188 sub-particles in total; average sub-particle radius: Region I: 20.4 µm; Region II: 13.3 µm; Region III: 8.57 µm.

Simulations of Contact Maturing Tests

The model went through static fatigue tests, where normal forces were exerted on the model and maintained constant through the two loading platens. The forces were maintained constant during the tests through a servo-mechanism by controlling the velocities of the two loading platens. The parallel-bonded stress corrosion model (PSC) was turned on for all the parallel bonds in the model to allow the stress corrosion bond-degradation process as mentioned in previous sections.

Model Calibration

The model was calibrated with the contact maturing test E reported in Chapter 4 with a constant normal force of 2.4 N. The calibration process was achieved by matching convergence curves from the simulation and Test E.

Results

The model was roughly calibrated with contact maturing test E. The comparison of the time-dependent increases in convergence in the model and contact maturing test E are shown in Figure 6.12. It needs to be pointed out that because only half of a sand grain is simulated in the model, the increase in convergence from Test E in Fig. 6.10 was divided by two by assuming the sand grain is symmetric along the middle horizontal plane. The calibrated parameters are reported in Table 6.4.
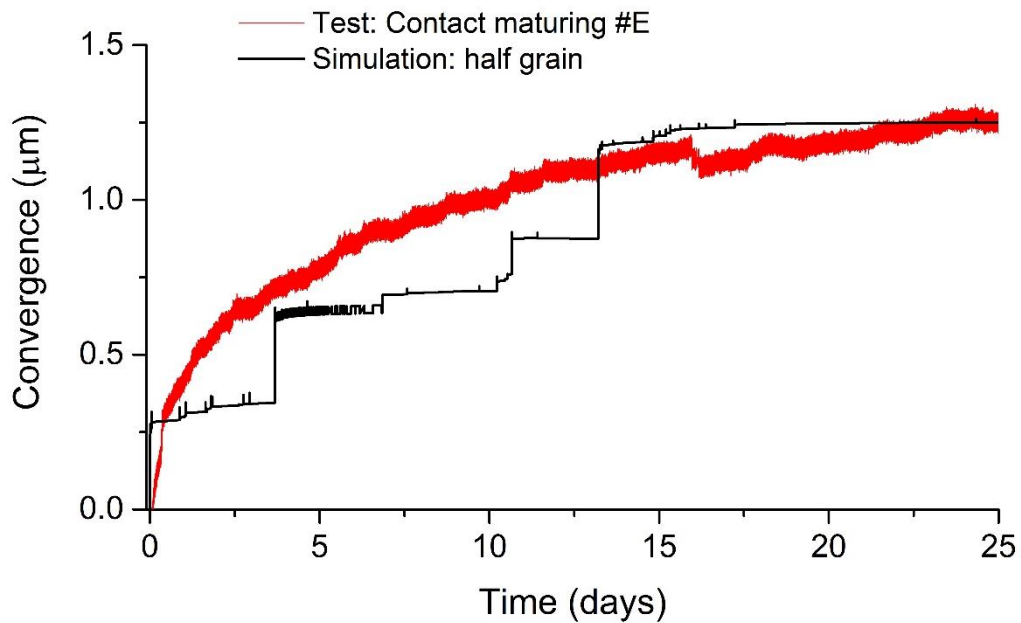
Figure 6.12. Model calibration with contact maturing Test E.

Table 6.4. The calibrated parameters in the 3D half-grain model

Parameter	Value
Diameter of agglomerate, D	0.8 mm
Wall stiffness	2×10^7 N/m
Refinement levels	
Region I	1
Region II	3
Region III	5
Sub-particle properties	
Mass density, ρ	4109 kg/m^3
Young's modulus, E_c	75 GPa
Minimum radius, R_{min}	20 µm*
R_{max}/R_{min}	1.66
Friction coefficient, μ	0.5
Normal stiffness/shear stiffness	2.5
Parallel bond	
Bond radius multiplier, λ	1
Young's modulus, $\overline{E}_C$	75 GPa
Mean normal strength, σ	300 MPa
Mean shear strength, τ	300 MPa
Normal and shear strength standard deviation	90 Mpa
PSC model parameters	
Threshold stress, $\overline{\sigma}_a$	7 MPa
Material damage-rate constant, β_1	6.4×10^{-19} m/s
Material damage-rate constant, β_2	30

Note: *This is the minimum particle radius before the refining process; for actual particle sizes after refining, please refer to Figure 6.11.

The model could only be roughly calibrated because even after refining, the particles at the contact area are still very coarse. A result of the coarse particle sizes is that the increase of convergence of the model consist of several abrupt increases rather than increasing smoothly as the test, as shown in Figure 6.12.
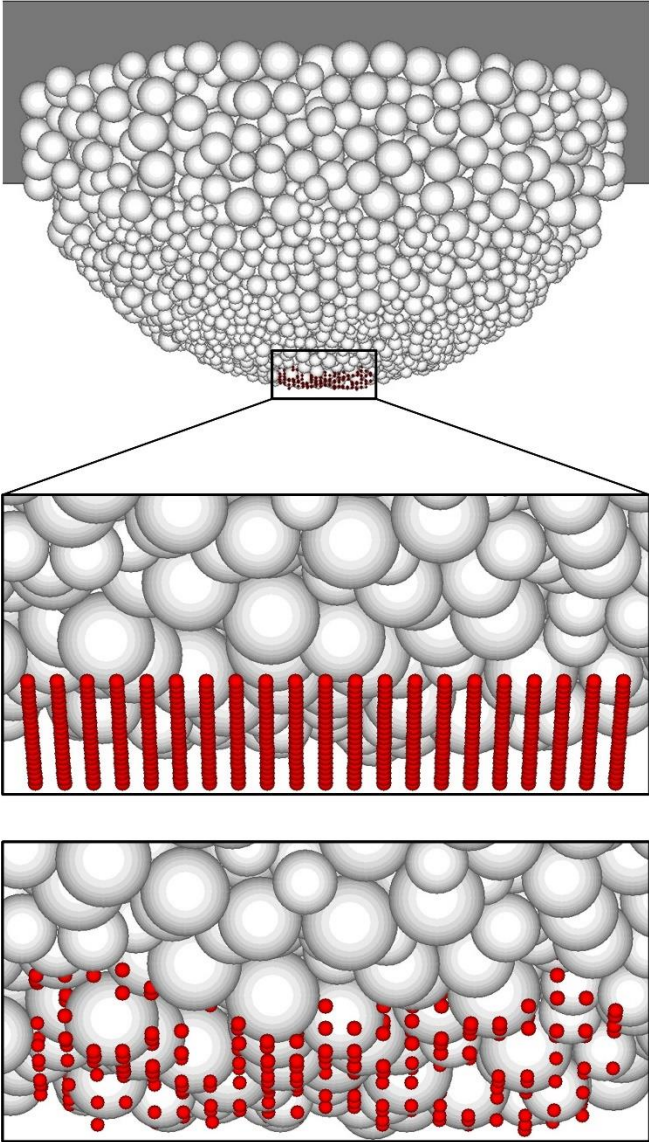
Figure 6.13. Measure surface topography of the model with "numerical profilometer".
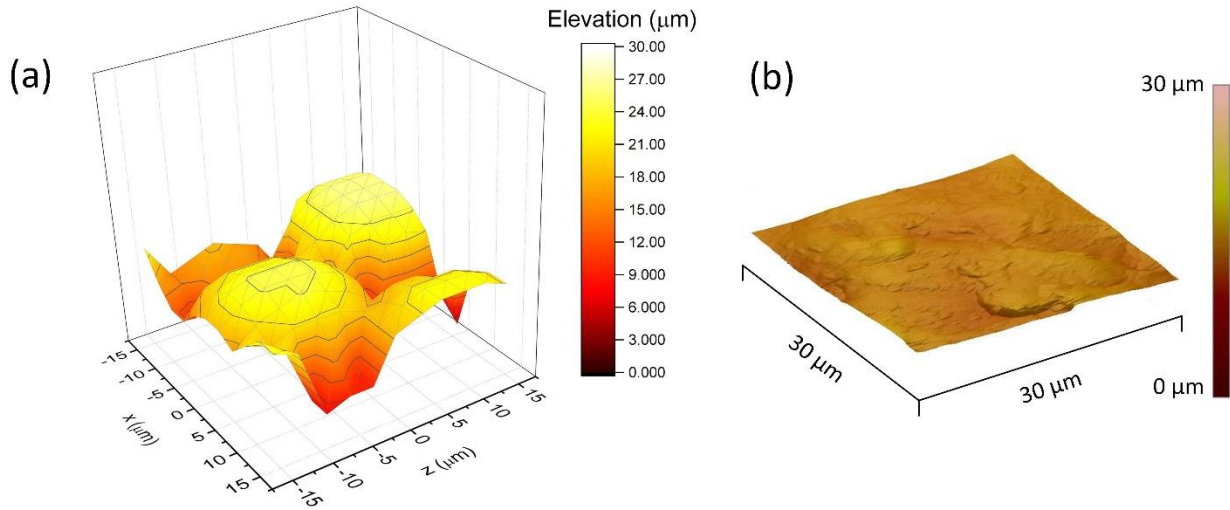
Figure 6.14. Surface topography of the model and real a sand grain: (a) a 30µm×30µm area on surface of the half-grain DEM model, and (b) a 30µm×30µm area on surface of the sand grain in contact maturing Test #E.

To quantitatively measure the topography of the surface at the contact area of the model, a program was written in FISH (the programming language of PFC codes) to carry out numerical profilometry on the surfaces of the model. The mechanism of the profilometer is shown in Figure 6.13. A layer of small particles as profilometry probes are generated a certain distance away from the surface to be measured. Then the "probes" are actuated vertically upwards until touching the surface of model (criterion of touching is a small predefined contact force is reached between the probes and the surface). The positions of the "probes" are used to generate a three dimensional topography of the measured surface. A 3D topography of a 30µm×30µm area measured by this numerical profilometer is shown in Figure 6.14(a) and the 3D topography of a 30µm×30µm area from AFM measurement of the grain in contact maturing test E is shown in Figure 6.14(b). The comparison between the surface of the model and a real sand grain verifies the previous argument that the particles at contact area are much coarser than what is needed to represent the surfaces of sand grains accurately. The comparison in Figure 6.14 also gives an explanation to the steps in increase of convergence in the model.
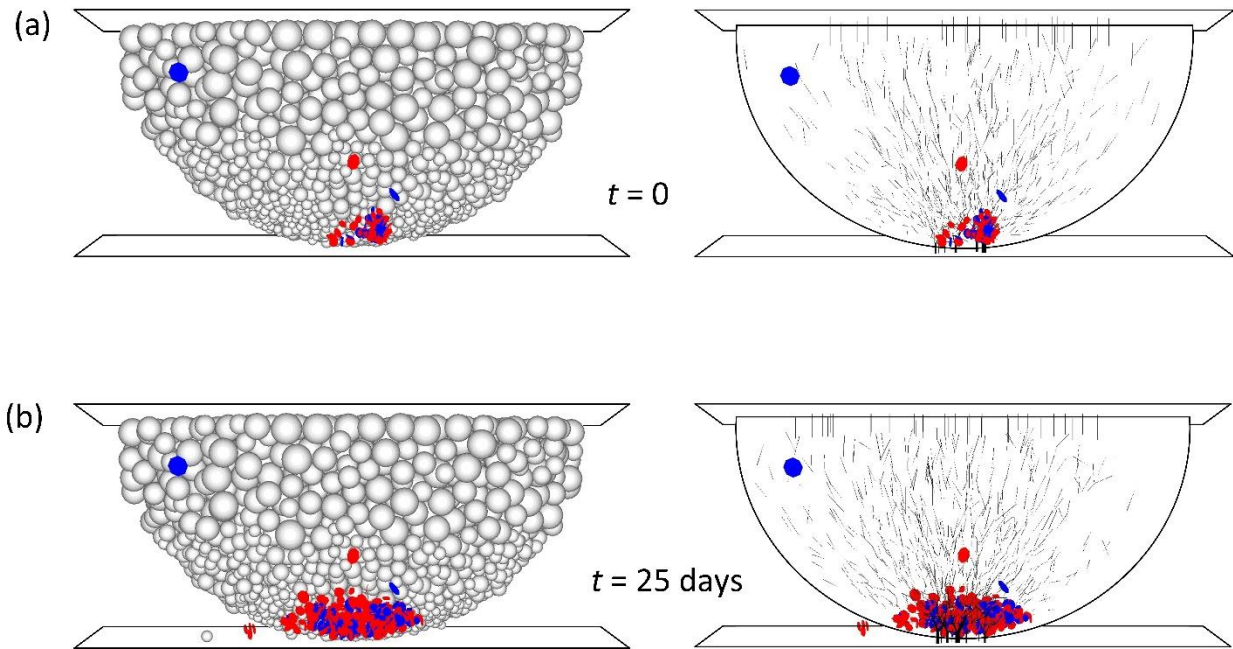
Figure 6.15. Time-dependent fracturing and evolution of force chains: (a) immediately after application of a normal force of 2.4 N, time-dependent convergence 0, number of micro-cracks 95, number of force chains across contact area 6, and (b) 25 days after constant load of 2.4 N, time-dependent convergence 1.25 µm, number of micro-cracks 496, number of force chains across contact area 10.

Snapshots of development of cracks and force chains in the half-grain model under a constant normal force of 2.4 N are shown in Figure 6.15. During the simulated 25-day period, the number of cracks increased four-fold near the contact area, from 95 to 496. Different from the simulation results from the two dimensional simulations, cracks cumulated around the contact area rather than growing across the whole semi-spherical model. This difference is probably due to the three dimensional geometry of the model. The area sustaining the normal force increases more significantly in two dimensions with the distance away from the contact comparing to the 2D model where the area only increases in one dimension. Thus, in the 3D model, stress drops faster with the distance from the contact than in the 2D model, making it hard for the cracks to grow in regions far from the contact.
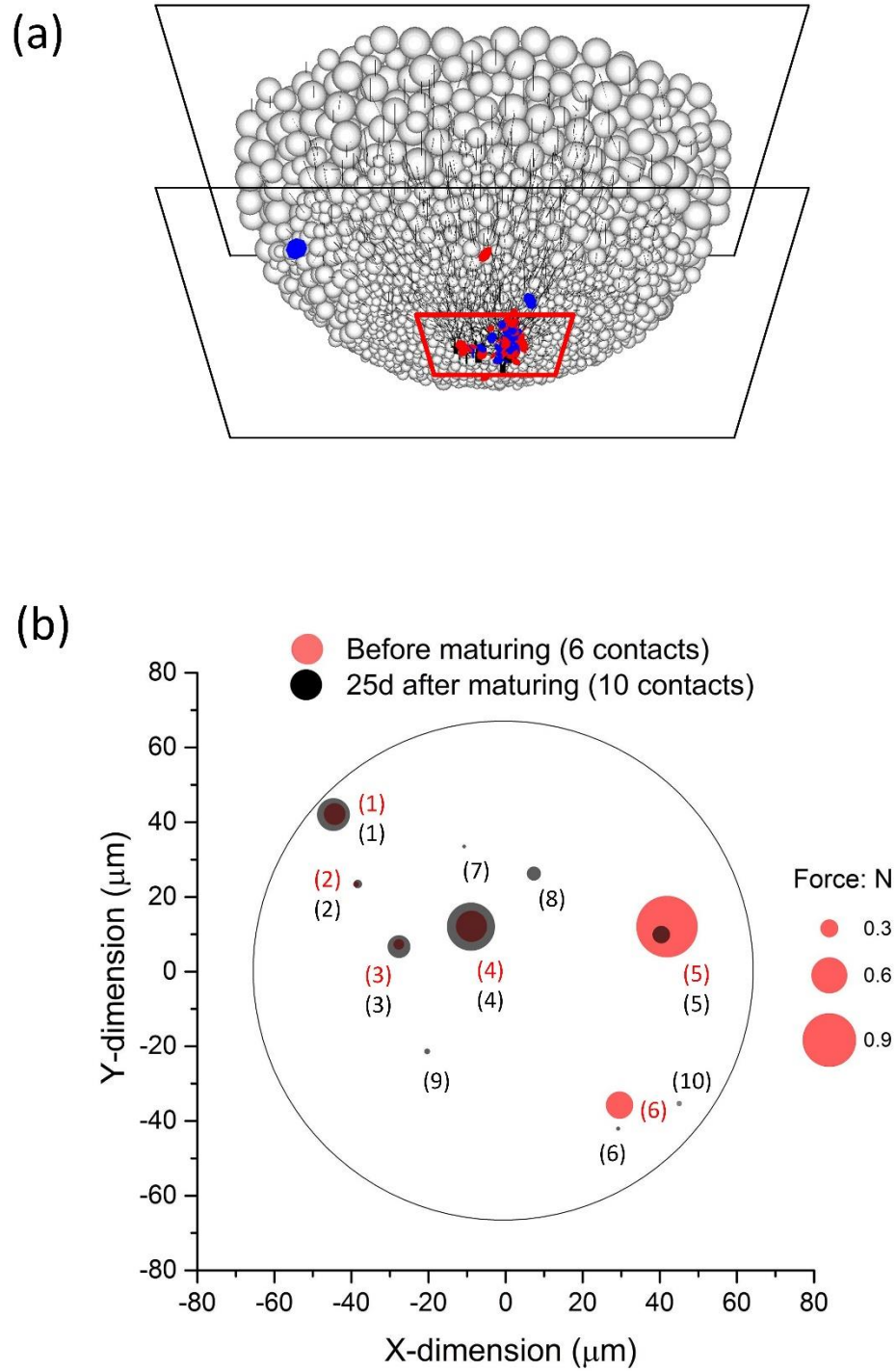
Figure 6.16. Increase in number of contact points during static fagiue: (a) the model, and (b) distributions and magnitudes of contact forces in a 120µm-diameter area before and after contact maturing.

Figure 6.17. Distribution of vertical stress in the half grain model under a normal force of 2.4 N: (a) all range color map, and (b) rescaled color map.
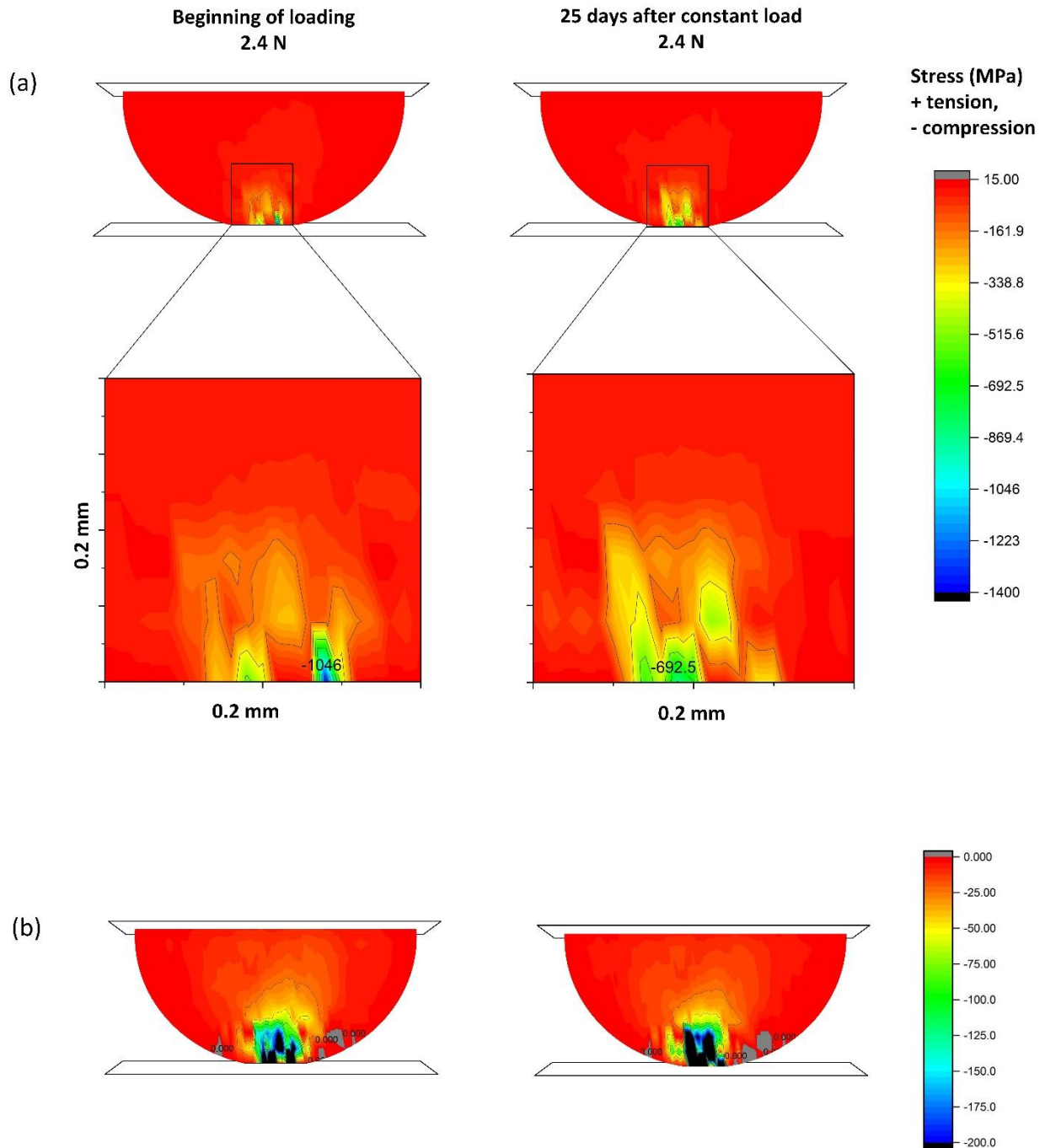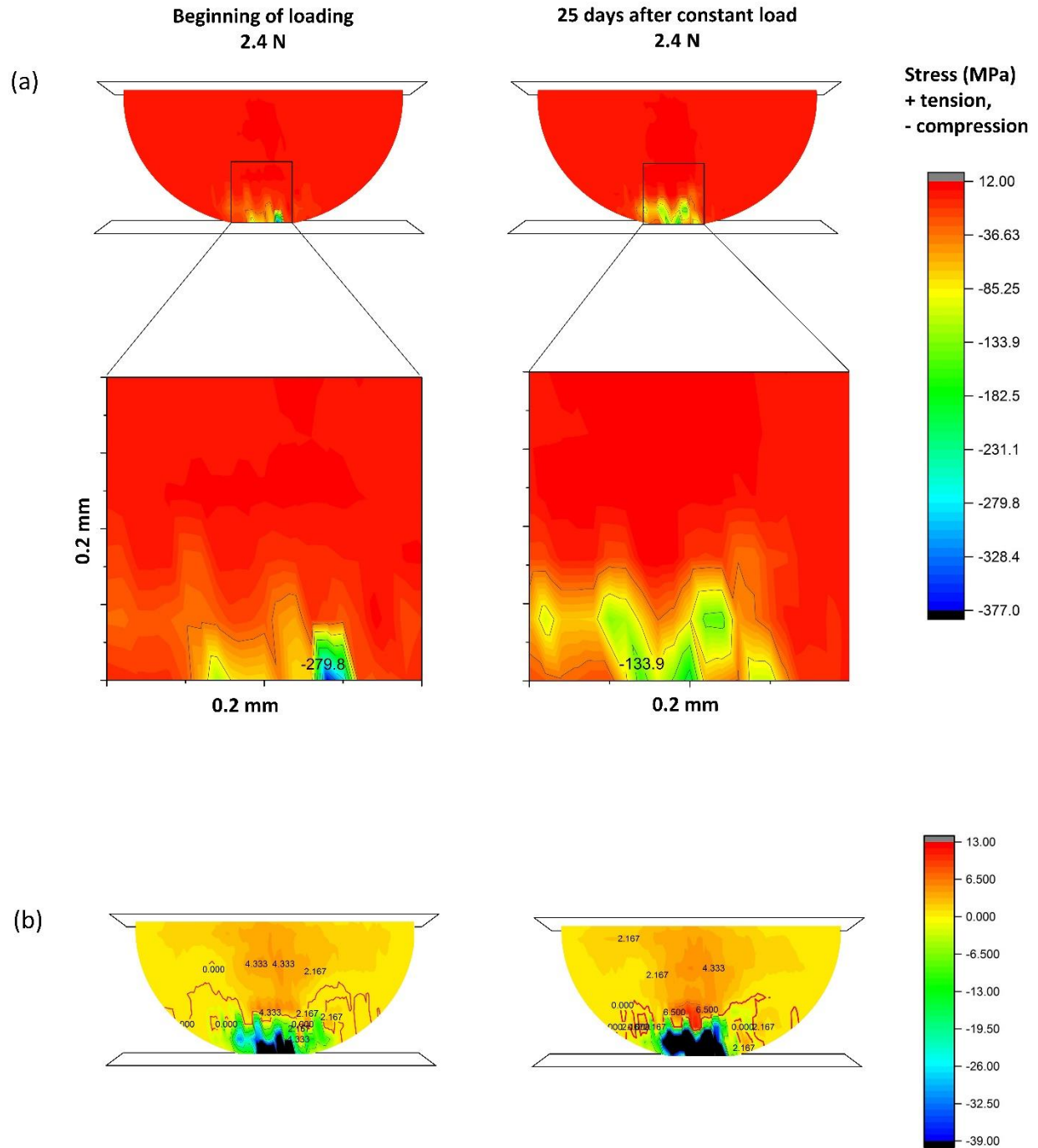
Horizontal stress contour

Figure 6.18. Distribution of horizontal stress in the half grain model under a normal force of 2.4 N: (a) all range color map, and (b) rescaled color map.

The number of force chains running across the contact area rose from 6 immediately after application of the normal force to 10 after 25 days, as shown in Figure 6.15(b) and Figure 6.16. Figure 6.16(b) shows a detailed distribution and magnitudes of the contact forces across the contact region before and after 25-day contact maturing process. The magnitudes of the contact forces (sizes of the bubbles in the Figure 6.16(b)) became more uniform after the contact maturing process. This trend indicates that more material gets involved in the load transfer process and possible consequences of this trend are increases in stiffness and friction of the contact. More detailed discussion about the micromechanical evolution of inter-grain contacts during contact maturing is elaborated in the following Discussion section.

The stress distributions in the model are measured by a network of measuring circles. The distributions of vertical stresses and horizontal stresses in the model are shown in Figure 6.17 and Figure 6.18, respectively. As shown in Figure 6.17, tremendous concentrations of vertical stresses are present at the contact region, with the stresses (700 to 1050 MPa) at the contact region 70 to 100 times that of the average stress in the area further away from the contact (~10 MPa). This explains why fracturing cumulates in the contact region, as shown in Figure 6.15. As shown in the close-up view of stress distribution near the contact in Figure 6.17(a), during the contact maturing process, the extreme concentrated stress dropped from 1050 MPa by 30% to 700 MPa. Also, stresses larger than 150 MPa distributed over a larger region after maturing. However, stress distribution in area with smaller stresses and further away from the contact did not change much, as shown in Figure 6.17(b).

The horizontal stress distribution evolves in a similar trend with the vertical stress distribution with some distinct characteristics. Overall, compressive horizontal stresses are about 1/3 of vertical stress and the majority of the region far from the contact is in tension. Similar to the vertical stress distribution, there is large stress concentration in the contact region and the most significant changes happen in this region over time. The maximum compression dropped by about 50% from 280 MPa to 134 MPa and the compressive stresses larger than 40 MPa spread over a larger area during maturing, as shown in Figure 6.18(a). Figure 6.18(b) shows a rescaled distribution to show more details in the area further from the contact. Lightly increase in tensile stress can be noticed along the vertical centerline over time.

These trends in stress concentrations explain why static fatigue fractures cumulate primarily in the contact region as observed in the simulations. These trends also indicate that geometry of the contact plays a crucial role in the stress concentration, thus static fatigue and time-dependent deformation of the contact region. This helps explain the dominant role of surface roughness on static fatigue convergence, as observed in the contact maturing tests in Chapter 4. The stress distributions also show relief of stress concentration near the contact during contact maturing. These trends support the static fatigue hypothesis.

Simulations of a Contact Between Two Grains

Model Construction

A 3D DEM model of a contact between two grains were constructed, with the calibrated parameters in Table 6.4. Two identical half spherical grains were generated, symmetric about the middle horizontal plane. Each of them were constructed with the same parameters and sub-particle size distribution. The model consists of a total number of 10775 sub-particles. A constant vertical force of 2.4 N was applied and maintained.

Results

The outcomes of the simulation are shown in Figure 6.19, Figure 6.20 and Figure 6.21. Developments of static fatigue cracking and contact forces across the contact area are shown in Figure 6.19(a) and Figure 6.19(b). Substantial growth in microcracks occurred on the surfaces of the two grains in vicinity of the contact area, from 78 at the beginning of the maturing process to 968 after 25 days. The number of contact points between the two grains increased from 5 immediately after application of the load to 25 after 25 days of maturing. Figure 6.19(c) shows the increases in convergence of the simulation with two grains and the calibration simulation with one grain against a flat surface. A higher rate of increase in convergence (8.7 µm in 25 days) was observed in the model with two grains than that with one grain (1.25 µm in 25 days). This difference in increase rate is not surprising as both of two surfaces in contact are subject to static fatigue in a contact with two grains, while only one could fatigue in the model with one grain.

Also, the stress field in the region of a contact between two rough grain surfaces is more complex, probably with more tensile components accelerating static fatigue cracking.

Figure 6.20 shows the magnitudes and distributions of the contact forces across the across the contact area. As illustrated by Figure 6.20, only 5 contact points were transferring the 2.4 N normal load between the two grains in contrast to 25 contact points after 25-day maturing. The average magnitudes of the contact forces decreased as more contact points getting involved in transferring the contact load during maturing. As discussed before, the increase in contact points is likely to lead to an increase in stiffness of the contact, eventually an increase in stiffness of a sand grain assembly.

Figure 6.21 shows the magnitudes and orientations, with respect to the horizontal plane, of the contacts forces between the two grains in contact. The magnitudes of the contact forces became more uniform after 25 days of maturing under a 2.4-N normal load, as also illustrated in Figure 6.20. Another important trend is that the orientations of the contact forces distributed more isotropically after maturing of 25 days, while most contact forces were nearly vertical. In the beginning of the maturing process, all the 5 contact forces were more than 65˚ with respect to the horizontal orientation, but after 25 days, the 25 forces widely spread in the range of 0˚ to 90˚. The author thinks that this more isotropic distribution in orientations of contact forces is an indication of increased interlocking and frictional resistance between the two surfaces in contact. Thus, maturing of a contact may result in increase in its frictional resistance.

Table 6.5. Summary of simulation results from the models of a grain-to-plate contact and a two-grain contact

Model	Increase in convergence	Increase in microcracks (percentage increase)	Increase in contact points (percentage increase)
Grain-to-plate contact	1.25 µm	401 (422%)	4 (66.7%)
Two-grain contact	8.75 µm	890 (1140%)	20 (400%)
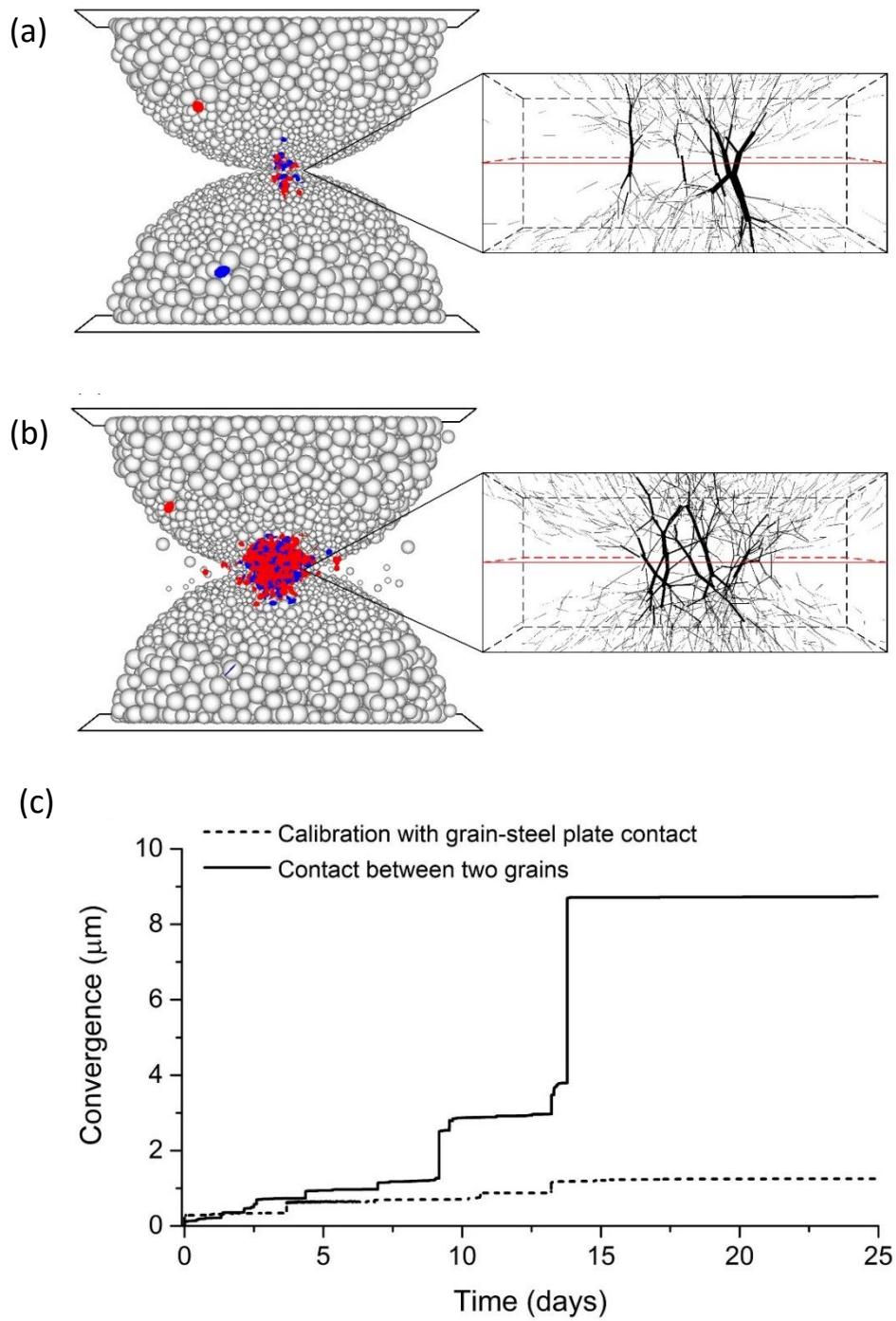
Figure 6.19. 3D DEM modeling of two half grains, 10,775 sub-particles: (a) immediately after application of a normal force of 2.4 N, time-dependent convergence 0, number of micro-cracks 78, number of force chains across contact area 5, and (b) 25 days after constant load of 2.4 N, time-dependent convergence 8.7 µm, number of micro-cracks 968, number of force chains across contact area 25.

154
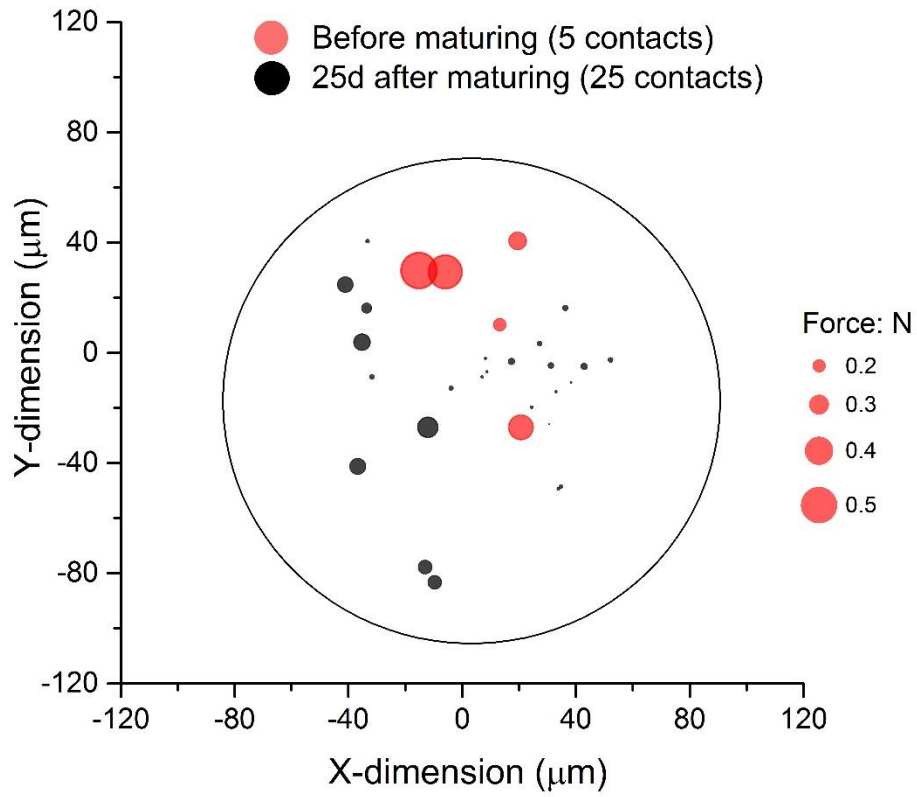
Figure 6.20. Increase in number of contact points during maturing of a contact between two grains.
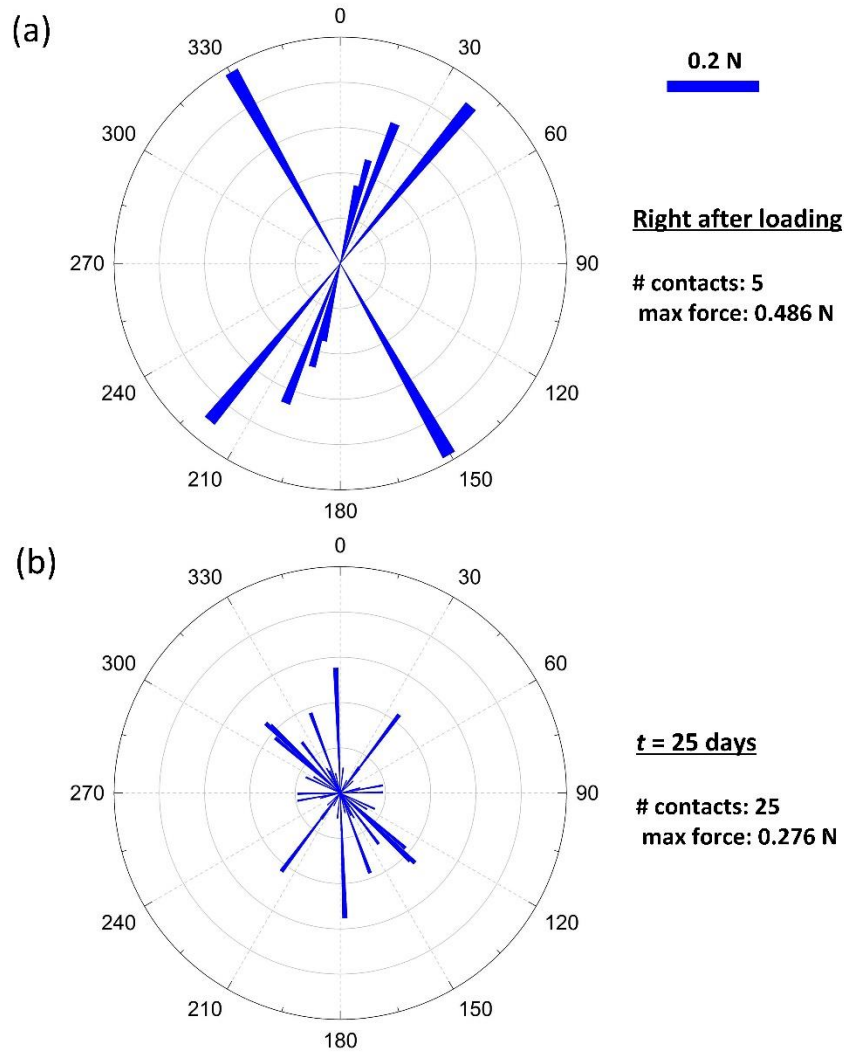
Figure 6.21. Orientations and magnitudes of contact forces at a contact between two grains: (a) before aging, and (b) 25 days after aging.

Model of a Small Grain-to-Grain Contact Region

Model Construction

As discussed above, the resolution of the half-grain model is not high enough to represent the roughness of sand grains, a model with a higher resolution to include the rich roughness of sand grain surfaces was constructed. Because of computational intensity, only small regions in the immediate proximity to the contact of two grains were simulated. An inference was made that the size of the active contact region between two grains would be of the same order as a contact between two elastic spheres; Hertz theory (Johnson 1985) was used to estimate the contact size (about 40 µm in diameter for grains of radius 0.4 mm, Young's modulus for quartz 72 GPa, and Poisson's ratio 0.17). The model constructed included a slightly smaller region of two grains in contact, both having a size of 30µ×30µm in the plane parallel to the contact and they were 15 µm in depth, Figure 6.22. One can distinguish stresses at three different spatial scales in regard to sand: (a) average stress in the sand deposit considered as continuum, (b) average stress in individual grains, and (c) stress at the contact region. The stress boundary conditions on the blocks in Figure 6.22 were estimated from the stresses measured in the simulation illustrated in Figure 6.11 and its stress distributions shown in Figure 6.17 and Figure 6.18. As discussed in previous parts, the stress distributions at the contact region was complicated and changed dramatically during contact maturing. Thus stresses deeper into the core which were relatively constant were selected. The horizontal confining stress on these blocks was determined to be 1.16 MPa and the vertical average stress on the upper boundary of the upper region and the lower boundary of the lower region was 12.70 MPa. These average stresses were maintained during the simulation through a numerical servo-mechanism, whereas the observation of the transmission of the load across the contact between the two blocks was the purpose of the simulation.

In order to model a realistic contact, the transmission surfaces of the lower and upper regions (contact area) were randomly generated with the goal of matching the true contact characteristics measured by atomic force microscopy and illustrated. The Diamond-Square

Algorithm (Kaya 2013, Voss 1985) was used to generate the two surfaces in Figure 6.23(a) and Figure 6.23(b) that match the roughness characteristics of the AFM measurement of a Ottawa sand grain in Figure 6.23(c). The number of iterations used to generate the surface was 6, Hurst roughness exponent H = 0.2, and the elevations were scaled to match the mean elevation in AFM measurements. The comparison of the elevation distribution from the measurements and that numerically generated is illustrated in Figure 6.23(d). The contact in the distinct element model was generated by carving the surfaces to approximately match the two that were randomly generated. To ensure a reasonable approximation, the average particle size in the model was chosen to be comparable to the size of square elements of the numerically generated surfaces.
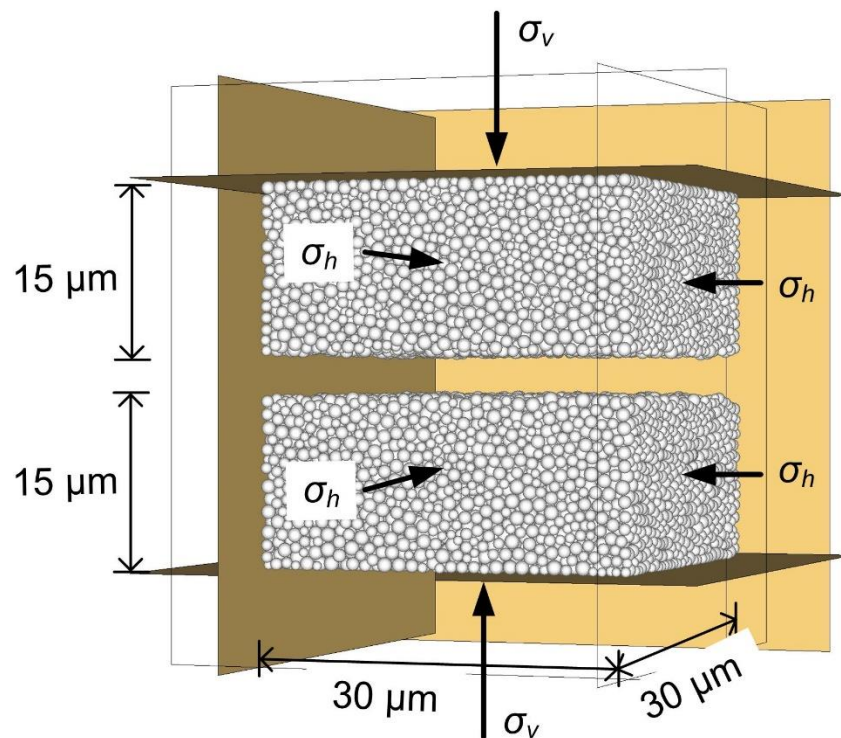
Figure 6.22. Simulated contact regions of size 30 x 30 x 15 µm in upper and lower grains; 7731 sub-particles in each region, with an average radius of 0.80 µm; constant boundary load: horizontal (confining) average stress 1.16 MPa and vertical average stress 12.70 MPa.
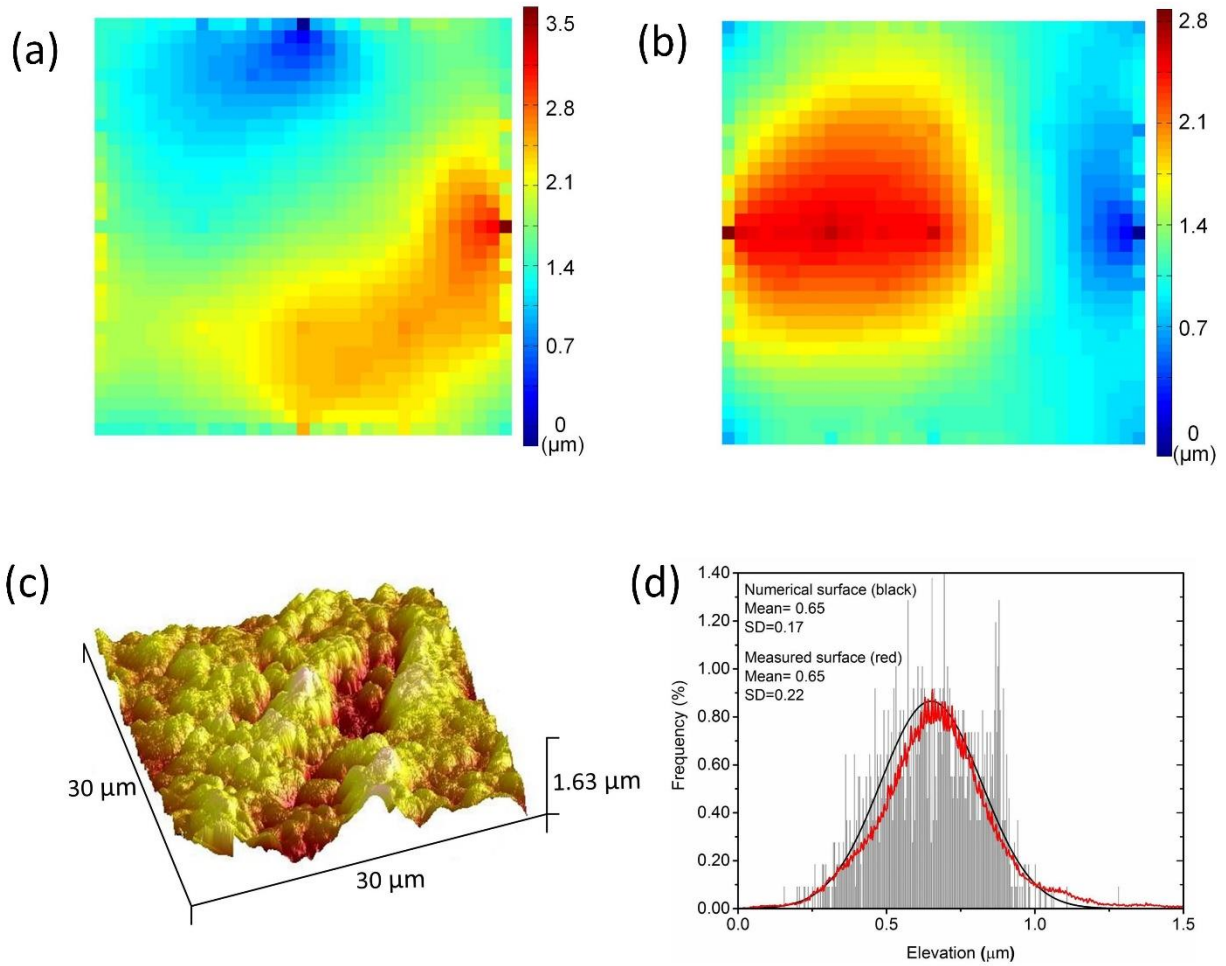
Figure 6.23. Two numerically generated fractal surfaces with Diamond Square Algorithm: (a) and (b), iteration # = 6, resolution = 33×33, h = 0.2, (c) AFM measurement of a 30µm×30µm area on surface of an Ottawa sand grain, and (d) comparison of elevation distributions of the measured surface and the numerical surfaces.
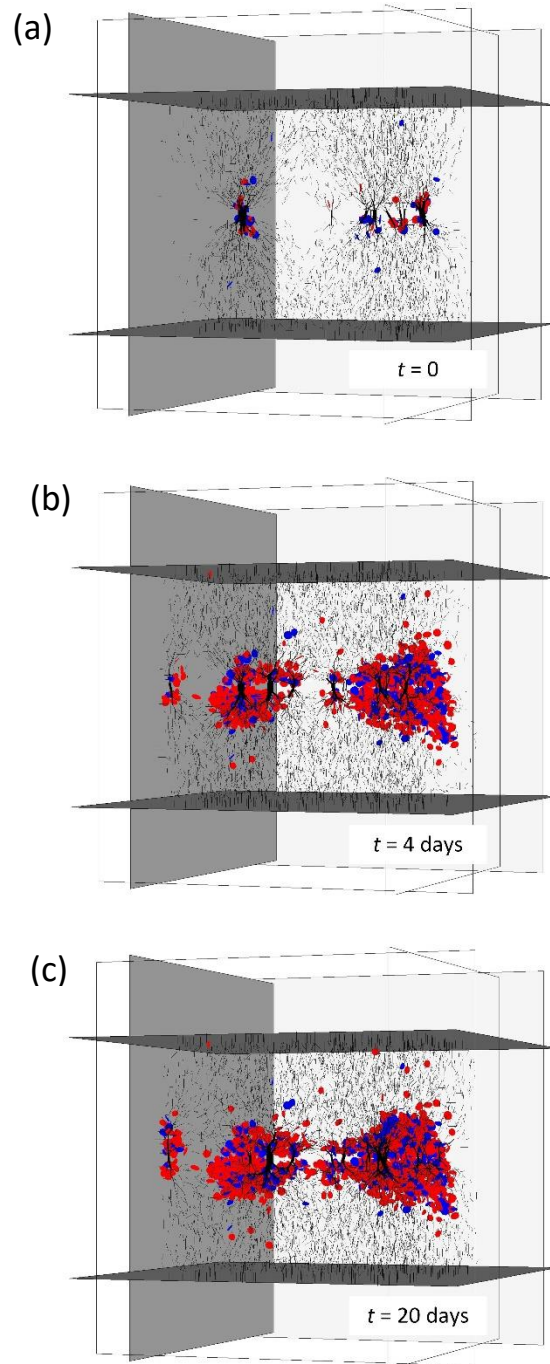
Figure 6.24. Inter-granular contact simulation: force chains and crack locations, particle contours removed for clarity; (a) time t = 0 immediately after load application, 0 convergence, 10 contact points, and 88 cracks, (b) t = 17 hours, convergence 0.24 μm, 18 contact points, and 1804 cracks, and (c) t = 20 days, convergence 0.27 μm, 31 contact points, and 2670 cracks.
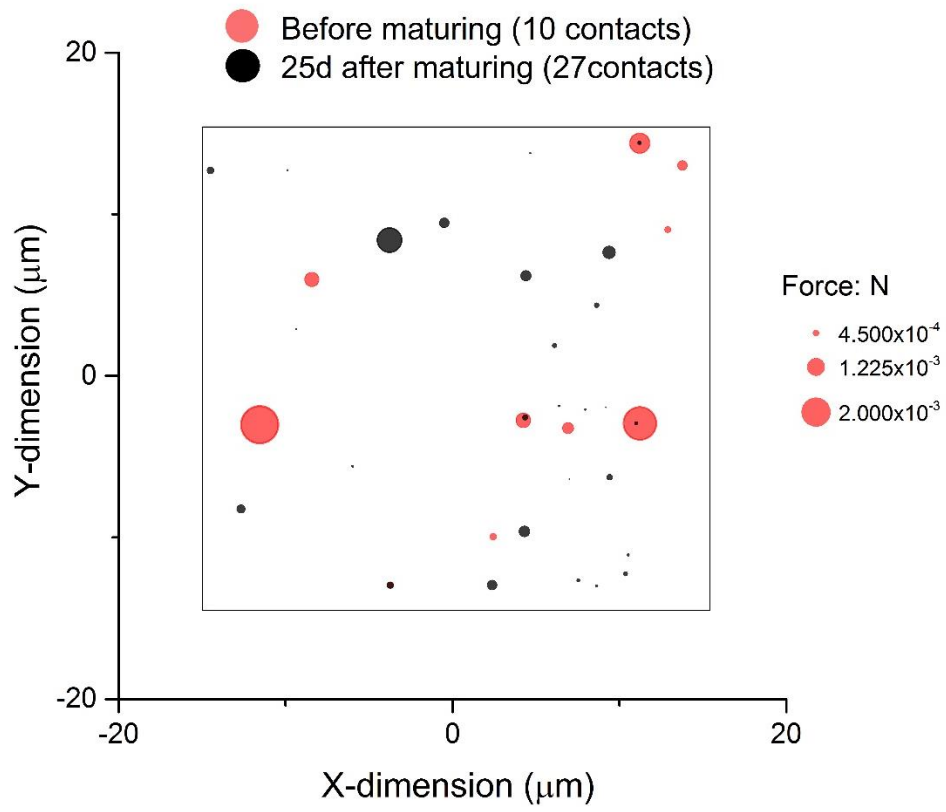
Figure 6.25. Contact points and contact forces of the contact region model before and after aging.
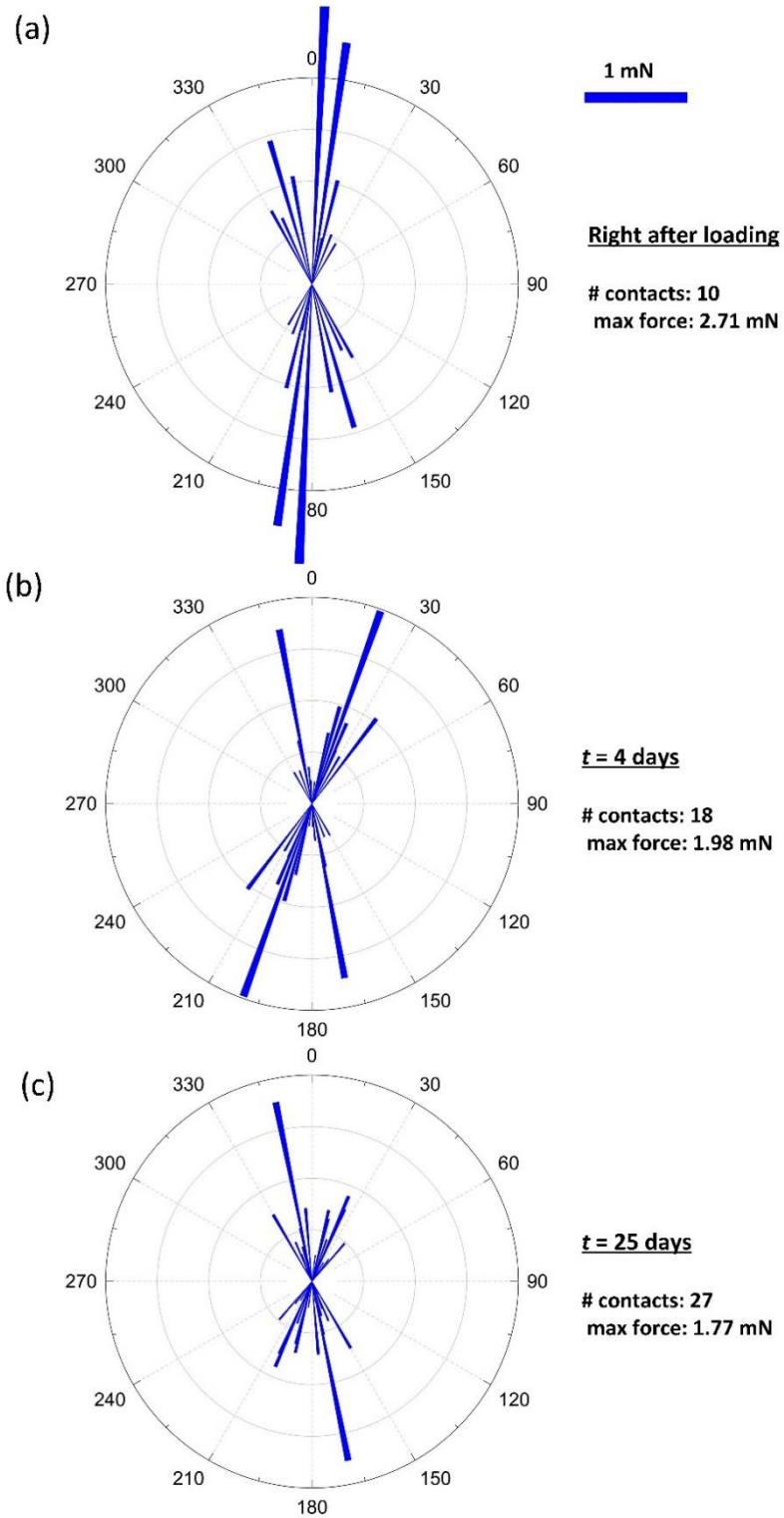
Figure 6.26. Orientations and magnitudes of contact forces of the contact region model: (a) before aging, (b) aging for 4 days, and (c) 25 days after aging.
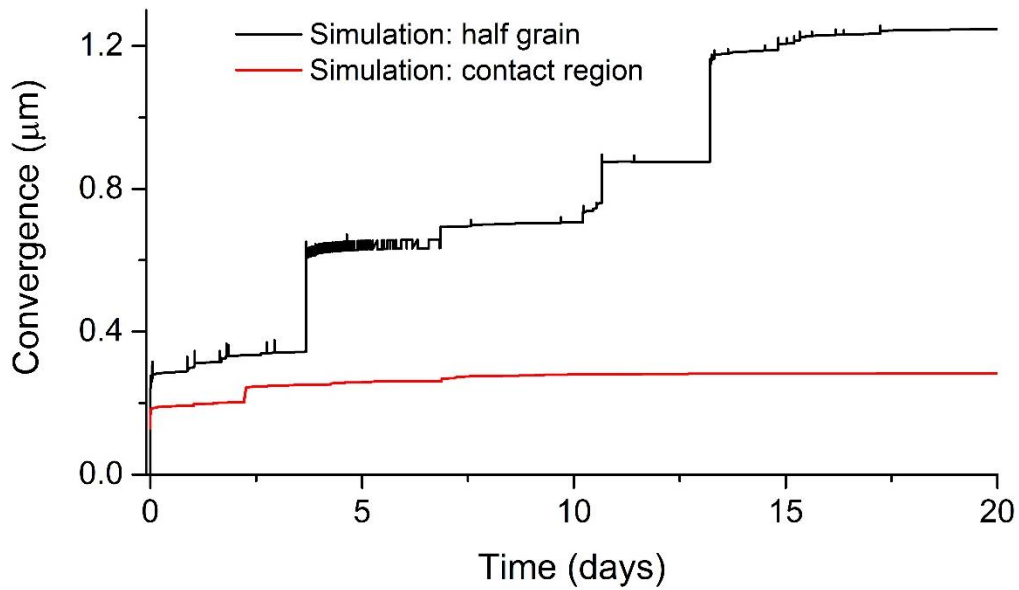
Figure 6.27. Increases in convergence over time of the half grain model and the contact region model.

Results

The results of the simulation are presented in Figure 6.24 to Figure 6.27. The graphs in Figure 6.24 show the force chains and the fractures occurring in time (red due to tension and blue particle debonding by shear). Very weak force chains are not shown giving an impression that some force chains terminate without reaction. The contours of the particles are not shown to preserve clarity of force chains. The three graphs in Figure 6.24 show the distribution of cracks and contact forces immediately after the load was applied, 17 hours later, and after 20 days. At time $t = 0$, there are only 10 force chains intersecting the contact, i.e., the entire load is transferred from grain to grain through only ten points on the contact area. Also, there are relatively few (88) fractures at this stage, demonstrated by the small discs within the blocks simulated. The number of fractures increases twenty-fold after 4 days (1804), and there are now 18 contact "points" through which the load is transferred from one grain to the other. The two blocks came closer together (they converged) by 0.24 µm. 20 days after load application, the convergence reached 0.27 µm, the number of force chains crossing the contact reached 31, and the number of fractures increased to

2670. The process has a decaying characteristic, there have been more fractures occurring in the first 17 hours than in the next 19 days.

The main purpose of the simulations with this model was to demonstrate the evolution of an inter-grain contact between two rough grain surfaces. Thus, the focus of these simulations was to observe the changes in the interactions of the two rough surfaces, not the magnitude of convergence. Also, it is challenging to compare the convergence from these simulations with that from the simulations with the half-grain model because: (1) the model only represents a part of the contact between two grains, not the whole contact, and (2) it is almost impossible to determine the boundary stresses accurately.

Figure 6.25 shows the magnitudes and distribution of the contact forces before and after 25 day maturing of the contact model. Similar to the results with the simulation of two grains, the contact forces distributed more uniformly in the $30\ \mu m \times 30\ \mu m$ area and the average magnitudes decreased during the maturing process.

Figure 6.26 shows the magnitudes and orientations of the contact forces at the $30\ \mu m \times 30\ \mu m$ contact area. Orientations of the contact forces with respect to the horizontal direction become slightly more isotropic, immediately after application of load, 4 days and 25 days later.

Figure 6.27 shows time-dependent increases in convergence of this model and the model in Figure 6.11. Notice that in Figure 6.27 the convergence in this model is significantly smaller than in the simulation of the half-grain contact with a flat plate (Figure 6.12). This could be because (1) the convergence in this simulation is an integral effect of the process in a relatively thin region of the material as opposed to the half-grain contact problem in Figure 6.11; (2) the parameters are sensitive to resolution so that the calibrated parameters in the simulation in Figure 6.11 with coarser particles cannot reproduce the same quantitative results in the simulation in Figure 6.22 with a higher resolution. Also notice that the convergence curve of this simulation in Figure 6.27 is smoother than that of the simulation in Figure 6.11. This verifies our previous discussion that the large steps in the convergence curve of the half-grain in Figure 6.12 is due to the coarse particle sizes. Thus, if computational capacity allows, a simulation with higher resolution could simulate this physical process more accurately.

164

This simulation is consistent with earlier conjecture (Michalowski and Nadukuru 2012) that with advancing static fatigue, the contacts become firmer because of the increase in the number of the contact "points", contributing to the increase in the small strain stiffness at the macroscopic scale. The latter is considered by many as one of the major consequences of sand aging.
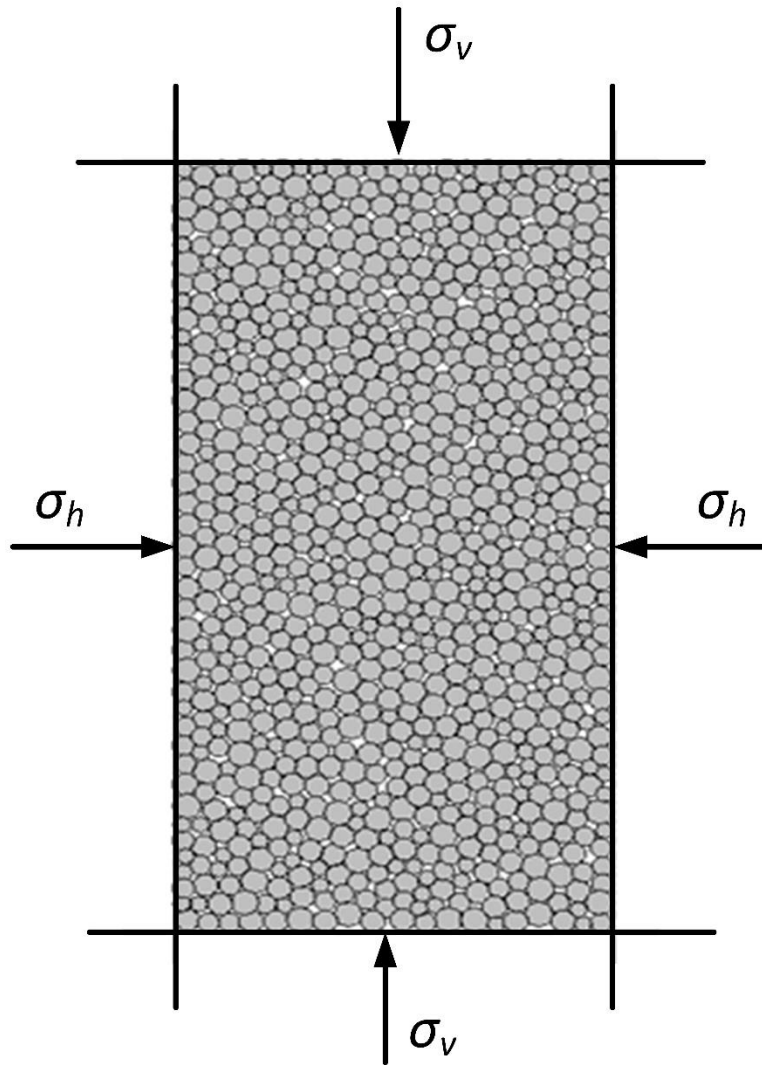
Figure 6.28. The model of a sand assembly in PFC2D. Specimen: 63.4 mm high and 31.7 mm wide; 863 disks with diameters from 0.62 mm to 1.03 mm.
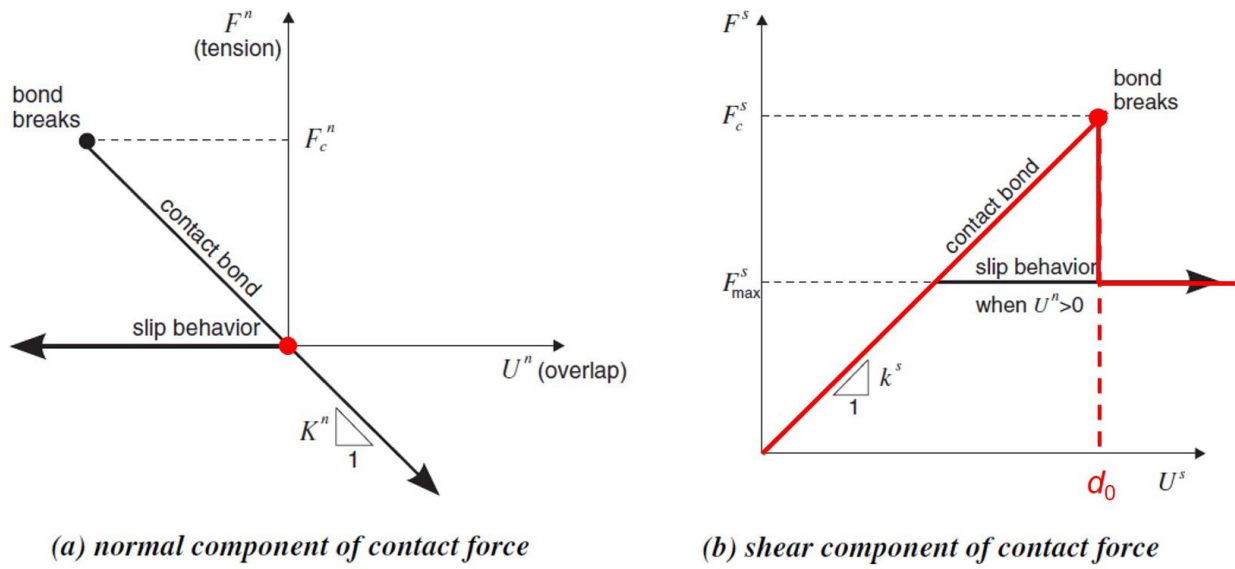
Figure 6.29. The contact model logic used for simulating increase in static friction due to aging.
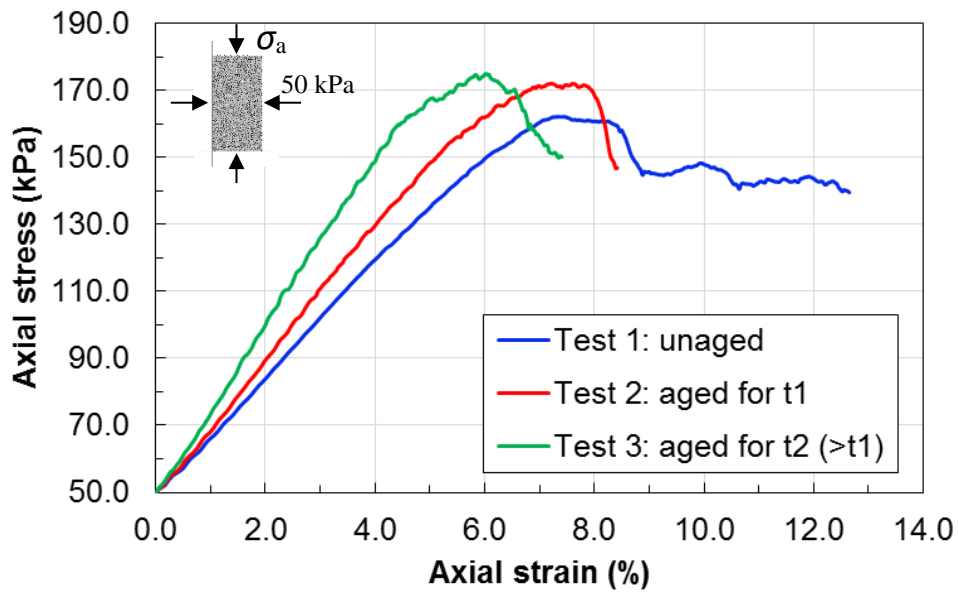
Figure 6.30. Biaxial tests on specimens with different contact parameters, confining stress 50 kPa.

6.5. Discussions

Effects of Contact Maturing on Grain Assemblies

To investigate effects of changes in properties of contacts on grain assemblies, preliminary simulations with a model of a two dimensional DEM model of a grain assembly were performed. Numerical biaxial tests were simulated on a grain assembly model. Different biaxial tests were carried out on the model. The contacts stiffness and friction was changes based on the observations from the grain-scale simulations to account for aging effects. Biaxial test results were consistent with previous laboratory observations.

A packing of 865 disks were generated according to the material generation process described in Potyondy and Cundall (2004), as shown in Figure 6.28. Biaxial tests were conducted on specimen with a confining stress of 50 kPa maintained by the vertical walls via a servo-mechanism and vertical load applied by the top and bottom walls. The parameters used in this model were adopted from Michalowski and Nadukuru (2012), as shown in Table 6.5. Three different tests were conducted on the same model with changing normal stiffness, K_n, shear stiffness, K_n, and friction coefficient, μ. Again, as exactly the same model of specimen was tested, for the same group of parameters, multiple tests was not necessary. The different parameters used in the three tests are summarized in Table 6.6.

Table 6.6. Parameters used in the model of sand grain assembly

Parameter	Value
Particle parameters	
Mass density, ρ	2650 kg/m^3
K_n	4.0×10^6 N/m
K_s	1.6×10^6 N/m
Minimum radius, R_{min}	0.62 mm
Ratio R_{max}/R_{min}	1.66
Friction coefficient, μ	0.65
Wall parameters	
K_n: horizontal/vertical	4.4×10^7 N/m / 0.4×10^7 N/m
K_s: horizontal/vertical	0 / 0
Friction coefficient, μ	0

Table 6.7. Values of stiffness and coefficient of friction in different tests

Test #	Particle μ	Particle K_n	Particle K_s
1	0.65	4.0×10^6 N/m	1.6×10^6 N/m
2	0.80	5.0×10^6 N/m	2.0×10^6 N/m
3	1.0	7.0×10^6 N/m	2.8×10^6 N/m

The authors argue that the micromechanical changes at contacts due to static fatigue only hold under small deformations. When the grain assembly is under large deformations, a large relative sliding or rolling displacement is likely to happen at an aged contact changing it back into a fresh contact with initial micromechanical properties. Therefore, to model the behavior of an aged specimen, the stiffness and friction coefficient have to be changed back to unaged values after a threshold relative displacement has happened at the contact. This behavior of friction can be considered as increase in static friction, not sliding friction and is well demonstrated in observations reported by Li, et al (2012). To simulate this increase in static friction for matured,

the contact-bond algorithm can be employed conveniently with a special contact bond. An introduction of the contact bond logic is shown in Figure 6.29. This frictional behavior can be simulated, if a contact bond as shown in Figure 6.29 is assigned a zero tensile strength and an shear strength equal to the increased friction after maturing. Please see the PFC2D manual for details. The effect of this type of contact bonds only increases the maximum static friction of the contact and has no effect on sliding friction and rolling. However, there is no easy way to automatically change the stiffness of an aged contact back to its initial values when sliding happens, so the increased stiffness of all contacts for an aged specimen were held throughout each test.

The results of biaxial tests on the grain assembly are shown in Figure 6.30. It can be seen from Figure 6.30 that the increase in stiffness and maximum static friction at contacts induced considerable increase in macroscopic stiffness of the grain assembly but only slightly increase in biaxial strength. This macroscopic time-dependent behavior of the grain assembly resembles the behavior of aged sand shown in triaxial test results obtained by Daramola (1980).

The simulation results with two dimensional models of a contact and a grain assembly support the static fatigue hypothesis. By incorporating static fatigue fracturing in the grain minerals, the contact model reproduced laboratory observations in the contact maturing tests and indicated likely changes in stiffness and friction of contacts during aging. Then these microscopic changes at contacts were introduced into a model of a grain assembly and successfully reproduced macroscopic aging behavior of sand. The assembly model behaved in a way resembling triaxial results of aged sand samples.

6.6. Conclusions

A single grain was modeled as an assembly of sub-particles fused together with bonds capable of carrying forces and moments (including torsion). This bonded particle model with the bonds sensitive to stress corrosion process was used to simulate the contact regions of grains, with the focus on the time-dependent response. The distinct elements model appeared to be very useful in identifying increasing time-dependent damage in the grain region adjacent to the contact. This damage is signified by fracturing of the bonds within the grain material. The consequence of this

process is the readjustment of the topography of the contact that leads to a time-dependent increase in the number of contact points within a single inter-granular contact. This, in turn, produces an increase of the contact stiffness leading to the increase of the small-strain stiffness at the macroscopic scale. The simulation is consistent with the static fatigue hypothesis and it is consistent with the experimental outcome of tests on loaded individual grains. While some components of the model require refinements, for instance, the stress corrosion function in the bond description, the distinct element method has been very successful in capturing the contact fatigue process. Detailed conclusions are listed below.

- Discrete element modeling (DEM) has successfully simulated the contact maturing process. By incorporating algorithms capable of simulating the static fatigue process in the grain material, the results from both the two-dimensional and three-dimensional simulations reproduced the time-dependent behavior a single inter-grain contact.

- Tremendous level of stress concentration develops in the grain material in the vicinity of a contact, but the concentration in stress is relieved during contact maturing. This stress concentration can explain the intense fracturing in the vicinity of contacts in the simulations. The relief in concentration can explain the decaying characteristics in convergence, as observed in the contact-maturing tests.

- Three-dimensional models, rather than two-dimensional models, and higher resolutions (smaller sub-particle sizes) are desirable for better simulation accuracy. Comparison of the 2D simulations and the 3D simulations of one grain against a flat surface showed that the 3D model was able to arrest the fracturing process in the vicinity of the contact, instead of developing a macro-crack through the entire grain, as was found typical in the 2D simulations. The 3D results with limited damage areas are consistent with the observations in the experiments. The simulation of a small region of grain-to-grain contact, with more geometric details and smaller particle sizes (higher resolution) generated a smoother convergence curve than the coarser models.

- An increase in the number of contact points transferring contact loads was observed in all simulations. This was manifested by an increase in the number of force chains across the

170

contact area during contact maturing. The increase in the number of contact points leads to an increase in contact stiffness, and, consequently, an increase in stiffness of granular assemblies.

- Simulations with the contact model of two grains showed that the orientations of contact forces (with respect to the nominal horizontal contact plane) became more isotropic as contact maturing progresses. At the beginning of aging, most of the contact forces were nearly vertical, but over time, as the number of contact points increased, the contact forces distributed over a larger range of angle. The author believes that the more isotropic distribution of contact force orientations indicates a strong interlocking which would lead to an increase in frictional resistance of a contact.

- A grain assembly-scale simulation showed that contact maturing leads to an increase in macroscopic stiffness, but a less significant increase in strength of a grain assembly. This simulation result is consistent with the experimental results of triaxial tests on freshly prepared and aged sand samples (Daramola 1980).

- The simulations in this thesis provide support to the hypothesis that the mechanism behind time effects in sand is delayed fracturing (static fatigue) of micromorphological features of sand grain surfaces. The delayed static fatigue fracturing of sand grain surfaces changes micromechanical properties of inter-grain contacts, and these micromechanical changes induce macroscopic time-dependent changes in properties of sand grain assemblies (in particular the small-strain stiffness).

Chapter 7

Finite Element Modeling of Contact Aging in a Coupled Chemo-Mechanical Field

7.1. Introduction

Chemical dissolution and precipitation have been observed to happen in silica sand, especially the latter, which is more easily to be observed, as shown in Figure 7.1. These chemical processes change surface textures of silica sand grains and in turn mechanical properties of sand. The results of contact maturing tests (Chapter 4) have revealed a strong correlation between aging rates of individual contacts and the roughness of the surfaces at the contact. Also, as shown in the results of aging tests with sand grain assemblies (Chapter 5), the rate of the aging process is largely influenced by the chemical properties of pore fluids.

In engineering practice, sand is generally used under pressure and if at the same time, chemically active groundwater is present, complicated surface migration of sand grain surfaces are

expected to occur. The migration of grain surfaces will finally result in changes in macroscopic sand properties. Knowing the kinetics of this process is crucial for proper predictions of time-dependent changes of sand properties in a coupled stress and chemical field.
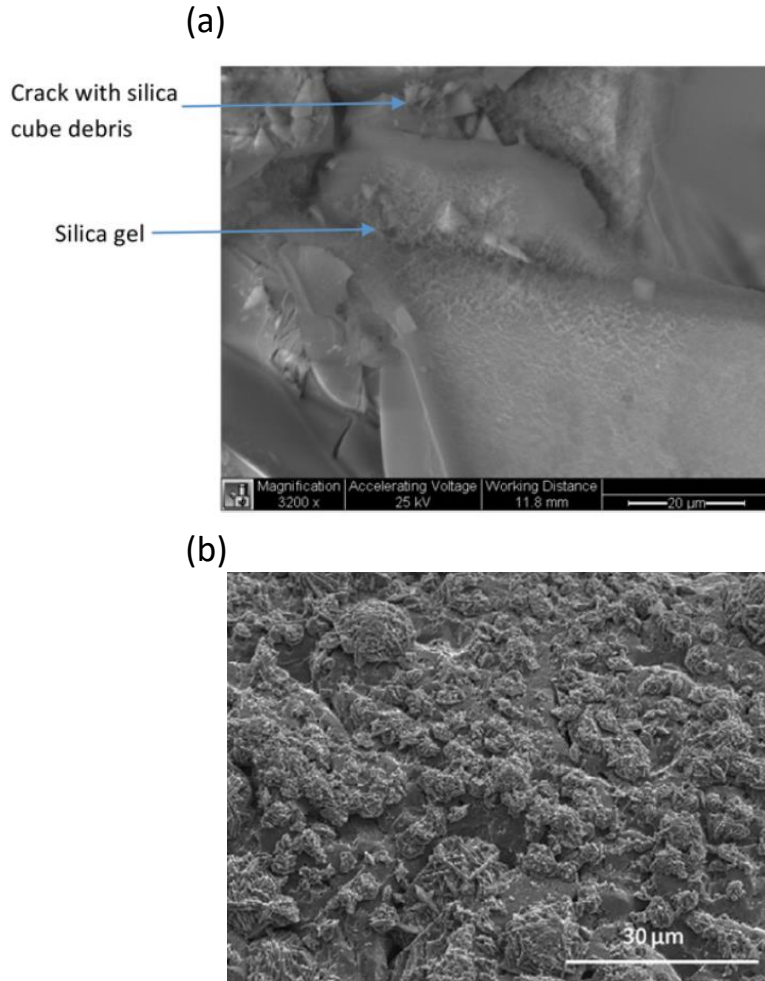
Figure 7.1. SEM images showing mineral precipitation: (a) silica gel precipitate on silica sand grain after aging in 400 ppm silica solution for 3 weeks (from Guo and Hueckel 2015), and (b) lepisphere-shaped aggregate of nitrate-cancrinite precipitate on silica sand grain (from Wang and Um 2012).

In this chapter, a theory of surface migration, incorporating multi-physical processes, is adopted to analyze the evolution of surface micro-topography of silica sand grains in a coupled chemo-mechanical field. Based on this theory, a finite element framework was developed with

173

linked COMSOL Multiphysics and MATLAB. Preliminary simulations with simple surface geometries were performed. The results showed effectiveness of the simulation framework. Based on the results, the effects of initial surface geometry, loading conditions, and chemical conditions on the evolution of the surface texture are discussed.

7.2. Theoretical Background

Theoretical derivations of this part are primarily from Sun et al (1997) and the class notes of ME 574, Nano/Micro Evolution prepared by Professor Wei Lu at the University of Michigan.

Basic Theory of Interface Migration

Consider a solid mass in a chemical environment, atoms either precipitate from the environment onto the solid, or dissolve from the solid into the environment. The two phases, environment and solid, are not in "equilibrium" with each other; rather one phase is growing at the cost of reducing the other. During these atom exchanges, the free energy of the entire system changes by:

$$G = \int \gamma dA + gV \tag{7.1}$$

where G is the change in total free energy of the system; γ is the surface tension of the interface, i.e., free energy per area of interface; A is the area of the interface; g is the difference in the free energy densities of the two phases; V is the volume of the dissolved or evaporated solid into the environment.

Figure 7.2 shows the interface of a solid mass and its environment. In reaching equilibrium, the interface undergoes a dynamic motion. During this motion, displacement at each point on the interfaces is labeled as δr_n. A thermodynamic force, P, is applied on the surface during the

174

interface migration. The relationship of P and change in free energy, δG, is governed by (Sun et al. 1997):

$$\int P\delta r_n dA = -\delta G \qquad (7.2)$$
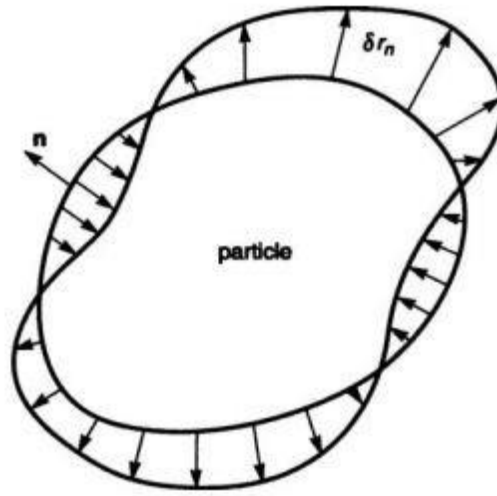
Figure 7.2. A diagram of surface migration (Sun et al. 1997).

If we define v_n as the velocity of an arbitrary point on the interface in the direction normal to the interface, and L as the mobility of the interface (a constant for a specific surface). The actual velocity is taken to be linearly proportional to the driving pressure,

$$v_n = LP \qquad (7.3)$$

Equation (7.3) defines the dynamics of surface motion and it is valid when $\Omega P \ll kT$. Ω is atomic volume, k the Boltzmann's constant (1.38×10-23 m²kg/(s²K)), and T the absolute temperature.

175

Substituting Eq. (7.3) into Eq. (7.2) gives,

$$\int \frac{v_n}{L} \delta r_n dA = -\delta G \tag{7.4}$$

Equation (7.4) is referred to as the *weak statement* of the interface migration problem. It is the basis for the finite element method for interface migration simulations.

Finite Element Modeling of Interface Migration

Geometry of an Element

The interface can be discretized into a series of node points and one basic element with two node points is shown in Figure 7.3. Based on geometry of the element, the normal displacement of any point on the straight line, δr_n, is related to the displacement of the two nodal points by,

$$\delta r_n = N_1 \delta x_1 + N_2 \delta y_1 + N_3 \delta x_2 + N_4 \delta y_2 \tag{7.5}$$

where δx_1, δy_1, δx_2 and δy_2 are the displacements of node 1 and 2 in x and y directions of a global coordinate system; factors N_1 to N_4 are defined as,

$$N_1 = -\left(\frac{1}{2} - \frac{s}{l}\right)\sin\theta \tag{7.6}$$

176

$$N_2 = \left(\frac{1}{2} - \frac{s}{l}\right)\cos\theta \tag{7.7}$$

$$N_3 = -\left(\frac{1}{2} + \frac{s}{l}\right)\sin\theta \tag{7.8}$$

$$N_4 = \left(\frac{1}{2} + \frac{s}{l}\right)\cos\theta \tag{7.9}$$

where l is the length of the straight line and s is the local coordinate along the element.
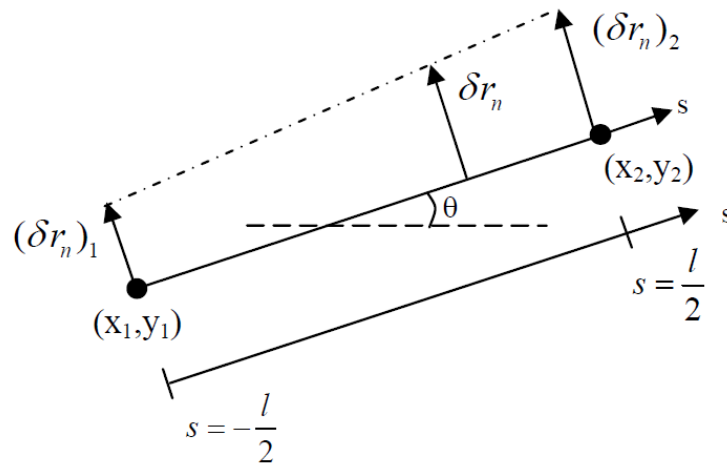
Figure 7.3. A two-node element (Lu 2014).

Eventually, velocity v_n of an arbitrary point on the straight line in Eq. (7.5) can be obtained as,

$$v_n = N_1\dot{x}_1 + N_2\dot{y}_1 + N_3\dot{x}_2 + N_4\dot{y}_2 \tag{7.10}$$

where $\dot{x}_1$, $\dot{y}_1$, $\dot{x}_2$ and $\dot{y}_2$ are velocity components of the two nodes in x and y directions.

Forces Acting on Nodes of an Element

Based on Eq. (7.1), the change in total free energy associated to the motion of the element is,

$$\delta G = \gamma \delta l + \frac{d\gamma}{d\theta} l \delta\theta - (g^I - g^{II}) l \frac{(\delta r_n)_1 - (\delta r_n)_2}{2} \tag{7.11}$$

where the first two terms represent the change in free energy due to surface tension and the third due to the difference in energy densities of the two phases. g^I and g^{II} are the energy densities of the two phases, respectively; $(\delta r_n)_1$ and $(\delta r_n)_2$ are the displacements of node 1 and 2, respectively.

If we express the free energy by work done by the forces acting on the nodes through virtual motions of the nodes then δG takes form

$$\delta G = -f_1 \delta x_1 - f_2 \delta y_1 - f_3 \delta x_2 - f_4 \delta y_2 \tag{7.12}$$

where f_1 to f_4 are the components of the forces acting on the nodes by the element in the two coordination directions. By combining Equations (7.11) and (7.12), and including elastic energy density to the change in free energy, we can obtain

178

$$\begin{Bmatrix} f_1 \\ f_2 \\ f_3 \\ f_4 \end{Bmatrix} = \gamma \begin{Bmatrix} \cos\theta \\ \sin\theta \\ -\cos\theta \\ -\sin\theta \end{Bmatrix} + \frac{d\gamma}{d\theta} \begin{Bmatrix} -\sin\theta \\ \cos\theta \\ \sin\theta \\ -\cos\theta \end{Bmatrix} + \frac{l}{2}\left(g^I - g^{II}\right) \begin{Bmatrix} -\sin\theta \\ \cos\theta \\ -\sin\theta \\ \cos\theta \end{Bmatrix} + \frac{l}{2} \begin{Bmatrix} \left(\dfrac{2}{3}W_1 + \dfrac{1}{3}W_2\right)\sin\theta \\ -\left(\dfrac{2}{3}W_1 + \dfrac{1}{3}W_2\right)\cos\theta \\ \left(\dfrac{1}{3}W_1 + \dfrac{2}{3}W_2\right)\sin\theta \\ -\left(\dfrac{1}{3}W_1 + \dfrac{2}{3}W_2\right)\cos\theta \end{Bmatrix} \qquad (7.13)$$

where the last term is the change in strain energy density of the two nodes; W_1 and W_2 are the elastic energy densities stored in the two nodes, respectively. W is given by

$$W = \frac{1}{2}\sigma_{ij}\varepsilon_{ij} \qquad (7.14)$$

where σ_{ij} and ε_{ij} are stress and strain of a nodal point.

Velocities of nodal points

The change of the left side of the weak statement, Eq. (7.4), caused by the virtual motion is

$$\int \frac{v_n \delta r_n}{L} ds = \{\delta x_1, \quad \delta y_1, \quad \delta x_2, \quad \delta y_2\}\left[H_{ij}\right]\begin{Bmatrix} \dot{x}_1 \\ \dot{y}_1 \\ \dot{x}_2 \\ \dot{y}_2 \end{Bmatrix} \qquad (7.15)$$

where $\left[H_{ij} \right]$ is a 4×4 symmetric matrix calculated from

$$\left[H_{ij} \right] = \frac{1}{L} \int_{-\frac{l}{2}}^{\frac{l}{2}} N_i N_j \tag{7.16}$$

which gives

$$\left[H_{ij} \right] = \frac{l}{6L} \begin{bmatrix} 2\sin^2\theta & -2\sin\theta\cos\theta & \sin^2\theta & -\sin\theta\cos\theta \\ -2\sin\theta\cos\theta & 2\cos^2\theta & -\sin\theta\cos\theta & \cos^2\theta \\ \sin^2\theta & -\sin\theta\cos\theta & 2\sin^2\theta & -2\sin\theta\cos\theta \\ -\sin\theta\cos\theta & \cos^2\theta & -2\sin\theta\cos\theta & 2\cos^2\theta \end{bmatrix} \tag{7.17}$$

Thus

$$\left[H_{ij} \right] \begin{Bmatrix} \dot{x}_1 \\ \dot{y}_1 \\ \dot{x}_2 \\ \dot{y}_2 \end{Bmatrix} = \begin{Bmatrix} f_1 \\ f_2 \\ f_3 \\ f_4 \end{Bmatrix} \tag{7.18}$$

From this equation, the velocities of the two nodes can be calculated.

Assemble All Elements

Now the assembling of elements to form a simulated interface is introduced. Figure 7.4 shows an example of a three-node, two-element system.
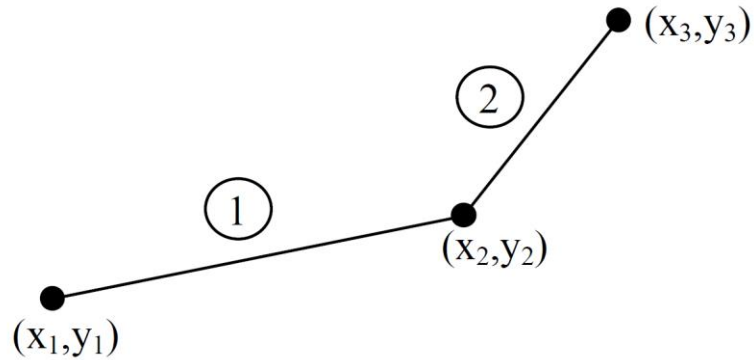
Figure 7.4. A two-element system of a discretized interface (Lu 2014).

The force-displacement equation for element 1 is

$$\begin{bmatrix} H_{11}^{1} & H_{12}^{1} & H_{13}^{1} & H_{14}^{1} \\ H_{21}^{1} & H_{22}^{1} & H_{23}^{1} & H_{24}^{1} \\ H_{31}^{1} & H_{32}^{1} & H_{33}^{1} & H_{34}^{1} \\ H_{41}^{1} & H_{42}^{1} & H_{43}^{1} & H_{44}^{1} \end{bmatrix} \begin{Bmatrix} \dot{x}_1 \\ \dot{y}_1 \\ \dot{x}_2 \\ \dot{y}_2 \end{Bmatrix} = \begin{Bmatrix} f_1^{1} \\ f_2^{1} \\ f_3^{1} \\ f_4^{1} \end{Bmatrix} \tag{7.19}$$

The force-displacement equation for element 2 is

$$
\begin{bmatrix}
H_{11}^{2} & H_{12}^{2} & H_{13}^{2} & H_{14}^{2} \\
H_{21}^{2} & H_{22}^{2} & H_{23}^{2} & H_{24}^{2} \\
H_{31}^{2} & H_{32}^{2} & H_{33}^{2} & H_{34}^{2} \\
H_{41}^{2} & H_{42}^{2} & H_{43}^{2} & H_{44}^{2}
\end{bmatrix}
\begin{Bmatrix}
\dot{x}_2 \\
\dot{y}_2 \\
\dot{x}_3 \\
\dot{y}_3
\end{Bmatrix}
=
\begin{Bmatrix}
f_1^{2} \\
f_2^{2} \\
f_3^{2} \\
f_4^{2}
\end{Bmatrix}
\tag{7.20}
$$

The total equation for this two-element system can be assembled by

$$
\begin{bmatrix}
H_{11}^{1} & H_{12}^{1} & H_{13}^{1} & H_{14}^{1} & 0 & 0 \\
H_{21}^{1} & H_{22}^{1} & H_{23}^{1} & H_{24}^{1} & 0 & 0 \\
H_{31}^{1} & H_{32}^{1} & H_{33}^{1}+H_{11}^{2} & H_{34}^{1}+H_{12}^{2} & H_{13}^{2} & H_{14}^{2} \\
H_{41}^{1} & H_{42}^{1} & H_{43}^{1}+H_{21}^{2} & H_{44}^{1}+H_{22}^{2} & H_{23}^{2} & H_{24}^{2} \\
0 & 0 & H_{31}^{2} & H_{32}^{2} & H_{33}^{2} & H_{34}^{2} \\
0 & 0 & H_{41}^{2} & H_{42}^{2} & H_{43}^{2} & H_{44}^{2}
\end{bmatrix}
\begin{Bmatrix}
\dot{x}_1 \\
\dot{y}_1 \\
\dot{x}_2 \\
\dot{y}_2 \\
\dot{x}_3 \\
\dot{y}_3
\end{Bmatrix}
=
\begin{Bmatrix}
f_1^{1} \\
f_2^{1} \\
f_3^{1}+f_1^{2} \\
f_4^{1}+f_2^{2} \\
f_3^{2} \\
f_4^{2}
\end{Bmatrix}
\tag{7.21}
$$

In the overlap regions, elements are added together.

Note that the dimension of the H matrix is $2n \times 2n$ for an interface represented by n nodes. For a system with n nodes, first generate a $2n \times 2n$ zero matrix for the H matrix, and two $2n \times 1$ zero vectors for the velocity and force vectors. Then the final H matrix, velocity and force vectors can be constructed by adding the H matrix, velocity and force vectors of each element to the corresponding locations. For instance, the H matrix, velocity and force vectors of the mth element is constructed into the final equation as demonstrated below

$$
\begin{bmatrix}
H_{11}{}^m & H_{12}{}^m & H_{13}{}^m & H_{14}{}^m \\
H_{21}{}^m & H_{22}{}^m & H_{23}{}^m & H_{24}{}^m \\
H_{31}{}^m & H_{32}{}^m & H_{33}{}^m & H_{34}{}^m \\
H_{41}{}^m & H_{42}{}^m & H_{43}{}^m & H_{44}{}^m
\end{bmatrix}
\begin{Bmatrix}
\dot{x}_i \\
\dot{y}_i \\
\dot{x}_j \\
\dot{y}_j
\end{Bmatrix}
=
\begin{Bmatrix}
f_1{}^m \\
f_2{}^m \\
f_3{}^m \\
f_4{}^m
\end{Bmatrix}
\tag{7.22}
$$

$$
\overbrace{\phantom{\hspace{8cm}}}^{2n}
$$

$$
2n \left\{
\begin{bmatrix}
\cdot & \cdot & \cdot & \cdot & \cdot & \cdot & \cdot & \cdot \\
\cdot & \cdot & \cdot & \cdot & \cdot & \cdot & \cdot & \cdot \\
\cdot & \cdot & +H_{11}{}^m & +H_{12}{}^m & +H_{13}{}^m & +H_{14}{}^m & \cdot & \cdot \\
\cdot & \cdot & +H_{21}{}^m & +H_{22}{}^m & +H_{23}{}^m & +H_{24}{}^m & \cdot & \cdot \\
\cdot & \cdot & +H_{31}{}^m & +H_{32}{}^m & +H_{33}{}^m & +H_{34}{}^m & \cdot & \cdot \\
\cdot & \cdot & +H_{41}{}^m & +H_{42}{}^m & +H_{43}{}^m & +H_{44}{}^m & \cdot & \cdot \\
\cdot & \cdot & \cdot & \cdot & \cdot & \cdot & \cdot & \cdot \\
\cdot & \cdot & \cdot & \cdot & \cdot & \cdot & \cdot & \cdot
\end{bmatrix}
\begin{Bmatrix}
\cdot \\
\cdot \\
\dot{x}_i \\
\dot{y}_i \\
\dot{x}_j \\
\dot{y}_j \\
\cdot \\
\cdot
\end{Bmatrix}
=
\begin{Bmatrix}
\cdot \\
\cdot \\
+f_1{}^m \\
+f_2{}^m \\
+f_3{}^m \\
+f_4{}^m \\
\cdot \\
\cdot
\end{Bmatrix}
\right.
\tag{7.23}
$$

7.3.   Simulation Implementation

Simulation Process

The simulations were executed with a coupled COMSOL Multiphysics® and MATLAB® framework. A flow chart of the simulation process is shown in Figure 7.5. Each calculation cycle comprised of four steps.

(1) ***Building model in COMSOL***. A 2D model of a small region of sand grain surface was generated with COMSOL,

183

(2) *computing stresses and strains of nodes*. Boundary conditions and load were applied on the model; the stresses and strains of each node in the model were computed with COMSOL,

(3) *calculating new positions of nodes*. A finite element model of the surface was constructed with the string of nodal points on the surface of the COMSOL model. The stress and strain of each nodal point is input from the COMSOL simulations. The velocities of the nodal points with the coupled effects of stresses and chemical conditions were calculated from Equations (((7.13) to (7.23). The position of each nodal point at the end of this timestep, δt, were calculated from the displacements of the nodal points during this timestep ($\delta x_i = \dot{x}_i \delta t$, $\delta y_i = \dot{y}_i \delta t$). These calculations were performed with MATLAB, and

(4) *updating the model in COMSOL*. The new nodal positions were input to COMSOL to update the geometry of the model. This completes one computation cycle and steps (1) to (4) are repeated.

There were totally eight simulation scenarios, as summarized in Table 7.1. Two different geometries were simulated. One with smooth sinusoidal asperities was used to represent surfaces generated primarily from long-term chemical weathering, while the other with more angular profile to represent surfaces resulted primarily from long-term physical weathering. Examples of these two types of surfaces are shown in Figure 7.6 (Lake Michigan Dune sand and Ottawa 20-30 sand grains). Two chemical conditions were applied, precipitation and dissolution. The boundary conditions of the model are shown in Figure 7.5. The bottom surface was restrained from movement in all directions; the two vertical surfaces were restrained from *x*-direction movement; load was applied on the asperities by displacing the tips of asperities at a small constant velocity of 4×10^{-8} m/s. The timestep in the simulations was 6.15×10^{-17} s. The very small displacement and timestep values were used to ensure stability of the calculations. As mentioned in the beginning of this chapter, the purpose of the simulations was to evaluate effectiveness of the model and to find qualitative trends in migration of grain surfaces in a coupled chemo-mechanical field, not quantitative results.

184
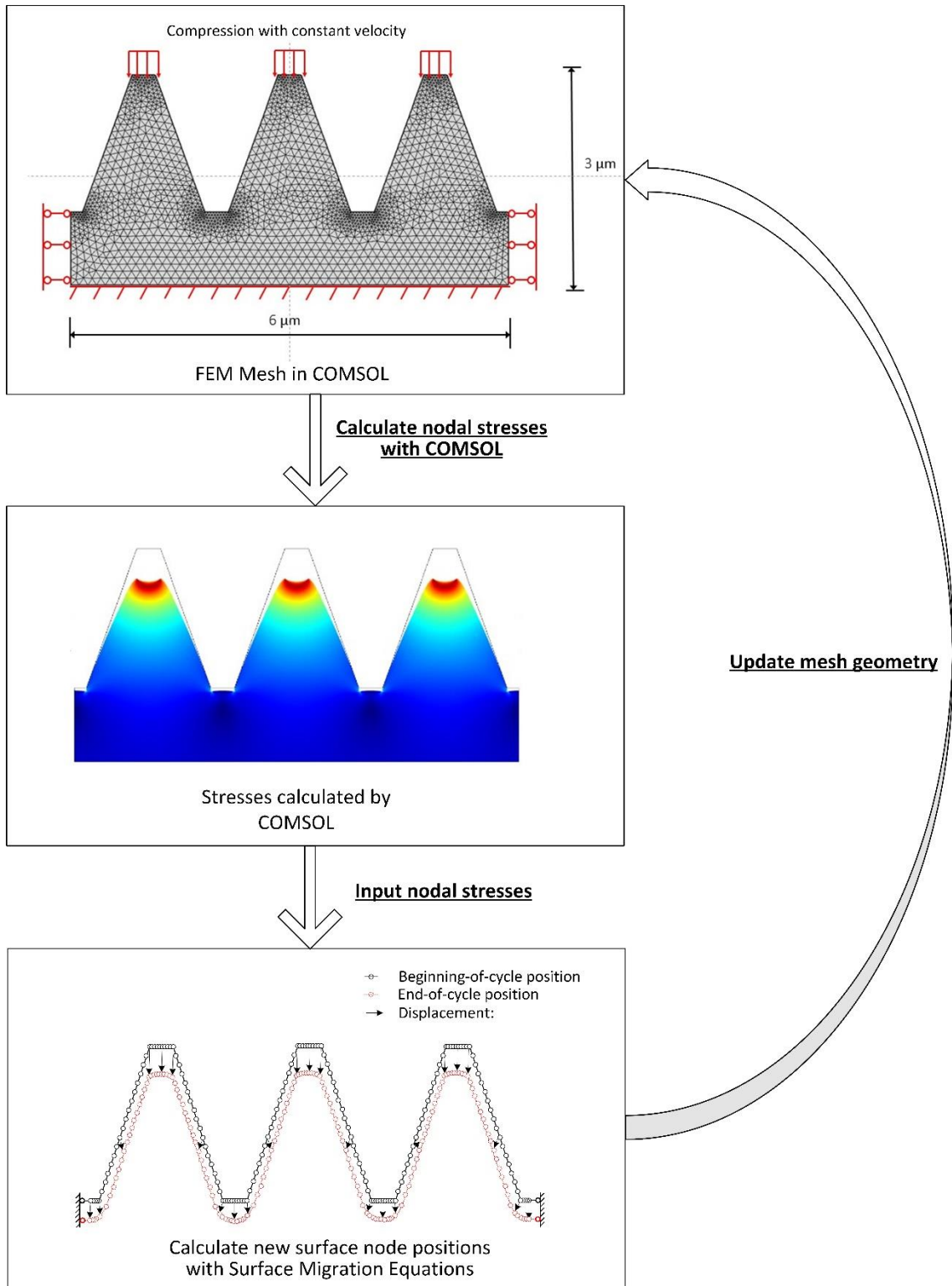
Figure 7.5. Flow chart of coupled COMSOL-MATLAB simulations.
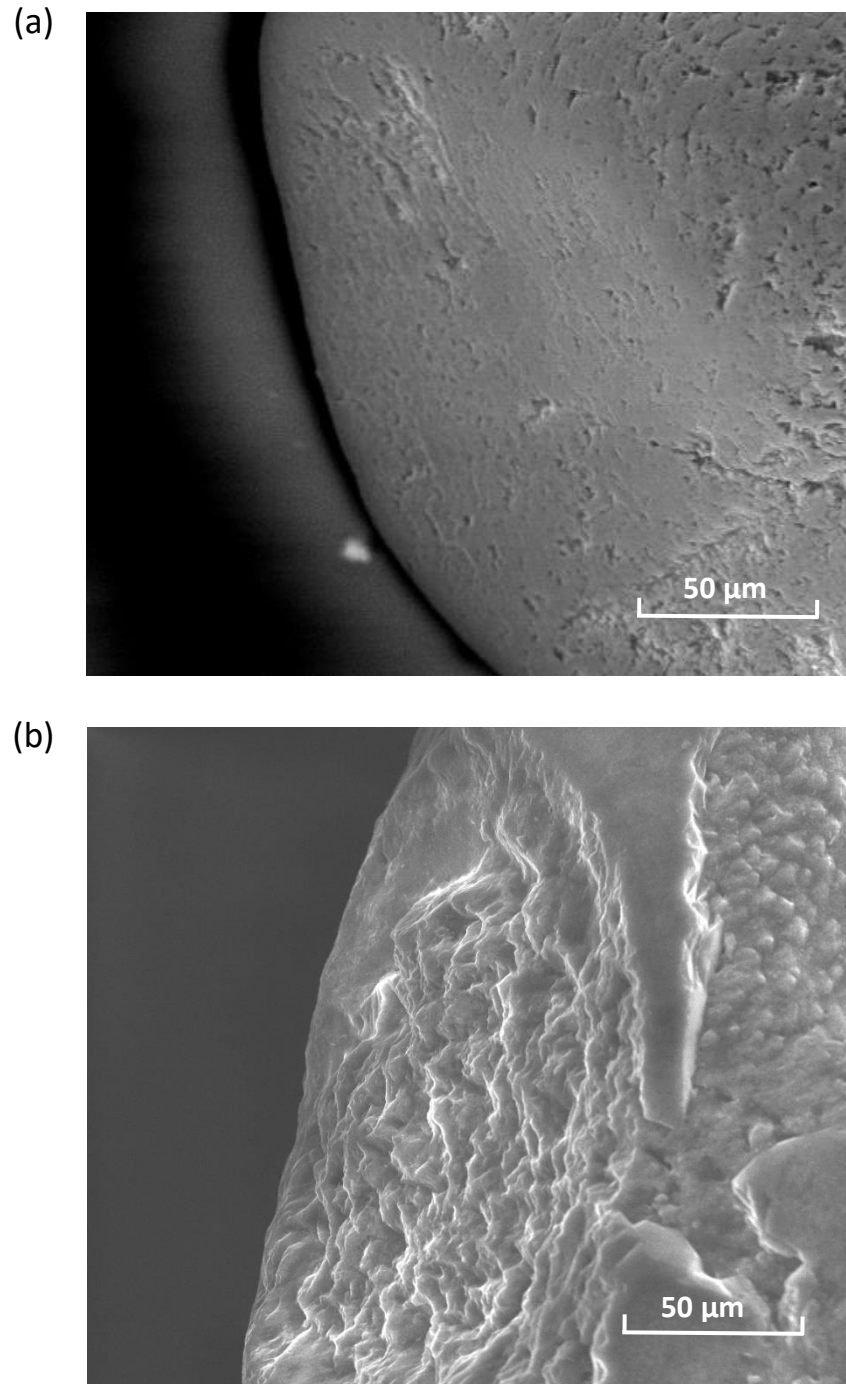
Figure 7.6. SEM images of silica sand grains: (a) surface of a Lake Michigan Dune sand grain with smooth texture, and (b) surface of an Ottawa 20-30 sand grain with angular texture (modified from Nadukuru 2013).

The parameters used in the simulations are summarized in Table 7.2.

Table 7.1. Simulation scenarios

Initial geometry	Chemical condition	Load condition
Sinusoidal	Precipitation	Loaded on asperity tips
		Not loaded
	Dissolution	Loaded on asperity tips
		Not loaded
Trapezoidal	Precipitation	Loaded on asperity tips
		Not loaded
	Dissolution	Loaded on asperity tips
		Not loaded

Table 7.2. Simulations parameters

Parameter	Value	
Mobility, L	1	
Surface tension, γ	0.2	
Energy density of environment, g^{I}	1×10^{6} (precipitation)	0.8 (dissolution)
Energy density of grain material, g^{II}	0.8 (precipitation)	1×10^{6} (dissolution)

Simulation Stability

There are some issues that might cause instability to the simulations and they were addressed. These issues are discussed and the approaches for addressing these issues are introduced.

Adding Boundary Conditions in MATLAB codes

Unlike with COMSOL where boundary conditions can be added by its build-in features, boundary conditions in the MATLAB codes were achieved through adjustments on the H-matrix. As shown in Figure 7.5, the two end points on the surface were fixed at x-direction. This boundary condition was applied by multiplying the corresponding elements in H-matrix by a large number (1×10^8 was used). In this case, the elements were $H[1][1]$ and $H[2N_n-1][2 N_n -1]$, where N_n is the number of nodes. This adjustment ensures zero values for the x-components of velocities of the two end points.

Singularity of H matrix

When part of the surface is flat or vertical, the H matrix has a risk of being singular, which makes it non-invertible and the velocities would not be calculated. One way of solving this problem is adding a small number to each of the four diagonal elements of the H matrix of each element. In the simulations introduced here, 1% of the mean of the values of the four diagonal elements was added to all the four diagonal elements.

Disorder of node points

The node points on the tips of asperities are very densely distributed. During simulation, the orders of these points may change due to x-direction migration. This change of orders causes an error if this updated geometry is fed back to COMSOL. To solve this problem, in the end of every computational cycle, the node points on the flat surfaces (crated by loading) of asperity tips are redistributed per their original orders. The model ran stably with this mechanism, while the calculated migrated surface was not affected.

7.4.   Results

The results of the simulations are shown in Figure 7.7 to Figure 7.14. Migration of the surfaces was affected by chemical conditions, initial surface geometry, and loading conditions. The observed trends are discussed below.

Both chemical dissolution and precipitation tend to create a flatter surface and reduce surface roughness, as shown in Figure 7.8, Figure 7.10, Figure 7.12 and Figure 7.14, when there was no load applied on the asperities. During chemical dissolution, the asperities dissolved faster than the rest of the surface area until a relative flatter surface was created and dissolution continued at relatively uniform rates across the whole area. During chemical precipitation, mineral first precipitated at the bottom of the valleys between asperities until the valleys were almost filled to create a relative flat surface, after which precipitation continued uniformly across the whole area. This characteristic of chemical precipitation is consistent with the observation shown in Figure 7.1(a). The two different surfaces (sinusoidal and trapezoidal) did not show any obvious difference in migration when no load was applied.

Compressive load on the asperity tips affected migration of the surfaces significantly, especially on the more angular trapezoidal surface. As shown in Figure 7.7 and Figure 7.11, no mineral could precipitate on the surfaces with compression on asperity tips. Rather, the asperities were flattened and grooving developed at the corners of the valleys, much faster on the trapezoidal surface. Migration of the surface was catastrophic for the trapezoidal surface under load during chemical dissolution as shown in Figure 7.13. The surface "melt down" with the combined effect of stresses and chemical dissolution. Chemical dissolution was accelerated by compressive load on the sinusoidal surface too, as shown in Figure 7.9 and Figure 7.10, but the acceleration was not as significant as on the trapezoidal surface.

Texture features of the surfaces had significant effects on their migration. The trapezoidal surface, with sharp corners and concaves migrated much faster under load than the smoother sinusoidal surface, as demonstrated in Figure 7.11 and Figure 7.13. This was likely a result of higher levels of stress concentrations developed in the trapezoidal surface with compression on asperity tips.
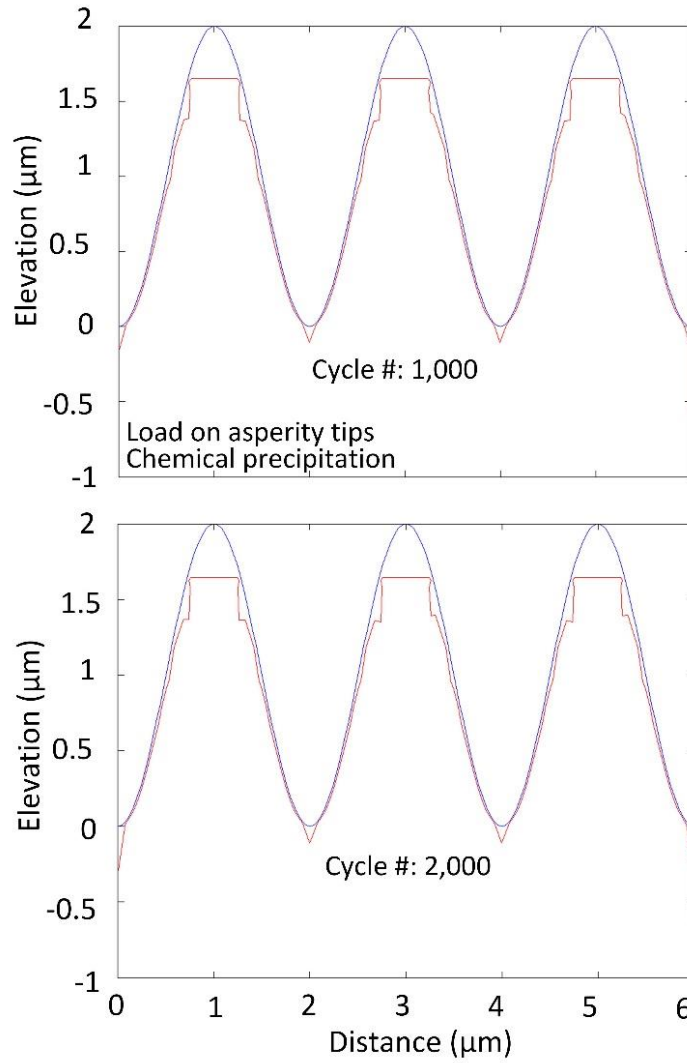
Figure 7.7. Migration of a sinusoidal surface – vertical load, chemical precipitation.
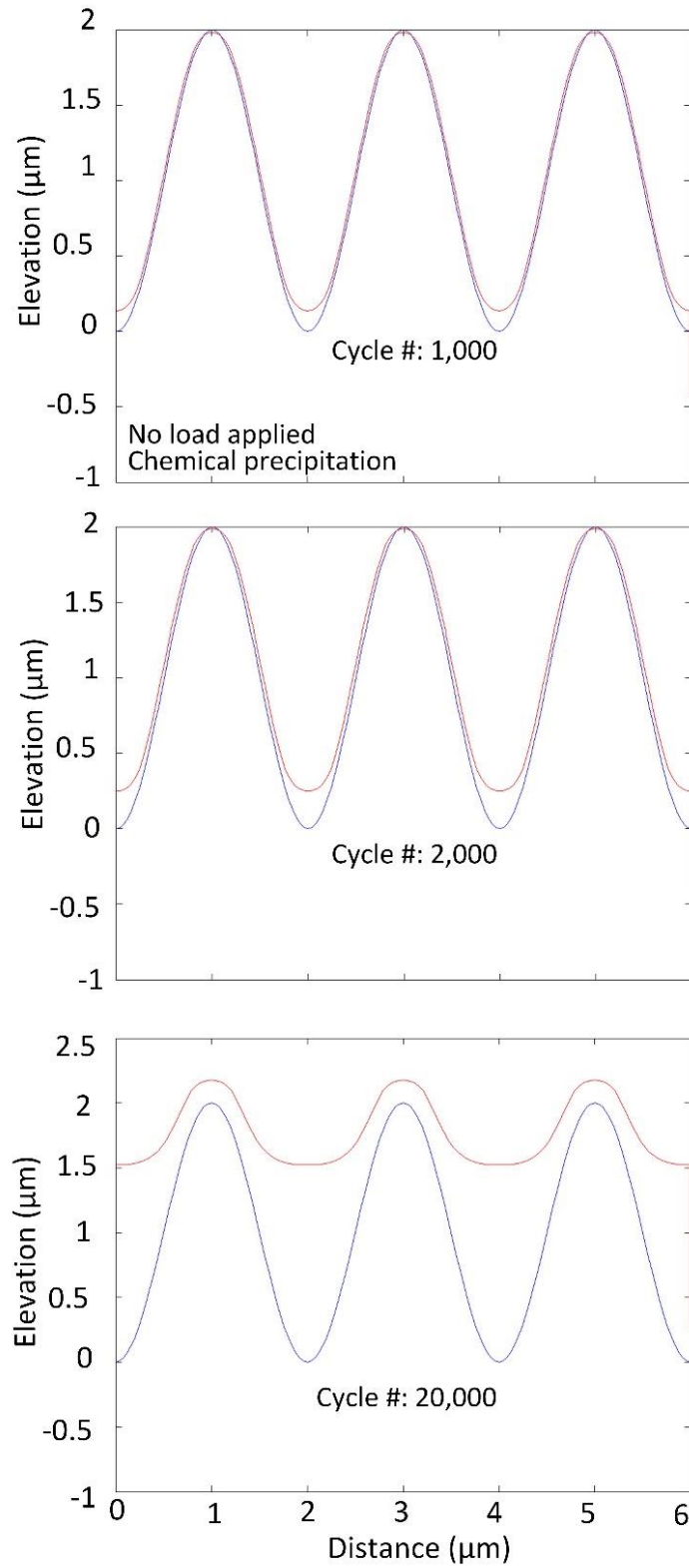
Figure 7.8. Migration of a sinusoidal surface – not loaded, chemical precipitation.
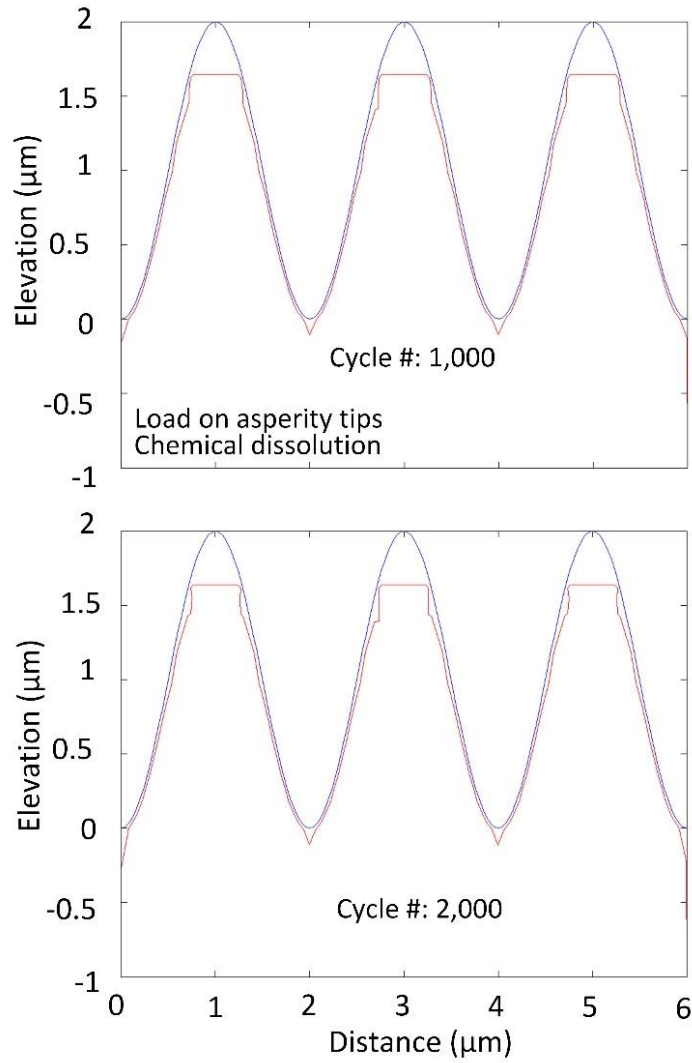
Figure 7.9. Migration of a sinusoidal surface – vertical load, chemical dissolution.
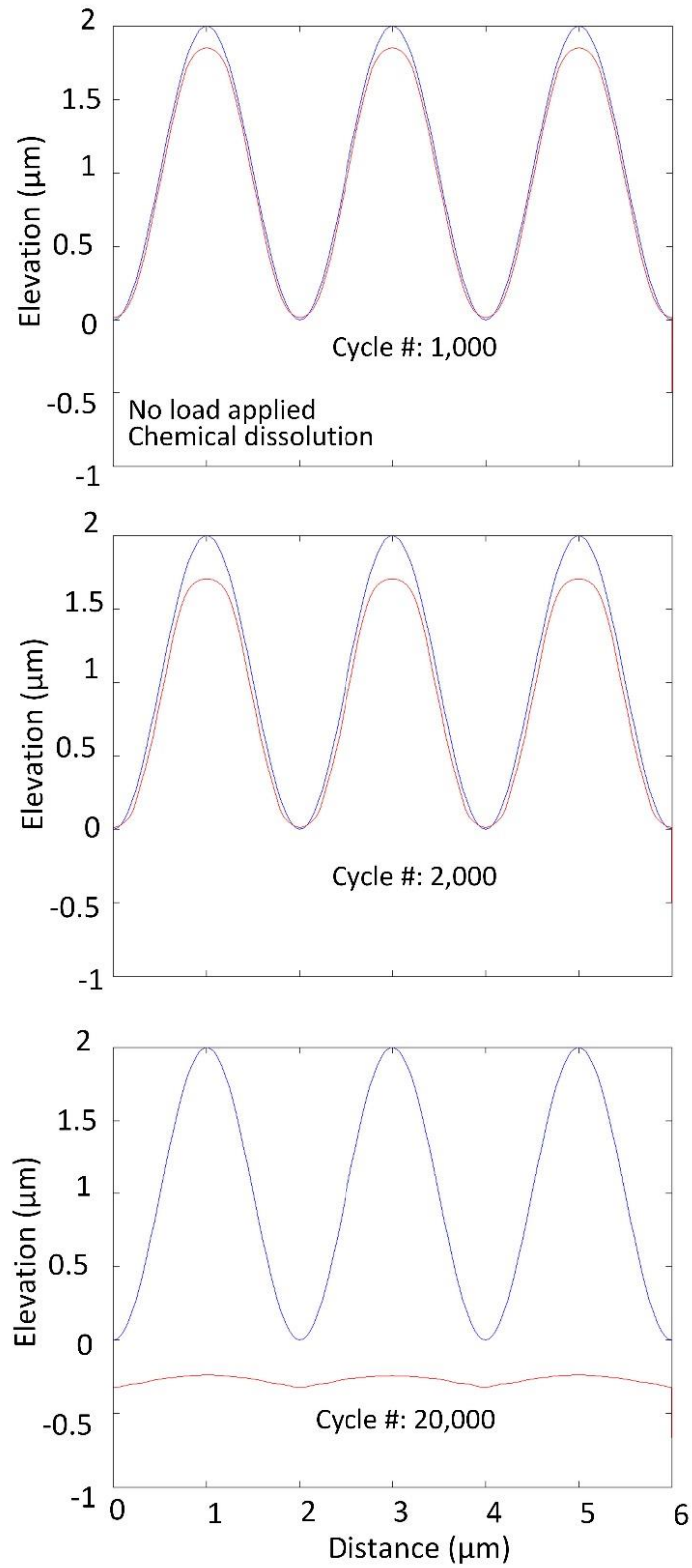
Figure 7.10. Migration of a sinusoidal surface – not loaded, chemical dissolution.
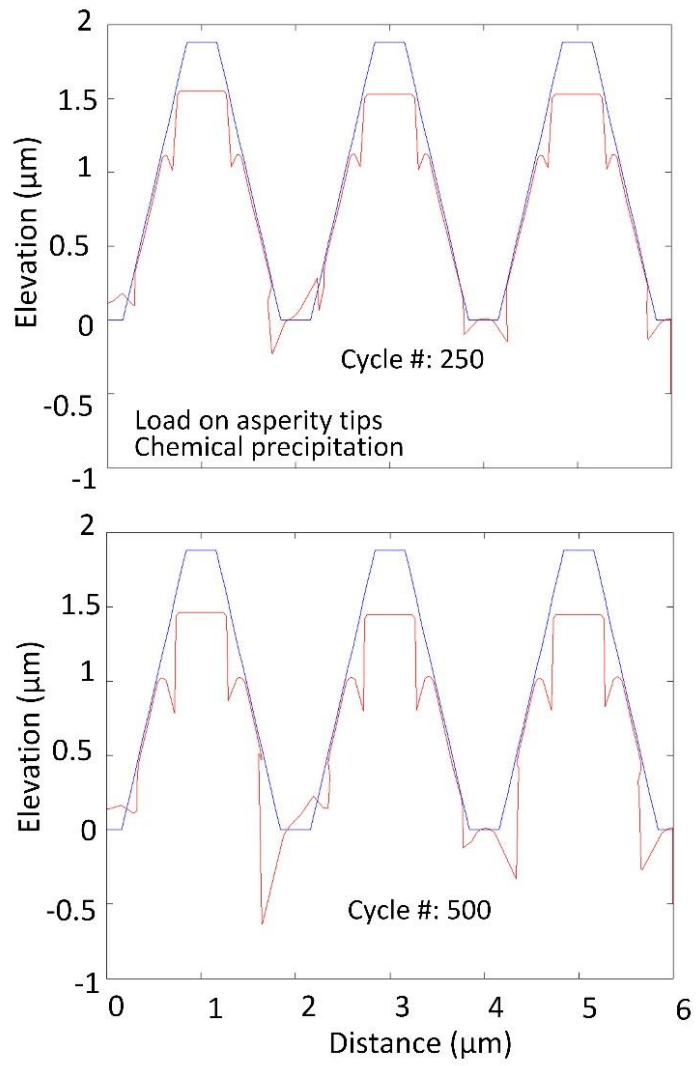
Figure 7.11. Migration of a trapezoidal surface – vertical load, chemical precipitation.
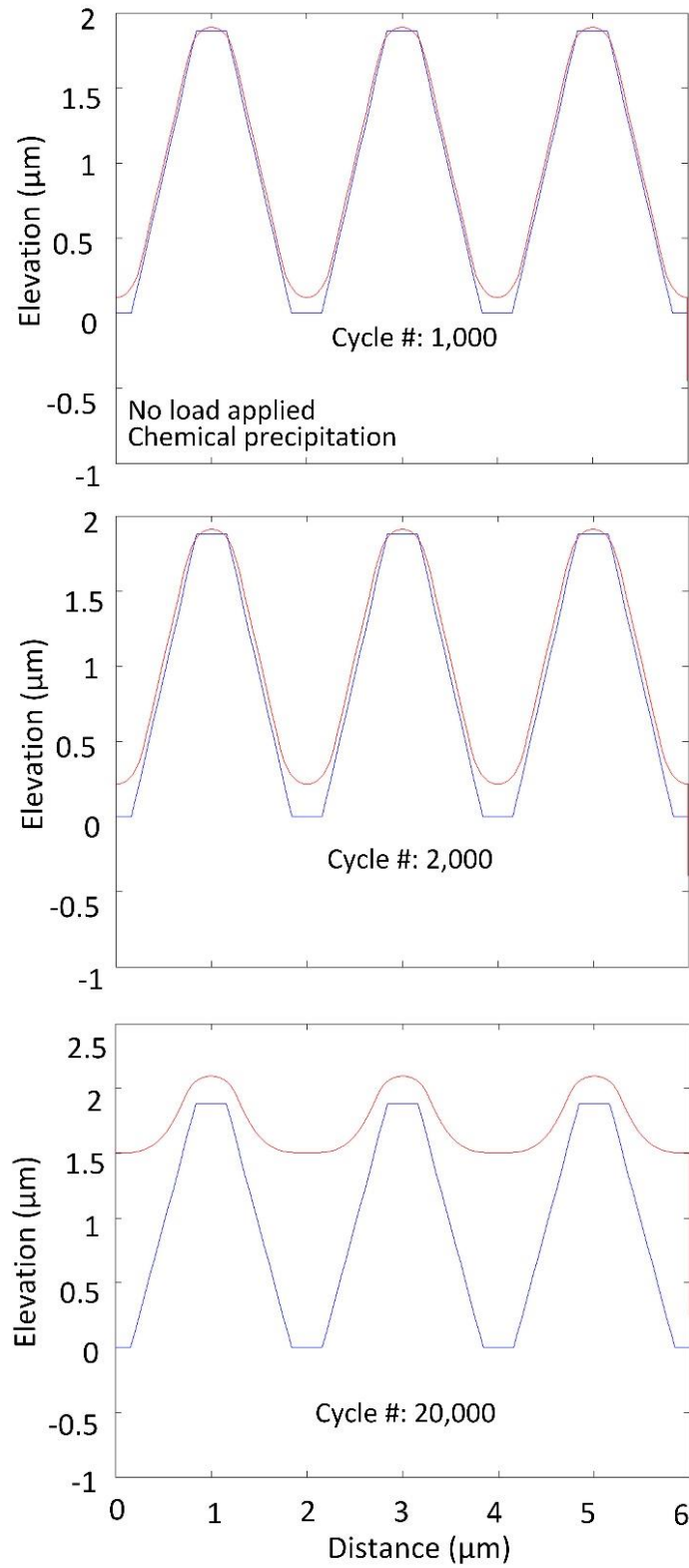
Figure 7.12. Migration of a trapezoidal surface – not loaded, chemical precipitation.
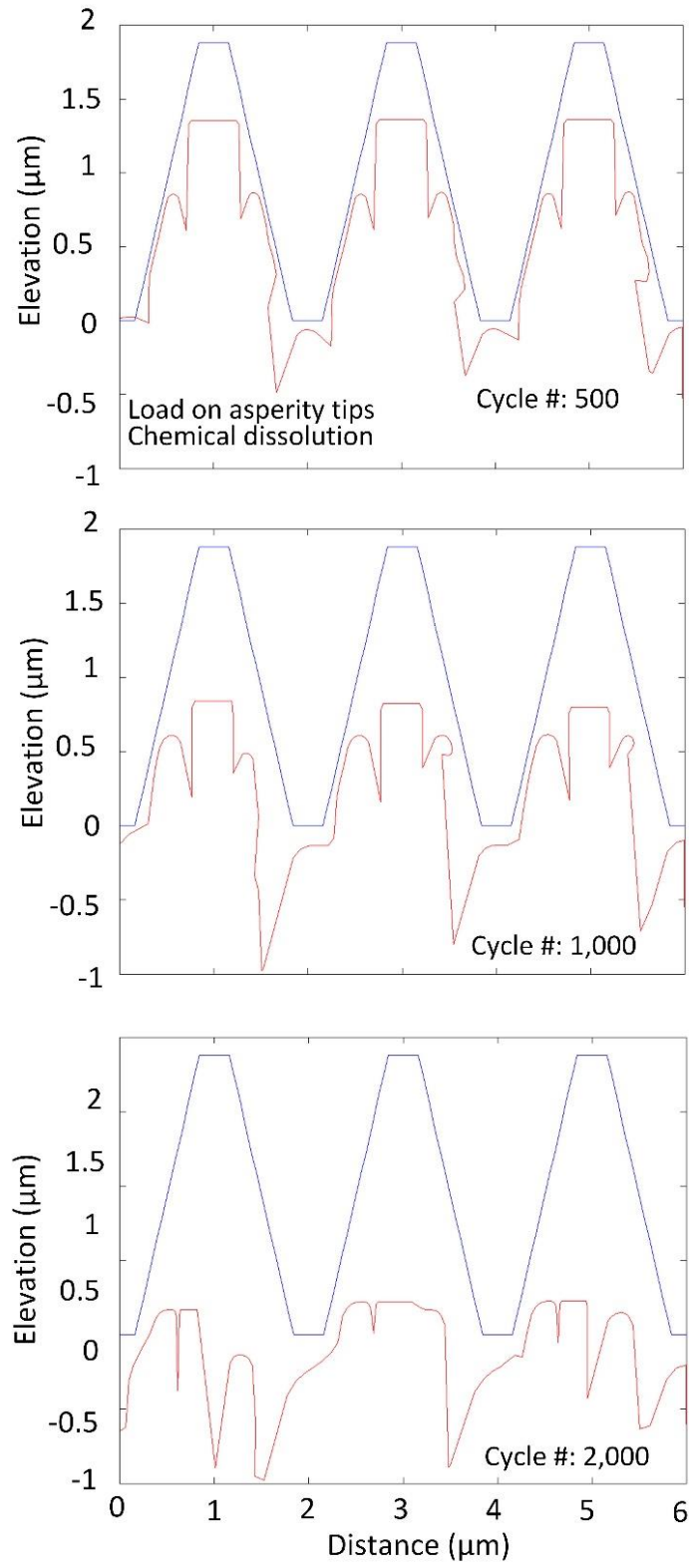
Figure 7.13. Migration of a trapezoidal surface – vertical load, chemical dissolution.

196
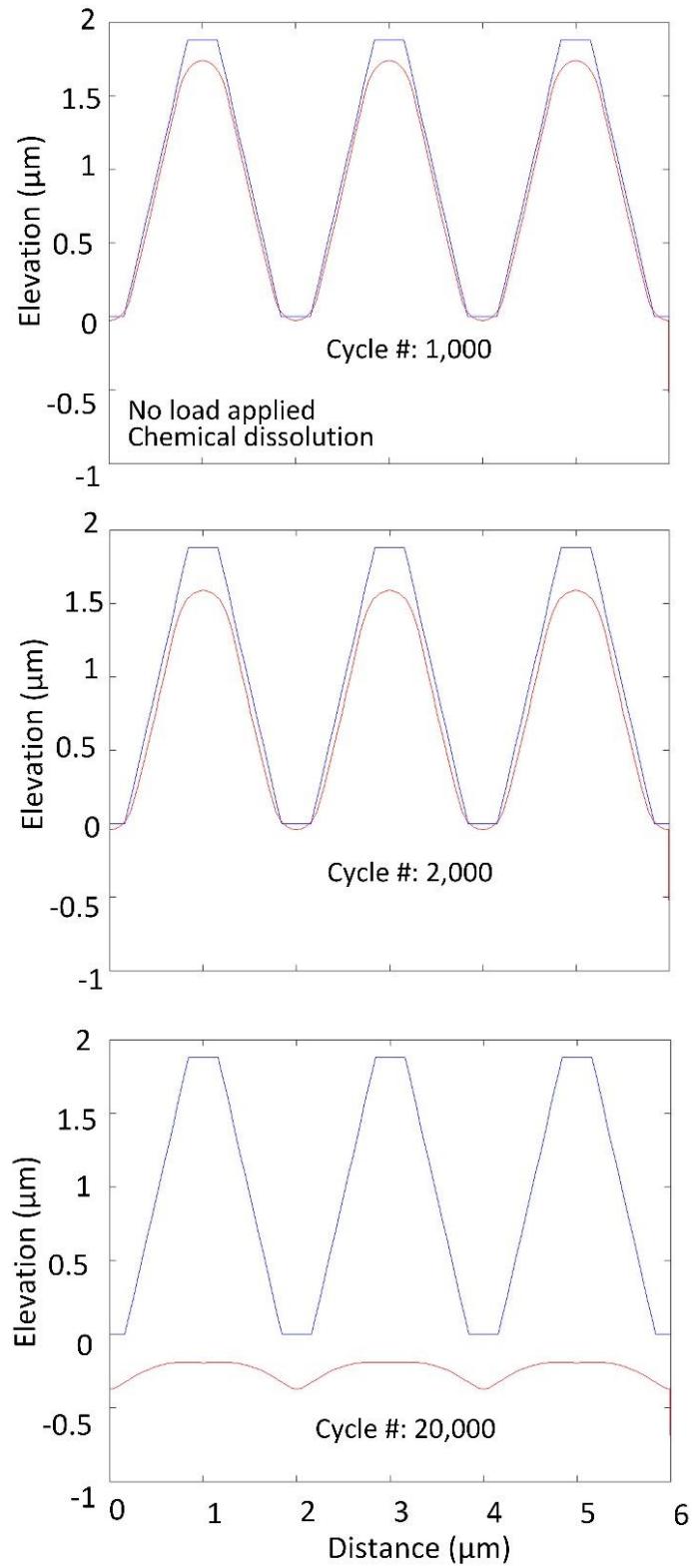
Figure 7.14. Migration of a trapezoidal surface – not loaded, chemical dissolution.

7.5. Summary

A theory of interface migration was adopted to simulate the evolution of silica sand grain surface texture in a coupled chemo-mechanical field. Simulations were performed with a linked COMSOL Multiphysics – MATLAB framework. Eight scenarios were simulated: two different surface geometries, two chemical conditions, with/without load. The observations are summarized below.

- If no mechanical load is applied, the surfaces become flatter both with chemical dissolution and precipitation. During chemical dissolution, the asperities dissolved faster than the rest of the surface area, while during chemical precipitation, mineral first precipitated on the bottom of the valleys between asperities.

- Compressive load on the asperity tips affected migration of the surfaces significantly, especially on the more angular trapezoidal surface. The compressive load prevented chemical precipitation and accelerated dissolution.

- Texture features of the surfaces had significant effects on its migration. Surfaces with angular corners and concaves tended to migrate faster than smoother surfaces, likely due to higher stress concentrations.

- This method for now is only applicable to qualitatively understand the surface migration in a coupled chemo-mechanical field. Calibration of the model with testing results is needed in the future for this method to be used for quantitative analysis of surface migration of silica sand grains. Also, interactions of two surfaces in contact have to be simulated, where cementation could develop with chemical precipitation.

Chapter 8

Conclusions

8.1. Summary of Work

(1) A literature review was conducted on previous research focusing on aging effects in sand. The literature review was organized by: (1) the reported field and laboratory observations of time-dependent changes of sand properties, (2) numerical simulations of aging effects, and (3) the driving mechanisms of sand aging proposed by previous researchers.

(2) A *static fatigue* hypothesis was adopted, which states that the delayed fracturing of micro-morphological features (asperities) at sand grain surfaces under loading is the key cause of sand aging. The static fatigue process at inter-grain contacts induces changes in properties of the contacts and triggers structuration of sand grain assemblies over time. These changes, in turn, are the cause of the observed changes in the macroscopic engineering properties of sand over time.

(3) A microscopic laboratory test was developed to investigate time-dependent response of single sand grains to sustained normal loads. The observed convergence rates over

time showed a strong dependency on roughness of the grain surfaces. The testing results provided support for the static fatigue hypothesis.

(4) A soft-ring oedometer test was developed to analyze time-dependent settlement and increase in horizontal stress in sand grain assemblies. Tests were performed with sand samples with different particle sizes. Both dry and saturated samples were tested; pore fluids with different pH values were used in the saturated samples. The results showed that the rates of settlement and increase in horizontal stress in the samples were significantly affected by particle sizes, presence of pore fluid and pH of the pore fluid.

(5) Time-dependent response of an inter-grain contact was simulated using the distinct element method (DEM). Sand grains were simulated as groups of sub-particles bonded together and a stress corrosion model (with parallel bonds) was used to allow *static fatigue* of the grain material. The model was calibrated with the laboratory single-grain tests and then contacts between two grains were simulated. The simulation results showed development of static fatigue fracturing and the evolution of load transferring at inter-grain contacts over time. Based on the simulation results, changes in mechanical properties of an inter-grain contact over time was discussed and the conclusions were consistent with the static fatigue hypothesis.

(6) A finite element modeling (FEM) framework was developed to investigate the evolution of surface textures of sand grains during aging in a coupled chemo-mechanical environment. The FEM framework was developed based on an interface-migration theory. The usefulness of the framework was tested with preliminary qualitative simulations. The simulation results demonstrated patterns of evolution of the geometry of a surface and the evolution might be accelerated by an angular surface texture and presence of surface mechanical loads. The simulations helped explain effects of chemical properties of pore fluids on rates of aging effects, as observed in the sample-scale experiments.

8.2. Conclusions

Aging effects in sand have been observed and reported for more than three decades. They are manifested as an increase in stiffness of sand, increase in cone penetration resistance, an increased resistance to liquefaction, and pile setup.

The author adopted a static fatigue hypothesis to explain the micromechanical processes at inter-grain contacts that cause continued rearrangements of grains and changes in properties of the contacts. The static fatigue hypothesis states that fracturing of micro-features at grain surfaces in contact occurs over time, and it is the process that gives rise to aging in silica sand. The consequences of this process are twofold: (1) continued variation of force chains in sand, and (2) changes in mechanical properties of the contacts. As a result, the grains undergo periodic structuration events (minute adjustments of grain positions).

Contact maturing tests with single sand grains provided evidence to the static fatigue hypothesis, showing time-dependent deflection of grain surfaces in contact. Soft-ring oedometer tests on sand samples provided evidence that contact maturing can cause sand aging. The process is dependent on sand particle size and the chemistry of pore fluid. Distinct element modeling successfully reproduced contact maturing and the simulation results showed possible increase in contact stiffness and friction during maturing. A finite element model was developed for simulations of grain surface evolution in a coupled chemo-mechanical field and was demonstrated with preliminary simulations, to explain effects of chemical properties of pore fluids on rates of aging.

Literature Review

- Observations of aging effects in freshly deposited or disturbed sand have been reported for three decades. The mostly reported changes as results of aging effects are: soil stiffness, cone penetration resistance, shear strength, liquefaction resistance, and pile setup.

- Some aging-caused changes in sand, such as an increase in small strain stiffness of sand and an increase in shaft resistance during pile setup, roughly follow a linear relationship

with log cycle of time. These correlations could provide guidance in predicting future sand properties. However, the readers are suggested to use these correlations with great caution as aging effects have been found to vary largely under various environmental conditions.

- The rate of deformation and variation in sand properties over time (stiffness in particular) are largely affected by grain sizes, temperature, relative humidity, chemical composition of pore fluids, or disturbance energy.

- Numerical simulations have reproduced some key characteristics of aging behavior of sand. However, the simulation efforts were all based on predetermined microscopic properties of particles and contacts, due to lack of experimental data from tests with individual grains and contacts.

- Chemical, micro-biological, and mechanical processes have been proposed to be the driving mechanisms behind aging effects in sand. Among the three, mechanical processes, specifically continued minute rearrangements of particle structure, have so far been considered as the key mechanism.

Laboratory Contact-Maturing Tests

- An apparatus was developed to monitor time-dependent deflection of a single sand grain under sustained loads. In each of the tests, a single sand grain was compressed between two smooth steel platens with a constant normal load. The time-dependent deformation of the grain was measured through the change in the distance between the two loading platens (convergence).

- In the tests, silica sand grains with 0.60 to 0.85-mm diameters were loaded with two constant loads: 1.3 N and 2.4 N. During the tests, the two loading platens gradually came closer together by 0.3 μm to 2.4 μm between the period of 30 minutes after application of the loads and 20 days later with sustained loads.

- The rates of convergence of the two loading platens over time in the tests was strongly dependent on the roughness of the surface of the sand grain tested. The convergence of the

platens for a grain with a very low roughness (RMS = 28.6 nm) developed additional 0.31 μm of deflection in the 20 days following application of a normal load of 2.4 N. A grain with much larger roughness (RMS = 621 nm), subjected to the same process, converged 2.39 μm during the same period.

- The creep of the grain core material was found to be of secondary importance, compared to maturing of contacts. This conclusion is supported by the results of the tests with sand grains and a glass bead with small surface roughness, which showed very small delayed increase in convergence compared to the results from grains with larger roughness, which showed multiple times larger convergence.

- The result of a test with a high-molybdenum stainless steel sphere (not expected to be subject to static fatigue) showed nearly no convergence, confirming that roughness and fatigue of asperities are the key ingredients of the aging process.

Soft-Ring Oedometer Aging Tests on Sand Grain Assemblies

- Time effects were observed in the sand samples tested under sustained (constant) loads, supporting the static fatigue hypothesis.

- The increase in radial stress is the consequence of an increase in macroscopic stiffness in a confined assembly of grains, which is a result of contact maturing on individual contacts. Once contact maturing was not present in the grain assembly, as in the tests with an assembly of stainless steel spheres, no time-dependent increase in radial stress or settlement were observed.

- The increase in the radial stress in time was faster in sands with small grain sizes. This can be attributed to the larger number of inter-grain contacts in finer sand, causing a more significant cumulative impact on macroscopic aging of sand.

- A larger load did not speed up the increase in radial stress in sand samples. This is possibly because a larger load produces larger damage immediately after application of the load. This reduces the contacts' potential for maturing, thus slower increase in radial stress.

- The increase in radial stress was accelerated by saturation with distilled water, and an even larger increase occurred when the sample was saturated with an alkaline water solution. The latter causes pressure dissolution at contacts, thereby accelerated contact maturing and faster increase in radial stress (and settlement).

Distinct Element Modeling of Aging/Maturing of Contacts

- Discrete element modeling (DEM) has successfully simulated the contact maturing process. By incorporating algorithms capable of simulating the static fatigue process in the grain material, the results from both the two-dimensional and three-dimensional simulations reproduced the time-dependent behavior a single inter-grain contact.

- Tremendous level of stress concentration develops in the grain material in the vicinity of a contact, but the concentration in stress is relieved during contact maturing. This stress concentration can explain the intense fracturing in the vicinity of contacts in the simulations. The relief in concentration can explain the decaying characteristics in convergence, as observed in the contact-maturing tests.

- Three-dimensional models, rather than two-dimensional models, and higher resolutions (smaller sub-particle sizes) are desirable for better simulation accuracy. Comparison of the 2D simulations and the 3D simulations of one grain against a flat surface showed that the 3D model was able to arrest the fracturing process in the vicinity of the contact, instead of developing a macro-crack through the entire grain, as was found typical in the 2D simulations. The 3D results with limited damage areas are consistent with the observations in the experiments. The simulation of a small region of grain-to-grain contact, with more geometric details and smaller particle sizes (higher resolution) generated a smoother convergence curve than the coarser models.

- An increase in the number of contact points transferring contact loads was observed in all simulations. This was manifested by an increase in the number of force chains across the contact area during contact maturing. The increase in the number of contact points leads to an increase in contact stiffness, and, consequently, an increase in stiffness of granular assemblies.

- Simulations with the contact model of two grains showed that the orientations of contact forces (with respect to the nominal horizontal contact plane) became more isotropic as contact maturing progresses. At the beginning of aging, most of the contact forces were nearly vertical, but over time, as the number of contact points increased, the contact forces distributed over a larger range of angle. The author believes that the more isotropic distribution of contact force orientations indicates a strong interlocking which would lead to an increase in frictional resistance of a contact.

- A grain assembly-scale simulation showed that contact maturing leads to an increase in macroscopic stiffness, but a less significant increase in strength of a grain assembly. This simulation result is consistent with the experimental results of triaxial tests on freshly prepared and aged sand samples (Daramola 1980).

- The simulations in this thesis provide support to the hypothesis that the mechanism behind time effects in sand is delayed fracturing (static fatigue) of micromorphological features of sand grain surfaces. The delayed static fatigue fracturing of sand grain surfaces changes micromechanical properties of inter-grain contacts, and these micromechanical changes induce macroscopic time-dependent changes in properties of sand grain assemblies (in particular the small-strain stiffness).

Finite Element Modeling of Contact Aging in a Coupled Chemo-Mechanical Field

- Simulation results showed degradation of grain surface roughness during chemical reactions, which helped explain the observed accelerations of aging effects in sand saturated with an alkaline pore fluid (Chapter 5).

- If no mechanical load is applied, the roughness of grain surfaces decreases with both chemical dissolution and precipitation. During chemical dissolution, the asperities dissolved faster than the rest of the surface area. During chemical precipitation, mineral precipitated first at the bottom of the valleys between asperities.

- Compressive load on the asperity tips affected migration of the surfaces significantly, especially on the more angular trapezoidal surfaces. The compressive load prevented chemical precipitation and accelerated dissolution.

- Texture features of the surfaces had significant effects on its migration. Surfaces with corners and concave features tended to migrate faster than smoother surfaces, likely due to higher stress concentrations.

- This method was used only to qualitatively describe the surface migration in a coupled chemo-mechanical field. Calibration of the model with testing results is needed in the future for this method to be used for quantitative analysis of surface migration of silica sand grains. It is yet to be found if this method can simulate the cementation process.

8.3. Recommendations for Future Research

The following aspects of research should be continued or conducted to deepen understanding of aging effects in sand, and for better predictions of variation in sand properties over time.

Better Understanding of Contact Maturing

Microscopic behavior of inter-grain contacts is crucial in understanding and predicting aging behavior of sand. Results from laboratory tests and simulations reported in this thesis have shown some aspects of the evolution of contacts under sustained normal loads. However, there are a lot more aspects to be explored. For instance, contact maturing under more complex loading conditions need to be investigated to complete understanding of time-dependent behavior of contacts. Contacts in sand, under true conditions, are subject to far more complicated loading conditions than a simple normal loading. Rather, in most cases, the contacts are loaded with normal and shear forces, and, possibly, a torque. Time-dependent response of contacts under different

combinations of these loads needs to be better understood to improve understanding of the behavior of contacts during sand aging.

Bridging Microscopic Contact Maturing and Macroscopic Sand Aging

The research on microscopic aging behavior of contacts only helps understanding the macroscopic aging behavior of sand if there is an effective way to bridge the behavior at these two scales. Currently, the distinct element method (DEM) seems to be the most promising tool to facilitate this bridging effort. To successfully bridge behavior at these two scales, DEM simulations of sand grain assemblies should, at least, be able to improve effective simulations of two aspects: maturing of contacts, and more complex geometry of grain particles. The importance of the former has been discussed throughout this thesis. The latter aspect, the particle shapes, is equally important because the particle shapes control the fabrics of a sand grain assembly as the grains rearrange over time, and the fabric of a granular material largely controls its mechanical properties. Simulating either aspects with DEM today is challenging. A satisfactory constitutive law capable of describing contact maturing over time needs to be developed to simulate the first aspect. For the second aspect, complex-shaped particles (with bonded sub-particles) need to be used in the simulations, which requires an overwhelming computational power.

Sand Aging in Emerging Geotechnical Systems

The emerging geotechnical systems have created needs for understanding on sand properties that were not explored before, such as heat transferring properties, and aging effects under more complicated environmental conditions. For example, geo-energy systems are witnessing rapidly growing application and their long-term behavior in thermo-hydro-mechanical fields has yet to be well understood. In the energy foundations, for instance, soil-pile interactions develop in a thermo-hydro-mechanical field. Sand-pile heat transferring properties affects both the loading and the heat exchange between sand and the energy piles. Thus, knowing the long-term change in the sand-pile heat transfer property is important. More types of emerging geotechnical applications can be foreseen, which will bring more attention to sand aging.

References

Abraham, S. and Golay, M.J.E. (1964). "Smoothing and differentiation of data by simplified least squares procedures." *Analytical Chemistry,* 36(8), 1627-1639.

Al-Sanad, H.A. and Ismael, N.F. (1996). "Effects of Aging on Freshly Deposited or Densified Calcareous Sands." *Transportation Research Record* 1547, 76-81.

Afifi, S.S. and Richart, F.E., Jr. (1973). "Stress History Effects on Shear Modulus of Soils." *Soils and Foundations*, 13(1), 77-95.

Afifi, S.S. and Woods, R.D. (1971). "Long-term pressure effects on shear modulus of soils." *ASCE J. Soil Mech. Found. Div*., 97(10), 1445-1460.

Anderson, D.G. and Stokoe, K.H., II (1978). "Shear modulus: A time dependent soil property." *Dynamic Geotechnical Testing*, ASTM STP 654, 66–90.

Arango, I., Lewis, M.R., and Kramer, C. (2000). "Updated Liquefaction Potential Analysis Eliminates Foundation Retrofitting of Two Critical Structures." *Soil Dynamics and Earthquake Engineering* 20(1), 17-25.

Ashford, S.A., Rollins, K.M., and Lane, J.D. (2004). "Blast-Induced Liquefaction for Full-Scale Foundation Testing." *Journal of Geotechnical and Geoenvironmental Engineering*, 130(8), 798-806.

Attaway, S. (2012). *MATLAB: A practical introduction to programming and problem solving,* Elsevier Inc., Oxford, UK.

Axelsson, G. (2000). "Long Term Set-up of Driven Piles in Sand." Ph.D. Dissertation, Royal Institute of Technology, Stockholm, Sweden.

Bažant, Z.P. and Pang, S.D. (2007). "Activation energy based extreme value statistics and size effect in brittle and quasibrittle fracture." *J. Mech. Phys. Solids*, 55(1), 91-131.

Berkovich, E.S. (1950). "Three-Faceted Diamond Pyramid for Studying Microhardness by Indentation." *Zavodskaya Laboratoria*, 13(3), 345-347 (in Russian).

Baxter, C.D.P. and Mitchell, J.K. (2004). "Experimental Study on the Aging of Sands." *Journal of Geotechnical and Geoenvironmental Engineering,* 130(10), 1051-1062.

Bowman, E.T. and Soga, K. (2003). "Creep, Ageing and Microstructural Change in Dense Granular Materials." *Soils and Foundations*, 43(4), 107-117.

Bowman, E.T. and Soga, K. (2005). "Mechanisms of Setup of Displacement Piles in Sand: Laboratory Creep Tests." *Can. Geotech. J.,* 42(5), 1391-1407.

Cavarretta, I., Coop, M.R. and O'Sullivan, C. (2010). "The Influence of Particle Characteristics on the Behaviour of Coarse Grained Soils." *Géotechnique,* 60(6), 413-423.

Cavarretta, I., Rocchi, I. and Coop, M.R. (2011). "A New Interparticle Friction Apparatus for Granular Materials." *Canadian Geotechnical Journal,* 48, 1829-1840.

Charles, S.J. (1958). "Static fatigue of glass. I." *Journal of Applied Physics*, 29(11), 1549-1553.

Charlie, W.A., Rwebyogo, M.F. and Doehring, D.O. (1992). "Time-Dependent Cone Penetration Reisitance Due to Blasting." *Journal of Geotechnical Engineering,* 118(8), 1200-1215.

Chow, F.C., Jardine, R. J., Brucy, F. and Nauroy, J. F. (1997). "Time Related Increases in the Shaft Capacities of Driven Piles in Sand." *Géotechnique*, 47(2), 353–361.

Chow, F.C., Jardine, R.J., Brucy, F., and Nauroy, J.F. (1998). "Effects of Time on Capacity of Pipe Piles in Dense Marine Sand." *Journal of Geotechnical and Geoenvironmental Engineering*, 124(3), 254-264.

Cole, D.M., Mathisen, L.U., Hopkins, M.A., and Knapp, B.R. (2010). "Normal and Sliding Contact Experiments on Gneiss." *Granular Matter*, 12(1), 69–86.

Cole, D.M. and Peters, J.F. (2008). "Grain-Scale Mechanics of Geologic Materials and Lunar Simulants Under Normal Loading." *Granular Matter,* 10(3), 171–185.

COMSOL Inc. (2012). "Introduction to COMSOL Multiphysics." Stockholm, Sweden.

COMSOL Inc. (2012). "COMSOL Multiphysics User's Guide." Stockholm, Sweden.

COMSOL Inc. (2012). "COMSOL Live Link for MATLAB Users Guide." Stockholm, Sweden.

Cuallar, E., Roberts, D. and Middleman, L. (1987). "Static fatigue lifetime of optical fibers in bending." *Fiber and Integrated Optics*, 6(3), 203 – 213.

Cundall, P.A. and Strack, O.D.L. (1979). "A discrete numerical model for granular assemblies. Geotechnique." 29(1), 47–65.

Daramola, O. (1980). "Effect of consolidation age on stiffness of sand." *Géotechnique*, 30(2), 213-216.

DeJong, J.T., Fritzges, M.B., and Nüsslein, N. (2006). "Microbially Induced Cementation to Control San Response to Undrained Shear." *Journal of Geotechnical and Geoenvironmental Engineering,* 132(11), 1381-1392.

Dowding, C.H. and Hryciw, R.D. (1986). "A Laboratory Study of Blast Densification of Saturated Sand." *J. Geotech. Engrg.,* 132(11), 187-199.

Dumas, J.C. and Beaton, N.F. (1988). "Practical Problems from Surprising Soil Behavior." *J. Geotech. Engrg.,* 114(3), 367-368.

Einav, I. (2007). "Breakage Mechanics – Part I: Theory." *J. Mech. Physics Solids*, 55(6), 1274–1297.

Glasstone, S., Laidler, K.J. and Eyring, H. (1941). *The Theory of Rate Processes*, McGraw-Hill: New York.

Gohl, W.B., Howie, J.A., Hawson, H.H., and Diggle, D. (1994). "Field Experience with Blast Densification in an Urban Setting." *Proc. 5th U.S. National Conf. on Earthquake Engineering*, Chicago, Illinois, 221-230.

Guo, R. and Hueckel, T. (2015). "Silica polymer bonding of stressed silica grains: An early growth of intergranular tensile strength." *Geomechanics for Energy and the Environment,* 1, 48-59.

Howie, J.A., Shozen, T. and Vaid, Y.P. (2002). "Effect of Ageing on Stiffness of Very Loose Sand." *Canadian Geotechnical Journal*, 39(1), 149-156.

Hu, L.B. and Hueckel, T. (2007). "Coupled chemo-mechanics of intergranular contact: Toward a three-scale model." *Computers and Geotechnics*, 34(4), 306-327.

Hueckel, T., Cassiani, G., Tao, F., Pellegrino, A. and Fioravante, V. (2001). "Aging of oil/gas-bearing sediments, their compressibility, and subsidemce." *J. Geotech. Geoenv. Eng.*, 127(11), 926-938.

Human, C.A. (1992). "Time Dependent Property Changes of Freshly Deposited or Densified Sand." Ph.D. Dissertation, Department of Civil Engineering, University of California, Berkeley.

Itasca Consulting Group, Inc. (2008). "PFC2D (Particle Flow Code in 2 Dimensions) User's Guide, Version 4.0." Minneapolis, MN.

Itasca Consulting Group, Inc. (2008). "PFC3D (Particle Flow Code in 3 Dimensions) User's Guide, Version 4.0." Minneapolis, MN.

Jamiolkowski, M. and Manassero, M. (1995). "The Role of Insitu Testing in Geotechnical Engineering – Thoughts about the Future." *Proceedings of the International Conference in Advances in Site Investigation Practice*, ICE, London, Thomas Telford, 929-951.

Jardine, R. J., Standing, J. R. and Chow, F. C. (2006). "Some observations of the effects of time on the capacity of piles driven in sand." *Géotechnique*, 56(4), 227–244.

Jefferies, M.G. and Rogers, B.T. (1993). "Discussion of 'Time-Dependent Cone Penetration Resistance Due to Blasting' by W.A. Charlie, M. F.J. Rwebyogo and D.O. Doehring." *Journal of Geotechnical Engineering*, 119(12), 2008-2012.

Johnson, K.L. (1985). *Contact Mechanics*, Cambridge University Press, Cambridge, UK.

Joshi, R. C., Achari, A., Kaniraj, S.R., and Wijeweera, H. (1995). "Effect of aging on the Penetration Resistance of Sands." *Canadian Geotechnical Journal*, 32(5), 767-782.

Kaya, H. (2013). "Fractal landscape generation with diamond-square algorithm." <http://cn.mathworks.com/matlabcentral/fileexchange/44714-fractal-landscape-generation-with-diamond-square-algorithm>, *MATLAB Central File Exchange*, retrieved Dec 17, 2013.

Kolymbas, D. and Bauer, E. (1993). "Soft oedometer - A new testing device and its application for the calibration of hypoplastic constitutive laws." *Geotechnical Testing Journal,* 16(2), 263-270.

Krinsley, D.H. and Doornkamp, J.C. (1973). *Atlas of quartz sand surface textures*, Cambridge University Press, Cambridge, UK.

Krauskopf, K.B. (1959). "The geochemistry of silica in sedimentary environments." Silica in Sediments (SP7), The Society of Economic Paleontologists and Mineralogists (SEPM).

Krausz, A.S. and Krausz, K. (1988). *Fracture Kinetics of Crack Growth*, Kluwer, Boston.

Kroll, R.G. (1990). "Alkalophiles". *Microbiology of Extreme Environments,* edited by C. Edwards, McGraw-Hill, New York, 55-92.

Kuhn, M.R. (1987). "Micromechanical Aspects of Soil Creep." Ph.D. Dissertation, University of California, Berkeley, California.

Kulhawy, F.H. and Mayne, P.W. (1990). "Manual on Estimating Soil Properties for Foundation Design." *EL-6800, Research Project 1493-6*, Electric Power Research Institute, Palo Alto, CA.

Lade, P.V. and Karimpour, H. (2010). "Static Fatigue Controls Particle Crushing and Time Effects in Granular Materials." *Soils and Foundations*, 50(5), 573-583.

Leon, E., Gassman, S. and Talwani, P. (2006). "Accounting for Soil Aging When Assessing Liquefaction Potential." *Journal of Geotechnical and Geoenvironmental Engineering,* 132(3), 363-377.

Liao, T. and Mayne, P.W. (2006). "Cone Penetrometer Measurements During Mississippi Embayment Seismic Excitation Experiment." *Earthquake Engineering and Soil Dynamics,* GSP 133, 1-12.

Lu, W. (2014). ME 576 Nano/Micro Structure Evolution, Class Notes, the University of Michigan, Ann Arbor.

Mahaney, W.C. (2002). *Atlas of Sand Grain Surface Textures and Applications*, Oxford University Press, Oxford, UK.

McDowell G. R. and Bolton, M. D. (1998). "On the micromechanics of crushable aggregates.*" Géotechnique*, 48(5), 667-679.

Mesri, G., Feng, T.W. and Benak, J.M. (1990). "Postdensification penetration resistance of clean sand." *J. Geotech. Eng.*, 116(7), 1095-1115.

Mesri, G. and Vardhanabhuti, B. (2009). "Compression of granular materials." *Canadian Geotechnical Journal,* 46, 369-392.

Michalowski, R.L. (2005). "Coefficient of earth pressure at rest." *Journal of Geotechnical and Geoenvironmental Engineering*, 131(2), 1429-1433.

Michalowski, R.L. and Nadukuru, S.S. (2010). "Stress corrosion cracking and relaxation of deviatoric stress after dynamic compaction of sand." 37th Solid Mechanics Conference (SolMech 37), Warsaw, Sept. 6-11.

Michalowski, R.L. and Nadukuru, S.S. (2012). "Static fatigue, time effects, and delayed increase in penetration resistance after dynamic compaction of sand." *Journal of Geotech. Geoenv. Engineering*, 138(5), 564-574.

Michalowski, R.L. and Nadukuru, S.S. (2014). "Contact fatigue: A key mechanism of time effects in silica sand." *IS-Cambridge 2014, From Micro to Macro*, edited by K. Soga et al., Cambridge, U.K., Sept. 1-3, 2014; Taylor & Francis, London, 1201-1204.

Mitchell, J.K. (2008). "Aging of sand – a continuing Enigma?" *6th Int. Conf. on Case Histories in Geotechnical Engineering*. Arlington, VA, Aug. 11-16, 2008, 1-21.

Mitchell, J.K. and Santamarina, J.C. (2005). "Biological Considerations in Geotechnical Engineering." *Journal of Geotechnical and Geoenvironmental Engineering*, 131(10), 1222-1233.

Mitchell, J.K. and Solymar, Z.V. (1984). "Time-dependent strength gain in freshly deposited or densified sand." *J. Geotech. Eng.*, 110(11), 1559-1576.

Nadukuru, S.S., O'Connor, S.M. and Michalowski, R.L (2012). "Static fatigue and delayed effects in sand and Lunar regolith." *ASCE Earth and Space 2012*, April 15-18, 2012, Pasadena, CA, 256-263.

Nadukuru S.S. (2013). "Static Fatigue: A Key Cause of Time Effects in Sand." Ph.D. Dissertation, Department of Civil and Environmental Engineering, University of Michigan, Ann Arbor.

Narsilio, G.A., Santamarina, J.C., Hebeler, T., and Bachus, R. (2009). "Blast Densification: Multi-Instrumented Case History." *J. Geotech. Geoenviron. Eng.,* 135(6), 723-734.

National Instruments Corp. (2007). "Operating Instructions and Specifications for NI 9219." Austin, Texas.

National Instruments Corp. (2007). "Operating Instructions and Specifications for NI 9234." Austin, Texas.

National Instruments Corp. (2007). "Operating Instructions and Specifications for NI 9237." Austin, Texas.

National Instruments Corp. (2007). "Operating Instructions and Specifications for NI 9263." Austin, Texas.

National Instruments Corp. (2015). "NI CompactDAQ USB Data Acquisition Systems." Austin, Texas.

Novotechnik U.S. Inc. (2009). "T/TS/TR/TRS Instructions for Use." Southborough, Massachusetts.

Novotechnik U.S., Inc. (2007). "Position Transducers with Restoring Spring, 10, 25, 50, 75, 100 mm, TR, TRS Series." Southborough, Massachusetts.

Obrzud R. and Truty, A. (2012). "The Hardening Soil Model - A Practical Guidebook." *Zace Services, Z Soil PC 100701 report,* Lausanne, Switzerland.

Potyondy, D.O. and Cundall, P.A. (2004). "A bonded-particle model for rock." *Int. J. Rock Mech. Min. Sci.*, 41 (8), 1329-1364.

Potyondy, D.O. (2007). "Simulating stress corrosion with a bonded-particle model of rock." *Int. J. Rock Mech. Min. Sci.,* 44(5), 677-691.

Rimoy, S., Silva, M., Jardine, R., Yang, Z.X., Zhu, B.T., and Tsuha, C.H.C. (2015). "Field and Model Investigations into the Influence of Age on Axial Capacity of Displacement Piles in Silica Sands." *Géotechnique*, 65(7), 576–589.

Saftner, D.A. (2011). "Time-Dependent Strength Gain in Recently Disturbed Granular Materials." Ph.D. Dissertation, Department of Civil and Environmental Engineering, University of Michigan, Ann Arbor, Michigan.

Schmertmann, J.H. (1987). "Time-dependent strength gain in freshly deposited or densified sand." Discussion, *J. Geotech. Eng.* 113(2), 173-175.

Schmertmann, J.H. (1991). "The mechanical aging of soils." *J. Geoecht. Eng.*, 117(9), 1288-1330.

Scholz, C.H. (1968). "Mechanism of creep in brittle rock." *J. Geophys. Res.,* 73(10), 3295-3302.

Scholz, C.H. (1972). "Static fatigue of quartz." *J. Geophys. Res.,* 77(11), 2104-2114.

Seed, H.B. (1979). "Soil Liquefaction and Cyclic Mobility Evaluation for Level Ground During Earthquakes." *Journal of Soil Mechanics and Foundations Division*, 105(2), 201-235.

Senetakis, K., Coop, M.R. (2013). "The development of a new micro-mechanical inter-particle loading apparatus." *Geotechnical Testing Journal*, 37(6), 1-12.

Skempton, A.W. (1986). "Standard Penetration Test Procedures and the Effects in Sands of Overburden Pressure, Relative Density, Particle Size, Ageing, and Overconsolidation." *Geotechnique*, 36(3), 425-447.

Suarez, N.R. (2012). "Micromechanical Aspects of Aging in Granular Soils." Ph.D. Dissertation, Department of Civil and Environmental Engineering, Virginia Polytechnic Institute and State University (Virginia Tech), Blacksburg, Virginia.

Sun, B, Suo, Z, and Yang, W. (1997) "A finite element method for simulating interface motion – I. Migration of phase and grain boundaries." *Acta Metallurgica,* 45(5), 1907-1915.

Tatsuoka, F., Di Benedetto, H., Kongkitkul, W., Kongsukprasert, L., Nishi, T. and Sano, Y. (2008). "Modelling of ageing effects on the elastic-viscoplastic behaviour of geomaterials." *Soils and Foundations*, 48(2), 155-174.

Tavenas, F. and Audy, R. (1972). "Limitations of the Driving Formulas for Predicting the Bearing Capacities of Piles in Sands." *Can. Geotech. J.,* 9(1), 47-62.

Towhata, I. (2008). *Geotechnical Earthquake Engineering*, Springer Berlin Heidelberg, Berlin, Germany.

Troncoso, J.H. and Garcés, E. (2000). "Ageing effects on the shear modulus of soils", *Soil Dynamics and Earthquake Engineering*, 19(8), 595-601.

Vishay Precision Group, Inc. (2011). "Surface Preparation for Strain Gage Bonding." *Micro-Measurements Application Note B-129,* Raleigh, North Carolina.

Vishay Precision Group, Inc. (2010). "Strain Gage Applications with M-Bond AE-10, AE-15 and GA-2 Adhesive Systems." *Micro-Measurements Application Note B-137,* Raleigh, North Carolina.

Vishay Precision Group, Inc. (2010). "Strain Gage Accessories Micro-Measurements." *Micro-Measurements Interactive Data Book*, Raleigh, North Carolina.

Vishay Precision Group, Inc. (2010). "Quality Control of Strain Gage Installations." *Micro-Measurements Application Note VMM-15*, Raleigh, North Carolina.

Vishay Precision Group, Inc. (2015). "General Purpose Strain Gages—Tee Rosette." *Micro-Measurements Technical Booklet*, Raleigh, North Carolina.

Vishay Precision Group, Inc. (2010). "Protective Coatings, General Information." *Micro-Measurements Technical Booklet*, Raleigh, North Carolina.

Voss, R.F. (1985). *Random fractal forgeries,* Springer, Berlin 1985.

Wang, Y.H, Gao, Y. and Ooi, G.L. (2016). "Experimental characterizations of an aging mechanism of sands." *Journal of Geotech. Geoenv. Engineering*, 142(2), 06015016.

Wang, Z. and Michalowski, R.L. (2015). "Contact Fatigue in Silica Sand - Observations and Modeling." *Journal of Geomechanics for Energy and the Environment*, 4, 88-99.

Wang, Y.H. and Tsui, K.Y. (2009). "Experimental Characterization of Dynamic Property Changes in Aged Sands." *J. Geotech. Geoenviron. Eng.,* 135(2), 259-270.

Wang, G., and Um, W. (2012). "Mineral dissolution and secondary precipitation on quartz sand in simulated Hanford tank solutions affecting subsurface porosity." *Journal of Hydrology,* 472, 159-168.

Wiederhorn, S.M., Yi, F., LaVan, D., Richter, L.J., Fett, T. and Hoffmann, M.J. (2014). "Volume Expansion Caused by Water Penetration into Silica Glass." *J. Am. Ceram. Soc.*, 98(1) 78–87.

Williams, E.D. and Bartlett, N.C. (1991). "Thermodynamics of surface morphology." *Science*, 251, 393-400.

Yang, Z., Guo, W., Jardine, R., and Chow, F. (2016). "Design Method Reliability Assessment from an Extended Database of Axial Load Tests on Piles Driven in Sand." *Can. Geotech. J.,* available online August 2016, 1-16.

Zhang, Z. and Wang, Y.H. (2016). "DEM Modeling of Aging or Creep in Sand Based on the Effects of Microfracturing of Asperities and Evolution of Microstructural Anisotropy during Triaxial Creep." *Acta Geotechnica,* 11(6), 1303-1320.

Zhang, Z. and Wang, Y.H. (2015). "Examining Setup Mechanisms of Driven Piles in Sand Using Laboratory Model Pile Tests." *J. Geotech. Geoenviron. Eng.,* 141(3), 04014114, 1-12.

Zhao, B., Wang, J., Coop, M.R., Viggiani, G. and Jiang, M. (2015). "An investigation of single sand particle fracture using X-ray micro-tomography." *Géotechnique,* 65(8), 625-641.